Electronic Thesis and Dissertation Repository

January 2020

Seismic Performance of Superelastic Shape Memory Alloy Reinforced Concrete Shear Wall Systems

Emad A. Abraik, *The University of Western Ontario*

Supervisor: Maged A. Youssef, *The University of Western Ontario*
A thesis submitted in partial fulfillment of the requirements for the Doctor of Philosophy degree in Civil and Environmental Engineering
© Emad A. Abraik 2020

Follow this and additional works at: https://ir.lib.uwo.ca/etd

Part of the Structural Engineering Commons

ABSTRACT

A major sustainability issue for reinforced concrete (RC) structures is the residual deformations caused by the yielding of the steel bars during extreme seismic events. Numerous efforts have been made to develop self-centering structures, which minimize these deformations and the associated seismic damage. Superelastic shape memory alloys (SE-SMA) can be utilized in concrete elements to achieve such behaviour. This thesis focuses on the use of SE-SMA bars in RC walls.

First, the thesis starts by conducting a fragility analysis to assess the seismic performance and vulnerability of ten and twenty-story SE-SMA RC walls. SE-SMA bars are used within the plastic hinge length of the walls and are assumed to replace all longitudinal steel bars or those reinforcing the boundary elements. The considered walls were found to possess an adequate margin of safety against collapse as compared to steel RC walls.

Due to the unique properties of SE-SMA material, the ductility and overstrength factors for SE-SMA RC walls are then evaluated. Nine-hundred and seventy-two walls were analyzed to investigate the effects of different design parameters on the ductility and overstrength factors. Suggested values for the design factors were then evaluated by conducting nonlinear time history analyses for three, six, and nine-story buildings.

The seismic performance of SE-SMA RC dual systems is evaluated. Incremental dynamic analysis is carried out under considering different seismic load events. Results allowed choosing a suitable SE-SMA layout for dual systems to achieve good seismic performance.

The seismic performance of RC core walls is significantly different from rectangular RC walls because of their ability to resist bidirectional and torsional loading. The seismic performance

of reinforced concrete core walls under unidirectional and bidirectional seismic excitations, while accounting for variations in the torsional eccentricity, was examined. SE-SMA bars reduced not only the mean lateral displacements but also the floor rotations.

Finally, and to mitigate the seismic residual deformations and corrosion problems associated with steel RC walls, the seismic performance of walls reinforced with SE-SMA bars or hybrid (SMA-FRP) bars over the plastic hinge length and fiber-reinforced polymers (FRP) elsewhere is examined. The SMA-FRP bars resulted in a significant improvement in the wall capacity as compared to SE-SMA bars. Also, they resulted in lower seismic damage.

Keywords: Shear wall; Superelastic shape memory alloy; Cyclic behaviour; Seismic performance; Response modification factor; Overstrength; Ductility; Multi-strip analysis; Inter-story drift; Residual displacement; Fiber reinforcement; Dynamic analysis; Core wall; Mass eccentricity; Dual system; Incremental dynamic analysis; Local and global response; Fiber reinforcement.

SUMMARY FOR LAY AUDIENCE

Reinforced concrete shear walls are commonly used to resist lateral loads. Although they were able to prevent failure during major earthquakes, they had experienced severe damage and were permanently deformed. In most cases, such damage had led to demolishing the affected buildings. The thesis proposes the use of a novel material, superelastic shape memory alloy (SE-SMA), to mitigate such damage and achieve sustainable buildings. The use of SE-SMA in typical RC lateral load systems including: cantilever walls, dual systems, and core walls are examined and recommendations for their use are given. The thesis also introduces a new resilient lateral load system that can be used in areas where steel corrosion is expected to be a problem.

COPYRIGHT AND CO-AUTHORSHIP

This doctoral thesis is prepared according to the regulations for an integrated-article format thesis stipulated by the faculty of Graduate and Post-Doctoral Studies at Western University. All design and analytical studies were conducted by the author of this thesis under the supervision of Dr. Maged A. Youssef. Major portions of the work outlined in this thesis have been published or are under review for possible publication in peer-reviewed technical journals and conferences. The author wrote the initial drafts of the manuscripts, while his research advisor, Maged A. Youssef, contributed to the final version of the manuscripts. The publications are as follows:

REFEREED JOURNAL PUBLICATIONS

- **Abraik**, **E**., & Youssef, M. A. (2018). Seismic fragility assessment of superelastic shape memory alloy reinforced concrete shear walls. Journal of Building Engineering, 19, 142-153.

- **Abraik**, **E**., & Youssef, M. A. Ductility and overstrength of shape-memory-alloy reinforced concrete shear walls. Bulletin of Earthquake Engineering. Submitted (under review).

- **Abraik**, **E**., Youssef, M. A., & El-Fitiany, S. F. Seismic performance of reinforced concrete core walls equipped with shape memory alloy bars. To be submitted.

- **Abraik**, **E**., Youssef, M. A., & El-Fitiany, S. F. Seismic performance of hybrid concrete shear walls reinforced with shape memory alloy and fiber. To be submitted.

REFEREED CONFERENCE PROCEEDINGS

- **Abraik**, **E**. A., Youssef, M. A., & El-Fitiany, S. F. (2019). Damage mitigation of conventional RC shear walls in high seismic zones. 12th Canadian Conference on Earthquake Engineering (12CCEE), Quebec City, QC, Canada.

- **Abraik**, **E**., & Youssef, M. A. (2018). Seismic performance of shape memory alloy reinforced concrete dual systems. 16th European Conference on Earthquake Engineering (16ECEE), Thessaloniki, Greece.

- **Abraik**, **E**. A., & Youssef, M. A. (2016). Performance assessment of three-story shape memory alloy reinforced concrete walls. Annual Conference of the Canadian Society of Civil Engineering (CSCE). London, ON, Canada.

- **Abraik**, **E**., & Youssef, M. A. (2015). Cyclic performance of shape memory alloy reinforced concrete walls. In Fifth International Workshop on Performance, Protection & Strengthening of Structures under Extreme Loading, Lansing, MI, USA. No. 5: pp. 326-333.

DEDICATION

To my parents
Ehmida and Weddad

To my lovely wife
Fatma Boshiha

To my kids
Weddad, Mohammed, Ahmed, and Maria

To my brother and my sisters
Abdulsalam, Faiza, and Zobiuda.

ACKNOWLEDGEMENT

I would like to express my sincere appreciation to my advisor, Professor Maged A. Youssef, for his guidance and invaluable support throughout the years and for giving me the opportunity to work under his supervision. Without his help, the thesis could not be completed. The advice, support, and editing by Dr. Salah Fitiany is extremely appreciated.

Special thank goes out to my parents for their unconditional love and support throughout the years. I am truly grateful for the sacrifices they made in their lives to give me the best possible education. I am blessed to have them. I also wish to express my gratitude to all those who have given me emotional support and encouragement: to my brother, Abdulsalam, to my sisters, Faiza and Zobiuda.

I would like to express my deepest gratitude to my wife Fatma for being with me at every step of my life and for making me smile every day. Thank you for your true love and support for all these years. I wish to thank my lovely children, Weddad, Mohammed, Ahmed, and Maria, for being with me to accomplish this work.

Finally, I would also like to thank the Libyan Ministry of Higher Education for their financial support for this research and to my colleagues at Western University for their help and support.

<div align="right">Emad A. Abraik</div>

TABLE OF CONTENTS

LIST OF TABLES

LIST OF FIGURES

LIST OF ABBREVIATIONS

ACMR	Adjusted collapse margin ratio
AR	Aspect Ratio
CMR	Collapse margin ratio
CMS	Conditional mean spectra
CM	Center of mass
CR	Center of rigidity
DAF	Displacement amplification factor
IDA	Incremental dynamic analysis
GFRP	Glass-fiber-reinforced polymer
MCE	Maximum considered earthquake
MSA	Multi-strip analysis
MID	Mean inter-story drift ratio
MRID	Mean residual inter-story drift ratio
MSE	Mean square error
RC	Reinforced Concrete
SFI-MVLE	Shear-Flexural-Interaction Multi-Vertical-Line-Element
SSF	Spectra shape factor
SE-SMA	Superelastic shape memory alloy

LIST OF NOTATIONS

P	Axial load ratio
P_s	Axial force on columns
a_f	Allowable floor acceleration
$\varepsilon_{y,j}$	Average normal strain
d_b	Bar diameter
b	Beam width
h	Beam height
L	Beam length
A_g	Cross-section area
f_c'	Concrete compressive strength

I_g	Column second moment of inertia
E_c	Concrete modulus of elasticity
G_c	Concrete shear modulus
R_μ	Ductility response factor
μ, R_d	Ductility factor
V	Design base shear
S_{DS}	Design spectra in a short period
V_e	Elastic base shear
I_e	Effective column second moment of inertia
A_{cv}	Effective shear area
V_{eff}	Effective shear stiffness
V_s	First yield strength
M_f	Factored moment
IM	Ground motion intensity
ID	Inter-story Drift
K_1	Initial stiffness
E_{SMA}	Initial modulus of elasticity of shape memory alloy
B_x	Irregularity ratio
l_{bl}	Length of wall boundary element
Δ_{max}	Maximum displacement corresponding to peak shear strength
$\hat{S}_{CT}$	Median collapse capacity
S_{MT}	Maximum considered earthquake corresponding to the fundamental period
T_{1s}	Minimum fundamental period
E	Modulus of elasticity
M_r	Moment of resistance
n	Number of ground motions considered
n_j	Number of ground motions causing collapses
M	Number of intensity measure levels
$\Omega = R_0$	Overstrength factor
F_y	Peak base shear
μ_T	Period based ductility
L_P	Plastic hinge length
	Plastic curvature

$\emptyset_p$	
K_2	Post-Activation Stiffness
R	Response modification factor
x	Realized condition of the ground motion intensity measure
h_{sp}	Rigid link spacing
T_2	Second structure period
T_1	Structure fundamental period, Maximum fundamental period
f_y	Steel yield strength
E_s	Steel modulus of elasticity
f_{y-SMA}	Shape memory alloy yield strength
A_{sh}	Shear area
K_s	Shear flexibility stiffness for zero-spring
S_a	Spectra acceleration
C	Specific damage level
$P - \Delta$	Second-order analysis
h_{tot}	The roof height with respect to the base
V_y	Wall shear capacity
H	Wall height
L_w	Wall length
b_w	Wall thickness
l_w	Wall web length
t_w	Wall web thickness
t_f	Wall flange thickness
l_f	Wall flange length
M/V	Wall Shear span
D_y	Yield displacement
$\emptyset_y$	Yield curvature

LIST OF LATIN NOTATIONS

ε_c	Concrete strain
$\dot{\theta}$	Estimate for a median of the fragility function

$\dot{\beta}$	Estimate for standard deviation
Δ_y	Lateral yielding displacement
θ	Median of the fragility function
β_{TOT}	Modal uncertainty
ρ	Reinforcement ratio in beams or columns
ϕ	Standard normal cumulative distribution
α_c	Section property reduction factor used for column effective stiffness properties
ε_y	Steel yield strain
u_{sh}	Shear deformation
δ_x	Story displacement
β	The ratio of forward to reverse activation stress
u_y	Vertical deformation
ρ_{vb}	Wall vertical steel ratio in the boundaries
ρ_{hb}	Wall horizontal steel ratio in the boundaries
ρ_{vw}	Wall vertical steel ratio in the web
ρ_{hw}	Wall horizontal steel ratio in the web

CHAPTER 1

INTRODUCTION

1.1 BACKGROUND

Earthquakes take the lives of thousands of people and cause extensive structural damage. The 2011 New Zealand Christchurch earthquake resulted in losses of about NZ $40 billion (Marquis et al. 2017). The extensive damage required demolishing several tall buildings and caused the closure of the central business district for over two years. These facts indicate that the modern seismic design philosophy, which allows buildings to experience significant inelastic deformations to dissipate seismic energy, has achieved its target performance level and prevented collapse, but failed in achieving sustainable buildings. The residual deformations have made repairs economically unviable and forced demolition as the only option.

Reinforced Concrete (RC) walls, dual walls, and core walls are widely used structural elements that provide resistance against lateral loads caused by winds or earthquakes. Their high stiffness and strength control damage to the non-structural elements by limiting the inter-story drifts during moderate seismic events. However, severe damage, which is accompanied by significant residual deformations, is expected for strong seismic events. Steel rebars are the main reason for this severe damage due to their yielding behaviour. Steel bars are also highly susceptible to corrosion.

Currently, owners and engineers do not want to sacrifice their structures during an extreme event. The performance-based seismic design allows owners, researchers, and designers to select the performance objectives for structural and non-structural building components considering specific seismic events or the aggregate hazard. Most recently, new seismic protection concepts, such as resilience-based design by Bruneau and Reinhorn (2007), have emerged to minimize structural damage through new technologies and advanced materials.

Superelastic (SE) shape memory alloys (SMA) have widely attracted the attention of researchers due to their unique material properties. SE-SMA can undergo large deformations

of 7% strain and recover all the inelastic deformations upon unloading. Their utilization in concrete structures can significantly reduce seismic residual deformations, which can facilitate post-seismic retrofitting.

Although the existing literature provides some research data on using the SE-SMA material in concrete walls, previous research did not address their probability of failure, the need for new seismic design factors, their use in dual systems and core walls, and their hybrid use with other novel materials. This thesis addresses these shortcomings. The following sections present the objectives, scope and organization of the thesis.

1.2 OBJECTIVES

The main objective of the present study is to investigate the seismic performance of SE-SMA RC walls. This was achieved by pursuing the following objectives:

❖ Conduct a literature review that summarizes the behaviour of RC walls during seismic excitations, applications of SE-SMA in civil engineering, and approaches for seismic design.

❖ Compare the seismic behaviour of steel RC walls and SE-SMA RC walls by examining the seismic fragility curves.

❖ Define the overstrength and the ductility factors of SE-SMA RC walls that can be used for design purposes.

❖ Investigate the seismic performance of SE-SMA dual RC walls.

❖ Determine the torsional effects on SE-SMA RC core walls.

❖ Introduce the rational use of SE-SMA bars with Glass Fiber-Reinforced Polymer (GFRP) bars to achieve a resilient structural system.

1.3 ORGANIZATION AND OUTLINE

This dissertation is divided into eight chapters, including this introductory chapter. Chapter 2 provides a review of potential failure modes for shear walls, shape memory alloys, performance based-earthquake engineering, seismic applications of SMA in civil engineering, and numerical modeling. Chapters 3 to 7 address the stated objectives as summarized below.

Chapter 8 provides a general summary of the thesis, the obtained conclusions, major contributions, and limitations for the conducted research. It ends with suggested research topics for future research.

1.3.1 Seismic fragility assessment of superelastic shape memory alloy reinforced concrete shear walls (Chapter 3)

Mitigation of seismic damage can be achieved through self-centering techniques. One of the potential techniques involves the use of SE-SMA bars in RC structures. This chapter explores the use of these bars in the plastic-hinge regions of RC walls. The seismic performance and vulnerability of SE-SMA RC walls of ten- and twenty-story buildings are analytically assessed using fragility curves. The maximum inter-story drift, residual drift, and damage scheme were evaluated using multi-strip analyses. The results demonstrated the superior seismic performance of SE-SMA RC walls as compared to conventional steel RC walls.

1.3.2 Ductility and overstrength of shape memory alloy reinforced concrete shear walls (Chapter 4)

The unique properties of SE-SMA bars have motivated researchers to investigate their use as reinforcing bars for concrete elements. They were found to cause a significant decrease in seismic residual deformations while increasing seismic inelastic deformations. This characteristic deformation behaviour requires an assessment of the ductility and overstrength of SE-SMA RC walls. This chapter addresses this requirement. A total of 972 walls were analyzed under a quasi-static lateral load. Results indicated that the ductility and overstrength of SE-SMA RC walls depend on the amount and location of the SE-SMA bars. Suitable values for the overstrength and ductility factors were proposed for two proposed locations of SE-SMA bars. FEMA P695 was then used to evaluate the proposed seismic design parameters.

1.3.3 Seismic performance of shape memory alloy reinforced concrete dual systems (Chapter 5)

Reinforced concrete dual systems utilize concrete shear walls as well as moment frames to resist seismic loads. This system increases the energy dissipation capacity and is suitable for any building height. This chapter evaluates the effect of utilizing SE-SMA bars on the performance of 10-story RC dual-system buildings. Two designs are considered, which differ in the lateral seismic force resisted by the walls (72% and 50%). SE-SMA bars are utilized in the RC walls and frames at the plastic hinge locations. Incremental Dynamic Analysis (IDA) is then conducted to investigate their seismic behaviour under different ground motion intensity levels. SE-SMA RC dual systems showed superior seismic performance when compared with conventional steel RC dual systems.

1.3.4 Seismic performance of concrete core walls reinforced with shape memory alloy bars (Chapter 6)

RC core walls are widely used to resist lateral loads because of their high flexural and torsional stiffness. Their seismic performance parameters, including residual displacement, floor acceleration, and residual in-plane rotation, were examined by many researchers. However, reports from previous earthquakes highlighted the high repair cost associated with residual displacements and/or rotations. This chapter investigates the effect of using self-centering SE-SMA bars on the seismic performance parameters of RC core walls. A case study building was analyzed, assuming unidirectional and bidirectional seismic excitations. Different mass eccentricities were assumed. SE-SMA RC core walls were found to have significantly reduced floor accelerations, residual displacements, and residual in-plane rotations compared to steel RC core walls.

1.3.5 Seismic Performance of Hybrid Corrosion-Free Self-Centering Concrete Shear Walls (Chapter 7)

RC walls are extensively used in high-rise buildings to resist lateral loads while ensuring an adequate level of ductility. Durability problems, including low corrosion resistance of

conventional steel reinforcement, necessitate exploring alternative types of reinforcement. GFRP is a potential solution. However, it cannot be used in seismic applications because of its brittleness and inability to dissipate seismic energy. SE-SMA is a corrosion-free material with high ductility and unique self-centering ability. Its high cost is a major barrier to its widespread use in construction projects. This chapter investigates the hybrid use of SE-SMA and GFRP in concrete shear walls. An extensive parametric study was conducted to study the effect of different design parameters on the seismic performance of hybrid RC walls. The hybrid usage of GFRP and SE-SMA in RC walls not only solved the durability problem but also significantly improved the seismic performance, as measured by the maximum residual displacements and the damage schemes.

1.4 SUMMERY

The thesis starts by investigating the use of SE-SMA material in RC walls, then, proposes ductility and overstrength factors for SE-SMA RC walls. To cover other potential lateral load systems, the thesis also evaluates the seismic performance of dual systems and core walls. The thesis ends by examining the performance of hybrid corrosion-free SE-SMA RC walls.

1.5 REFERENCES

Bruneau, M., & Reinhorn, A. (2007). Exploring the concept of seismic resilience for acute care facilities. Earthquake Spectra, 23(1), 41-62.

Marquis, F., Kim, J. J., Elwood, K. J., & Chang, S. E. (2017). Understanding post-earthquake decisions on multi-storey concrete buildings in Christchurch, New Zealand. Bulletin of earthquake engineering, 15(2), 731-758.

CHAPTER 2

LITERATURE REVIEW

Under strong earthquakes or extreme lateral loads, RC buildings may exhibit significant residual drifts and, therefore, require major retrofitting. Smart materials, including SE-SMA, have been introduced to replace conventional steel bars in RC structures. SE-SMA can undergo excessive inelastic deformations but can return to their original shape after load removal (Moni, 2011). The following sections present details about the seismic behaviour of shear walls, SMA characteristics and behaviour, applications of SMA in civil engineering, and the seismic design approaches.

2.1 SEISMIC BEHAVIOUR OF SHEAR WALLS

In concrete buildings, the main lateral-load resistance system can be composed of moment-resisting frames and/or structural walls. The walls can be designed to be ductile by following special detailing requirements. Several wall configurations are widely used, including low-rise and high-rise (slender), as illustrated in **Figure 2.1**.

Wall's behaviour is generally classified according to their aspect ratio (H_w/L_w) or based on their shear-to-span ratio (M/VL_w).

where H_w is the wall height, L_w is the wall length.

Shear behaviour dominates for aspect ratios of 1.5 or less (squat walls) (Kolozvari, 2013). Flexure behaviour becomes dominant for aspect ratios higher than 2.0 (slender walls). For aspect ratios between 1.5 to 2.0, the behaviour is controlled by both shear and flexure (moderate walls). The seismic behaviour of slender and squat walls was experimentally evaluated by a number of researchers (Thomsen and Wallace, 2004; Farvashany et al., 2008; Brueggen and French, 2010). For moderate walls, it was found that the nonlinear shear behaviour may be significant, which can lead to lower elastic stiffness and flexural strength (Massone et al., 2006).

Figures 2.2 to **2.5** provide a summary of the expected failure modes for RC walls, which are also listed below.

1. Flexural failure:

   This failure is characterized by flexural cracks near the bottom of the wall, yielding of tensile steel bars, and crushing of concrete. Buckling of steel rebars may also occur after spalling off the concrete cover, as shown in **Figure 2.2.**

2. Shear failure:

   This failure is characterized by severe cracking of the concrete wall web. This type of failure occurs when the wall is subjected to high axial load and very high shear stresses, as shown in **Figure 2.3**.

3. Sliding failure:

   This type of failure occurs along the construction joints after or along weakened sections, which result from the yielding of the vertical reinforcement. **Figure 2.4** shows a wall with a weakened surface along the foundation interface.

4. Diagonal compression failure:

   If the vertical and horizontal reinforcements are sufficient to resist high shear stress, failure can occur by crushing the diagonal compression struts, as shown in **Figure 2.5**.
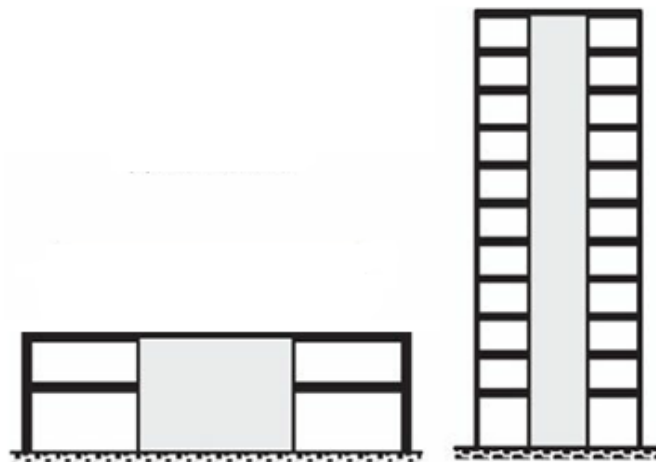
Figure 2.1. Sample structural wall configurations (Moehle, 2014)

(a)	(b)

Figure 2.2. Failure of RC walls: (a) Chile earthquake; (b) Christchurch, New Zealand (Marius, 2013)

(a)	(b)	(c)

Figure 2.3. Shear failure of RC walls: (a) L'Aquila, Italy; (b) Christchurch, New Zealand; (c) conception, Chile (Marius, 2013)
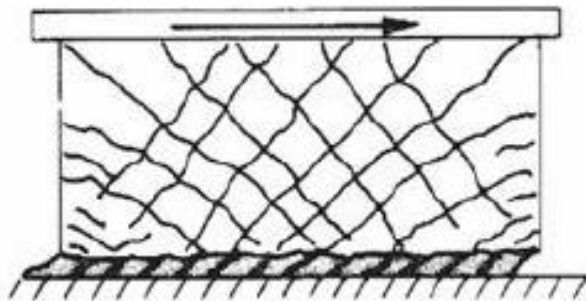
Figure 2.4. Sliding shear failure of RC walls (Moehle, 2014)
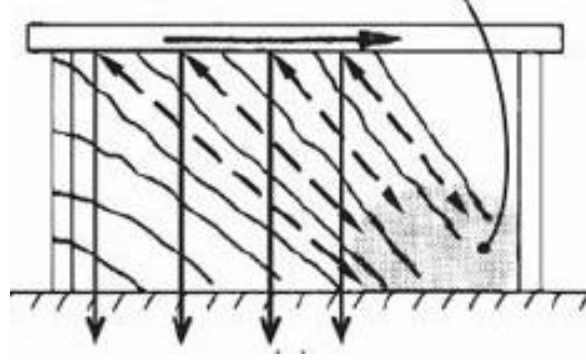
Figure 2.5. Diagonal compression failure of RC walls (Moehle, 2014)

2.2 LATERAL BEHAVIOUR OF RC WALLS

2.2.1 Load-deflection response

The lateral load-deflection response of RC walls can be described as a linear response followed by a nonlinear response. The linear response is referring to the wall response before yielding of longitudinal reinforcement or concrete crushing. Flexural displacement (Δ_f), shear displacement (Δ_v), and sliding displacement (Δ_s) are the three components, which should be considered to calculate the total displacement (Δ) as expressed by Eq. 2.1 [Segura, 2017].

$$\Delta = \Delta_f + \Delta_v + \Delta_s \tag{2.1}$$

$$\Delta_f = \frac{\phi_y {H_w}^2}{3} \tag{2.2}$$

$$\Delta_v = \frac{V H_w}{A_{cv} G} \tag{2.3}$$

$$\Delta_s = \theta H_w \tag{2.4}$$

where ϕ_y is yield curvature, H_w is the wall height, V is the shear force, A_{cv} is the effective shear area, G is the effective shear modulus, and θ is the rigid body rotation resulting from the slip.

Beyond the yield point (nonlinear response), the effects of the interaction between the flexural and shear should be considered. For flexural deformation, the moment diagram and curvature diagram can be used to determine the flexural deformation (Δ_f) by integrating along each of

the linear segments of the curvature diagram. The shear deformation (Δ_v) can be calculated using Eq 2.2. The slip deformation (Δ_s) occurs when the longitudinal reinforcement yields in tension. A plastic hinge is developed, and it will control the flexural response, as shown in Figure 2.6. The plastic rotation θ_p can be calculated using Eq. 2.5 [Segura, 2017].

$$\theta_p = \left(\frac{\varepsilon_c}{c} - \phi_y\right) . L_p \qquad (2.5)$$

where ε_c is the extreme fiber compression strain, c is neutral axis depth, and L_p is the plastic hinge length.
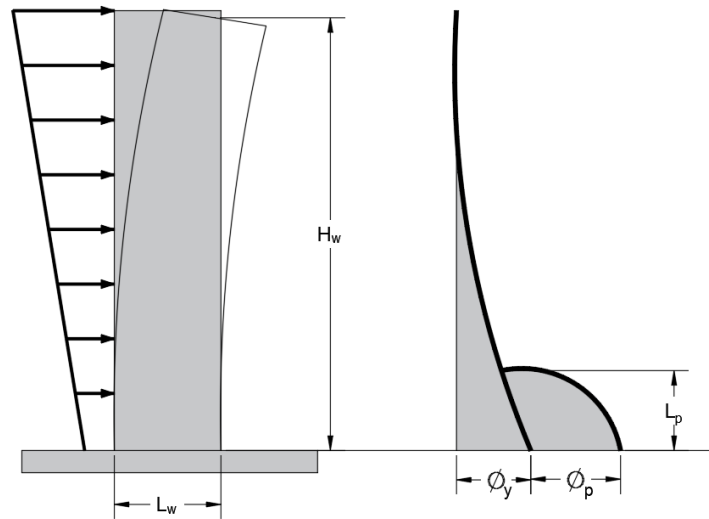
Figure 2.6. Plastic hinge model for cantilever wall (Segura, 2017)

2.2.2 Cyclic response

Three RC walls with different aspect ratios, ranging from 1.0 to 2.2, are selected to illustrate the cyclic behaviour. **Figure 2.7(a)** shows the cyclic response of a slender RC wall with an aspect ratio of 2.2 tested by Abdulridha and Palermo (2017). The tested wall exhibited a flexural response. Flexural cracks were performed near the wall base, followed by inclined shear cracks developed from the flexural cracks. By increasing the lateral load, the flexural cracks became wider. The cyclic response of an intermediate RC wall with an aspect ratio of 1.5 tested by Tran and Wallace (2012) is shown in **Figure 2.7(b)**. Flexural cracks occurred between the wall-foundation interface to a height of L_w at the wall edges, and there were major shear cracks on each side of the wall. Finally, gradual strength degradation occurred after the peak capacities in the subsequent cycles.
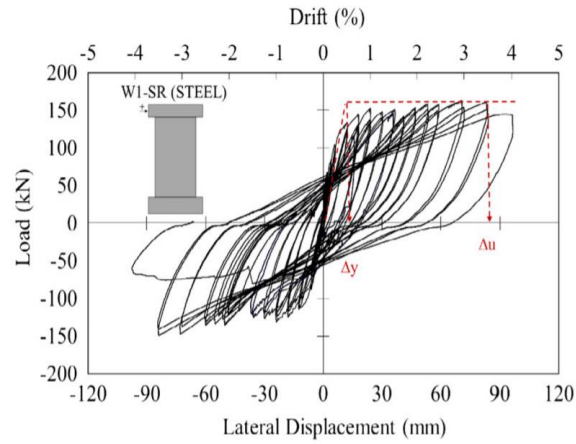
(a)
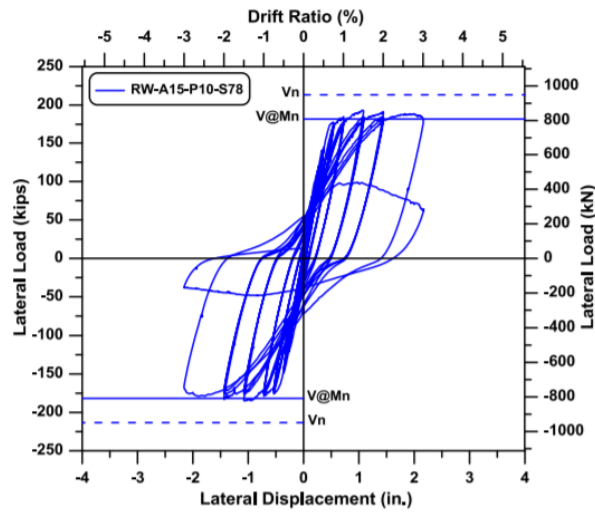
(b)
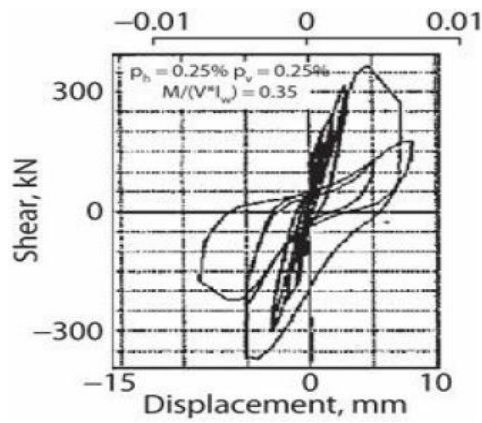
(c)

Figure 2.7. Cyclic load response: (a) slender wall (Abdulridha and Palermo, 2017); (b) intermediate wall (Tran, 2012); (c) squat wall (Hidalgo et al., 2002)

Figure 2.7(c) shows the cyclic response of a squat wall tested by Hidalgo et al. (2002). Inclined cracks associated with shear were developed and pinching in hysteresis loops with higher shear was observed.

2.4 SHAPE MEMORY ALLOY

The most suitable shape memory alloy for construction applications is composed of Nickel and Titanium (55.9% Nickel and 44.1% Titanium) (McCormick et al. 2007). The NiTi alloy has two phases: austenite and martensite. Characteristic temperatures for this alloy are: martensite-start temperature (M_S), martensite-finish temperature (M_f), austenite-start temperature (A_S), and austenite-finish temperature (A_f). **Figure 2.8** illustrates the hysteric behaviour of NiTi SMA during cooling and heating. At temperatures below M_f, stressing the SMA will change its structure from twinned martensite to detwinned martensite allowing for large deformations to occur (6%-8%). By heating the SMA to a temperature above A_f, it transforms to the austenite phase and regains its undeformed shape. This characteristic is called the shape memory effect. Stressing the SMA while the temperature is higher than A_f induces large deformations due to phase transformation from austenite to stressed detwinned martensite. By removal of the load, the material returns to the austenite phase and, thus, regains its original shape without applying heat. This effect is known as superelasticity. **Table 2.1** lists the typical properties of NiTi SMA compared to conventional steel bars (Alam, 2009).
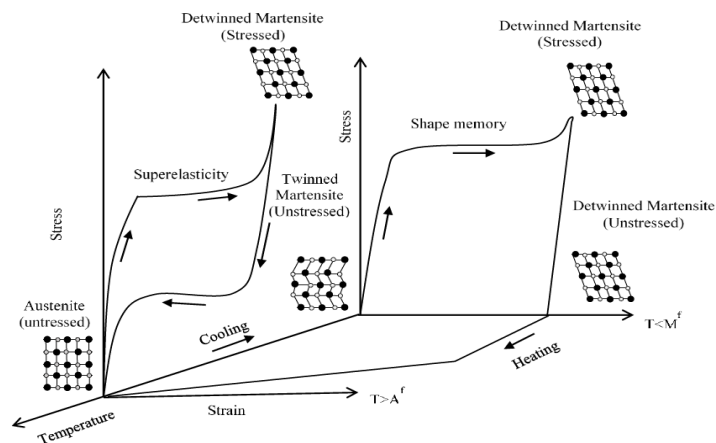
Figure 2.8. Three-dimensional stress-strain-temperature diagram of NiTi shape memory alloy (DesRoches et al., 2010)

Table 2.1. Typical parameters of NiTi SMA compared with steel (Alam et al., 2009)

Properties	NiTi SMA		Steel
	Austenite	**Martensite**	
Physical			
Melting Point	1240-1310^{0}C		1500^{0}C
Density	6.45 g/cm^3		7.85 g/cm^3
Thermal Conductivity	0.28 W/cm ^{0}C	0.14 W/cm ^{0}C	0.65 W/cm ^{0}C
Thermal Expansion	11.3×10^{-8} /^{0}C	6.6×10^{-8} /^{0}C	11.7×10^{-8} /^{0}C
Magnetite	No		Yes
Electrical Resistivity	80 to 100 $\mu\Omega cm$		72 $\mu\Omega cm$
Mechanical			
Recovered Elongation	up to 8%		0.2%
Young's Modulus	30-83 GPa	21-41 GPa	200 GPa
Yield Strength	195-690 MPa	70-140 MPa	248-517 MPa
Ultimate Tensile Strength	895-1900 MPa		448-827 MPa
Elongation at Failure	5-50% (typically 25%)		20%
Possion's Ratio	0.33		0.27-0.30
Hardness	30-60 R$_c$		Varies
Weldability	Quite good		Very good
Biocompatibility	Excellent		Fair
Torqueablity	Excellent		Poor
Chemical			
Corrosion performance	Excellent		Fair

2.4.1 Behaviour of SMAs under axial load (tension and compression)

Figure 2.9 shows the typical stress-strain curve of SMA under tension and compression. A linear elastic response with a modulus of elasticity, E_y, is observed in the first segment. Increasing the axial load, such that the stress and strain exceed f_y and ε_y leads to starting the second phase. In this stage (martensitic phase), the modulus of elasticity is E_{p1} up to a strain limit of ε_{p1}. The third stage has a modulus of elasticity of E_{p2}, which is 50% to 60% of the

initial modulus of elasticity E_y. The final stage occurs when the strain exceeds ε_{p2}, leading to the start of the plastic deformations. The modulus of elasticity for the final stage is donated by E_u, which ranges between 3% and 8% of E_y. Table 2.2 provides typical mechanical properties of NiTi SMAs
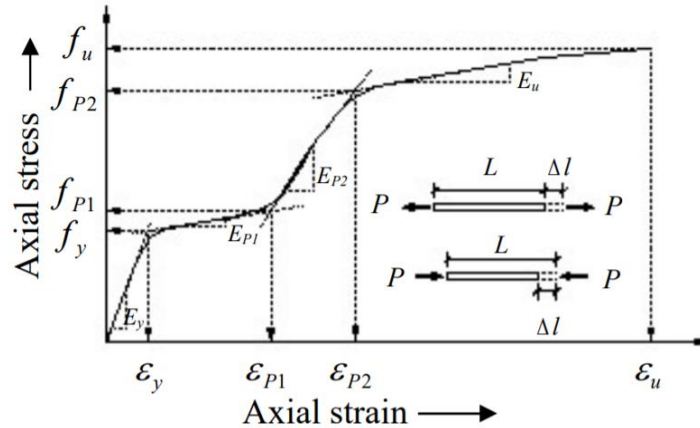
Figure 2.9. Typical stress-strain curve of SMAs under axial load (Alam, 2009)

Table 2.2. Mechanical properties of NiTi SMA alloys under axial (Alam, 2009)

Test types		Austenite	Martensite
Tension	Young's Modulus, E_{SMA}	30-98 GPA	21-52 GPa
	Yield strength, f_{y-sma}	100-800 MPa	50-300 MPa
	Ultimate strength, f_u	800-1900 MPa	800-2000 MPa
	Elongation at failure, ε_u	5-50 %	20-60 %
	Recovered strain, ε_{p1}	≤ 8 %	-
	Maximum recovery stress, f_{p1}	600-800 MPa	-
Compression	Young's Modulus, E_{SMA}	56-69 GPa	20-80 GPa
	Yield strength, f_{y-SMA}	550-800 MPa	125-190 MPa
	Ultimate strength, f_u	1500 MPa	1800-2120 MPa
	Elongation at failure, ε_u	-	17-24 %
	Recovered strain, ε_{p1}	3-6 %	-
	Maximum recovery stress, f_{p1}	650-820 MPa	-

2.4.2 Behaviour of SMAs under cyclic loading

Over the last decade, several studies have investigated the cyclic performance of SMA wires and large diameter bars with respect to strain amplitude, loading frequency, ambient temperature, and the number of reverse cycles. **Figure 2.10(a)** illustrates the stress-strain

curves of NiTi SMA wires at 0.1 Hz. The energy dissipation from each cycle increases with increasing the strain amplitudes. The variation of equivalent viscous damping with strain amplitude at different frequencies is shown in **Figure 2.10(b)**. It is clear that the equivalent damping ratio is constant.

(a)   (b)
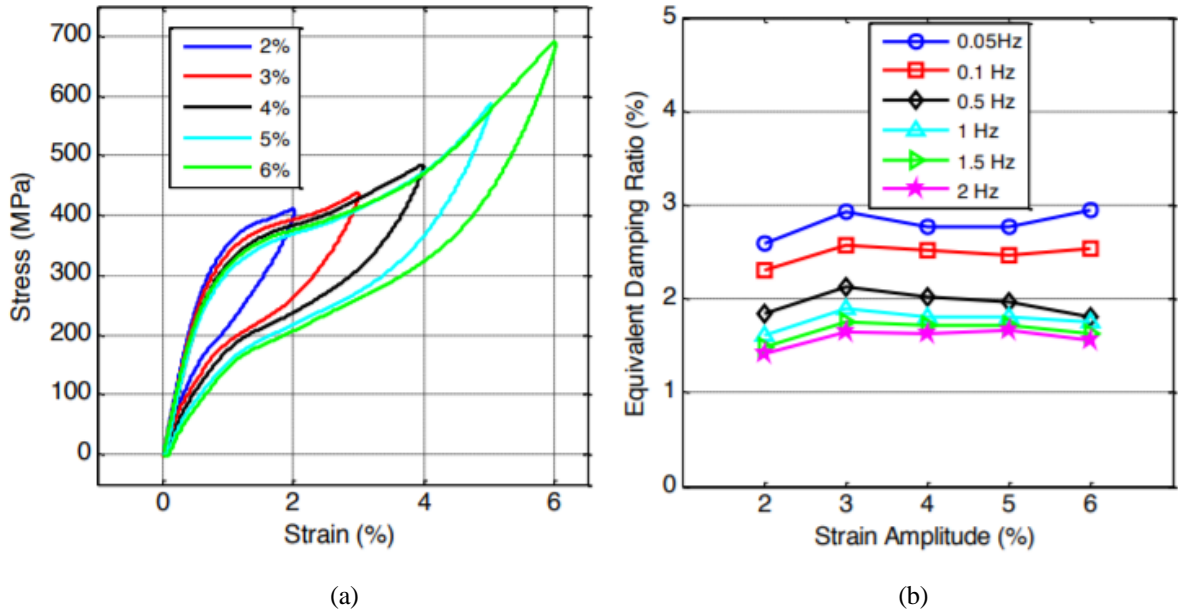
Figure 2.10. Stress-strain curve of SMAs under various strain amplitudes (Ozbulut and Hurlebaus, 2010)

The loading frequency effect at a different temperature on the stress-strain curve of NiTi SMA wires is shown in **Figure 2.11**. Two different load frequencies are selected to compare the stress-strain curve. The 0.05 Hz load frequency represents a quasi-static load, and 1 Hz is typical of a low to moderate dynamic load. The hysteresis loops of SMA shift upward as the temperature increases. However, there is about a 1% residual strain at 0°C and 0.05 Hz loading frequency. The energy dissipation decreases by 5% when the temperature increases from 0°C to 40°C (Ozbulut and Hurlebaus, 2010). The same observation is noticed for 1 Hz loading frequency with a slight reduction in the damping ratio.

The effect of the number of cycles (fatigue) on the stress-strain relationship of SMA is shown in **Figure 2.12**. The shape of the hysteresis loops tends to be almost identical. The maximum stress and residual strain remain approximately constant. The loading and unloading transformation, however, tends to decrease, which results in a reduction of energy dissipated in each cycle.
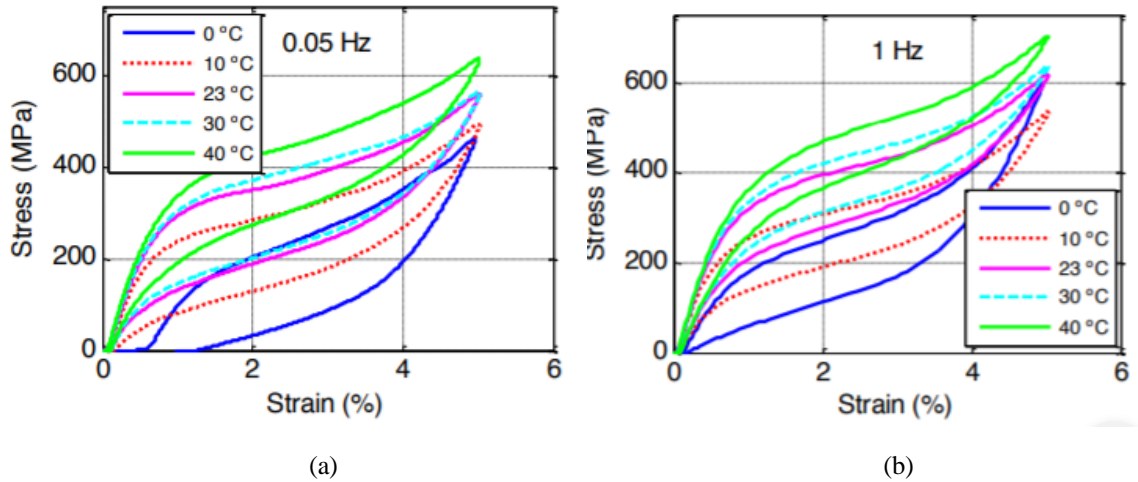
Figure 2.11. Stress-strain curves of NiTi SMA wire at various temperatures and loading frequency (Ozbulut and Hurlebaus, 2010)
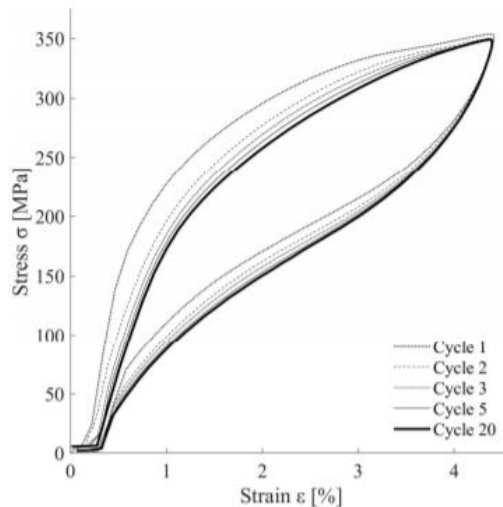
Figure 2.12. Hysteresis loops of SMA (González-Sanz, 2019)

Wolons et al. (1998) compared the cyclic response of trained and untrained SMA wires. Their results suggested that a significant amount of cycling is required to stabilize SMA properties due to residual strains that appear in the initial cycles. Wang and Zhu (2018b) reported that NiTi SMA bars were fully stabilized after nine loading cycles, with a 6% strain amplitude.

Dolce and Cardone (2001) investigated the cyclic response of NiTi SMA wires having a 1-2 mm diameter. Their results showed that the SMA wires possess adequate self-centering and energy dissipation to be fully suited for seismic applications. DesRoche et al. (2004) compared

the cyclic performance of 1.8 mm and 25.4 mm diameter bars to investigate the effect of bar size and loading history on the damping, strength, and re-centering ability. As shown in **Figure 2.13**, a flag-shaped response was obtained for both the wire and the bar. However, the wire-cyclic response demonstrated higher strength and damping properties compared to the bar. The mechanical performance of large diameter SMA bars under different tensile cyclic protocols was reported by Wang et al. (2016). The results confirmed the feasibility of using such bars for seismic applications. Recently, Wang and Zhu (2018a) studied the cyclic behaviour of SMA bars with buckling restraint devices when subjected to reverse cyclic loading. The seismic applications were evaluated in terms of strain amplitude, strain rates, and loading protocols. Results indicated a stable flag-shaped hysteretic response without any strength degradation after multiple tension and compression cycles, in addition to the SMA self-centering capability.

Zhang et al. (2008) examined the suitability use of SMA wires in bridge restrainers located in cold regions. The test results demonstrate that the SMA wires exhibited a superelastic behaviour at cold temperature down to -85 ^{0}C.

(a)   (b)
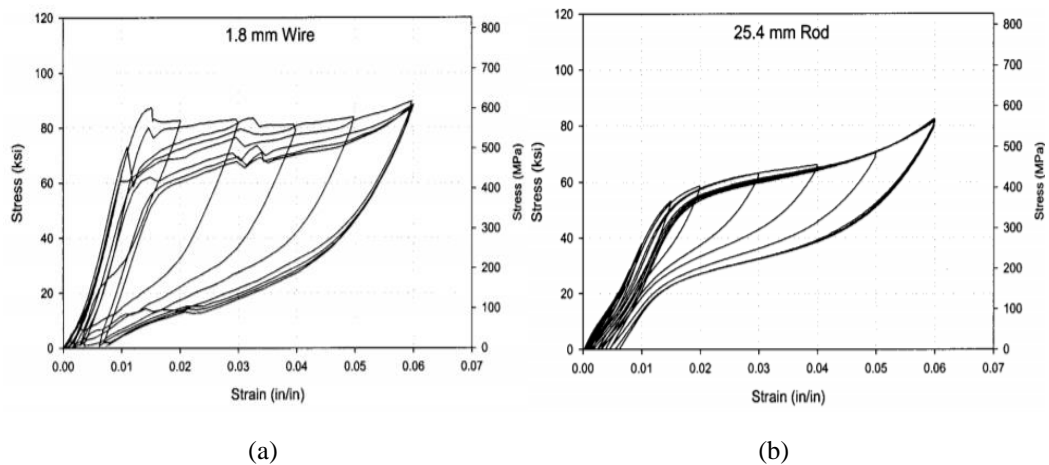
Figure 2.13. Cyclic stress-strain for NiTi SMA (DesRoche et al. 2004): (a) for 1.8 mm diameter wire; (b) for 25.4 mm diameter bar

Qiu and Zhao (2018) examined the temperature effect on the seismic performance of CBFs equipped with external SMA braces. Results indicated that peak deformation, absorbed energy, and residual displacement are not affected by the change of environmental temperature.

2.4.3 Applications of SE-SMA in civil engineering

Several studies have been conducted to improve the seismic performance of steel and concrete structures by utilizing the unique flag-shape of SE-SMA material (Zhang and Zhu, 2007). In steel structures, Ocel et al. (2004) integrated the SE-SMA into conventional steel connections, which significantly enhanced the frame ductility, and damping capacity, and mitigated the residual deformations. Chowdury et al. (2019) investigated numerically the seismic performance of an extended SE-SMA end-plate connection. The results illustrated a significant improvement in terms of moment capacity, post-stiffness, and energy dissipation capacity.

The seismic performance of a steel braced frame that utilizes SE-SMA in the bracing members was studied by Auricchio et al. (2006). The global seismic performance of two-story moment frames with SE-SMA connections was studied by DesRoches et al. (2010). SE-SMA connections were found to control the overall structural response and reduce residual deformations. Sultana and Youssef (2018) explored the use of SMA in the bracing members of steel buildings and concluded that SMA has led to an improvement in the overall structural response.

The applications of SE-SMAs have also covered RC structural elements. Wang (2004) conducted a shake table test to investigate the seismic performance of RC columns, reinforced with SMA bars in the plastic hinge and steel bars in the remaining column height. The SMA led to a reduction in the observed residual displacements. Ayoub et al. (2004) tested an RC beam that utilizes SMA bars. Results showed that SMA bars reduced the residual deformations by more than 75%. Youssef et al. (2008) tested an RC-beam-column joint reinforced with SE-SMA bars. Results showed the superior seismic performance of the SE-SMA RC joints in terms of residual displacements. Alam et al. (2009) investigated the seismic performance of SE-SMA RC frames located in a high seismic zone of Canada. Results indicated that SE-SMA RC frames recovered their large inelastic deformations after strong seismic excitations. Billah and Alam (2012) incorporated SMA and fiber-reinforced polymer bars in RC columns to reduce seismic residual deformations and enhance corrosion resistance. Superelastic SMA was used in the plastic hinge regions to reduce the permanent damage, and FRP was used in remaining regions to enhance its corrosion resistance. The corrosion-resistant hybrid-column had significantly reduced seismic residual deformations. Abdulridha and Palermo (2017)

compared the cyclic behaviour of RC beams reinforced with SE-SMA bars at their plastic hinges. Results showed that the residual deformations for SE-SMA RC beams are much lower than steel RC beams.

Considering RC walls, Abdulridha and Palermo (2017) conducted an experimental test of the SE-SMA RC wall under cyclic loading. Their test demonstrated the effectiveness of using SE-SMA bars to recover seismic residual deformations. Wang and Zhu (2018b) proposed a new technique for self-centering of RC walls using unbonded SE-SMA bars, which can be used to mitigate the damage in existing RC walls.

The use of SE-SMA bars for retrofitting of existing structures has been reported in several studies. Dolce et al. (2005) retrofitted a 2-story RC frame using SE-SMA braces. The frame showed re-centering capability and increased value for the collapse margin. Cardon et al. (2004) utilized SE-SMA braces for retrofitting an RC frame designed for gravity loads only. A shake table test confirmed the ability of SE-SMA braces to recover the residual deformation caused by the seismic ground motions. Effendy et al. (2006) investigated the potential use of external SE-SMA braces to retrofit a squat RC wall. Results showed a 26% increase in wall shear capacity as compared to the steel one. Elbahy (2018) investigated the flexural behaviour of RC elements retrofitted using external unbonded SMA bars and proposed equations to decide on the optimum length and amount of SMA bars.

Several researchers have also investigated the seismic performance of SE-SMA bars as base isolators (Dezfuli et al. 2017; Zheng et al. 2018), SMA dampers (Nespoli et al. 2017; Alipour et al. 2017); and bridge restrainers (Johnson et al. 2008; Choi et al. 2009). Those studies demonstrated a significant recovery in the inelastic deformations.

Although using SMA to equip RC structures with the recentering ability is quite promising, it has not been widely used yet. One of the major obstacles is the high cost of SMA bars. Also, large-diameter SMA rebars are not available commercially. Even though the cost of SMA has decreased over the last two decades, the current price is still much higher than the price of other novel materials. Frick et al. (2004) determined that the source of this cost is related to the process of producing the NiTi SMA material. Several other low costs SMA materials were introduced for research purposes or industrial uses, e.g. Fr-Mn-Si-Cr (Janke et al., 2005) and SMA-FRP (Zafar and Andrew, 2012).

2.3 DESIGN APPROACHES FOR RC WALLS

Different design practices may be applied based on building complexity, seismic category, and performance objectives. The following sections outline three seismic design approaches:

2.3.1 Strength-based design

Several building codes follow the strength-based design approach, such as the National Building Code of Canada (NBCC, 2015) and the International Building Code (IBC, 2015). This approach defines the seismic design forces. The elastic design forces are reduced, allowing the structure to undergo inelastic deformations in case of extreme seismic loading. The seismic force-resisting system is then chosen to have adequate deformation capacity to safely withstand the expected seismic events. While designing the seismic force-resisting system, capacity design criteria need to be followed. However, the use of this approach is restricted to specific building height, materials, and lateral load systems.

2.3.2 Displacement-based design

The displacement-based design has been used for the assessment of existing buildings (ASEC 41, 2013) and new buildings and bridges (Priestley et al. 2007). In this approach, the first mode is defined using structural analysis or an approximate method. The story drift is then calculated and compared with the maximum allowable drift. The structural strength is evaluated after designing the structure to meet the displacement demand. This approach is suited to buildings with primarily a first-mode displacement response.

2.3.3 Performance-based design

The performance-based seismic design allows the owner to select performance objectives for the structural and non-structural building components. Seismic performance levels have been defined, which include: immediate occupancy, life safety, and collapse prevention. **Figures 2.14** and **2.15** illustrate the performance objectives.

ATC-33 (1996) project for the seismic retrofit of buildings, which was sponsored by the Federal Emergency Management Agency (FEMA), was the first standardized form of performance-based design. FEMA-273 (1997) and the National Earthquake Hazard Reduction Program (NEHRP) define the current state of practice in performance-based engineering.

The performance objectives should include at least two objectives: (1) The building shall have a small probability of damage requiring repair, given that it has been subjected to the more frequent ground motion defined as the Service Level Earthquake (SLE), and (2) The building shall have a small probability of life-threatening collapse given that it has been subjected to a rare seismic ground motion defined as the Maximum Considered Earthquake (MCE) (TBI, 2017). Nonlinear dynamic structural analysis is used to ensure that the designed building is meeting the performance objectives. ATC-72 (2010) provides guidelines for defining the properties of the different elements. The NBCC (2015) addresses the collapse prevention and life safety, and the code is mute on the building serviceability during smaller seismic events.
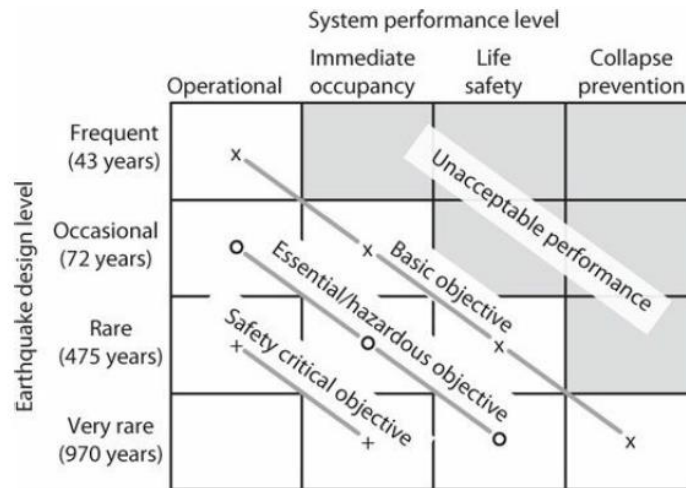
Figure 2.14. Performance objectives suggested by SEAOC (1995)
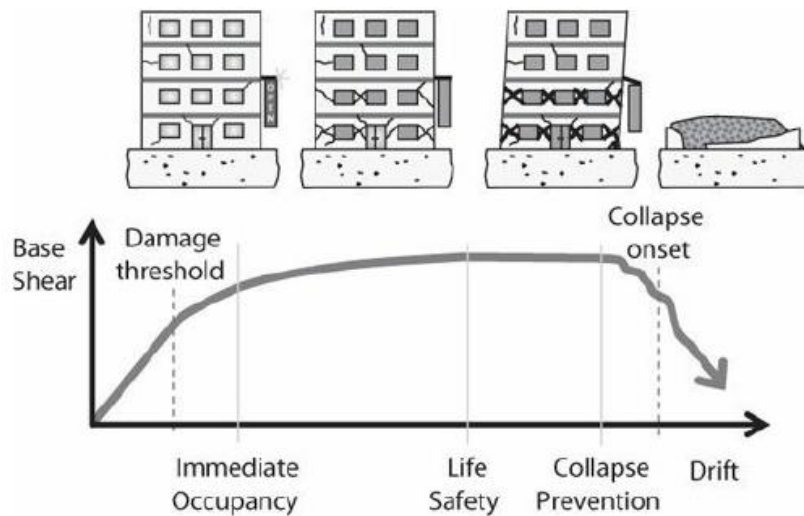
Figure 2.15. FEMA 273 performance levels

2.4 NUMERICAL MODELING OF RC WALLS

Different numerical models are used throughtout the thesis. The shear-flexural interaction multi-vertical line element model (SFI) (Kolozvari, 2013) is used in chapters 3-5. This 2-D numerical model is able to capture the shear-flexural interaction for intermediate and slender RC walls. To capture the unique torsional response of core walls, a wide column model (WCM) (Beyer, 2008), is used in chapter 6 to simulate the 3-D core wall system. In chapter 7, the displacement beam-column model (Mazzoni, 2006), is used to examine the hybrid RC walls. Each numerical model is described and validated in the mentioned chapters.

2.5 REFERENCES

Abdulridha, A., & Palermo, D. (2017). Behaviour and modelling of hybrid SMA-steel reinforced concrete slender shear wall. Engineering Structures, 147, 77-89.

Alam, M.S. (2009). Utilizing Shape Memory Alloys to Enhance the Seismic Performance of RC Beam-Column Joints. Doctoral dissertation, Western University.

Alam, M. S., Nehdi, M., & Youssef, M. A. (2009). Seismic performance of concrete frame structures reinforced with superelastic shape memory alloys. Smart Struct Syst, 5(5), 565-585.

Alipour, A., Kadkhodaei, M., & Safaei, M. (2017). Design, analysis, and manufacture of a tension-compression self-centering damper based on energy dissipation of pre-stretched superelastic shape memory alloy wires. Journal of Intelligent Material Systems and Structures, 28(15), 2129-2139.

Auricchio, F., Fugazza, D., & Desroches, R. (2006). Earthquake performance of steel frames with nitinol braces. Journal of Earthquake Engineering, 10(spec01), 45-66.

Ayoub, C., Saiidi, M. S., & Itani, A. (2003). A study of shape-memory-alloy reinforced beams and cubes (No. RDT 04-046).

ASCE 41. (2013). Seismic Evaluation and Retrofit of Existing Buildings, ASCE/SEI Standard 41–13, American Society of Civil Engineers, Reston, VA.

Beyer, K., Dazio, A., & Priestley, M. J. (2008). Inelastic wide-column models for U-shaped reinforced concrete walls. Journal of Eartthquake Engineering, 12(S1), 1-33.

Billah, A. M., & Alam, M. S. (2012). Seismic performance of concrete columns reinforced with hybrid shape memory alloy (SMA) and fiber reinforced polymer (FRP) bars. Construction and Building Materials, 28(1), 730-742.

Brueggen, B. L., & French, C. E. (2010, December). Simplified modeling of non-rectangular RC structural walls. In the 9th US National and 10th Canadian Conference on Earthquake Engineering 2010, Including Papers from the 4th International Tsunami Symposium (pp. 4026-4035).

Bruneau, M., & Reinhorn, A. (2007). Exploring the concept of seismic resilience for acute care facilities. Earthquake Spectra, 23(1), 41-62.

Cardone, D., Dolce, M., Ponzo, F. C., & Coelho, E. (2004). Experimental behaviour of R/C frames retrofitted with dissipating and re-centring braces. Journal of Earthquake Engineering, 8(03), 361-396.

Choi, E., Lee, D. H., & Choei, N. Y. (2009). Shape memory alloy bending bars as seismic restrainers for bridges in seismic areas. International Journal of Steel Structures, 9(4), 261-273.

Chowdhury, M. A., Rahmzadeh, A., & Alam, M. S. (2019). Improving the seismic performance of post-tensioned self-centering connections using SMA angles or end plates with SMA bolts. Smart Materials and Structures.

Dolce, M., Cardone, D., & Ponzo, F. C. (2007). Shaking-table tests on reinforced concrete frames with different isolation systems. Earthquake Engineering & Structural Dynamics, 36(5), 573-596.

Dolce, M., Cardone, D., Ponzo, F. C., & Valente, C. (2005). Shaking table tests on reinforced concrete frames without and with passive control systems. Earthquake engineering & structural dynamics, 34(14), 1687-1717.

DesRoches, R., McCormick, J., & Delemont, M. (2004). Cyclic properties of superelastic shape memory alloy wires and bars. Journal of Structural Engineering, 130(1), 38-46.

DesRoches, R., Taftali, B., & Ellingwood, B. R. (2010). Seismic performance assessment of steel frames with shape memory alloy connections. Part I—analysis and seismic demands. Journal of Earthquake Engineering, 14(4), 471-486.

Dezfuli, F. H., Li, S., Alam, M. S., & Wang, J. Q. (2017). Effect of constitutive models on the seismic response of an SMA-LRB isolated highway bridge. Engineering Structures, 148, 113-125.

Doaré, O., Sbarra, A., Touzé, C., Moussa, M. O., & Moumni, Z. (2012). Experimental analysis of the quasi-static and dynamic torsional behaviour of shape memory alloys. International Journal of Solids and Structures, 49(1), 32-42.

Effendy E, Liao W I, Song G, Mo Y L, Loh C H (2006) Seismic behavior of low-rise shear walls with SMA bars. Earth & Space 3: 1-8.

Elbahy Y. (2018). Flexural behaviour of reinforced concrete elements retrofitted using external unbonded superelastic shape memory alloy bars. Doctoral dissertation, Western University.

El-Tawil, S., & Ortega-Rosales, J. (2004). Prestressing concrete using shape memory alloy tendons. Structural Journal, 101(6), 846-851.

FEMA 273 (1997). NEHRP Guidelines for the Seismic Rehabilitation of Buildings, FEMA-273, Federal Emergency Management Agency, Washington, DC.

Farvashany, F. E., Foster, S. J., & Rangan, B. V. (2008). Strength and deformation of high-strength concrete shearwalls. ACI structural journal, 105(1), 21.

Frick, C. P., Ortega, A. M., Tyber, J., Gall, K., & Maier, H. J. (2004). Multiscale structure and properties of cast and deformation processed polycrystalline NiTi shape memory alloys. Metallurgical and Materials Transactions A, 35(7), 2013-2025.

Gulec, C. K., Whittaker, A. S., and Stojadinovic, B., 2009, "Shear Strength of Squat Reinforced Concrete Walls with Boundary Flanges or Barbells," ACI Structural Journal, Vol. 106, No. 3, May-June, pp. 368-377.

González-Sanz, G., Galé-Lamuela, D., Escolano-Margarit, D., & Benavent-Climent, A. (2019). Hysteretic Behavior and Ultimate Energy Dissipation Capacity of Large Diameter Bars Made of Shape Memory Alloys under Seismic Loadings. Metals, 9(10), 1099.

Hidalgo, P. A., Ledezma, C. A., & Jordan, R. M. (2002). Seismic behavior of squat reinforced concrete shear walls. Earthquake Spectra, 18(2), 287-308.

Johnson, R., Padgett, J. E., Maragakis, M. E., DesRoches, R., & Saiidi, M. S. (2008). Large scale testing of nitinol shape memory alloy devices for retrofitting of bridges. Smart materials and structures, 17(3), 035018.

Janke, L., Czaderski, C., Motavalli, M., & Ruth, J. (2005). Applications of shape memory alloys in civil engineering structures—overview, limits and new ideas. Materials and Structures, 38(5), 578-592.

Kolozvari K (2013) Analytical modeling of cyclic shear-flexural interaction in reinforced concrete structural walls. Doctoral dissertation, University of California.

IBC (2012). International Building Code, International Code Council, Country Club Hills, IL.

Maji, A. K., & Negret, I. (1998). Smart prestressing with shape-memory alloy. Journal of engineering mechanics, 124(10), 1121-1128.

Massone, L. M., Orakcal, K., & Wallace, J. W. (2006). Shear-flexure interaction for structural walls. Special Publication, 236, 127-150.

Mazzoni, S., McKenna, F., Scott, M. H., & Fenves, G. L. (2006). OpenSees command language manual. Pacific Earthquake Engineering Research (PEER) Center, 264.

Moehle, J. (2014). Seismic design of reinforced concrete buildings. McGraw Hill Professional.

Marquis, F., Kim, J. J., Elwood, K. J., & Chang, S. E. (2017). Understanding post-earthquake decisions on multi-story concrete buildings in Christchurch, New Zealand. Bulletin of earthquake engineering, 15(2), 731-758.

Moni, M. (2011). Performance of shape memory alloy reinforced concrete frames under extreme loads (Doctoral dissertation, University of British Columbia).

McCormick, J., Tyber, J., DesRoches, R., Gall, K., & Maier, H. (2007). Structural engineering with NiTi. II: mechanical behavior and scaling. J Eng Mech, 133(9), 1019-1029.

Ma, H. W., & Yam, M. C. (2012). Experimental study on a beam-to-column connection using shape memory alloy. In Advanced Materials Research (Vol. 374, pp. 2176-2179). Trans Tech Publications.

Nespoli, A., Bassani, E., Della Torre, D., Donnini, R., Villa, E., & Passaretti, F. (2017). An experimental study on pseudoelasticity of a NiTi-based damper for civil applications. Smart Materials and Structures, 26(10), 105041.

Ocel, J., DesRoches, R., Leon, R. T., Hess, W. G., Krumme, R., Hayes, J. R., & Sweeney, S. (2004). Steel beam-column connections using shape memory alloys. Journal of Structural Engineering, 130(5), 732-740.

Opara, N., & Naaman, A. E. (2000). Self-stressing fiber composites. Structural Journal, 97(2), 335-344.

Ozbulut, O. E., & Hurlebaus, S. (2010). Neuro-fuzzy modeling of temperature-and strain-rate-dependent behavior of NiTi shape memory alloys for seismic applications. Journal of Intelligent Material Systems and Structures, 21(8), 837-849.

Priestley M, Calvi G, Kowalsky M (2007) Displacement-based seismic design of structures. IUSS Press: Pavia, Italy.

Qiu, C., & Zhao, X. (2018). Temperature effect on seismic performance of CBFs equipped with SMA braces. Smart Structures and Systems, 22(5), 495-508.

Sultana, P., & Youssef, M. A. (2018). Seismic Performance of Modular Steel-Braced Frames Utilizing Superelastic Shape Memory Alloy Bolts in the Vertical Module Connections. Journal of Earthquake Engineering, 1-25.

Segura, C. (2017). Seismic Performance Limitation of Slender Reinforced Concrete Structural Walls (Doctoral dissertation, UCLA).

SEAOC, V. (1995). Performance based seismic engineering of buildings. Sacramento (CA): Structural Engineers Association of California, USA.

Tazarv, M., & Saiid Saiidi, M. (2014). Reinforcing NiTi superelastic SMA for concrete structures. Journal of Structural Engineering, 141(8), 04014197.

Tolou Kian M J, Cruz-Noguez C (2018) Reinforced concrete shear walls detailed with innovative materials: seismic performance. Journal of Composites for Construction 22(6): 04018052.

Thomsen IV, J. H., & Wallace, J. W. (2004). Displacement-based design of slender reinforced concrete structural walls—experimental verification. Journal of structural engineering, 130(4), 618-630.

Tran, T. A. (2012). Experimental and analytical studies of moderate aspect ratio reinforced concrete structural walls (Doctoral dissertation, UCLA).

TBI. (2017). Guidelines for performance-based seismic design of tall buildings, Report No. 2010/05. Pacific Earthquake Engineering Research Center, University of California, Berkeley, CA.

The National Building Code of Canada (NBCC). (2015). Ottawa: Canadian Commission on Building and Fire Code, National Research Council.

Wolons, D., Gandhi, F., & Malovrh, B. (1998). Experimental investigation of the pseudoelastic hysteresis damping characteristics of shape memory alloy wires. Journal of Intelligent Material Systems and Structures, 9(2), 116-126.

Wang, H. (2004). A study of RC columns with shape memory alloy and engineered cementitious composites. University of Nevada, Reno.

Wang, W., Fang, C., & Liu, J. (2016). Large size superelastic SMA bars: heat treatment strategy, mechanical property and seismic application. Smart Materials and Structures, 25(7), 075001.

Wang, B., & Zhu, S. (2018a). Cyclic tension–compression behavior of superelastic shape memory alloy bars with buckling-restrained devices. Construction and Building Materials, 186, 103-113.

Wang, B., & Zhu, S. (2018b). Seismic behavior of self-centering reinforced concrete wall enabled by superelastic shape memory alloy bars. Bulletin of Earthquake Engineering, 16(1), 479-502.

Youssef M A, Alam M S, Nehdi M (2008) Experimental investigation on the seismic behaviour of beam-column joints reinforced with superelastic shape memory alloys. Journal of Earthquake Engineering 12(7): 1205-1222.

Zafar, A., & Andrawes, B. (2012). Incremental dynamic analysis of concrete moment resisting frames reinforced with shape memory composite bars. Smart Materials and Structures, 21(2), 025013.

Zhang, Y., Camilleri, J. A., & Zhu, S. (2008). Mechanical properties of superelastic Cu–Al–Be wires at cold temperatures for the seismic protection of bridges. Smart Materials and Structures, 17(2), 025008.

Zheng, Y., Dong, Y., & Li, Y. (2018). Resilience and life-cycle performance of smart bridges with shape memory alloy (SMA)-cable-based bearings. Construction and Building Materials, 158, 389-400.

Zhang Y, Zhu S (2007) A shape memory alloy-based reusable hysteretic damper for seismic hazard mitigation. Smart Mater Struct 16(5):1603–1613.

CHAPTER 3

SEISMIC FRAGILITY ASSESSMENT OF SUPERELASTIC SHAPE MEMORY ALLOY REINFORCED CONCRETE SHEAR WALLS

3.1 INTRODUCTION

The main function of reinforced concrete (RC) structural walls is to resist the lateral forces. Extensive studies have been conducted to explore their behaviour under various load conditions (Su and Wong, 2006; Riva and Giruriani, 2003; Ganesan et al., 2013). The seismic design philosophy, which aims at preserving life, leaves RC walls vulnerable to damage during strong seismic excitations. This damage was observed following many earthquakes, including the 1985 Mexico earthquake (Aguilar et al. 1989), the 1999 Chi-Chi earthquake (Tsai et al., 2000). The 2010 Maule earthquake (Westenenk et al. 2012), and the 2011 Christchurch earthquake (Elwood et al., 2011).

Residual drifts are one of the measures to evaluate the seismic performance of a structure. FEMA P-58 (2012) introduced four damage states related to residual drift ratios and defined the limit for repairable structural elements to correspond to a 1% residual inter-story drift. McCormick et al. (2008) concluded that the economical repair limit is 0.5%. To mitigate the residual displacements of RC walls, self-centering methods that rely on unbounded post-tensioned tendons and supplementary energy dissipation devices were proposed (Belleri et al. 2014; Buddika and Wijeyewickrema, 2016; Guo et al. 2014). Although these methods have resulted in improved seismic performance, replacing the unbounded post-tension after seismic events is not easy.

Superelastic shape memory alloy (SE-SMA) can recover its inelastic deformations upon the removal of the applied load. This unique property has been utilized by many researchers (Saiidi et al. 2008, Tazarv and Saiidi, 2013; Youssef et al. 2008; Alam et al. 2008; Youssef and Elfeki,

2012; Elfeki and Youssef, 2017). The flag-shaped hysteresis of SE-SMA can eliminate the seismic residual drifts on the cost of lower energy dissipation as compared to steel reinforcement. Also, the lower modulus of elasticity of SE-SMA bars leads to higher seismic deformations. Researchers have addressed these disadvantages by minimizing the amount of SE-SMA materials (Youssef and Elfeki, 2012; Elfeki and Youssef, 2017). The potential use of SE-SMA was extended to RC walls by a number of researchers. Effendy et al. (2006) used external diagonal SE-SMA bars to upgrade the seismic performance of existing squat walls. Test results showed a significant reduction in the residual displacements combined with a 16-26% increase in the peak shear strength. Abdulridha (2012) experimentally studied the cyclic behaviour of a concrete wall, reinforced with longitudinal SE-SMA bars within its boundaries for the length of the plastic hinge region. The SE-SMA bars increased the wall ductility and significantly reduced the residual displacements. Abraik and Youssef (2015) conducted an analytical study to identify the performance of SE-SMA RC squat and intermediate walls considering different SE-SMA bar locations. The results highlighted that the locations of SE-SMA bars have a significant effect on the wall seismic performance.

Research addressing the seismic vulnerability of tall concrete walls reinforced with SE-SMA bars is missing in the literature. This chapter starts by determining the plastic hinges for 10 and 20-story steel RC walls that are designed and detailed per CSA A23.3 (2014) and NBCC (2015). The influence of replacing steel rebars with SE-SMA bars is then evaluated. Fragility curves are presented considering various damage states.

3.2 NUMERICAL MODEL

The geometry of a typical RC wall is given in **Figure 3.1(a)**. Shear-Flexural Interaction Multi-Vertical Line Element Model (SFI-MVLEM), shown in **Figure 3.1(b)**, was implemented in the Open System for Earthquake Engineering Simulation software (OpenSees) (2018) by Kolozvari (2013). This model allows simulating the seismic response of RC walls by using two-dimensional membrane panels. The edge and interior panels represent the boundary elements and the web, respectively. The panels are modeled using a fixed angle crack approach. The rigid beams at the top and bottom enforce a plane section assumption. The

flexural response of a wall is captured through the axial deformations of the RC panels in the vertical direction. The average normal vertical strain is determined by dividing the average vertical deformation by the element height (h). The relative rotation between the top and bottom of the wall element is assumed to happen at a height (ch), measured from the bottom face. The value of the height coefficient *c* was recommended to be taken as 0.4 by Orakcal and Wallace (2004). The shear deformation of the SFI-MVLEM element is determined by transferring the external deformation components to a point at a height (ch). The shear strain for each panel is calculated by dividing the shear deformation by the element height (h). The normal strain in the horizontal direction is obtained by dividing the horizontal deformation at the internal degrees of freedom by the panel width. The effect of increasing or decreasing the number of RC panels or the number of SFI-MVLEM on the total displacement was found to be insignificant (Kolozvari, 2013).

The built-in nonlinear material constitutive relationships, proposed by Menegotto and Pinto (1973) and ConcreteCM based on Chang and Mander (1994), were used to model the steel reinforcing bars [**Figure 3.2(a)**] and the concrete [**Figure 3.2(b)**]. **Figure 3.2(c)** illustrates the symmetric SE-SMA self-centering model. The SE-SMA model parameters were evaluated experimentally by Tazarv and Saiidi (2013) and Varela and Saiidi (2014). The modulus of elasticity of the SE-SMA bars (E_{SMA}), the stress at which inelastic deformations initiate f_{y-SMA}, and the post-yield strength K_2 are assumed to be 38,000 MPa, 380 MPa, and 1725 MPa, respectively. The ultimate strain for SE-SMA is assumed to correspond to the point at which it loses the ability to recover its original shape (a strain of 7%).

The local failure is defined when the strain in the longitudinal steel reinforcement reaches the yield strain ε_y and the concrete compressive strain reaches 0.2% (Ghorbanirenani et al. 2012; Priestley et al. 2007). The structural and non-structural elements are expected to have sustained significant damage at this stage (Ghorbanirenani et al. 2012).

An experimental shake table test of a slender eight-story concrete wall, tested by Ghorbanirenani et al. (2012), was selected to further validate the SFI-MVLEM model. The wall, shown in **Figure 3.3(a)**, was designed per NBCC (2005) with a force reduction factor of 2.8. A simulated time history ground motion developed for eastern North America was used to experimentally test the wall. The inelastic flexural response was developed at the wall base

and at the sixth story. Flexural-shear cracks at the wall base and flexural cracks at the sixth level were observed. The wall was modeled using eight SFI-MVLEM elements. The predicted results matched closely the experimental ones, as shown in **Figure 3.4(a)**.

Abdulridha (2012) performed a large-scale test on a SE-SMA RC wall to evaluate its performance when subjected to incremental lateral loading, as shown in **Figure 3.3(b)**. The experimental load-displacement response is compared with OpenSees (2018) and VecTor2 (Vecchio, 1989) models, as shown in **Figure 3.4(b)**. The predicted initial stiffness by the numerical models is approximately 12% higher than that observed from the experimental test. The yield displacement form both models is only 8% greater than that of the tested wall. The SFI-MVEL and VecTor2 models predicted accurately the ultimate strength and the corresponding displacement (73 mm).
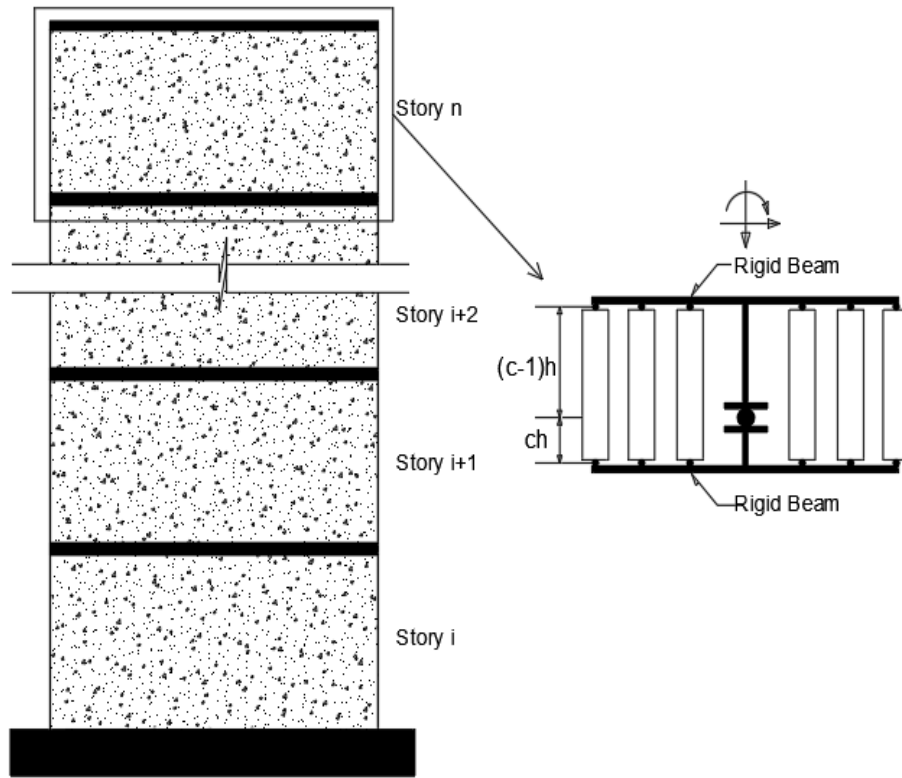
(a)   (b)

Figure 3.1. MVLE model (a) RC wall; (b) one-story model
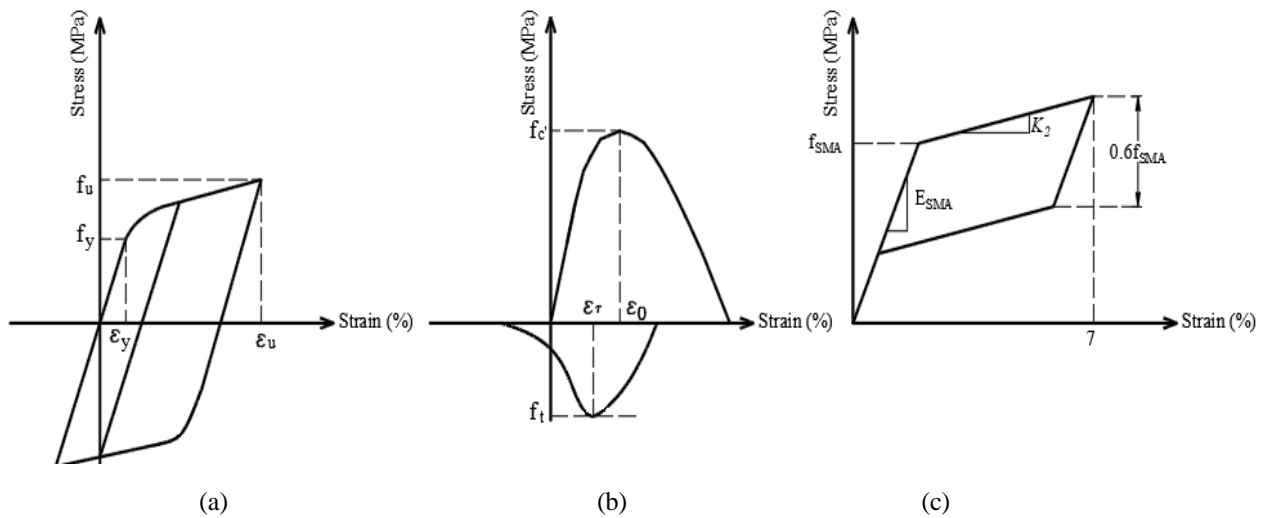
(a)   (b)   (c)

Figure 3.2. Materials model (a) steel bars; (b) concrete; (c) SE-SMA
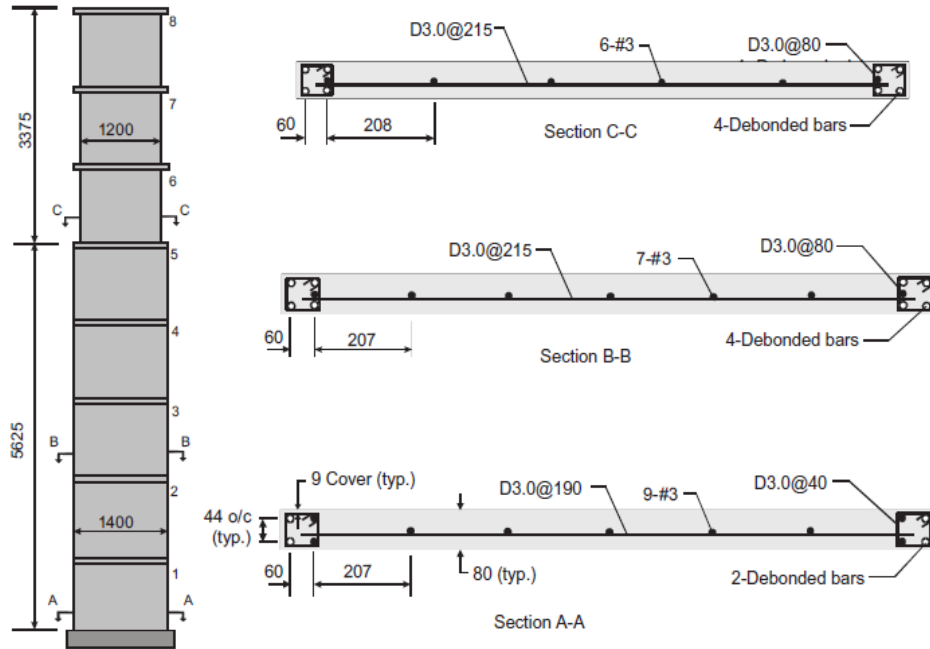
(a)
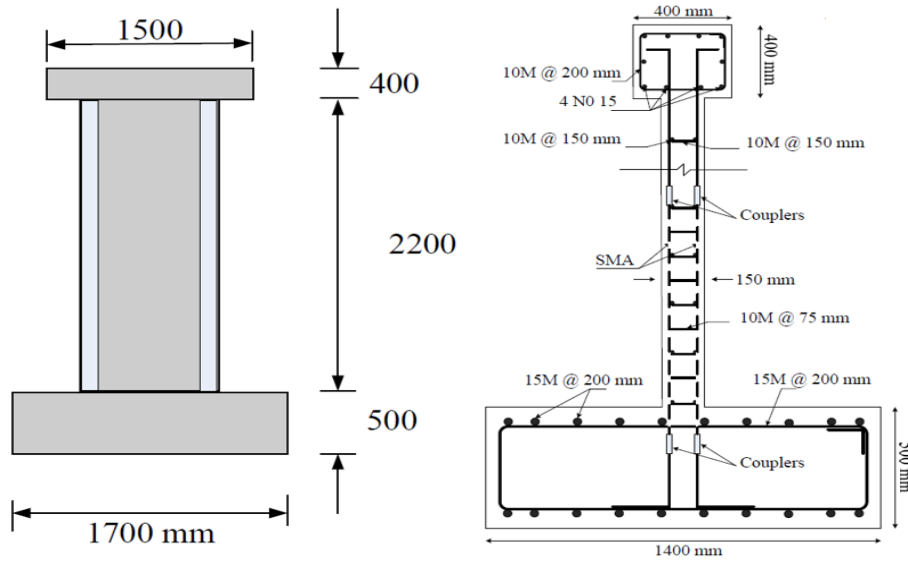
(b)

Figure 3.3. Tested walls: (a) steel RC Wall (Ghorbanirenani et al. 2012); (b) SE-SMA RC wall (Abdulridha, 2012) (dimensions are in mm)

(a)   (b)
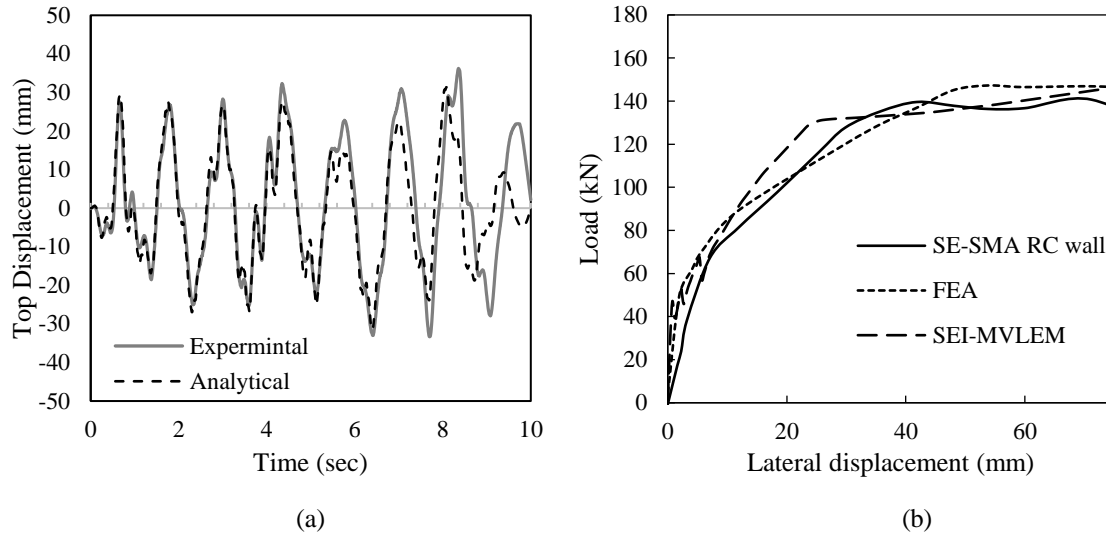
Figure 3.4. Numerical model versus the experimental data: (a) steel RC wall tested by Ghorbanirenani (2012); (b) SE-SMA RC wall tested by Abdulridha (2012)

3.3 STEEL RC WALLS

The structural plan of the considered RC buildings is shown in **Figure 3.5**. The buildings were assumed to be located in southern British Columbia. The concrete shear walls were designed and detailed using CSA A23.3 (2014) and NBCC (2015). The overstrength R_0 and ductility R_d factors are equal to 1.6 and 3.5, respectively. The concrete compressive strength and the yield strength of the steel rebars are assumed to be 30 MPa and 450 MPa, respectively. The structural lumped mass, which includes the self-weight, and 25% of the floor live load, was assumed 2.8 kN/m^2. The characteristics of the considered walls are shown in **Figure 3.5(c)** and are summarized in **Table 3.1**.

Table 3.1. Characteristics of considered walls

Parameters	10 stories	20 stories
Wall thickness (b_w)	250 mm	350 mm
Wall length (l_w)	4060 mm	6000 mm
Length of wall boundary element (l_{bl})	500 mm	600 mm
Floor height	2800 mm	
Axial load per story	233 kN	
Weight per story	1248 kN	
Vertical and horizontal steel ratio in the web (ρ_{vw}, ρ_{hw})	0.25%	
Horizontal steel ratio in the boundary elements (ρ_{hb})	0.67%	
Vertical and horizontal steel ratio in the web at the plastic hinge (ρ_{vw}, ρ_{hw})	0.5%	
Vertical steel ratio in the boundary elements (ρ_{vb})	1.28%	1.90%
Axial load ratio ($\frac{P}{A_g f_c}$)	0.1	0.12

Steel RC walls are designed based on CSA A23.3 (2014), which assumes that the plastic hinge develops at the wall base. Detailing requirements of CSA A23.3 (2014) ensures a certain level of ductility along the wall height by modifying the factored moment M_f, as shown in **Figure 3.6**. The design shear forces are increased over the wall height by the ratio of the moment of resistance M_r to the factored moment M_f. The corresponding shear values must exceed the smaller of the shear corresponding to the probable moment capacity and the shear demand calculated assuming $R_d R_0$ equal to 1.3. Although CSA ensures an adequate level of ductility to mitigate yielding at any point outside the plastic hinge zone, there is a possibility for the spread of plasticity along the wall height (Panagiotou, 2008; Priestley et al. 2007; Ghorbanirenani et al. 2012; Panneton et al. 2006).

(a)   (b)

(c)
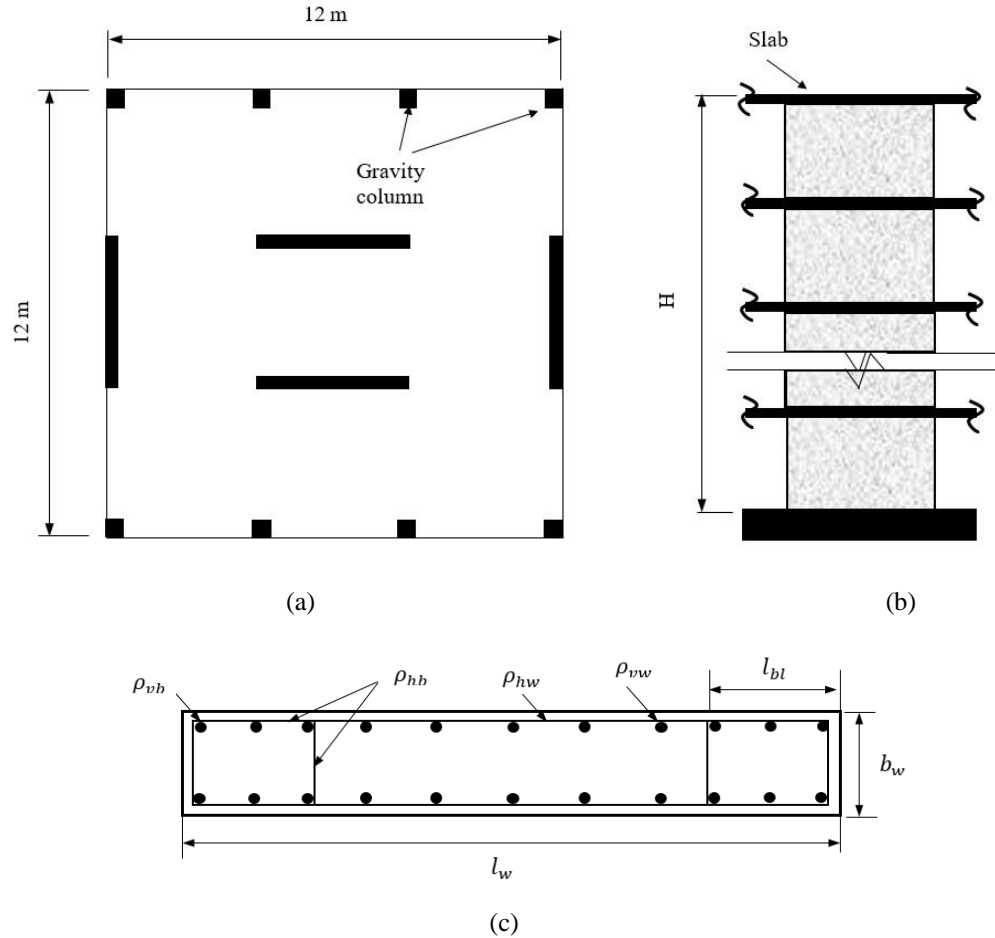
Figure 3.5. Considered building (a) structural plan; (b) wall elevation; (c) typical wall section

(a)   (b)
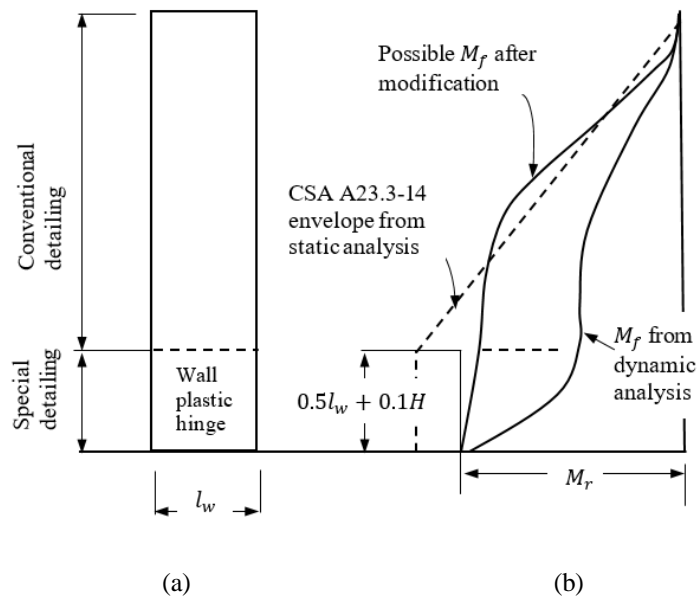
Figure 3.6. Capacity design moment envelope for RC wall: (a) detailing requirements; (b) variation of moments along wall height

3.4 SEISMIC GROUND MOTIONS

The Conditional Mean Spectrum (CMS) proposed by Baker (2011) was utilized to select the ground motions. The method is based on choosing the spectrum that has a target amplitude for a specific structural period. An eigenvalue analysis was used to determine the structural period for the steel RC walls. The resulting periods were 1.67 s and 3.06 s for the 10 and 20-story walls, respectively. Seven levels of hazards with return periods ranging from 72 years to 2475 years (**Table 3.2**) were then selected. Soil class D with shear wave velocity ranging from 180 to 360 m/s was assumed. Each of the hazard levels is represented by 20 ground motions scaled to the spectral accelerations shown in **Table 3.2**.

Table 3.2. Hazard levels considered for Southern British Columbia

Hazard Level	Return Period (years)	$S_{a10}(T_1 = 1.67)(g)$	$S_{a20}(T_1 = 3.06)(g)$
1	72 [50% in 50]	0.06	0.05
2	224 [20% in 50]	0.17	0.09
3	336 [20% in 75]	0.21	0.12
4	475 [10% in 50]	0.25	0.15
5	975 [5% in 50]	0.34	0.19
6	1462 [5% in 75]	0.40	0.26
7	2475 [2% in 50]	0.46	0.30

3.5 SMA RC WALLS

Multi-Strip Analysis (MSA) was used to evaluate the seismic response of the 10 and 20-story steel RC walls. Strain profiles along the height of the walls were used to determine the length and locations of the SE-SMA bars. **Figure 3.7(b)** shows the mean strains in the longitudinal bars of the 10- and 20-story steel RC walls when subjected to 20 earthquakes with 2475 years return period. The main plastic hinge is formed at the base. However, an additional plastic hinge is formed at mid-height of the wall. The steel strain at the 5th and 6th stories of the 10-story RC wall exceeded the yield strain. The same trend is observed for the 20-story wall, where the strain in the rebars at 10th, 11th, 12th, and 13th stories exceeded the yield strain. In both buildings, the plastic hinge length is about 20% of the total wall height.

SE-SMA bars are assumed to replace the steel rebars at the plastic hinges of the boundary elements. The modulus of elasticity of the SE-SMA bars and the stress at which inelastic deformations initiate are assumed to be 38,000 MPa and 380 MPa, respectively. The ultimate strain for SE-SMA is assumed to correspond to the point at which it loses the ability to recover its original shape (a strain of 7%). The resulting periods for SE-SMA RC walls were 1.71 s and 3.1 s for 10 and 20-story, respectively.

(a)   (b)
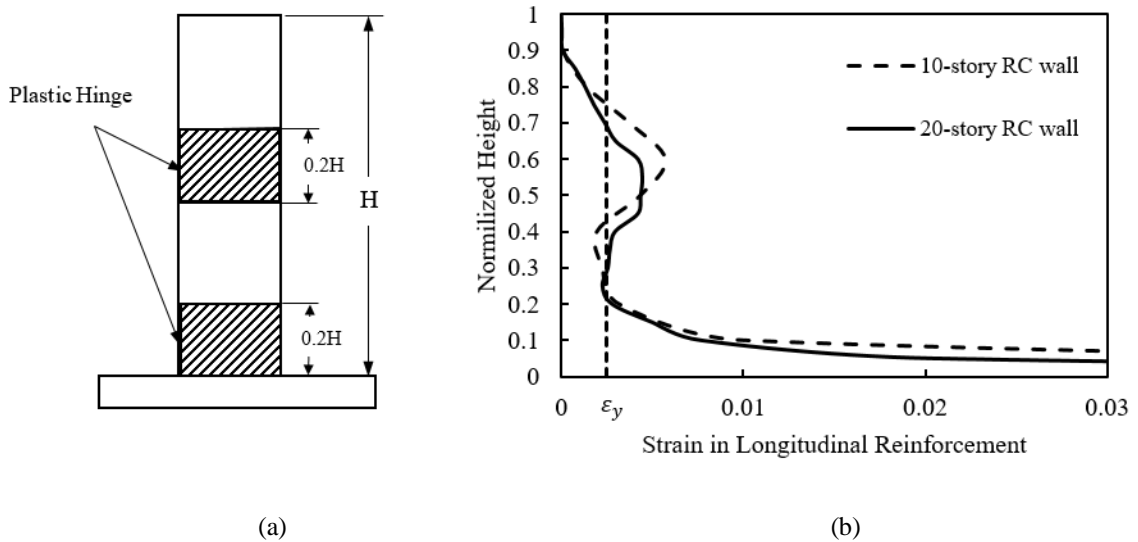
Figure 3.7. Plastic hinges in the considered walls: (a) location of plastic hinges; (b) strain profile along the wall height

3.6 SEISMIC PERFORMANCE OF STEEL AND SMA RC WALLS

Figures 3.8 and **3.9** compare the shear forces and bending moments for the steel and SE-SMA RC walls at the first and second periods. The shear forces for the steel RC walls were higher than the SMA walls by about 5 to 10%. A similar trend is noticed for the bending moment, which was higher by about 8 to 12% at the wall base and 3 to 15% at mid-height. The flexibility of the SE-SMA rebars slightly lengthens the wall natural period, which decreases the bending moments and shear forces.
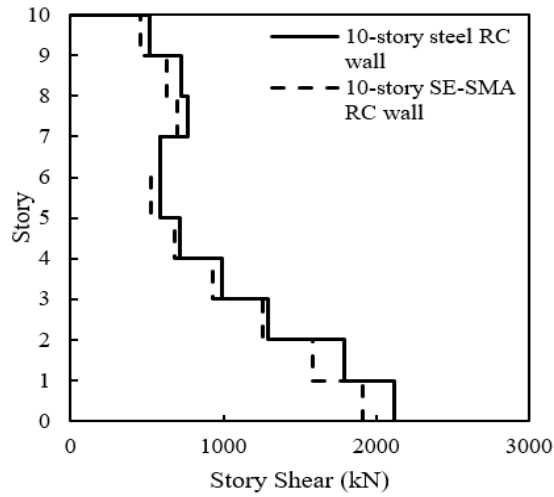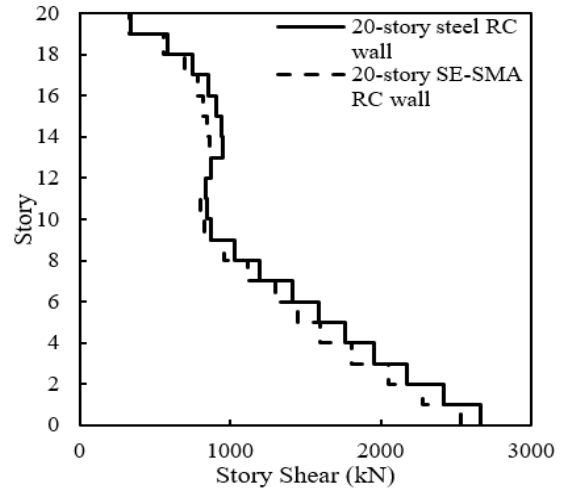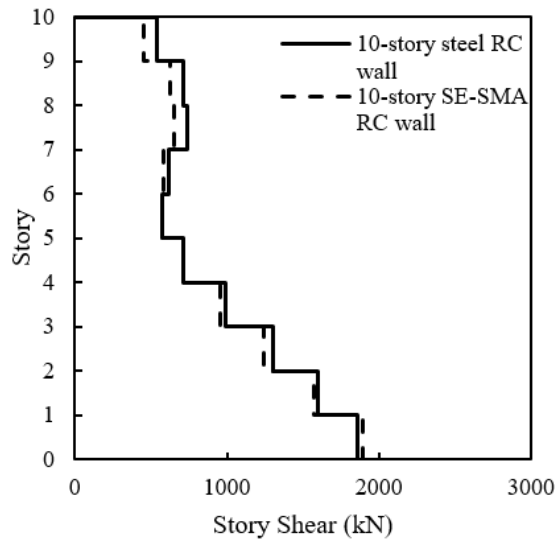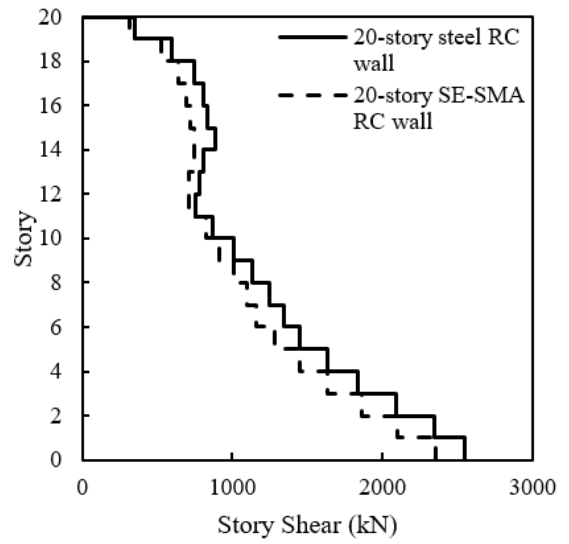
Figure 3.8. Shear force along wall height at: (a) 10-story first period; (b) 20-story first period; (c) 10-story second period; (d) 20-story second period
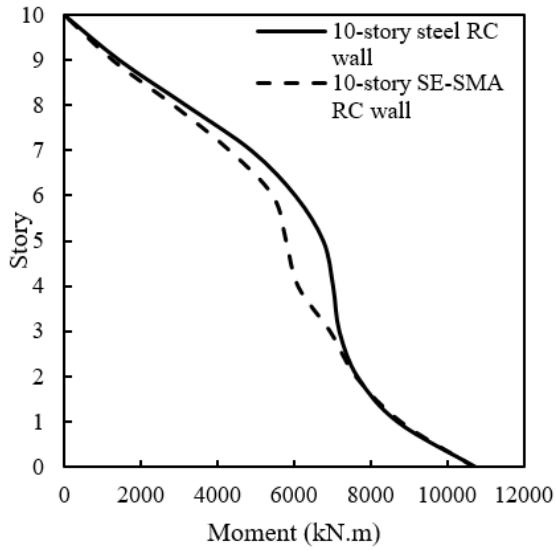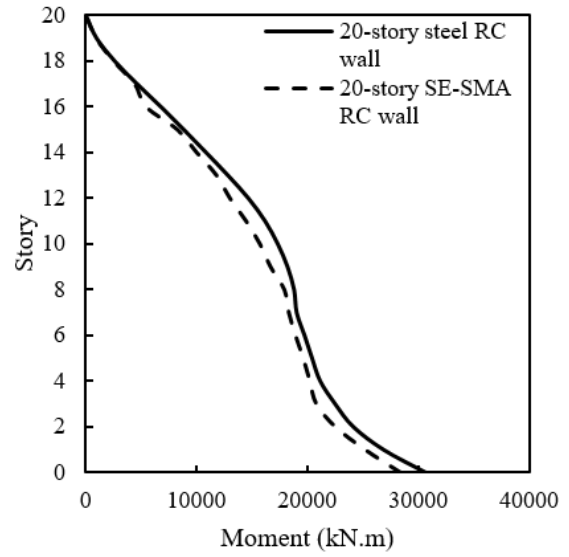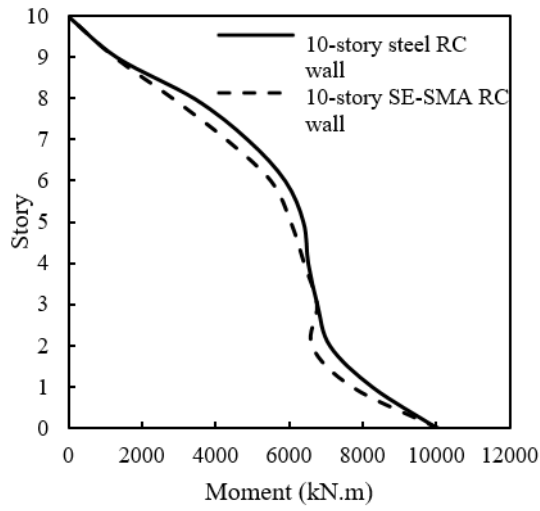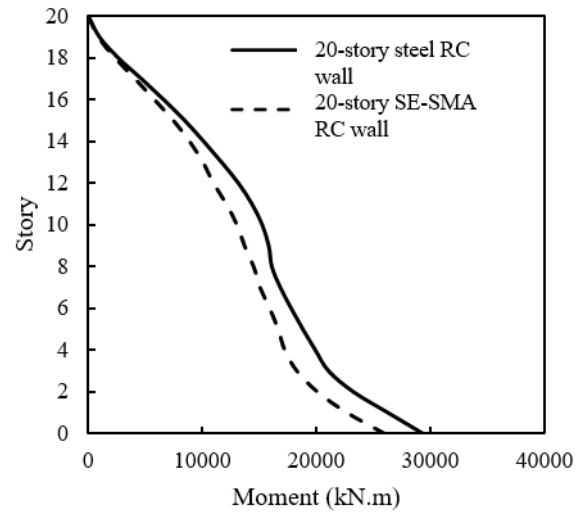
Figure 3.9. Bending moment along wall height at: (a) 10-story first period; (b) 20-story first period; (c) 10-story second period; (d) 20-story second period

The lateral displacement envelopes are plotted in **Figure 3.10** for 2475-, 475-, and 72-year events. The displacements of the considered walls follow almost a linear trend. The lateral displacements of the SE-SMA RC walls are higher than the steel RC walls by 6 to 16%. This increase is due to the lower stiffness of the SE-SMA bars.

The residual displacement envelopes are plotted in **Figure 3.11**. For low-intensity seismic ground motions, the residual displacements of the SE-SMA RC walls are not significantly different from the steel RC walls as the behaviour was in the elastic range. The use of SE-SMA bars reduces the residual displacements by 19 to 50% for moderate and high-level seismic ground intensities. The reduction was more pronounced for the 10-story wall, which is less flexible as compared to the 20-story wall. Lateral and residual displacement envelopes for different ground motion intensity levels are summarized in **Table 3.3**.
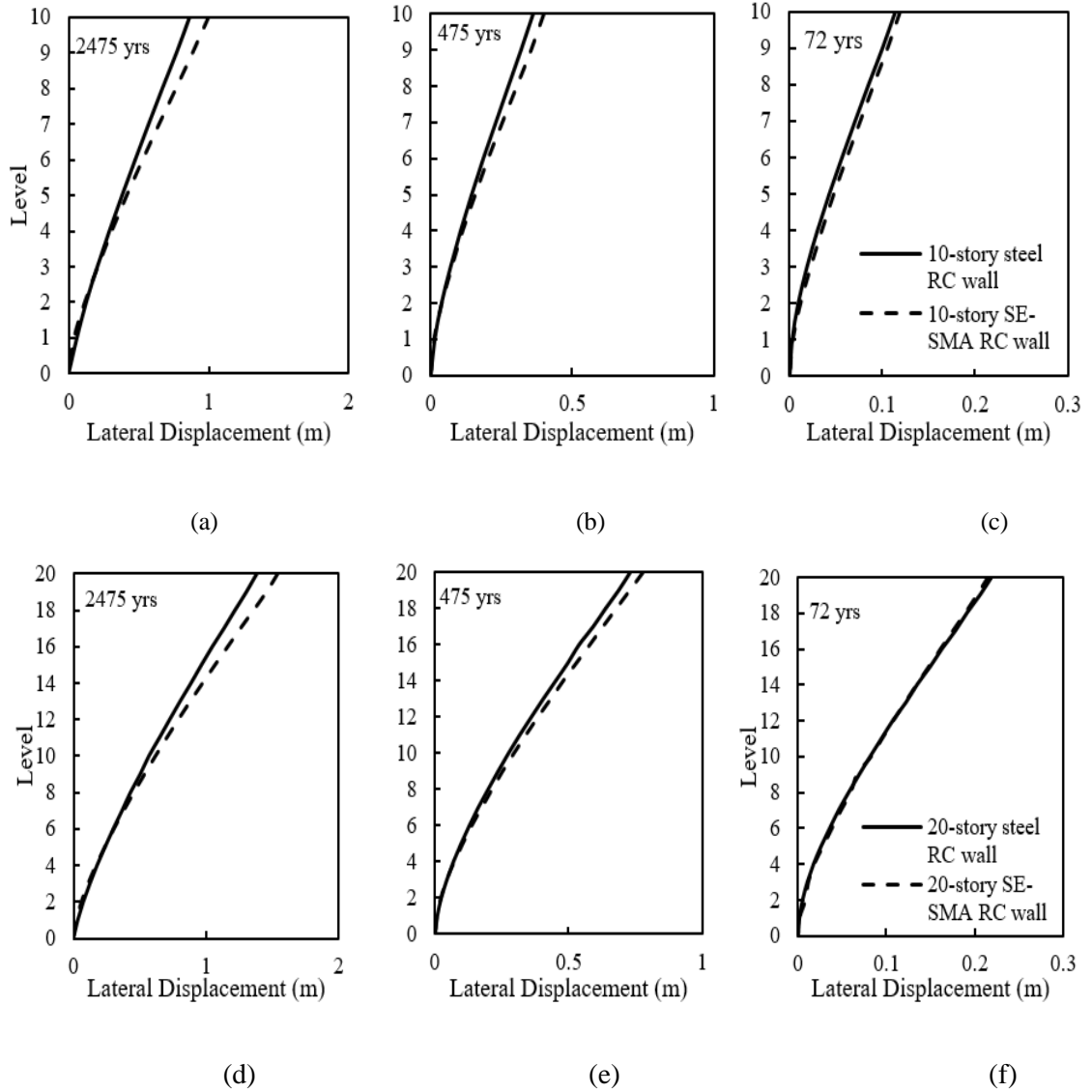
Figure 3.10. Lateral displacement envelopes for: (a) return period 2475 yrs/ 10-story wall; (b) return period 475 yrs/ 10-story wall; (c) return period 72 yrs/ 10-story wall; (d) return period 2475 yrs/ 20-story wall; (e) return period 475 yrs/ 20-story wall; (f) return period 72 yrs/ 20-story wall

(a) (b) (c)

(d) (e) (f)
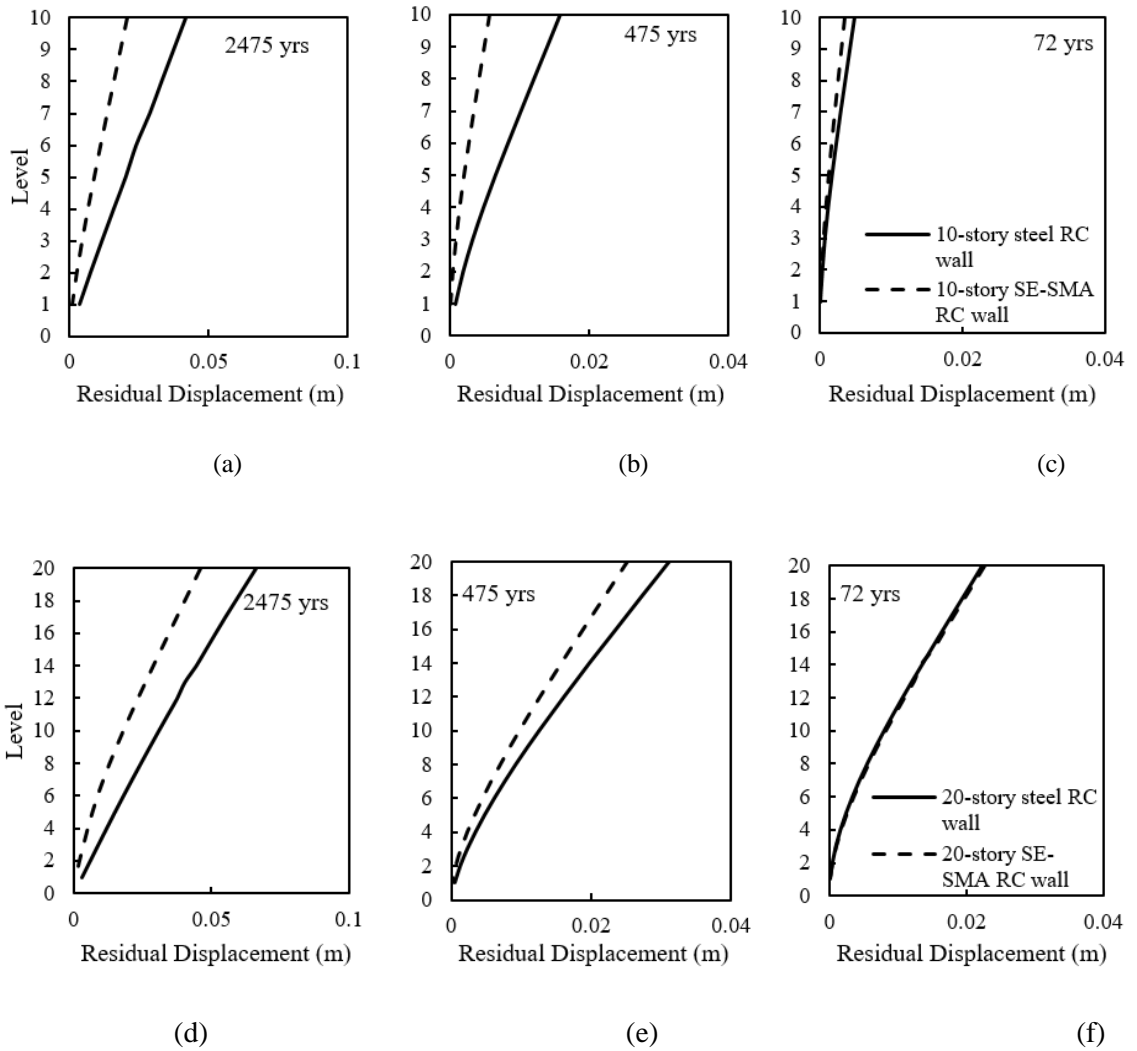
Figure 3.11. Residual displacement envelopes for: (a) return period 2475 yrs/ 10-story wall; (b) return period 475 yrs/ 10-story wall; (c) return period 72 yrs/ 10-story wall; (d) return period 2475 yrs/ 20-story wall; (e) return period 475 yrs/ 20-story wall; (f) return period 72 yrs/ 20-story wall

Table 3.3. Peak lateral and residual displacements of the considered walls

Events	10-story wall				20-story wall			
	Steel	SE-SMA	Steel	SE-SMA	Steel	SE-SMA	Steel	SE-SMA
	Lateral Displacement (m)		Residual Displacement (m)		Lateral Displacement (m)		Residual Displacement (m)	
2475	0.86	1.00	0.042	0.020	1.30	1.54	0.06	0.040
475	0.36	0.40	0.016	0.005	0.73	0.77	0.05	0.03
72	0.11	0.12	0.005	0.003	0.21	0.21	0.02	0.02

3.7 FRAGILITY FUNCTION

Seismic damage can be assessed using the story drift ratio (Brown, 2008) or inter-story drifts (Kinali and Ellingwood, 2007). The damage level for steel RC walls and SE-SMA RC walls can be judged as similar based on the story drifts (**Figure 3.10**) or significantly different based on the residual drifts (**Figure 3.11**). In this section, fragility curves are presented for both inter-story and residual drifts.

A fragility function describes the probability of damage for a given seismic intensity (IM). It can be expressed using Equation 3.1 (Baker, 2015):

$$P(C \backslash IM = x) = \Phi \left[\frac{\ln\left(\frac{x}{\theta}\right)}{\beta} \right] \tag{3.1}$$

where P is the probability of exceeding a specific damage level C, Φ is the standard normal cumulative distribution, θ is the median of the fragility function, and β is the standard deviation of the response. The fragility curve can be obtained using incremental dynamic analysis (Vamvatsikos and Cornell, 2004). In this approach, the seismic intensity is incrementally increased until the collapse. However, this method is time-consuming and raises the concern of whether scaling moderate-intensity ground motions can represent high-intensity ground motions (Baker, 2005; Baker, 2015). Multi-Strip Dynamic Analysis (MSA) is an efficient

approach that addresses this concern (Baker, 2015). In this approach, the structure is subjected to a number of ground motions representing each hazard level.

3.7.1 Fragility curves

The mean roof inter-story drifts (ID) and the residual roof drifts (RD) for seven seismic hazard levels representing return periods of 72 years to 2475 years are summarized in **Table 3.4**. **Figure 3.12** displays the MSA curves that depict the relationship of the mean roof inter-story drift against the seven hazard intensity levels. The mean roof inter-story drift for the 10-story SE-SMA wall is 19% higher than that of the steel RC wall. The 20-story walls have similar behaviour up to a hazard intensity of 0.2g. At higher intensity levels, the 10-story SE-SMA RC wall experiences slightly higher inter-story drifts compared to the 20-story SE-SMA RC wall. This apparent difference in the inter-story drift is due to differences in the wall heights and boundary element reinforcement ratios. **Figure 3.13** shows the relationship between the residual roof displacement and the ground motion intensity level. The residual displacements for the 10 and 20-story steel RC walls are higher than the corresponding SE-SMA RC walls.

Table 3.4. Mean inter-story and residual drifts for the considered walls

Event (years)	10-story				20-story			
	Steel		SE-SMA		Steel		SE-SMA	
	ID (%)	RD (%)	ID (%)	RD (%)	ID (%)	RD (%)	ID (%)	RD (%)
2475	3.07	0.23	3.74	0.072	2.72	0.13	2.82	0.08
1462	2.69	0.18	3.20	0.071	2.77	0.11	2.90	0.07
975	2.28	0.10	2.84	0.054	1.93	0.095	1.95	0.053
475	1.63	0.034	1.43	0.025	1.52	0.060	1.71	0.049
336	1.52	0.050	1.60	0.030	1.26	0.063	1.36	0.060
224	1.36	0.035	1.49	0.025	1.00	0.069	1.12	0.054
72	0.40	0.004	0.40	0.003	0.48	0.039	0.46	0.04
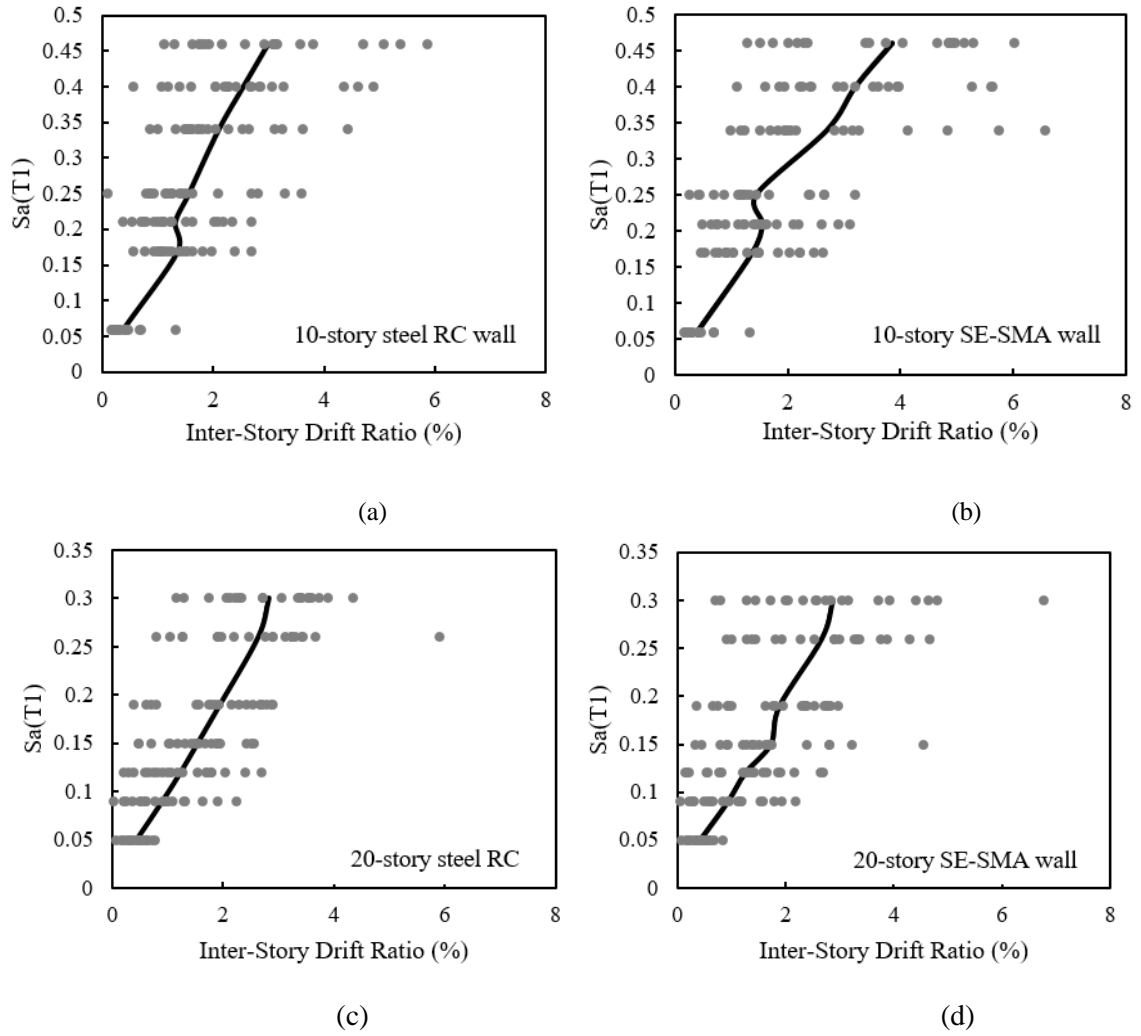
Figure 3.12. Maximum inter-story drift ratios as a function of ground motion intensity, for (a) 10-story steel RC wall; (b) 10-story SE-SMA RC wall; (c) 20-story steel RC wall; (d) 20-story SE-SMA RC wall
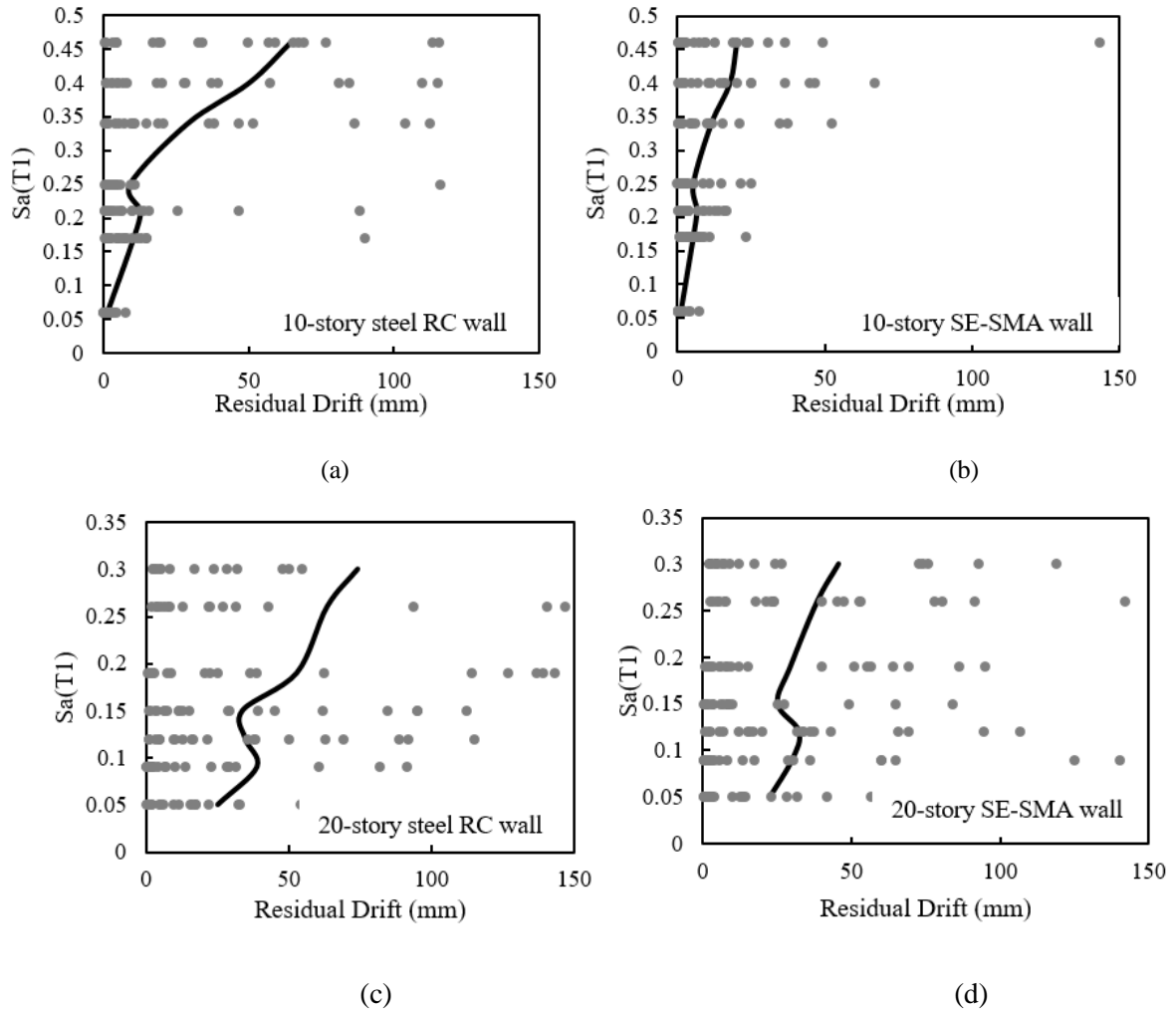
Figure 3.13. Maximum residual drift as a function of ground motion intensity: (a) 10-story steel RC wall; (b) 10-story SE-SMA RC wall; (c) 20-story steel RC wall; (d) 20-story SE-SMA RC wall

The collapse fragility curve, which shows the collapse probability as a function of ground motion intensity (Sa), is provided in **Figure 3.14(a)**. The fragility function fitting method proposed by Baker (2005) is used to generate the fragility curves. At low levels of seismic excitations, a significant reduction in wall fragility is observed for walls reinforced with SE-SMA bars. Collapse probabilities of the steel RC-walls are 80% at S_a of 0.46g for the 10-story wall and 73% at S_a of 0.3g for the 20-story wall. Utilizing SE-SMA bars at wall boundaries in the plastic hinge zones significantly diminishes the collapse probability of the 10 and 20-story walls by 66% and 50%, respectively. The effect of using SE-SMA bars is more pronounced for the 10-story wall. However, the considered walls reach the same probability of collapse at

the seismic intensity of about 0.65g, which is significantly higher than the spectral acceleration of the maximum considered earthquake.

The fragility curves for the considered walls as a function of the maximum inter-story drift ratio (ID) are shown in **Figure 3.14(b)**. The 10 and 20-story steel RC walls have similar probabilities of collapse. The 10 and 20-story SE-SMA RC walls exhibit a lower probability of collapse compared to the steel RC walls. The probability of collapse against the roof residual drift ratio (RRD), which is normalized by the maximum residual drift, is presented in **Figure 3.14(c)**. The probability of collapse is negligible for RRD less than or equal to 0.3. At RRD of 1.0, the 10-story and 20-story steel RC walls suffer major damage with a probability of collapse of about 80% and 73%, respectively. The SE-SMA walls have a significantly lower probability of collapse. Results confirm the significance of considering both ID and RID when evaluating the SE-SMA RC wall fragility. At inter-story drift ratio of 2.4%, both buildings exhibit the same fragility of collapse; whereas, the dispersion of fragility results between the SE-SMA and steel building is large at different RID ratio levels.
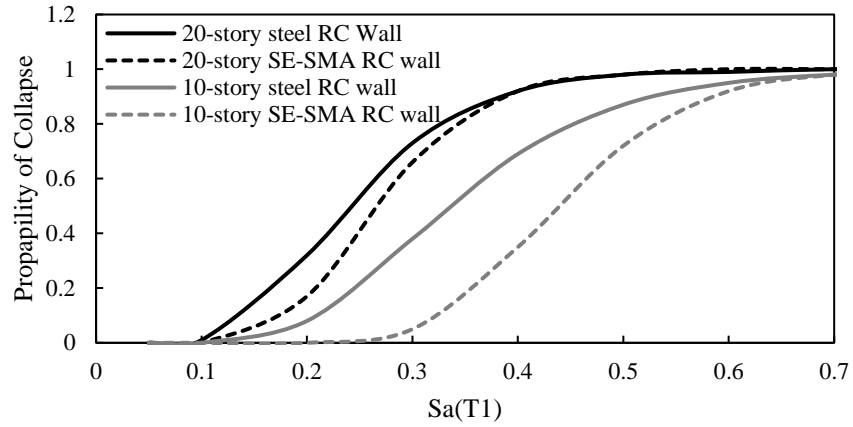
(a)
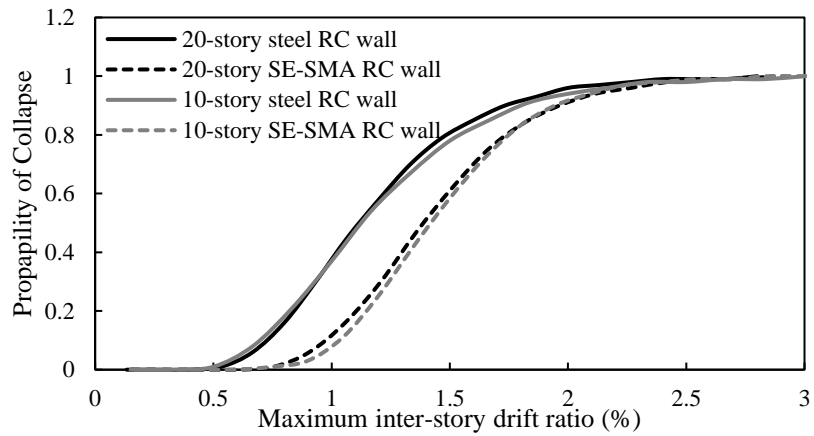
(b)
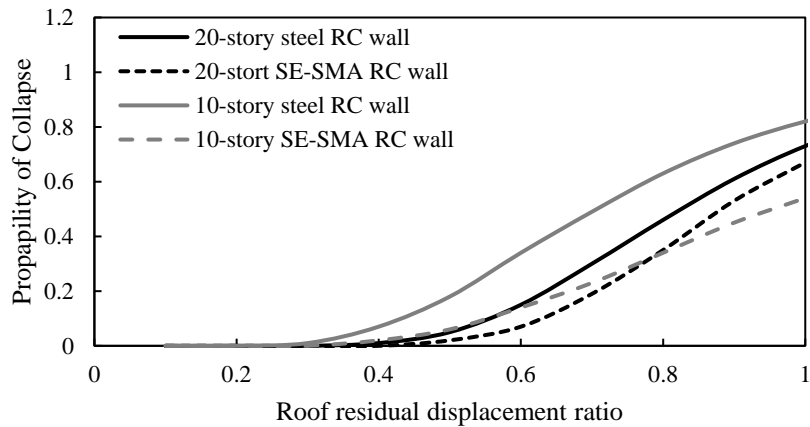
(c)

Figure 3.14. Collapse fragility curves with respect to (a) spectra acceleration; (b) maximum inter-story drift ratio; (c) roof residual displacement ratio

3.8 CONCLUSIONS

This chapter investigates the effect of utilizing SE-SMA bars in RC shear walls designed according to the current Canadian code. The seismic performance of ten and twenty-story steel and SE-SMA RC walls is compared using a multi-hazard dynamic analysis. The strain profile along the steel RC wall height identified two plastic hinges at the wall base and mid-height. The length of each plastic hinge is about 20% of the wall's height. Steel bars within the boundary elements at the plastic hinge locations are replaced with SE-SMA bars. The study led to the following conclusions:

1. The use of novel SE-SMA bars at both wall hinges improved the seismic performance compared to steel RC walls because they resulted in reducing the shear forces and bending moments at wall mid-height. The residual displacement of the SE-SMA walls was 42% on average lower than that of the steel RC walls.

2. Although the steel RC walls perform well under low probability seismic events, using SE-SMA bars in the plastic hinge regions significantly reduces the permanent lateral deformations compared to those of steel RC walls. However, the efficiency in recovering the inter-story drifts is reduced for low-intensity seismic events and higher walls.

3. The dispersion of fragility results associated with residual drifts is considerably larger than the dispersion of fragility results associated with inter-story drifts. Hence, the results of this study suggest that the fragility results relying on inter-story drifts cannot be used to assess damage state in steel versus SE-SMA RC walls.

4. Steel RC walls exhibit higher fragility than SE-SMA RC walls in terms of inter-story drifts and residual drifts. This renders SE-SMA RC walls as less vulnerable to seismic damage. However, a negligible difference exists between steel and SE-SMA walls in term of inter-story drifts.

3.9 REFERENCES

Abdulridha A. (2012) Performance of superelastic shape memory alloy reinforced concrete elements subjected to monotonic and cyclic loading. Doctoral dissertation, University of Ottawa.

Alam, M. S., Youssef, M. A., & Nehdi, M. (2008). Analytical prediction of the seismic behaviour of superelastic shape memory alloy reinforced concrete elements. Engineering Structures, 30(12), 3399-3411.

Abraik, E., & Youssef, M. A. (2015). Cyclic performance of shape memory alloy reinforced concrete walls. In Fifth International Workshop on Performance, Protection & Strengthening of Structures under Extreme Loading (No. 5, pp. 326-333).

Aguilar, J., Juarez, H., Ortega, R., & Iglesias, J. (1989). The Mexico earthquake of September 19, 1985—Statistics of damage and of retrofitting techniques in reinforced concrete buildings affected by the 1985 earthquake. Earthquake Spectra, 5(1), 145-151.

Baker, J. W. (2011). Conditional mean spectrum: Tool for ground-motion selection. Journal of Structural Engineering, 137(3), 322-331.

Baker, J. W., & Allin, Cornell, C. (2005). A vector-valued ground motion intensity measure consisting of spectral acceleration and epsilon. Earthquake Engineering & Structural Dynamics, 34(10), 1193-1217.

Baker, J. W. (2015). Efficient analytical fragility function fitting using dynamic structural analysis. Earthq. Spectra, 31(1) 579-600.

Belleri, A., Schoettler, M. J., Restrepo, J. O. S. É., & Fleishman, R. B. (2014). Dynamic behavior of rocking and hybrid cantilever walls in a precast concrete building. American Concrete Institute.

Brown, P. C. (2008). Probabilistic earthquake damage prediction for reinforced concrete building components (Doctoral dissertation, University of Washington).

Buddika, H. S., & Wijeyewickrema, A. C. (2016). Seismic performance evaluation of post-tensioned hybrid precast wall-frame buildings and comparison with shear wall-frame buildings. Journal of Structural Engineering, 142(6), 04016021.

CSA A23.3-14 (2014) Design of concrete structures. Canadian Standards Association. Mississauga, ON, Canada.

Chang, G. A., & Mander, J. B. (1994). Seismic energy-based fatigue damage analysis of bridge columns: part 1-evaluation of seismic capacity.

Effendy, E., Liao, W. I., Song, G., Mo, Y. L., & Loh, C. H. (2006). Seismic behavior of low-rise shear walls with SMA bars. In Earth & Space 2006: Engineering, Construction, and Operations in Challenging Environment (pp. 1-8).

Elfeki, M. A., & Youssef, M. A. (2017). Shape memory alloy reinforced concrete frames vulnerable to strong vertical excitations. Journal of Building Engineering, 13, 272-290.

Elwood, K. J., Pampanin, S., & Kam, W. Y. (22). February 2011 Christchurch earthquake and implications for the design of concrete structures. In Proceedings of the International Symposium on Engineering Lessons Learned from the 2011 Great East Japan Earthquake (pp. 1157-1168).

FEMA (Federal Emergency Mangement Agency). Seismic performance assessment of buildings: volume 1-methodology, FEMA P-58-1, Washington, DC, 2012.

Ganesan, N., Abraham, R., Beena, P. R., & Anil, R. (2013). Influence of horizontal reinforcement on ultra-high-performance concrete wall panels under two way in plane action. CONTRIBUTORY PAPERS, 147.

Ghorbanirenani, I., Tremblay, R., Léger, P., & Leclerc, M. (2011). Shake table testing of slender RC shear walls subjected to eastern North America seismic ground motions. Journal of Structural Engineering, 138(12), 1515-1529.

Guo, T., Zhang, G., & Chen, C. (2014). Experimental study on self-centering concrete wall with distributed friction devices. Journal of Earthquake Engineering, 18(2), 214-230.

Kolozvari K (2013) Analytical modeling of cyclic shear-flexural interaction in reinforced concrete structural walls. Doctoral dissertation, University of California.

Kinali, K., & Ellingwood, B. R. (2007). Seismic fragility assessment of steel frames for consequence-based engineering: A case study for Memphis, TN. Engineering structures, 29(6), 1115-1127.

McCormick, J., Aburano, H., Ikenaga, M., & Nakashima, M. (2008, October). Permissible residual deformation levels for building structures considering both safety and human elements. In Proceedings of the 14th world conference on earthquake engineering (pp. 12-17).

Menegotto, M., & Pinto, P. (1973). Method of analysis for cyclically loaded RC plane frames including changes in geometry and non-elastic behavior of elements under combined normal force and bending. In Proc. of IABSE Symposium on resistance and ultimate deformability of structures acted on by well defined repeated loads (pp. 15-22).

NBCC (2015) National Building Code of Canada. Canadian Commission on Building and Fire Codes, National research council of Canada, Ottawa.

OpenSees (2018) Open system for earthquake engineering simulation. Berkeley, CA.

Orakcal K, Wallace J W, Conte J P (2004) Nonlinear modeling and analysis of reinforced concrete structural walls. ACI Structural Journal 101(5): 688-698.

Panagiotou M (2008) Seismic design, testing, and analysis of reinforced concrete wall buildings. Doctoral dissertation, University of California.

Panneton, M., Léger, P., & Tremblay, R. (2006). Inelastic analysis of a reinforced concrete shear wall building according to the National Building Code of Canada 2005. Canadian Journal of Civil Engineering, 33(7), 854-871.

Riva, P., Meda, A., & Giuriani, E. (2003). Cyclic behaviour of a full-scale RC structural wall. Engineering Structures, 25(6), 835-845.

Saiidi, M. S., O'Brien, M., & Sadrossadat-Zadeh, M. (2009). Cyclic Response of Concrete Bridge Columns Using Superelastic Nitinol and Bendable Concrete. ACI Structural Journal, 106(1).

Su, R. K. L., & Wong, S. M. (2007). Seismic behaviour of slender reinforced concrete shear walls under high axial load ratio. Engineering Structures, 29(8), 1957-1965.

Tazarv, M., & Saiidi, M. S. (2013). Analytical studies of the seismic performance of a full-scale SMA-reinforced bridge column. International Journal of Bridge Engineering, 1(1), 37-50.

Tsai, K. C., Hsiao, C. P., & Bruneau, M. (2000). Overview of building damages in 921 Chi-Chi earthquake. Earthquake Engineering and Engineering Seismology, 2(1), 93-108.

Westenenk, B., de la Llera, J. C., Besa, J. J., Jünemann, R., Moehle, J., Lüders, C., ... & Hwang, S. J. (2012). Response of reinforced concrete buildings in Concepción during the Maule earthquake. Earthquake Spectra, 28(S1), S257-S280.

Youssef, M. A., Alam, M. S., & Nehdi, M. (2008). Experimental investigation on the seismic behavior of beam-column joints reinforced with superelastic shape memory alloys. Journal of Earthquake Engineering, 12(7), 1205-1222.

Youssef, M. A., & Elfeki, M. A. (2012). Seismic performance of concrete frames reinforced with superelastic shape memory alloys. Smart Structures and Systems, 9(4), 313-333.

Varela, S., & Saiidi, M. S. (2014). Dynamic performance of novel bridge column with CuAlMn shape memory and ECC, international. J. Bridge. Eng, 2(3), 29-58.

Vecchio, F. J. (1989). Nonlinear finite element analysis of reinforced concrete members. ACI structural journal, 86(1), 26-35

CHAPTER 4

DUCTILITY AND OVERSTRENGTH OF SHAPE MEMORY ALLOY REINFORCED CONCRETE SHEAR WALLS

4.1 INTRODUCTION

During the past decade, researchers proved that using Superelastic (SE) Shape Memory Alloy (SMA) bars in concrete elements results in sustainable structures. Following strong seismic events, such structures can be easily repaired, leading to significant cost savings (Youssef and Elfeki, 2012). With the current demand for self-centering structures, the use of SE-SMA bars in RC structures is expected to be a reality in the soon future.

Extensive experimental and analytical studies have been conducted to explore the use of SE-SMA in concrete structures. Youssef et al. (2008) experimentally examined the cyclic performance of a beam-column joint that utilized SE-SMA bars in the plastic hinge region. The SE-SMA RC beam-column joint recovered most of its post-yield deformations. The seismic performance of full-scale frames reinforced with SE-SMA bars was analytically investigated by Alam et al. (2008) and Youssef and Elfeki (2012). Test results showed that SMA RC frames could recover their inelastic deformations even after strong seismic events. Abdulridha (2012) conducted a large-scale cyclic test on an intermediate wall that utilized SE-SMA bars in the plastic hinge region and observed significant deformation recovery. Tazarv and Saiidi (2013) experimentally assessed the seismic performance of a full-scale SE-SMA RC bridge column. The results showed that SE-SMA bars reduced the residual drifts and limited the damage in the plastic hinge zone.

Effendy et al. (2006) used external superelastic SE-SMA bars to improve the seismic performance of existing squat walls. Ghassemieh et al. (2012) investigated the seismic performance of RC walls equipped with SE-SMA bars. Results indicated lower residual strains and reasonable seismic performance. Abraik and Youssef (2015, 2016) highlighted the significant effect of the number and locations of SE-SMA bars on the residual displacements

of RC walls. SE-SMA bars were also found to reduce damage to coupling beams and residual displacements of RC coupled walls (Ghassemieh et al., 2017; Rezapour and Ghassemieh, 2018). Abraik and Youssef (2018a) investigated the seismic performance and vulnerability of SE-SMA RC walls and confirmed the superior seismic performance of SE-SMA RC walls as compared to steel RC walls. The seismic performance of SE-SMA dual systems was analytically investigated by Abraik and Youssef (2018b). SE-SMA RC dual systems were found to have superior seismic performance as compared to steel RC dual systems. Kian and Cruz-Noguez (2018) experimentally showed that SE-SMA bars could reduce seismic residual drifts while offering significant levels of energy dissipation and ductility.

Previous experimental and numerical studies did not address the seismic design characteristics for SE-SMA RC walls. This chapter addresses this shortcoming, which will pave the way for their future use. The evaluated seismic design characteristics are the ductility μ, the response modification factor R, and the over-strength factor Ω.

4.2 DISPLACEMENT DUCTILITY AND OVERSTRENGTH

Figure 4.1 shows the relationship between the seismic base shear and the top displacement of a typical RC building. The ductility μ is equal to $\frac{\Delta max}{\Delta y}$, where Δmax is the displacement corresponding to the peak lateral strength Vy, and Δy is the displacement at which the lateral stiffness of the building is significantly reduced. FEMA 356 (2000), Park (1988), and Priestley (1987) proposed estimating Δy by using 0.6 Vy secant stiffness, 0.75Vy secant stiffness, or initial tangent stiffness, as shown in **Figure 4.2**. Mahin (1976) defined Δy by approximating the load-displacement curve to a bilinear curve using an equal area approach. In this chapter, the method proposed by Park (1988) is used to calculate the ductility μ.

The structure overstrength Ω results from design approximations, material overstrength, and redundancies in the lateral load system (Park, 1988). Ω can be defined as the ratio of nominal shear capacity V_y to the shear force V_s corresponding to the first yielding displacement (Uang, 1991). A study conducted by Salonikios et al. (2000) defined the first yield of steel RC walls to correspond to 75%-80% of their ultimate strength. FEMA P698 (2009) recommended using

the same definition to estimate the first yield displacement. For SE-SMA RC walls, Abdulridha (2012) found experimentally that the first yield displacement corresponds to 75% of the wall ultimate strength.
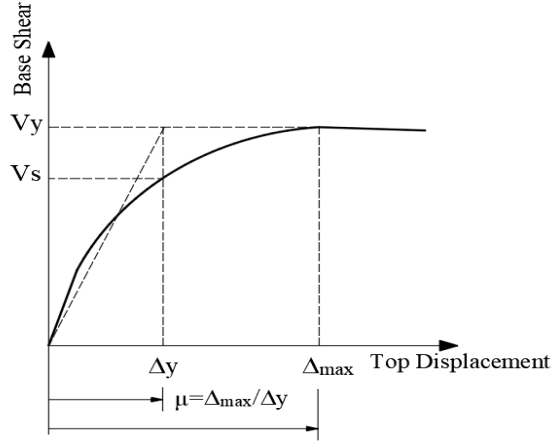
Figure 4.1. Relationship between base shear and top displacement
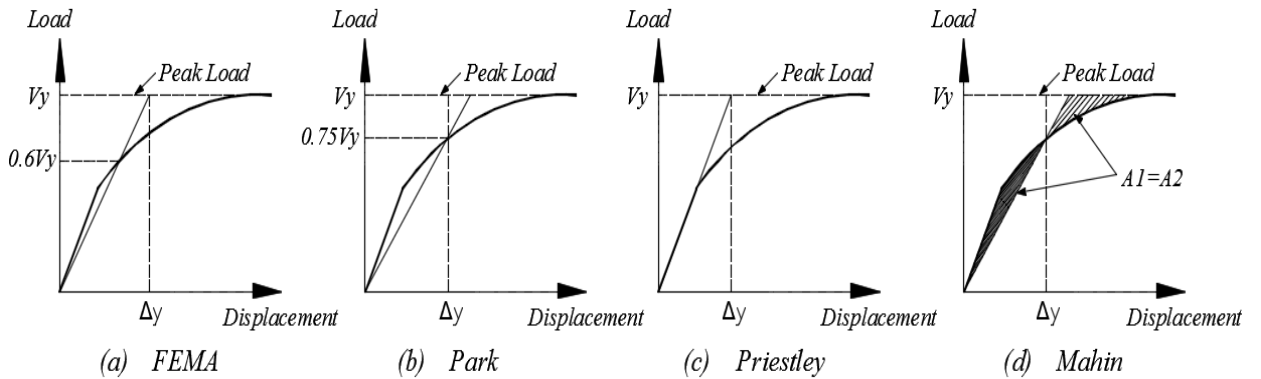
Figure 4.2. Definitions for yield displacement

μ and Ω can be used to calculate the force reduction factor R, which is equal to ΩR_μ. R_μ is calculated using Eq. 4.1, which was proposed by Newmark and Hall (1982).

$$R_\mu = \begin{cases} \mu & \text{for } T \geq 0.5 \text{ sec} \\ \sqrt{2\mu - 1} & \text{for } T < 0.5 \text{ sec} \end{cases} \tag{4.1}$$

where T is the fundamental structural period, which is determined using the effective stiffness K_{ef}.

$$K_{ef} = \alpha_v K_v \tag{4.2}$$

$$K_v = \frac{Gb_w d}{f.H_w} \tag{4.3}$$

where α_v is axial load reduction factor, K_v is the secant shear stiffness at the first yield displacement (Park and Paulay, 1975), G is the shear modulus, b_w is the wall thickness, d is the effective wall length, f =1.2 for rectangular RC walls, and H_W is the wall height.

The following sections provide details about the adopted modeling technique for SE-SMA RC walls, the conducted analytical study, the proposed values for Ω and R, and their evaluation using the FEMA P695 (2009).

4.3 NUMERICAL MODELING

To predict the nonlinear response of SE-SMA RC walls under reversed cyclic loading, the Shear-Flexural-Interaction Multi-Vertical-Line-Element Model (SFI-MVLE), developed and validated by Kolozvari (2013) in the Open System Earthquake simulation software (OpenSees, 2018), was utilized. The model accounts for the interaction between the flexural and shear behaviour of moderate and slender RC shear walls. The model and the material constitutive relationships are shown in **Figures 4.3** and **4.4**, respectively. The figure shows three MVLEs modeling a RC wall. Each element has six degrees of freedom. They represent the horizontal deformation, the vertical deformation, and the rotation at the center of top and bottom rigid beams. Two-dimensional membrane RC panels are utilized to capture the flexural and shear behaviour of RC walls. Each panel accounts for the shear resistance using a fixed angle approach (Kolozvari, 2013).

The flexural response is captured through the axial deformation u_y of the RC panels in the vertical direction. The average normal vertical strain $\varepsilon_{y,j}$ can be determined by dividing the average vertical deformation u_y by the element height h. The relative rotation between the top and bottom faces of the wall element is assumed to happen at a height ch, measured from the bottom. The value of height coefficient c is recommended to be taken as 0.4 (Orakcal et al., 2004). This rotation allows calculating the shear response (shear deformation u_{sh}) of the SFI-

MVLE element. The effect of increasing or decreasing the number of RC panels or the number of SFI-MVLEs on the load-displacement curve of RC walls was found to be insignificant (Kolozvari, 2013).

Figures 4.4(a) and **4.4(b)** show the Menegotto-Pinto hysteretic model with isotropic hardening (1973), and the biaxial concrete constitutive model by Chang and Mander (1994), respectively. Nickel-Titanium alloy (55.9% Nickel and 44.1% Titanium) is the most common type of superelastic SMA. **Figure 4.4(c)** describes the flag-shape of the NiTi SE-SMA material model proposed by Christopoulos (2008). The SE-SMA stress f_{y-SMA} marks the phase transformation from austenite to martensite, and the change in stiffness from K_1 to K_2. Upon unloading from any strain less than a recoverable strain ε_r, the slope of the unloading path is K_1 until reaching βf_{y-SMA}, then it becomes K_2.until meeting the initial loading branch.

(a) RC wall   (b) MVLE model
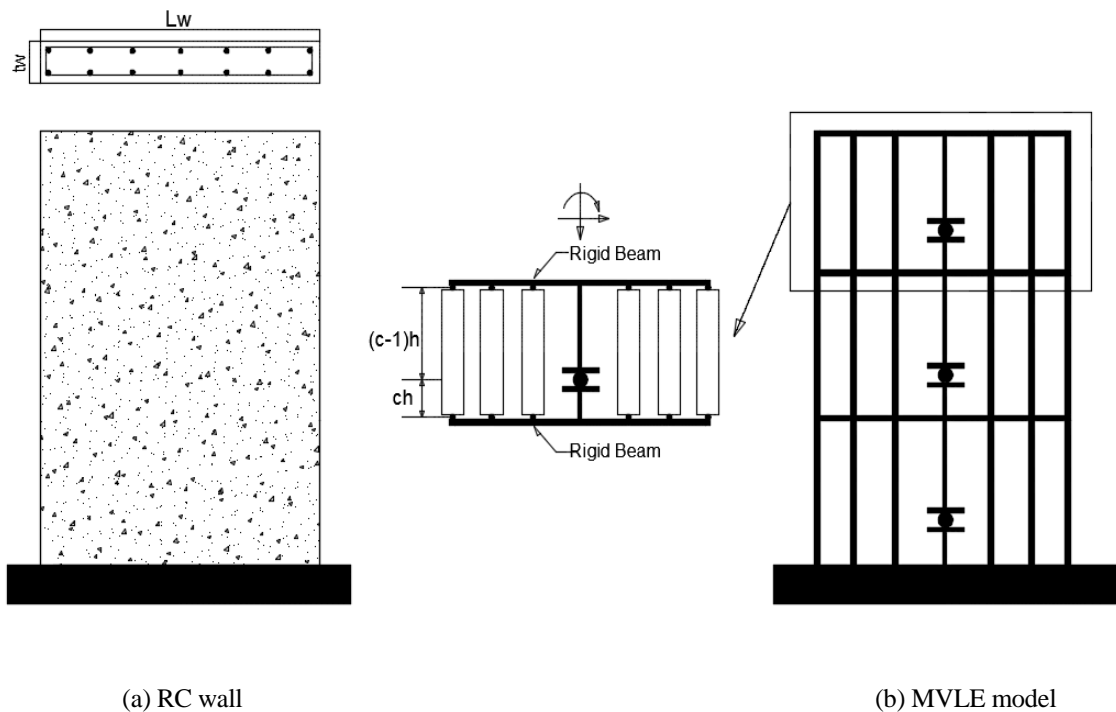
Figure 4.3. RC wall model: (a) RC wall; (b) MVLE model
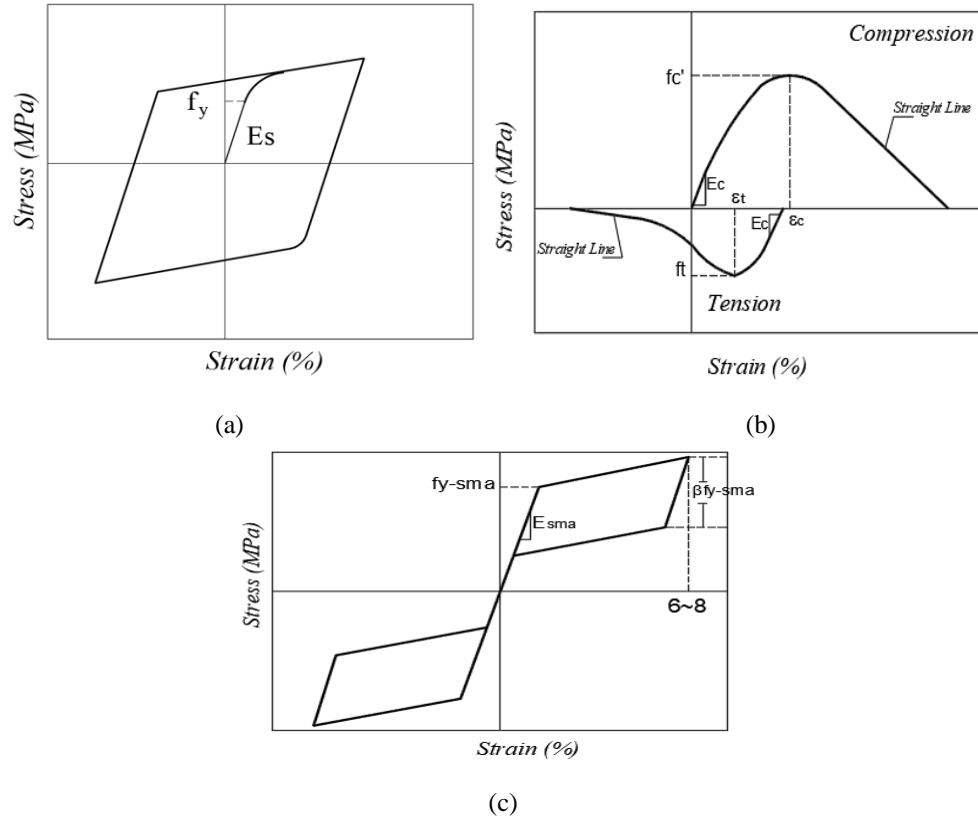
Figure 4.4. Material constitutive relationships: (a) steel; (b) concrete; (c) SE-SMA

4.3.1 Failure criteria

A strain limit of 5% was chosen to define failure for longitudinal steel bars (Blume et al. 1961; Scott et al. 1982; Pauley and Priestley 1992; Priestley et al. 2007; Panagiotou 2008). For SMA bars, the ultimate strain ε_r is assumed 7%, which is the limit for the superelastic range (Hurlebaus and Gaul 2006). The concrete compressive strain limit is assumed 2% (Panagiotou 2008).

4.3.2 Numerical validation

An intermediate SE-SMA RC wall, with an aspect ratio of 2.2, was experimentally tested by Abdulridha (2012). The SE-SMA bars were located at the wall boundaries for the plastic hinge length. The longitudinal reinforcement ratios in the wall boundaries and the wall web were 1.33% and 0.88%, respectively. The transverse reinforcement ratio was 0.88%. The values of $f_c', f_y,$ and f_{y-SMA} were 31, 425, and 380 MPa, respectively. The wall is modelled using the SFI-MVLE element. The experimental results and numerical predictions are shown in **Figure 4.5**. The SFI-MVLE model has accurately captured the peak shear strength (error of -5.7%),

ultimate displacement (error of +5.5%), and residual displacement (error of -1.0%). It should be noted that predicting the degradation in strength is not required to evaluate the seismic design parameters. However, degradation can be predicted using the adopted model following the recommendations of Rezapour and Ghassemieh (2018).

Kian and Cruz-Noguez (2018) performed a test on the SE-SMA RC wall. The reinforcement ratio in the transverse and longitudinal directions was 0.4%. The boundary element reinforcement, vertical web reinforcement, and the horizontal reinforcement had a ratio of 1.8%, 0.4%, and 1.0%, respectively. The values of $f'_c, f_y,$ and f_{y-SMA} were 51, 421, and 330 MPa, respectively. **Figure 4.6** compares the experimental and SFI-MVLEM predictions. It illustrates that the numerical model accurately captures the peak strength and corresponding displacement.
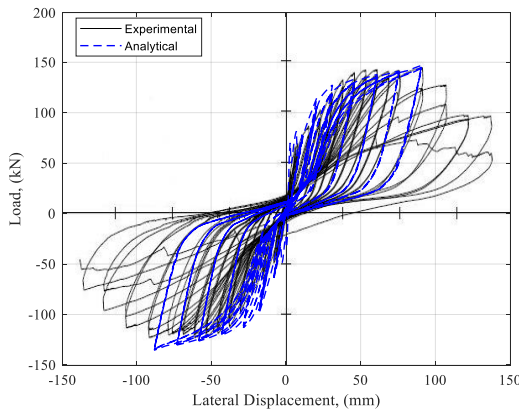
Figure 4.5. Comparison of experimental and numerical results for SE-SMA RC wall (Abdulridha, 2012)
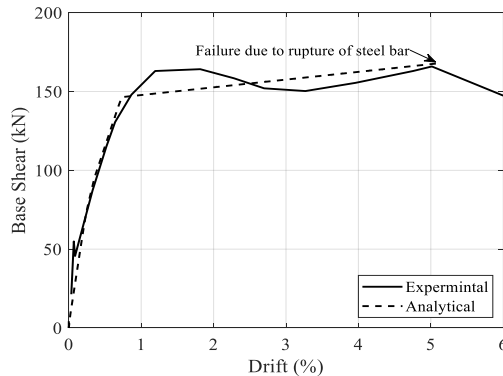
Figure 4.6 Comparison of experimental and numerical results for the SE-SMA RC wall (Kian and Cruz-Noguez, 2018)

An experimental shake table test of an eight-story RC wall by Ghorbanirenani et al. (2012) is used to investigate the sensitivity of the model discretization on the predicted results. **Figure 4.7(a)** shows the effect of using one versus two SFI-MVLEM per story. The variation of the height coefficient c is also investigated in **Figure 4.7(b)**. The results indicate that the number of vertical elements and the coefficient c have a minor effect on the overall response. The numerical model capability to capture the local wall response is also illustrated in **Figure 4.7(c)** by showing the strain history for an outer bar.

(a)   (b)

(c)
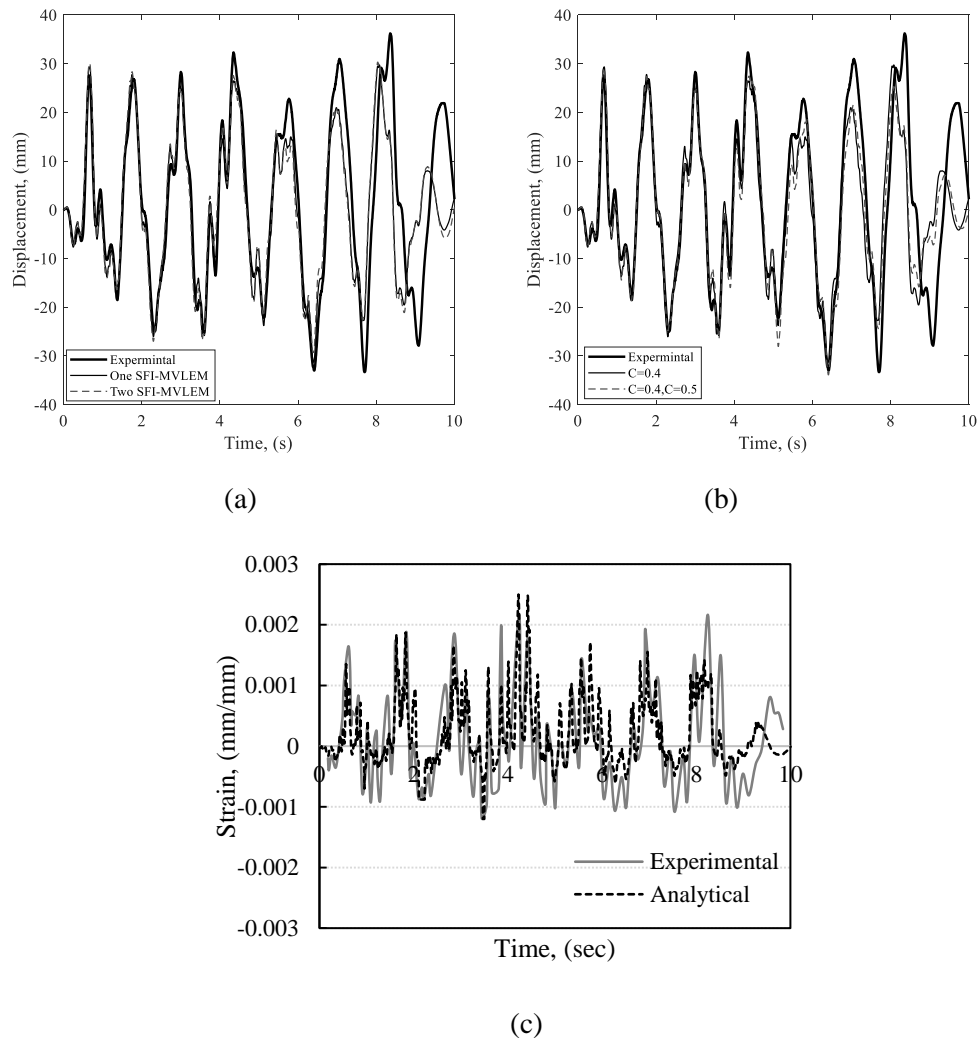
Figure 4.7 Comparison of experimental and numerical results for a SE-SMA RC wall: (a) effect of different elements/story; (b) effect of different C; (c) strain history of outer longitudinal steel bar

4.4 NUMERICAL STUDY

Nine-hundred and seventy-two SE-SMA concrete shear walls were analyzed. They cover the design parameters listed in **Table 4.1**. Axial load ratios were chosen within the range of $0 \leq P/(Ag\, fc') \leq 0.15$ as per the recommendation of Priestley at al. (2007) for low and midrise buildings. Three typical wall thicknesses were chosen. The minimum transverse, web, and boundary RFT ratios were chosen as per CSA A23.3 (2014). In some walls, higher transverse ratios were used to avoid shear failure. Three boundary reinforcement ratios were selected in this study based on the minimum code requirement, and previous studies (Wood, 1989; Bonelli et al., 1999). SE-SMA bars were assumed to replace the steel bars in the plastic hinge region either fully (SMAPH) or to only replace the steel bars within the boundary elements (SMABW), as shown in **Figures 4.8(a)** and **4.8(b)**, respectively.

Figure 4.8(c) shows that two SFI-MVLE elements are used to model the plastic hinge zone and the remaining wall height. The wall is fixed at its base. A typical wall cross-section is shown in **Figure 4.8(d)**. The axial load was first applied, and, then a reversed cyclic displacement-controlled loading protocol, shown in **Figure 4.8(e)**, was applied horizontally at the top of the wall. The loading protocol is based on the guidelines for cyclic seismic testing of components of steel structures (ATC-24, 1992) and was previously utilized by Abdulridha (2012) to experimentally test SE-SMA RC walls.
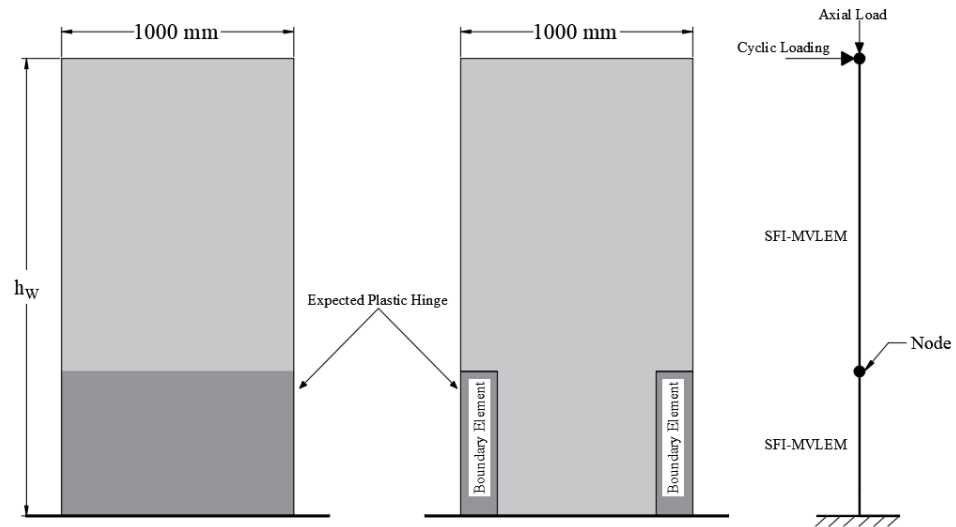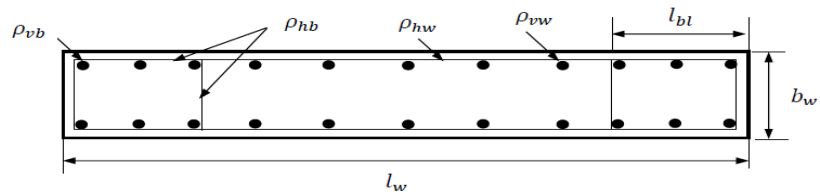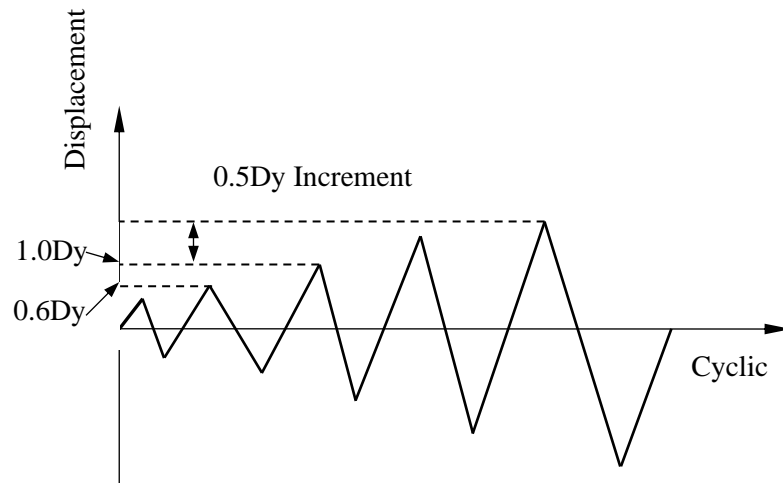
Figure 4.8 Numerical study details (a) SMAPH RC wall; (b) SMABW RC wall; (c) SFI-MVLE along the height; (d) typical wall section; (e) cyclic loading

Table 4.1. Range for the selected parameters for the considered walls

	Aspect Ratio AR	Period (sec)	Thickness b_w (mm)	Axial Load Ratio $\frac{P}{A_g f'_c}$ (%)	Transverse RFT ρ_{hw} (%)	Web RFT ρ_{vw} (%)	Boundary RFT ρ_{vb} (%)
Case 1	6.0	>0.5	150, 200, 230	2, 7.5, and 10	0.25, 0.5, and 1	0.5, 0.66, 0.75, and 1	0.5, 1.0, and 1.5
Case 2	3.0	<0.5	150, 200, 230	2, 7.5, and 10	0.25, 0.5, and 1	0.5, 0.66, 0.75, and 1	0.5, 1.0, and 1.5
Case 3	1.5	<0.5	150, 200, 230	2, 7.5, and 10	0.25, 0.5, and 1	0.5, 0.66, 0.75, and 1	0.5, 1.0, and 1.5

Figures **4.9(a)** and **4.9(b)** show the variation of the displacement ductility μ and the overstrength factor with the wall aspect ratio. For the three considered aspect ratios, the average displacement ductility and overstrength factor are 2.8 and 2.3 for SMAPH walls, and 3.7 and 2.7 for SMABW walls. The ductility and overstrength of the SMABW walls are almost constant as failure is controlled by fracture of the web rebars, whereas the failure mechanism for SMAPH walls is controlled by the SE-SMA bars.
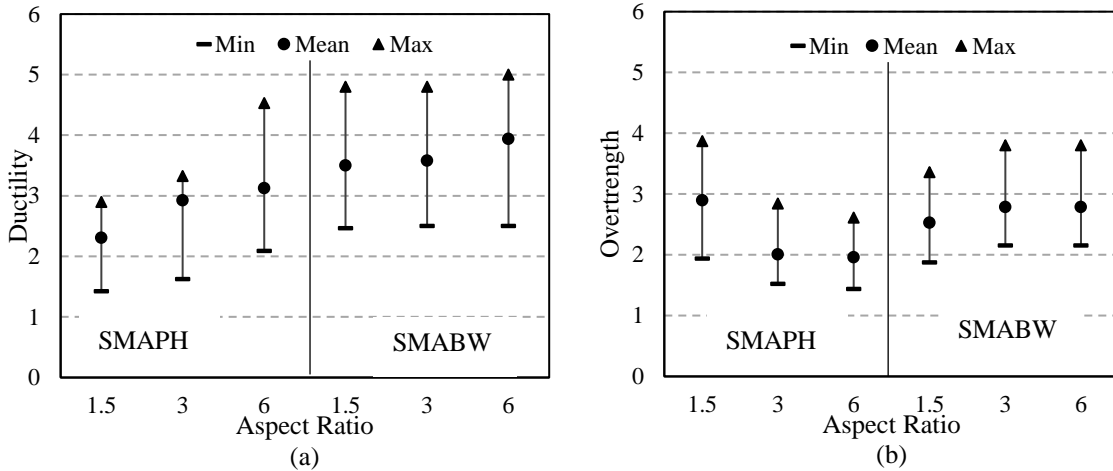
Figure 4.9. Effect of wall aspect ratio: (a) ductility; (b) overstrength

The variations of the ductility and overstrength factors with the axial load ratio are illustrated in **Figures 4.10(a)**, **4.10(b)**, **4.11(a)**, and **4.11(b)**. SMABW walls have a slightly higher ductility than SMAPH walls. Increasing the axial load ratio from 2% to 10%, slightly increases the displacement ductility of the considered walls. The source of this increase is related to the failure mode. At low axial load ratio (flexural only), failure occurred due to concrete crushing in the case of SMAPH walls and yielding of longitudinal web steel reinforcement in case of SMABW walls, which limited the ultimate displacement. Increasing the axial load ratio from 2% to 10% slightly reduces the overstrength factor due to the increase in Vs value.

The effect of varying the wall thickness on the displacement ductility and overstrength is shown in **Figures 4.10(c)**, **4.10(d)**, **4.11(c)**, and **4.11(d)**. The displacement ductility of SMAPH walls decreased slightly with increasing the thickness, and its average value was 2.6; whereas, the displacement ductility of SMABW walls was almost constant at about

3.2. Regarding the overstrength factor, its value was about 2.1 for SMAPH and SMABW walls, regardless of the thickness.

Figures 4.10(e), **4.10(f)**, **4.11(e)**, and **4.11(f)** show the effect of the amount of vertical web reinforcement on the displacement ductility and overstrength. Increasing SMABW wall web reinforcement from 0.66% to 1.0% marginally affects the displacement ductility, which is about 2.3 for SMAPH walls and 3.4 for SMABW walls. Regarding the overstrength factor, its value increased by about 25% when the amount of horizontal steel increased from 0.5% to 1.0%.

The influence of wall boundary reinforcement is shown in **Figures 4.10(g)**, **4.10(h)**, **4.11(g)**, and **4.11(h)**. The mean displacement ductility of the SMAPH wall was about 2.3 for boundary reinforcement ratios of 0.5% and 1.5%. SMABW wall displacement ductility reduced by 37% when the boundary reinforcement ratio increased from 0.5% to 1.5%. The reduction in displacement ductility value of SMABW walls is due to its large yield displacement value. Regarding the overstrength factor, it increased with the increase of the boundary reinforcement ratio. Increasing the reinforcement ratio from 0.5% to 1.5%, the overstrength factor increased by about 26% for both SMAPH and SMABW walls.

Figure 4.12 shows the effect of horizontal steel ratio on the load-displacement relationship for walls with an aspect ratio (AR) of 6. It is obvious that increasing the horizontal steel ratio from 0.25% to 1.0% does not affect the load-displacement curve.

The displacement recovery is defined as the ratio of the recoverable displacement to the maximum lateral displacement. The effect of SE-SMA bars on the cyclic displacement recovery is shown in **Figure 4.13**. It is evident that the SMAPH walls experienced greater displacement recovery than SMABW walls. Considering aspect ratios from 1.5 to 6.0 and wall thicknesses from 150 mm to 230 mm, the average displacement recovery is 96% for SMAPH walls and 73% for SMABW walls. Varying the axial load, shown in **Figure 4.12(c)**, from 2% to 10% did not affect the displacement recovery for SMAPH walls. However, it increased the displacement recovery for SMABW by about 40%. **Figure 4.12(d)** shows the effect of the horizontal steel ratio on the displacement recovery. SMABW walls achieved a maximum displacement recovery of 75% at 0.8% horizontal steel ratio, whereas SMAPH walls were not influenced by the horizontal steel ratio, and

they exhibited a stable displacement recovery of 96%. The variation of the displacement recovery with the web reinforcement and boundary wall reinforcement is shown in **Figures 4.13(e)** and **4.13(f)**, respectively. The displacement recovery of SMAPH walls was not affected by the amount of web and boundary reinforcement. SMABW walls recovered 82% of the applied displacement at 0.5% web reinforcement. Increasing the amount of web reinforcement from 0.5% to 1% led to a 35% reduction in the displacement recovery. Increasing the amount of SE-SMA reinforcement ratio at wall boundaries from 0.5% to 1.5% resulted in increasing the displacement recovery by 30%.
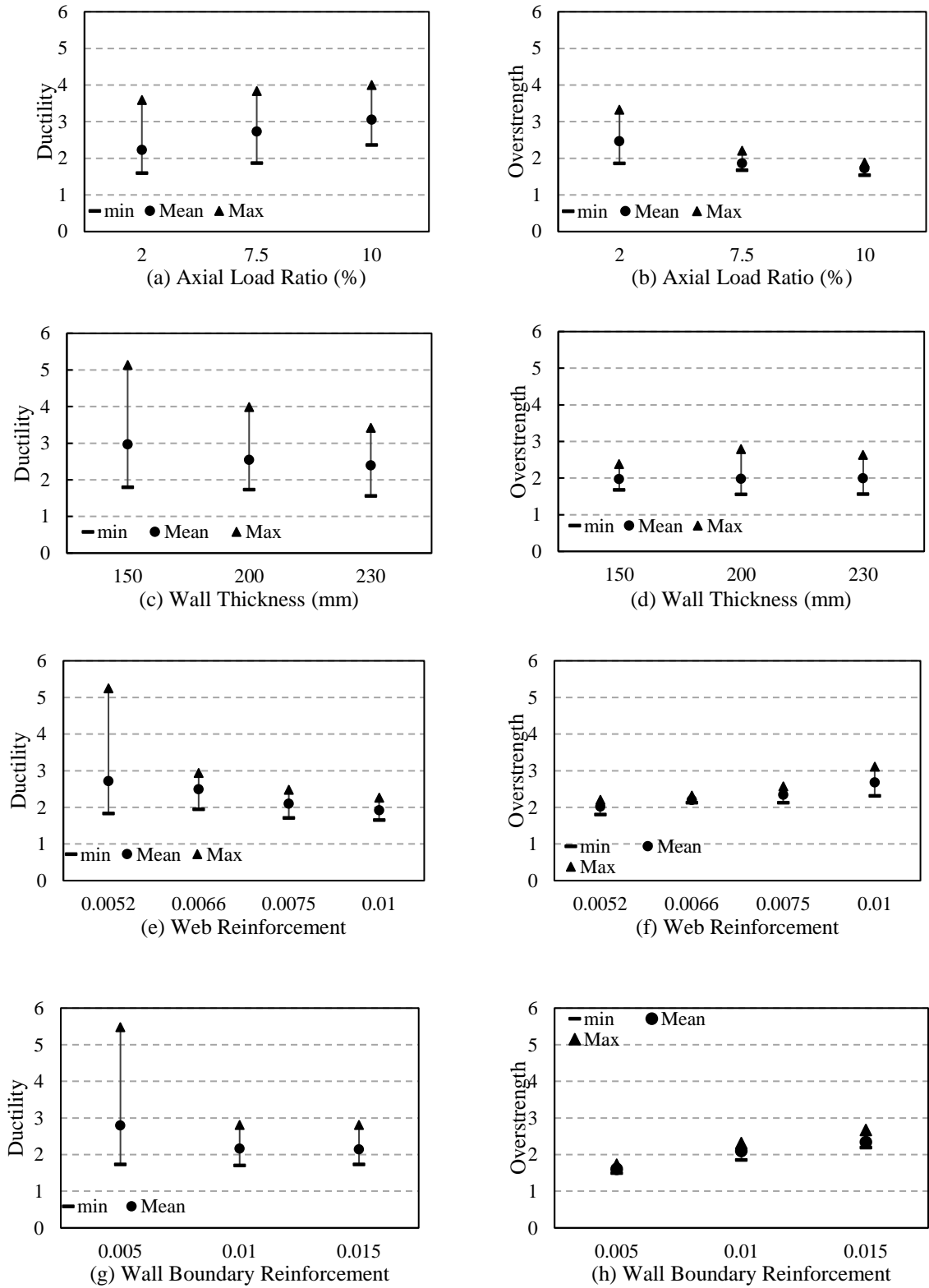
Figure 4.10. Effect of wall design parameters on the ductility and overstrength for SMAPH walls
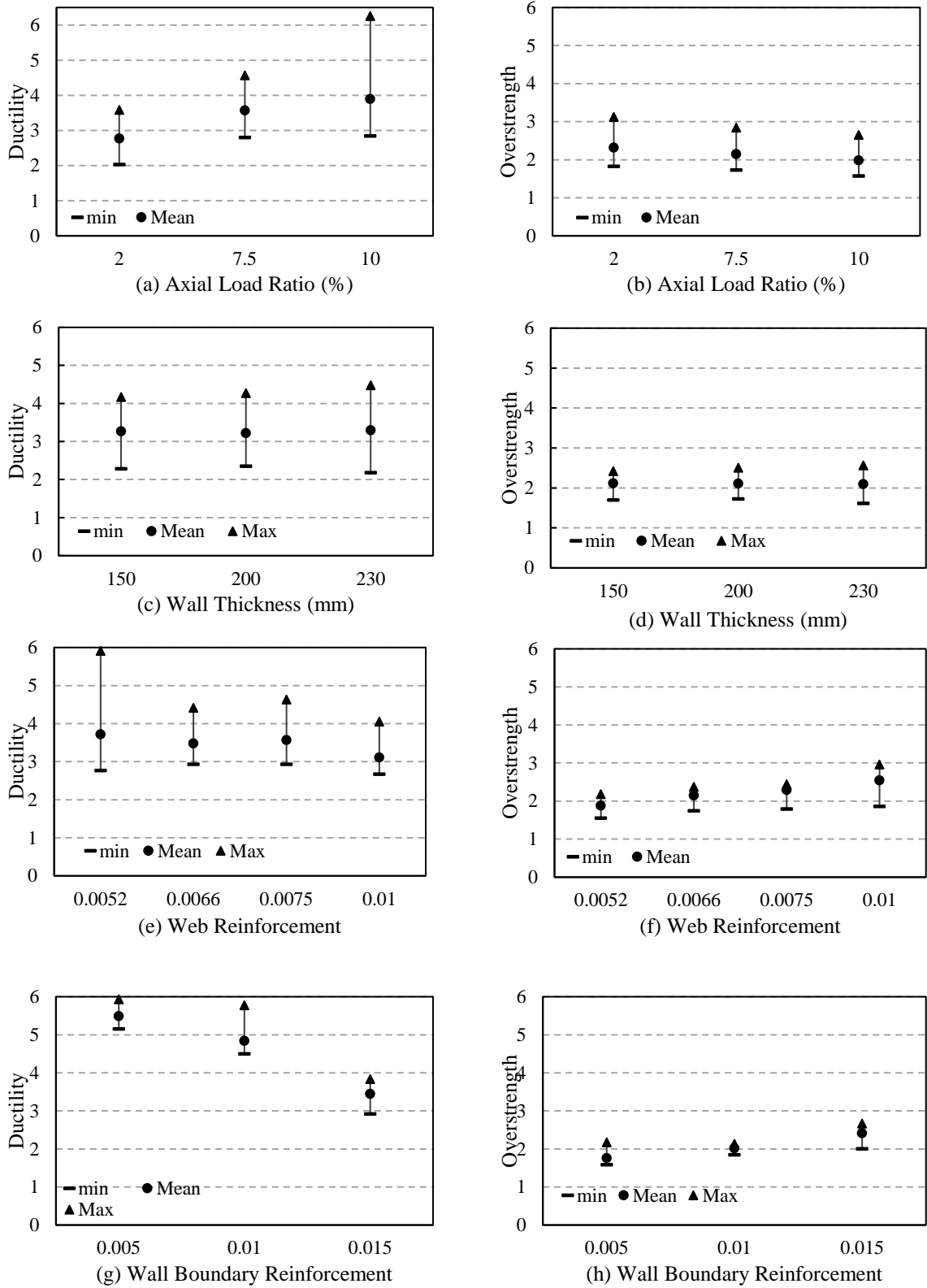
Figure 4.11. Effect of wall design parameters on the displacement and overstrength for SMABW walls
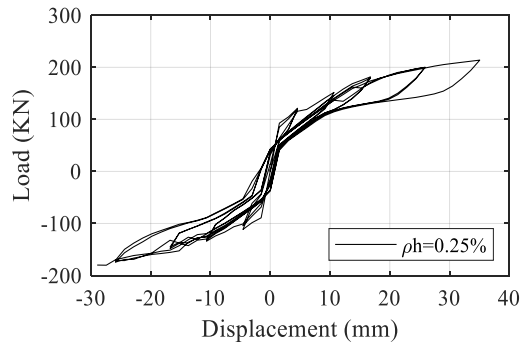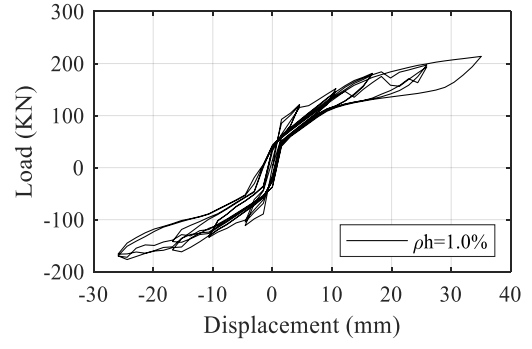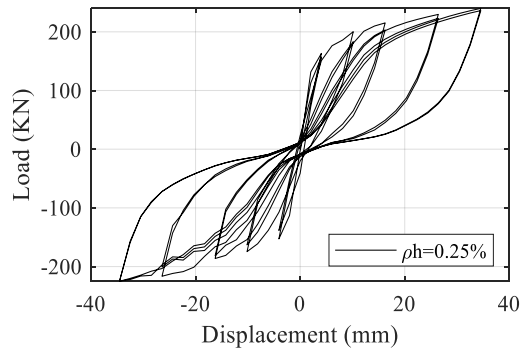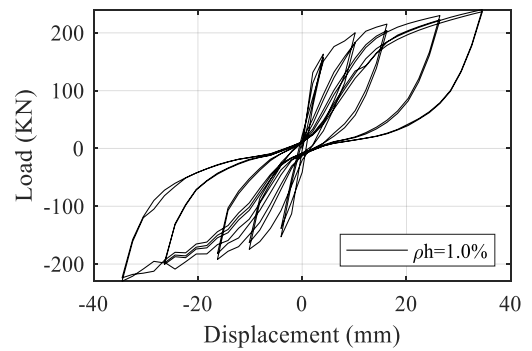
Figure 4.12 Effect of horizontal steel ratio on load-displacement relationship:(a) SMAPH $\rho_h = 0.25\%$; (b) SMAPH $\rho_h = 1.0\%$; (c) SMABW $\rho_h = 0.25\%$; (d) SMABW $\rho_h = 1.0\%$
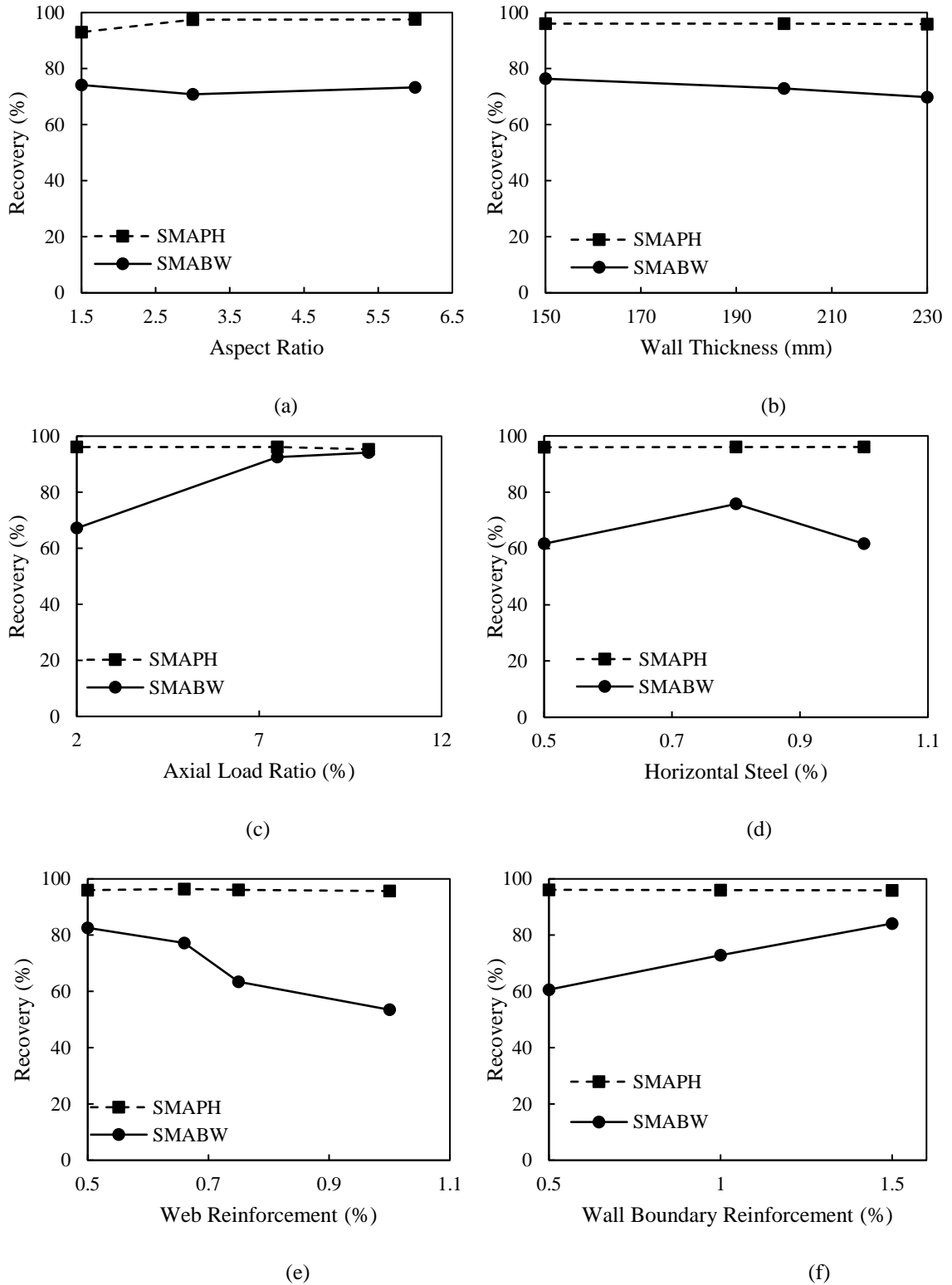
Figure 4.13. Displacement recovery considering different wall design parameters

4.5 SEISMIC DESIGN PARAMETERS

The response modification factor R and overstrength factor Ω were determined for the mentioned 972 walls. **Figure 4.14** shows the whisker chart, which includes the mean, maximum, minimum, 25%, and 75% of the estimated values for both SMAPH and SMABW walls based on their aspect ratio and SE-SMA bars location. The mean values of R are 2.5 and 3.0 for SMAPH walls with aspect ratio <2.0 and >2.0, respectively, whereas the mean values of R for SMABW walls with aspect ratio <2.0 and >2.0 are 3.0 and 4.0, respectively. The corresponding coefficient of variations (COV) is 20% and 16% for SMAPH walls with aspect ratio <2.0 and >2.0, respectively; and 20% and 19% for SMABW walls with aspect ratio <2.0 and >2.0, respectively. The mean value of Ω is 2.25 for SMAPH and SMABW walls. The corresponding COVs are 21% for SMAPH walls and 18% for SMABW walls.

(a) (b)
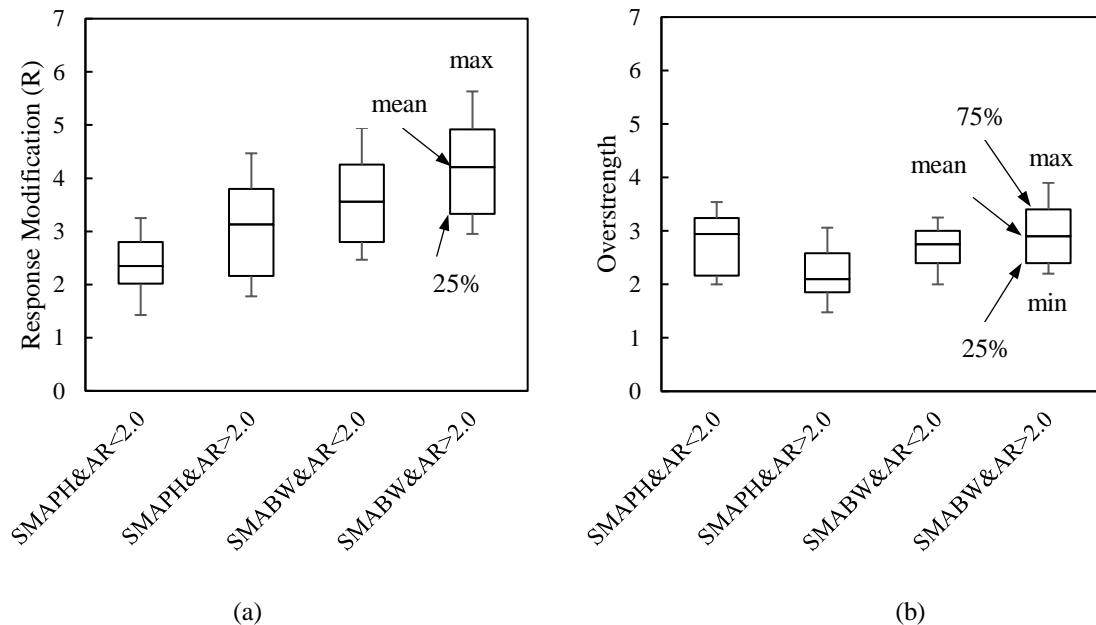
Figure 4.14. Response modification and overstrength factors:(a) R factor; (b) Ω factor

4.6 CASE STUDIES

Three buildings with different heights (3, 6, and 9 stories) are designed using the evaluated mean seismic design parameters, given in the previous section. A typical floor plan for the

designed buildings with a typical story height of 3 m, as shown in **Figure 4.15**. The buildings are assumed to be in Vancouver, BC. Their main lateral resistance system is composed of ductile moment-resisting frames in the longitudinal direction and ductile shear walls in the transverse direction. The walls are designed according to the current Canadian standards, CSA A23.3 (2014) and NBCC (2015). The concrete compressive strength and steel yield strength are assumed 30 MPa and 400 MPa, respectively. The length of SE-SMA bars was taken equal to the plastic hinge length (L_p) as given by Eq 4.3 (CSA A23.3, 2014).

$$L_p = 0.5L_w + 0.1H \tag{4.3}$$

Each building was designed twice, using either SMAPH or SMABW walls. The design of the considered walls is summarized in **Figure 4.8(a)**, and **Table 4.2**. The web and/or boundary bars are assumed to be SE-SMA bars for SMAPH and SMABW walls. Eigenvalue analysis is performed using OpenSees (2018) to obtain the first period T_1 for each building. The designed walls were analyzed using incremental dynamic analysis (IDA) to evaluate their seismic performance. The seismic design parameters were then assessed using FEMA P695 (2009).

4.6.1 Seismic performance of the designed walls

Incremental dynamic analysis (IDA) (Vamvatsikos and Cornell, 2001) was conducted to evaluate the seismic behaviour of the four designed walls. Twenty earthquake ground motions were selected from the PEER Next Generation Attenuation database (2018). The selected ground motions have magnitudes of 6.5 to 7.5. The site class is assumed to be D with shear wave velocity ranging from 180 m/s to 360 m/s. Each ground motion is scaled to match the site design spectra acceleration of Vancouver, BC at the first period. **Figure 4.16** shows the elastic response spectra of these ground motions assuming 5% damping. The analysis is stopped when local failure criteria is observed.
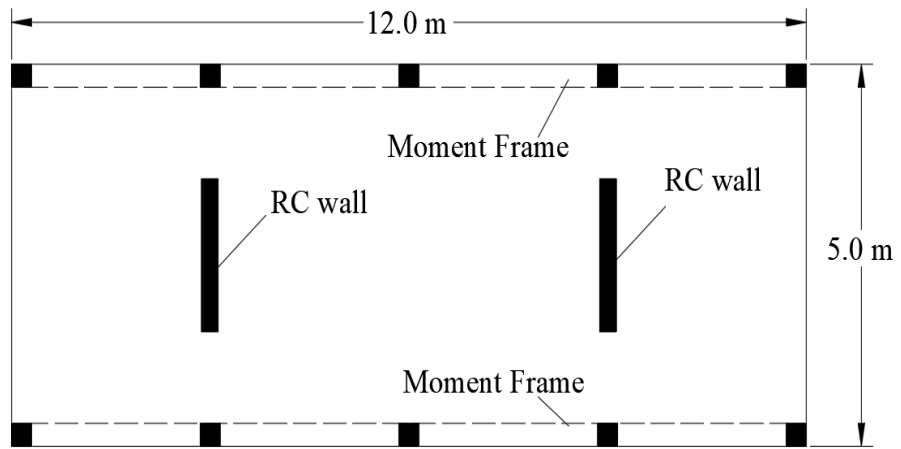
Figure 4.15. Considered structural plan

Table 4.2. Walls design details.

	3-story		6-story		9-story	
	SMAPH3	SMABW3	SMAPH6	SMABW6	SMAPH9	SMABW9
T_1 (sec)	0.61	0.69	1.13	1.15	1.90	2.10
Wall thickness (b_w)	250 mm	200 mm	250 mm		300 mm	250 mm
Wall length (L_w)	1200 mm		1800 mm		2000 mm	
Boundary element length (l_{bl})	300 mm		300 mm		400 mm	
Horizontal steel ratio (web) (ρ_{hb})	0.25%		0.25%		0.25%	
Horizontal steel ratio (boundary)	0.25%		0.25%		0.25%	
Vertical steel ratio (web) (ρ_{VW})	0.8%	1.0%	1.33%		1.11%	1.33%
Vertical steel ratio (boundary) (ρ_{Vb})	2.4%	3.0%	2.4%		2%	2.4%
Total volume of steel/SE-SMA (%)	5.0	5.17	5.70	6.80	6.30	7.13
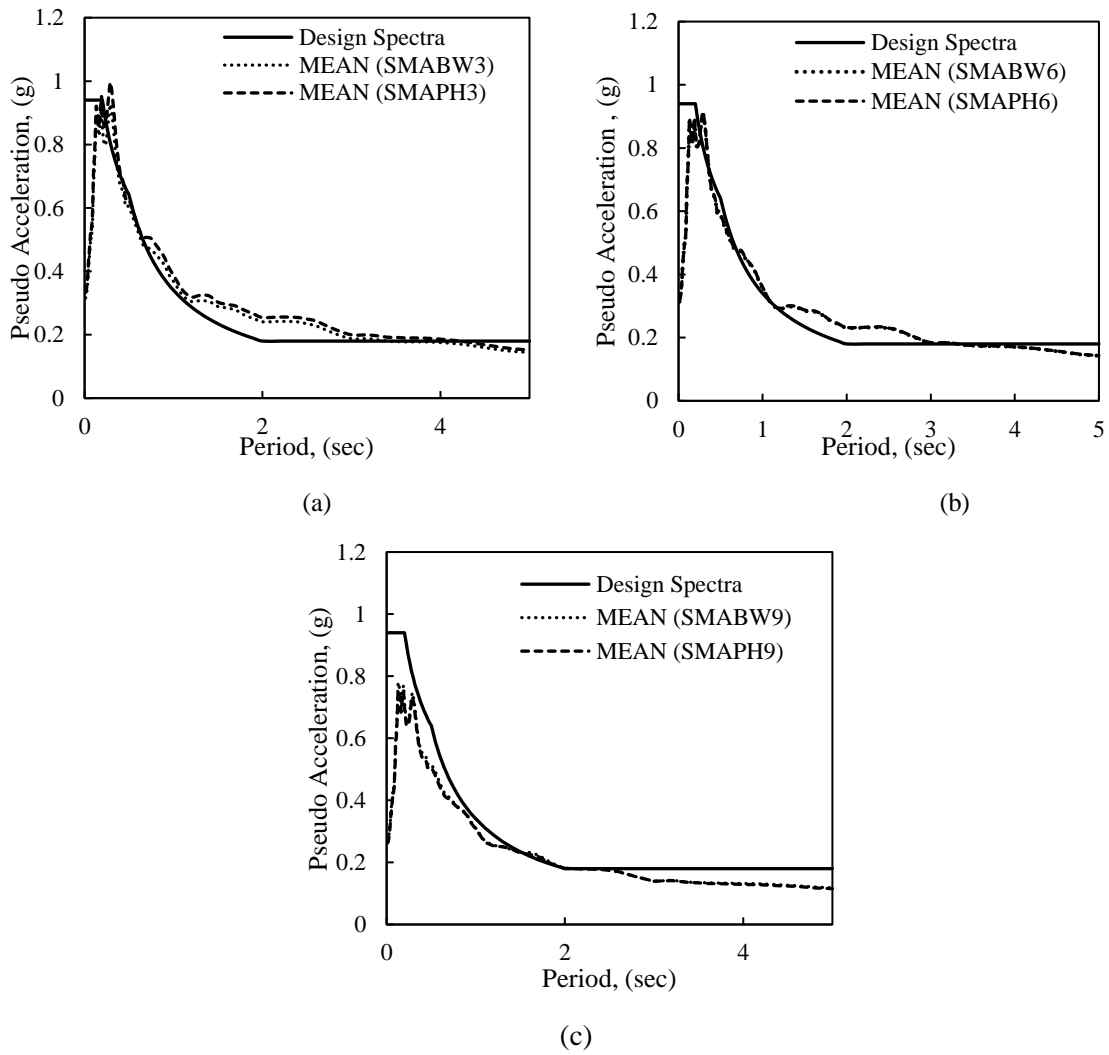
Figure 4.16. Design and pseudo acceleration: (a) three-story; (b) six-story; and (c) nine-story

The lateral and residual roof displacements for different intensity levels are shown in **Figure 4.17**. SMAPH walls experienced higher lateral roof displacement due to their lower initial stiffness as compared to the SMABW walls. At low and medium ground motion intensities and regardless of wall height, the difference in roof displacement between the two walls is negligible, as shown in **Figure 4.17(e)**. The same trend is observed for the roof residual displacement. The residual displacement of SMABW walls is lower than those exhibited in SMAPH walls. The displacement recovery is summarized in **Table 4.3**.

At high ground intensities, both SMAPH and SMABW walls experienced an average displacement recovery of about 93%.

Table 4.3. Displacement recovery of the considered buildings

3-Story			6-Story			9-Story		
$S_a(T_1)$	SMAPH	SMABW	$S_a(T_1)$	SMAPH	SMABW	$S_a(T_1)$	SMAPH	SMABW
1.16	97%	91%	0.62	91%	98%	0.40	92%	92%
0.80	97%	88%	0.50	91%	98%	0.30	97%	96%
0.60	98%	97%	0.40	93%	99%	0.20	94%	95%
0.40	98%	97%	0.30	94%	99%	0.15	94%	95%
0.20	98%	98%	0.20	95%	99%	0.10	97%	98%

(a) Three-story walls

(c) Roof Displacement, (mm)　　(d) Roof Residual Displacement, (mm)

(b) Six-story walls

(e) Roof Displacement, (mm)　　(f) Roof Residual Displacement, (mm)
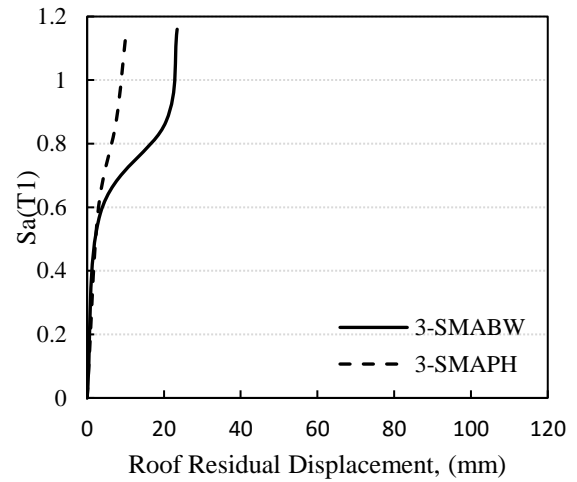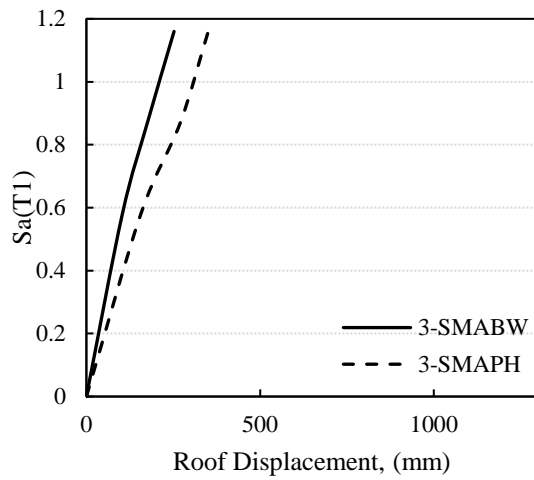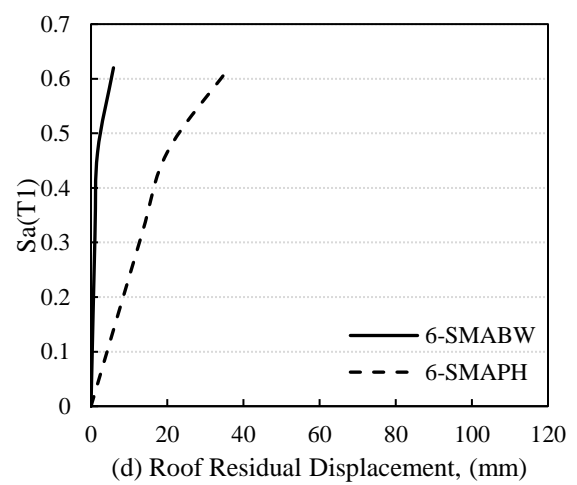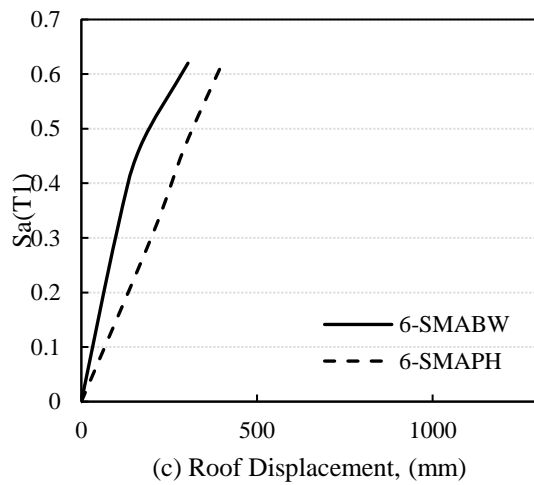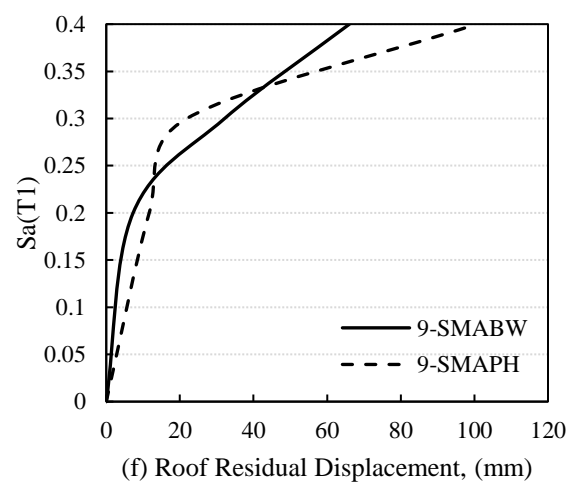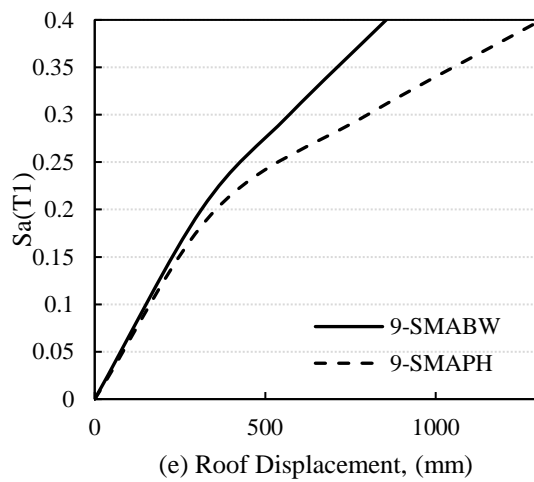
(c) Nine-story walls

Figure 4.17 Seismic response: (a) three-story, (b) six-story, and (c) nine-story

4.6.2 Assessment of the evaluated mean seismic design parameters

Collapse fragility curves showing the intensity measure of the ground motion versus the probability of collapse were developed using the fitting method (Baker, 2015) and are shown in **Figure 4.18**. The 5% damped spectral acceleration at the first period [Sa(T1, 5%)] defines the used intensity measure.

FEMA P695 (2009) defines the collapse probability at 50% as the median collapse capacity $(\hat{S}_{CT})$, as shown in **Figure 4.18**. The difference in the median collapse capacity $\hat{S}_{CT}$ of both walls decreases due to the increase of wall slenderness ratio. The collapse margin ratio (CMR) can be calculated as the ratio of $\hat{S}_{CT}$ to the spectral acceleration of the maximum considered earthquake corresponding to the fundamental period (S_{MT}) assuming a 5% damping ratio, Eqs. 4.4 through 4.6.

$$CMR = \frac{\hat{S}_{CT}}{S_{MT}} \tag{4.4}$$

$$S_{MT} = S_{MS} \quad \text{for} \quad T < T_s \tag{4.5}$$

$$S_{MT} = \frac{S_{M1}}{T} \quad \text{for} \quad T > T_s \tag{4.6}$$

where S_{MS} and S_{M1} are the modified spectral values at the fundamental period and at one second considering the maximum design earthquake, respectively.

The CMR ratio is then modified to account for the modal uncertainty (β_{TOT}) and spectral shape factor (SSF), as recommended by FEMA P695 (2009). The modification is based on the structure fundamental period and the period-based ductility, $\mu_T = \delta_u/\delta_{y,eff}$. β_{TOT} and SSF can be determined from Tables 9-4 and 9-5 in FEMA P695 (2009). μ_T is evaluated considering three options: (1) the maximum base shear and maximum displacement (Max Disp-Max V), (2) the maximum displacement and the corresponding base shear (Max Disp-V), and (3) the maximum base shear and the corresponding displacement (Max V-D). **Figure 4.19** shows the evaluated mean IDA displacement versus shear, considering the three options. The corresponding values of μ_T are summarized in **Table 4.4**. A lower value of μ_T provides a lower SFF value, which leads to a conservative design. In all cases, the

scaling factors were between 1.11–1.22 and the maximum base shear and the corresponding displacement (Max V-D) approach produce about 80% of μ_T values.

The modified collapse margin ratio (ACMR) for each wall can be calculated using Eq. 4.7. The calculated ACMR values are compared to the individual ACMR $_{limit}$ provided by FEMA P695 (2009). The average ACMR for SMAPH walls and SMABW walls are then compared to the mean ACMR $_{limit}$ provided by FEMA P695 (2009). **Table 4.5** summarizes the calculations for ACMR and the acceptance criteria. The designed walls met the acceptance criteria and provided an adequate margin of safety against collapse.

$$ACMR = SFF \times CMR \tag{4.7}$$

Regardless of the reinforcement configuration, the ACMR values were found to be similar for lower period structures, whereas the difference in the ACMR value between the SMABW and SMAPH wall increases with increasing the wall period. The ACMR values are attributed to differences in the frequencies and post-yield softening behaviour that influences the dynamic wall response, as shown in **Figure 4.19**.

Regardless of the SE-SMA configuration within the RC walls, the ACMR values were found to be similar for lower period structures (case of 3 and 6-story), whereas the difference in the ACMR value between the SMABW and SMAPH wall increases with increasing the wall period (case of 9-story). The ACMR values are attributed to differences in the frequencies and post-yield softening behaviour that influences the dynamic wall response.
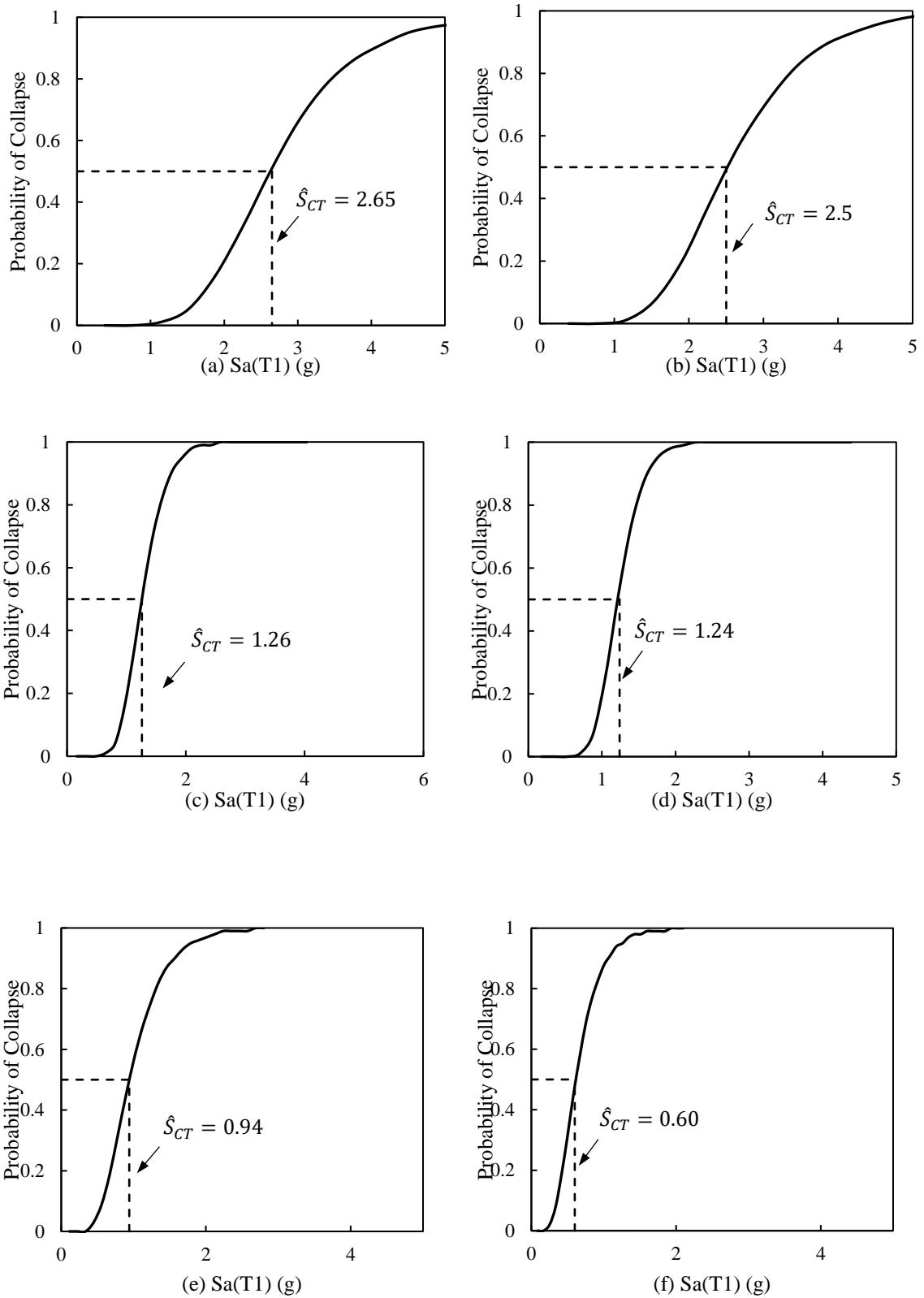
Figure 4.18. Fragility curves (a) 3-SMAPH; (b) 3-SMABW; (c) 6-SMAPH; (d) 6-SMABW; (e) 9-SMAPH; (f) 9-SMABW

Table 4.4. Period-based ductility

Building ID	Period-based ductility (μ_T)			
	Max Disp-Max V	Max Disp-V	Max V- D	Used
3-SMABW	2.7	2.8	1.8	1.8
3-SMAPH	3.5	3.6	1.7	1.7
6-SMABW	2.7	3.0	2.7	2.7
6-SMAPH	2.1	2.8	1.6	1.6
9-SMABW	2.4	2.2	3.3	2.2
9-SMAPH	2.5	4.3	2.5	2.5

(a) Three-story walls (Max V-D is used)

(b) Six-story walls (Max V-D is used)

(c) None-story walls (Max Disp-Max V is used)
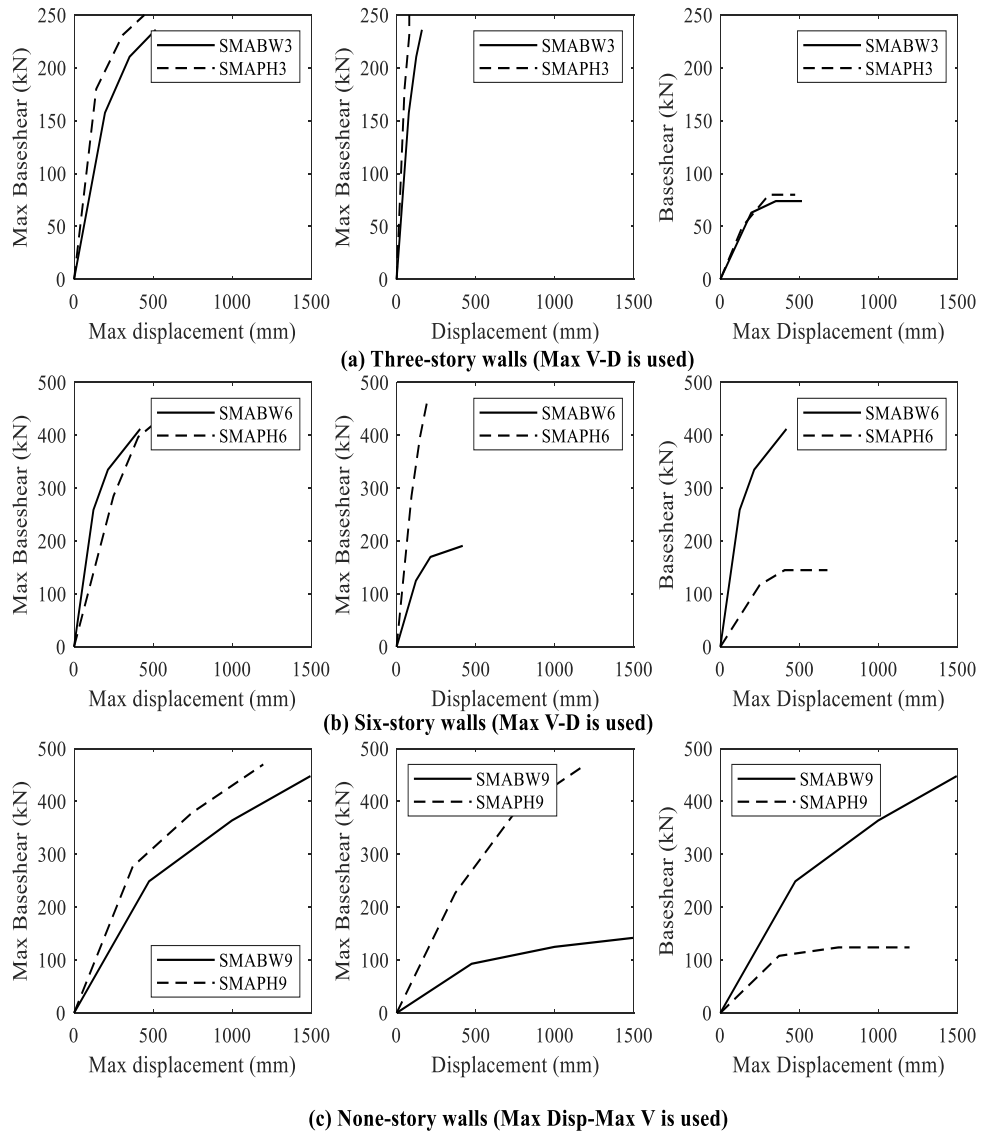
Figure 4.19. Pushover curve obtained from IDA: (a) three-story, (b) six-story, and (c) nine-story

Table 4.5. Assessment of seismic design parameters by FEMA P695 (2009)

Building Group	Building ID	Height (m)	Period	$\hat{S}_{CT}$	CMR	μ_t	SFF	ACMR	β_{TOT}	$ACMR_{limit}$	Pass/Fail
1	SMAPH	9	Long	2.65	3.00	1.70	1.11	3.30	0.50	1.52	Pass
		18		1.26	4.07	1.60	1.15	4.68	0.50	1.52	Pass
		36		0.94	4.73	2.50	1.19	5.63	0.50	1.52	Pass
	Mean Group				3.93	1.93	1.22	4.80	0.50	1.90	Pass
2	SMABW	9	Long	2.50	2.77	1.80	1.12	3.10	0.50	1.52	Pass
		18		1.24	3.74	2.70	1.24	4.64	0.50	1.52	Pass
		36		0.60	6.67	2.20	1.23	8.20	0.50	1.52	Pass
	Mean Group				4.40	2.23	1.22	5.37	0.50	1.90	Pass

4.7 CONCLUSIONS

In this chapter, the response modification factor (R) and the Overstrength factor (Ω) for SE-SMA RC walls were evaluated through a numerical study. The SE-SMA bars were only used at the plastic hinge zone. Two potential arrangements were considered: SE-SMA bars only at the wall boundary elements (SMABW) and SE-SMA bars replacing all web and boundary element steel bars (SMAPH). 972 wall cases were analyzed to identify the effect of wall design parameters on the seismic performance and to estimate the seismic design parameters. FEMA P695 (2009) methodology was then performed to assess the proposed seismic design parameters. The proposed values have led to an adequate margin of safety against collapse. Conclusions from this study are summarized below.

1- Analyzing trends of displacement ductility and the overstrength data, shown in **Figure 4.14**, indicated that the location of SE-SMA bars and wall aspect ratio are the main factors affecting these design factors. Thus, for code-based seismic design, the measuring data of ductility and overstrength are compiled in four groups according to the SE-SMA bar located within the RC wall and the wall aspect ratio.

2- For walls with $\frac{H_w}{L_w} < 2.0$, the mean proposed response modification factor R is 2.5 and 3.5 for SMAPH and SMABW walls, respectively. For walls with $\frac{H_w}{L_w} > 2.0$, the proposed R-value is 3.0 and 4.0 for SMABW and SMABW walls, respectively. The recommended overstrength factor is 2.25 for both SMAPH and SMABW walls.

3- Increasing wall thickness and web reinforcement has a negligible effect on ductility and overstrength. In contrast, the displacement ductility is slightly increased with increasing the axial load ratio, and this is related to the change of wall failure mode. Concrete crushing was found to limit the wall ductility, especially for the case of SMAPH walls.

4- Increasing the reinforcement ratio of the SE-SMA bars at the boundary elements from 0.5% to 1.0% results in a reduction in wall ductility by 17% on average. Increasing the reinforcement ratio of the SE-SMA bars above 1.0% does not affect the SMAPH wall ductility, whereas it reduced the SMABW wall ductility by 29%. This finding

suggests that a reinforcement ratio larger than 1.5% for SMAPH walls and 1.0% for SMABW walls should be avoided.

5- Utilizing SE-SMA bars in the RC walls designed using the proposed values has resulted in a significant displacement recovery and an adequate margin of safety against collapse. However, SMABW walls experienced a lower lateral displacement, which makes them a better design option.

4.8 REFERENCES

Abdulridha A. (2012) Performance of superelastic shape memory alloy reinforced concrete elements subjected to monotonic and cyclic loading. Doctoral dissertation, University of Ottawa.

Abraik E, Youssef M A (2015) Cyclic performance of shape memory alloy reinforced concrete walls. Response of structures under extreme loading (pp. 326-333). Lansing, MI: The fifth international workshop on performance, protection, and strength of structures under extreme loading.

Abraik E, Youssef M A (2016) Performance assessment of three-story shape memory alloy reinforced concrete walls. CSCE 5th International Structural Specialty Conference, 852. London, ON, Canada.

Abraik E, Youssef M A (2018, a) Seismic fragility assessment of superelastic shape memory alloy reinforced concrete shear walls. Journal of building engineering 19: 142-153.

Abraik E, Youssef M A (2018, b) Seismic performance of shape memory alloy reinforced concrete dual systems. 16th European Conference on Earthquake Engineering. Thessaloniki, Greece.

Alam M S, Youssef M A, Nehdi M (2008) Analytical prediction of the seismic behaviour of superelastic shape memory alloy reinforced concrete elements. Engineering Structures 30(12): 3399-3411.

ATC-24 (1992) (Applied Technology Council) Guidelines for cyclic seismic testing of components of steel structures. American Iron and Steel Institute 24. Redwood City. CA: ATC.

Baker J W (2015) Efficient analytical fragility function fitting using dynamic structural analysis. Earthquake Spectra 31(1): 579-599.

Blume J A, Newmark N M, Corning L H (1961) Design of multi-story reinforced concrete buildings for earthquake motions. Portland Cement Association, Chicago, IL, Vol 4, 318 pp.

Bonelli P, Tobar R, Leiva G (1999) Experimental study on failure of reinforced concrete building," ACI Structural Journal, Vol. 96, No. 1, pp. 3–8.

Chang G A, Mander J B (1994) Seismic energy based fatigue damage analysis of bridge columns: Part I-evaluation of seismic capacity. (NCEER Technical Report No. NCEER-94-0006) State University of New York. National Center for Earthquake Engineering and Research, State Univesity of New York at Buffalo, NY, USA.

Christopoulos C, Tremblay R, Kim H J, Lacerte M (2008) Self-centering energy dissipative bracing system for the seismic resistance of structures: development and validation. Journal of Structural Engineering ASCE 134(1): 96-107.

CSA A23.3-14 (2014) Design of concrete structures. Canadian Standards Association. Mississauga, ON, Canada.

Effendy E, Liao W I, Song G, Mo Y L, Loh C H (2006) Seismic behavior of low-rise shear walls with SMA bars. Earth & Space 3: 1-8.

FEMA (2009) Quantification of building seismic performance factors, federal emergency management agency. FEMA P695, Washington, DC.

FEMA356 (2000) Prestandard and Commentary for the seismic rehabilitation of buildings. Washington, DC: federal emergency management agency.

Ghassemieh M, Mostafazadeh M., Sadeh M S (2012) Seismic control of concrete shear wall using shape memory alloys. Journal of Intelligent Material Systems and Structures 23(5): 535-543.

Ghassemieh M, Rezapour M, Sadeghi V (2017) Effectiveness of the shape memory alloy reinforcement in concrete coupled shear walls. Journal of Intelligent Material Systems and Structures 28(5): 640-652.

Rezapour M, Ghassemieh M (2018) Macroscopic modelling of coupled concrete shear wall. Engineering Structures 169: 37-54.

Ghorbanirenani I, Tremblay R, Léger P, Leclerc M (2012) Shake table testing of slender RC shear walls subjected to Eastern North America seismic ground motions, ASCE Journal of Structure Engineering 138(12): 1515-1529.

Hurlebaus S, Gaul L (2006) Smart structure dynamics. Mechanical system and signal processing 20(2): 255-281.

Kolozvari K (2013) Analytical modeling of cyclic shear-flexural interaction in reinforced concrete structural walls. Doctoral dissertation, University of California.

Mahin S A, Bertero V V (1976) Problems in establishing and predicting ductility in structural design. Proceedings of international symposium on earthquake structural engineering, St. Louis, Mo 1: pp. 613-628.

Menegotto, M., & Pinto, P. (1973). Method of analysis for cyclically loaded RC plane frames including changes in geometry and non-elastic behavior of elements under combined normal force and bending. In Proc. of IABSE symposium on resistance and ultimate deformability of structures acted on by well defined repeated loads (pp. 15-22).

NBCC (2015) National Building Code of Canada. Canadian Commission on Building and Fire Codes, National research council of Canada, Ottawa.

Newmark N M, Hall W J (1982) Earthquake spectra and design. Engineering Monograph, Earthquake Engineering Research Institute. Berkeley, USA.

OpenSees (2018) Open system for earthquake engineering simulation. Berkeley, CA.

Orakcal K, Wallace J W, Conte J P (2004) Nonlinear modeling and analysis of reinforced concrete structural walls. ACI Structural Journal 101(5): 688-698.

Panagiotou M (2008) Seismic design, testing, and analysis of reinforced concrete wall buildings. Doctoral dissertation, University of California.

Park R (1988) Ductility evaluation from laboratory and analytical testing. In Proceedings of Ninth World Conference on Earthquake Engineering Tokyo-Kyoto, Japan, Vol. 8, pp. 605-616.

Park R, Paulay T (1975) Reinforced concrete structures. JohnWiley and Sons.

Paulay T, Priestley M N (1992) Seismic design of reinforced concrete and masonry buildings. New York, NY, USA: John Wiley & Sons.

PEER Ground Motion Database (2018) Retrieved from https://ngawest2.berkeley.edu/

Priestley M J, Park R (1987) Strength and ductility of concrete bridge columns under seismic loading. ACI Struct Journal 84(1): 61-76.

Priestley M, Calvi G, Kowalsky M (2007) Displacement based seismic design of structures. IUSS Press: Pavia, Italy.

Scott B D, Park R, Priestley M J N (1982) Stress-strain behaviour of concrete confined by overlapping hoops at low and high strain rates. ACI Journal Proceeding 79(1): 13-27.

Salonikios T N, Kappos A J, Tegos I A, Penelis G G (2000) Cyclic load behavior of low-slenderness reinforced concrete walls: failure modes, strength and deformation analysis, and design implications. ACI Structural Journal 97(1): 132-141.

Tazarv M, Saiidi M S (2013) Analytical studies of the seismic performance of a full-scale SMA-reinforced bridge column. International Journal of Bridge Engineering 1(1): 37-50.

Tolou Kian M J, Cruz-Noguez C (2018) Reinforced concrete shear walls detailed with innovative materials: seismic performance. Journal of Composites for Construction 22(6): 04018052.

TBI (2017) Guidelines for performance-based seismic design of tall buildings, Report No. 2017/06. Berkeley, CA: University of California.

Uang C M (1991) Establishing R (or RW) and Cd factors for building seismic provisions. Journal of Structural Engineering 117(1): 19-28.

Vamvatsikos D, Cornell C A (2001) Incremental dynamic analysis. Earthquake Engineering and Structural Dynamics 31(3): 491-514.

Youssef M A, Elfeki M A (2012) Seismic performance of concrete frames reinforced with superelastic shape memory alloys. Smart Structures and Systems 9(4): 313-333.

Youssef M A, Alam M S, Nehdi M (2008) Experimental investigation on the seismic behaviour of beam-column joints reinforced with superelastic shape memory alloys. Journal of Earthquake Engineering 12(7): 1205-1222.

Wood S L (1989) Minimum tensile reinforcement requirements in walls," ACI Structural Journal, Vol. 86, No. 5, pp. 582–591.

CHAPTER 5

SEISMIC RESPONSE OF SHAPE MEMORY ALLOY REINFORCED CONCRETE DUAL SYSTEMS

5.1 INTRODUCTION

A dual system combining Reinforced Concrete (RC) frames and RC walls is widely used in intermediate and tall buildings. During seismic excitations, moment resisting frames deform in a shear mode and restrain deformations of the upper stories. On the other hand, cantilever shear walls deform in flexure mode with the upper stories experiencing the highest drifts. The combined deformed shape follows a flexural profile in the lower stories and a shear profile in the upper stories. The frame-wall seismic response is sensitive to their relative stiffness.

Several studies investigating the seismic performance of dual frame-wall systems were conducted (Emori and Schnobrich, 1978; Goodsir et al. 1982; Aktan and Bertero, 1984; Tuna et al. 2012). The 1985 edition of the NBCC categorized the lateral load system as a dual system when the base shear for the frame system is equal to or greater than 25% of the total shear demand. The 2015 edition of the NBCC assigns low values for the ductility modification factor R_d and overstrength factor R_o for such a system.

Emphasis has been placed on mitigating seismic damage and reducing repair cost of RC structures by utilizing SE-SMA material (Youssef et al. 2008; Saiidi et al. 2008; Alam et al. 2008; Tazarv and Saiidi 2013). Abdulridha (2012) has experimentally studied the cyclic behaviour of a concrete wall reinforced with longitudinal SE-SMA bars within the boundary elements of the plastic hinge region. Abraik and Youssef (2015) identified the performance of SE-SMA RC squat and intermediate walls considering different SE-SMA bar locations. Abraik and Youssef (2016) assessed the performance of the three-story SE-SMA cantilever wall located in a high seismic zone.

This chapter evaluates the seismic response of 10-story dual systems that utilize SE-SMA bars using Incremental Dynamic Analysis (IDA). Both local and global responses are evaluated. The following sections provide details about the numerical model, case study building, time-history analysis results, and development of seismic fragility curves.

5.2 DEVELOPED NUMERICAL MODELS

Figure 5.1 shows the 2D nonlinear analysis model used to capture the behaviour of RC walls and RC moment frames. The model is developed using the Open System for Earthquake Engineering Simulation software (OpenSees, 2018). Shear-Flexural Interaction Multi Vertical Line Element Model (SFI-MVLEM) captures the behaviour of the walls. The model details are given by Kolozvari (2013). A nonlinear force-based fiber frame element is used to model all RC beams and columns. Each fiber element has five integration points along its length, as shown in **Figure 5.2**. The RC walls and RC frames are connected by link elements at each story along the building height. The stress-strain relationships developed by Chang and Mander (1994) and Giuffre'-Menegotto and Pinto (1973) are used to define the concrete and steel reinforcement, respectively. The self-centering uniaxial material proposed by Christopouls et al. (2008) is used to represent the SE-SMA reinforcement.

5.2.1 Global failure criteria

The global acceptance criteria specified by PEER-TBI (2017) are adopted in this research. The criteria include the following limits: (1) 3% for the mean inter-story drift, (2) 4.5% for the maximum inter-story drift, (3) 1% for the mean residual drift, and (4) 1.5% for the maximum residual drift.

5.2.2 Local failure criteria

Strains are utilized to identify local failures. Tensile steel strain (ε_s) of 5% and concrete strain (ε_c) of 2% are used for that purpose following the recommendation of Panagiotou (2008).
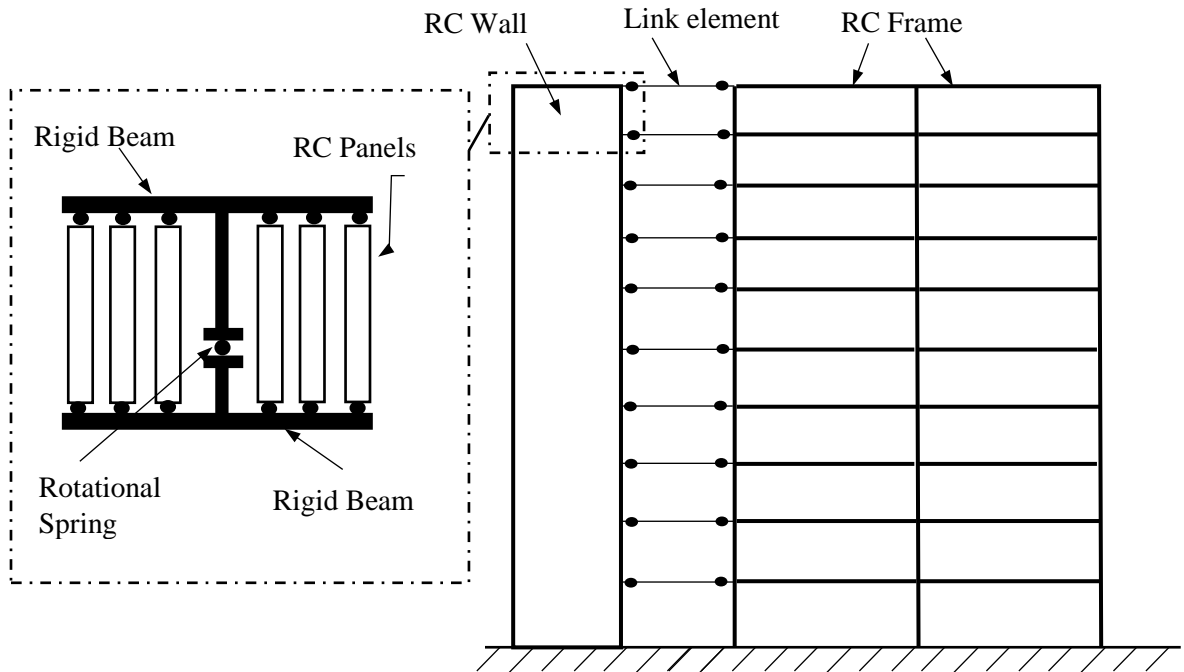
Figure 5.1. Modeling of frame-wall building
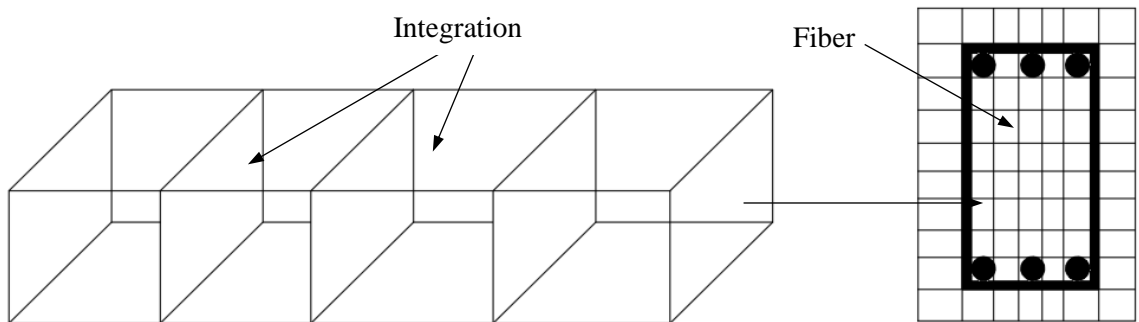
Figure 5.2. Fiber element (Spacone and Filippou 1996)

5.3 TYPICAL RC DUAL WALL-FRAME BUILDINGS

Two 10-story buildings (BL1 and BL2) are considered. **Figure 5.3** shows the plan view for both buildings. The story height is 3.0 m. The lateral load resisting system in both directions utilizes two ductile RC walls and two ductile RC frames. The walls of BL1 and BL2 are designed to resist 72% and 50% of the total seismic force, respectively. The buildings were designed according to the requirements of the Canadian standards (CSA

A23.3-14, NBCC 2015), assuming that they are located in Vancouver, BC, and constructed on class D soil. Concrete compressive strength is 30 MPa, and steel yield strength is 400 MPa. The peak ground acceleration (PGA) equals 0.46g assuming 5% damping. The structural lumped mass of each story includes its self-weight and 25% of the applied live load. Beams of the moment frames have a cross-section of 400 mm width by 600 mm height and top and bottom steel ratios of 0.55%. **Tables 5.1** and **5.2** present the design summary of the RC walls and RC columns, respectively.
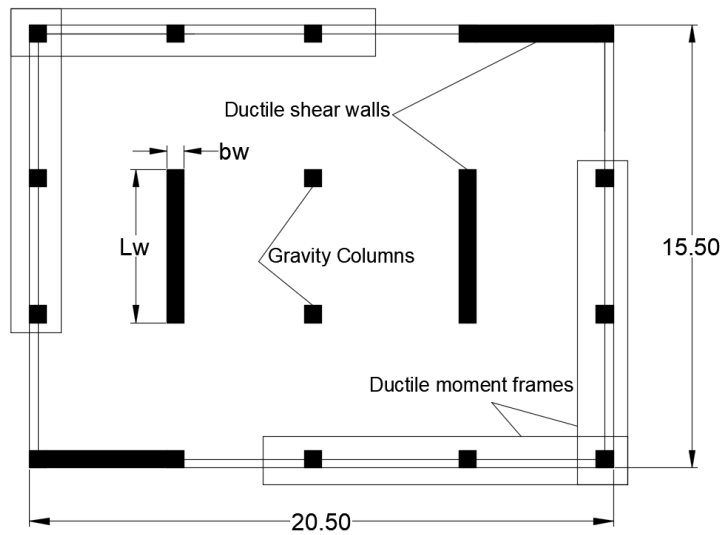
Figure 5.3. Typical floor plan

Table 5.1. Design details of RC walls of BL1 and BL2

Building	Building height (Stories)	Period (sec)	Base shear coeff (%)	L_w(mm)	b_w(mm)	ρ_{hw}(%)	ρ_{hb}(%)	ρ_{vw}(%)	ρ_{vb}(%)
BL1	10	1.15	72	2800	300	0.33	0.55	0.33	1.00
BL2		1.29	50	1800	300	0.66	0.66	0.33	1.00

Table 5.2. Design details of RC columns of BL1 and BL2

	(BL1)				(BL2)			
	Story 1-5		Story 6-10		Story 1-5		Story 6-10	
	Internal column	External column	Internal column	External column	Internal column	External column	Internal column	External column
b (mm)	700	600	600	500	800	700	700	600
h (mm)	700	600	600	500	800	700	700	600
ρ (%)	1	1	1	1	1	1	1	1

5.4 GROUND MOTIONS UTILIZED IN THIS STUDY

Figure 5.4 shows the mean spectral acceleration of the seven selected ground motions scaled to the site design spectrum of Vancouver BC, assuming a 2.5% damping ratio. The adopted scaling method is the Mean Square Error (MSE) (PEER, 2016; Michaud and Lèger, 2014). The ground motions are selected to represent a range between $0.2T_{1S}$ and $1.5T_1$, where T_{1S} and T_1 are the minimum and maximum fundamental periods of buildings, respectively. Incremental dynamic analysis (IDA) is then carried out, where each dual system is subjected to different amplitudes of each ground motion until reaching failure. The Intensity Measure (IM) represents the spectral acceleration at the first period. It ranges from 0.38g [$S_{a(design)}$] to 1.15g [$S_{a(max)}$] for building BL1 and from 0.16g [$S_{a(design)}$] to 0.60g [$S_{a(max)}$] for building BL2.
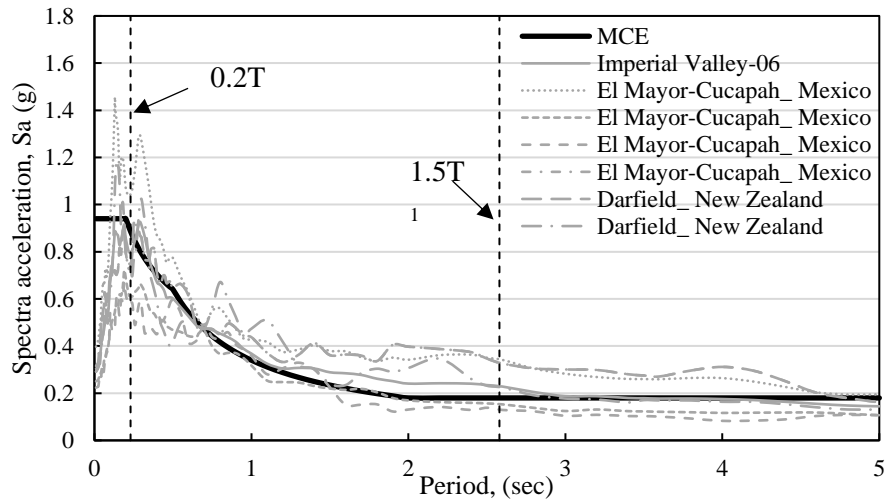
Figure 5.4. Scaled ground motions

5.5 DESIGN OF BL1 AND BL2 UTILIZING SE-SMA

Figure 5.5 shows the mean strain profile of the wall steel bars for BL1 and BL2 when subjected to two intensity hazard levels $S_{a(design)}$ and $S_{a(max)}$. Both walls experience an elastic response when subjected to low-intensity ground motions, i.e. $S_{a(design)}$. At $S_{a(max)}$, the wall strain profiles of BL1 and BL2 are similar, **Figure 5.5(d)**. For both buildings, increasing the intensity level from $S_{a(design)}$ to $S_{a(max)}$ results in the formation of plastic hinges at the wall base. The height of the plastic hinges does not exceed 10% of the wall height, measured from the base.

Youssef and Elfeki (2012) proposed using the SE-SMA bars in RC frames at the plastic hinges of the RC beams. Priestley and Park (1987) proposed the following formula to determine the plastic hinge length as a function of the beam length L_w, bar diameter d_b, and yielding stress f_y:

$$L_p = 0.08Lw + 0.022d_bf_y \tag{5.3}$$

To optimize the seismic performance of the RC dual system and minimize the additional cost, SMA bars will be used at the critical locations. The chosen locations for SE-SMA bars are illustrated in **Figure 5.6**. These locations are: (1) using SE-SMA bars over the plastic hinge length for the walls [BL1SW and BL2SW], (2) using SE-SMA bars over the plastic hinge length for the walls and the 1st and 7th story beams [BL1SWF and BL2SWF]. The 7th story was chosen based on the recommendations of Youssef and Elfeki (2012). Mechanical couplers are assumed to be used to connect the SE-SMA bars with conventional steel reinforcing bars. **Table 5.3** lists the mechanical properties of SE-SMA reinforcing bars.

Table 5.3. SE-SMA mechanical properties

Parameter	Value
Modulus of Elasticity (MPa)	38000
Yield stress (MPa)	380
Ultimate stress (MPa)	500
Superelastic strain (mm/m)	70
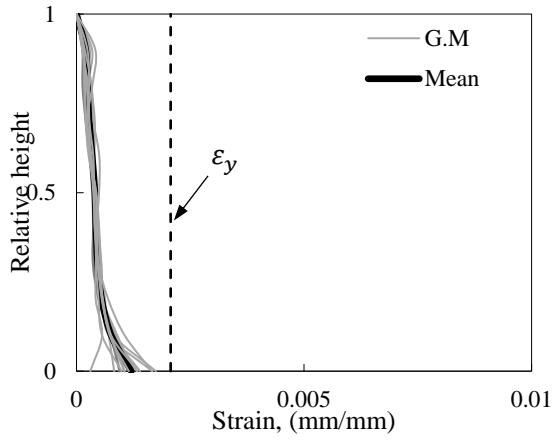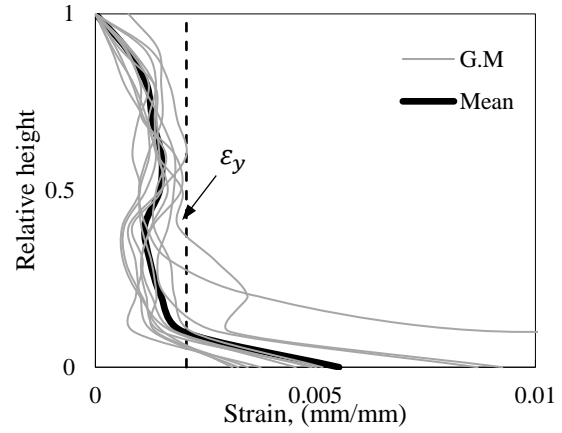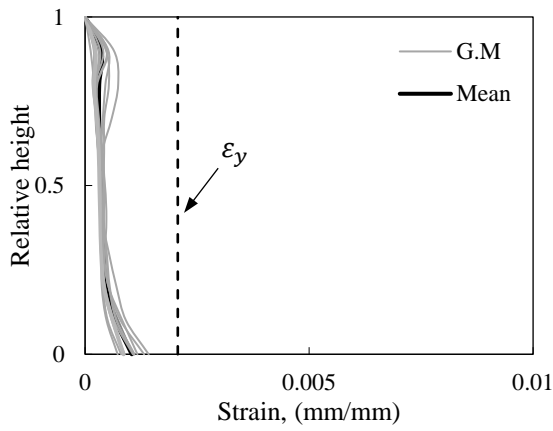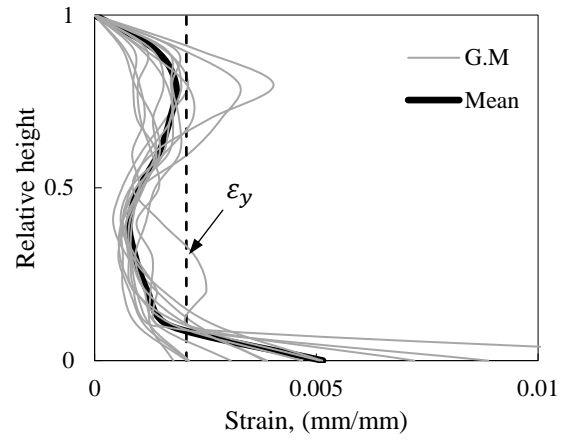
Figure 5.5. Mean reinforcement tensile strain in 10-story steel RC wall: (a) BL1[Sa(design)]; (b) BL1[Sa(max)] (c) BL2[Sa(design)]; (d) BL2[Sa(max)]

(a) BLSW   (b) BLSWF
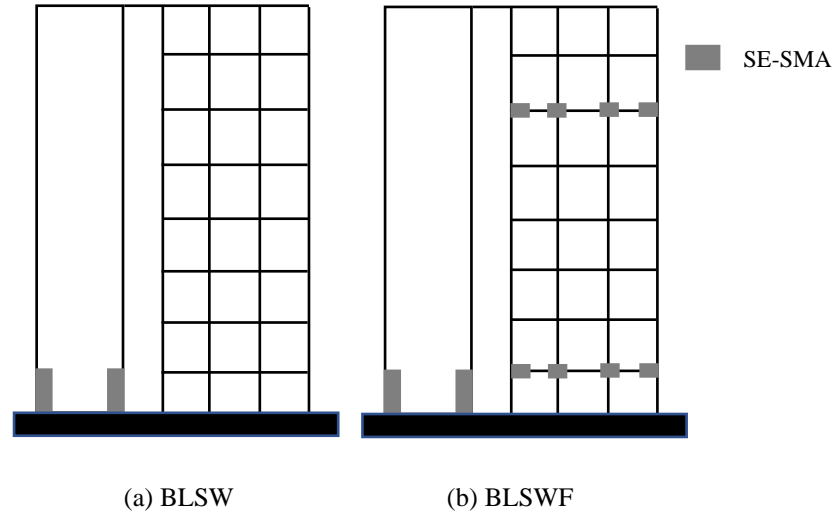
Figure 5.6. Locations of SE-SMA bars

5.6 NONLINEAR TIME HISTORY ANALYSIS RESULTS

Figure 5.7 shows the bending moments and shear forces for the studied 10-story buildings. The bending moments of building BL1 exceed the design moments at $S_{a(design)}$ by about 20%, On the opposite, the bending moments for building BL2 are below the design moment. The wall shear forces for BL1SW and BL1SWF are lower by 10% compared to the wall shear forces in BL1. The same trend is observed for BL2 buildings.

At the base of the walls, the bending moments in the SE-SMA buildings are lower by about 10% than the steel RC buildings. The mean shear force for SE-SMA buildings is below the design shear force assuming $R_d R_0 = 1.0$. The SE-SMA bars reduced the shear force at the base of BL2 by about 6%.
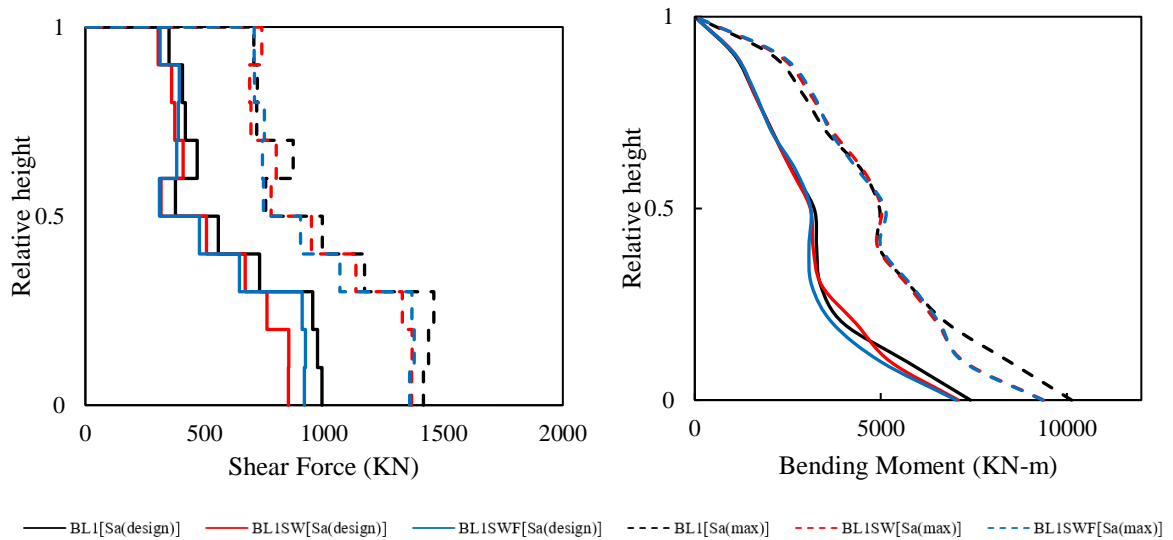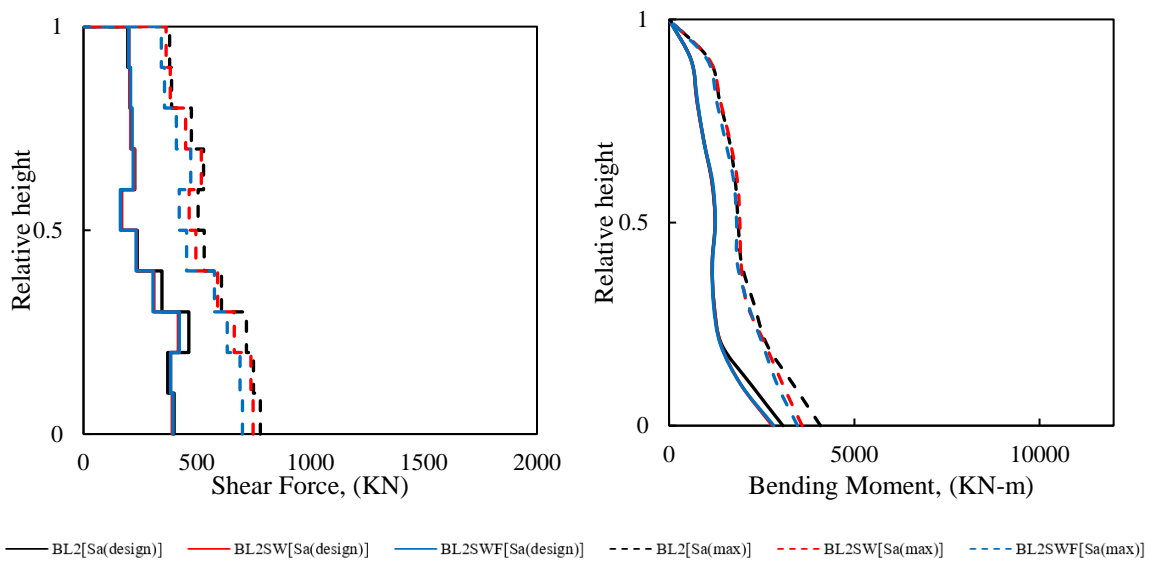
Figure 5.7. Mean shear forces and bending moments in the RC wall: (a) BL1; (b) BL2

The mean tensile strains of the longitudinal bars of the external and internal beams are shown in **Figure 5.8**. For seismic hazard $S_{a(design)}$, the RC beams remain in the elastic strain stage. However, for seismic hazard $S_{a(max)}$, inelastic strains are developed reaching values of about 0.003. A slight increase of about 6% in the strains is noted for BL1SWF and BL2SWF

compared to BL1SW and BL2SW. The source of this increase is related to the difference in the beam section sizes.
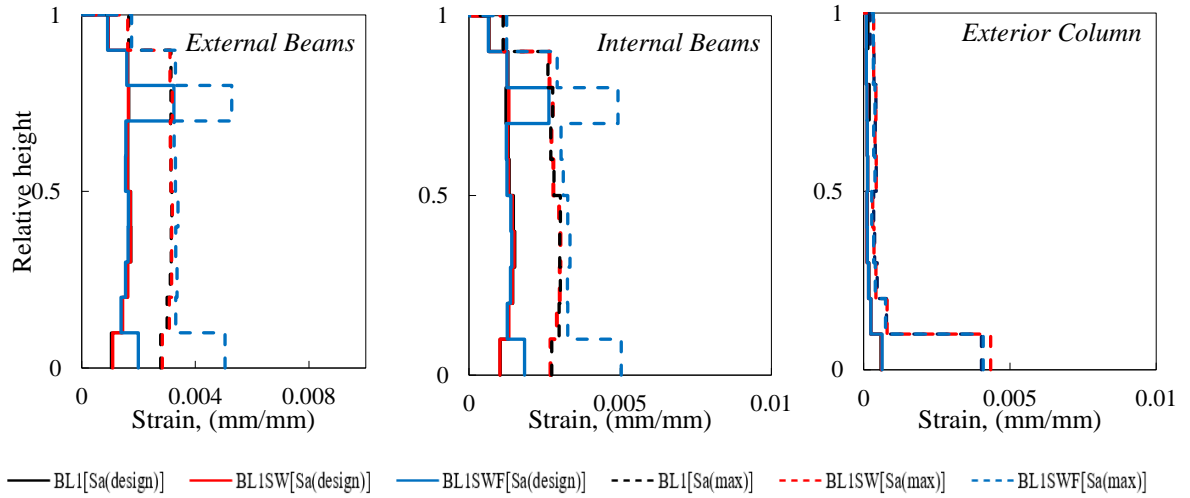
(a) Frames resisting 25% of seismic loads
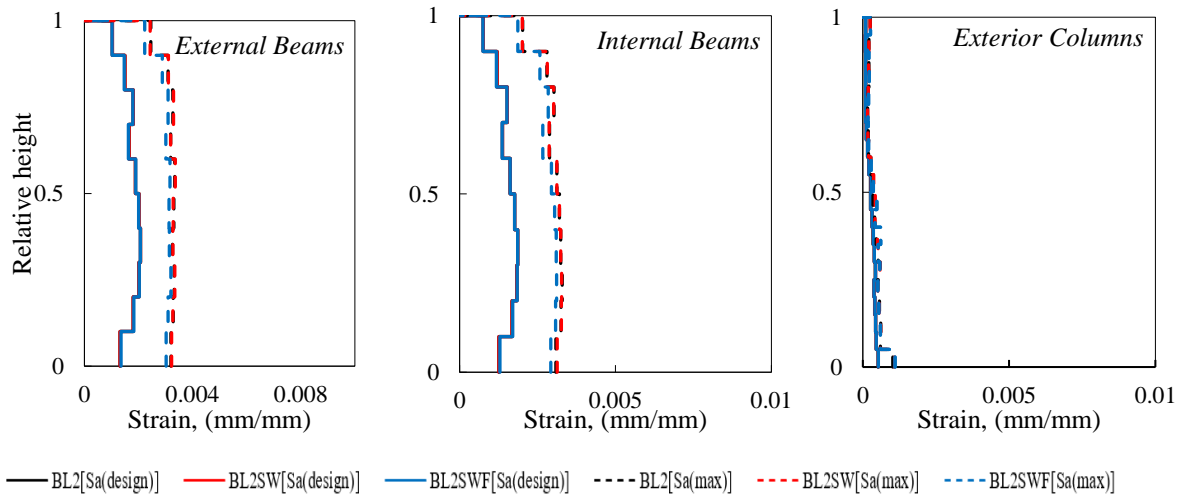
(b) Frames resisting 50% of seismic loads

Figure 5.8. Mean strains envelopes in RC beams

The exterior column axial load ratios are shown in **Figure 5.9**. Increasing the seismic hazard from $S_{a(design)}$ to $S_{a(max)}$ increases the axial load ratio by 44%. Considering a seismic hazard of $S_{a(max)}$, the axial load ratio for BL1SWF is 9% less than the BL1 and BL1SW. Due to the reduction in columns size at upper stories, the axial load ratio increases at the mid-height for the considered buildings. **Figure 5.9** shows the shear forces in the external columns. Assuming $R_d R_0 = 1.0$, the design shear force at the base of the external column is 123 kN. This is 25% lower than the computed shear forces considering seismic hazards of $S_{a(design)}$. Using SE-SMA reduces the shear forces at the column base of BL1SWF and BL2SWF by about 17%. The difference in the shear forces at the upper stories is negligible. Considering seismic hazard $S_{a(max)}$, the external column shear forces of BL1 and BL2 are 169 and 184 kN, respectively. The shear force for BL1SWF is 126 kN.

Figure 5.9 shows the bending moments in the external columns. For BL1, the maximum values are 493 kN.m and 1069 kN.m at $S_{a(design)}$ and $S_{a(max)}$, respectively. For BL2, the maximum values are 783 kN.m and 1600 kN.m, respectively. The base bending moment for BL2 exceeds the design moment by 29% at $S_{a(max)}$ hazard level. Utilizing SE-SMA bars in BL1SWF and BL2SWF reduce the base bending moment by about 18% considering seismic hazard $S_{a(max)}$.
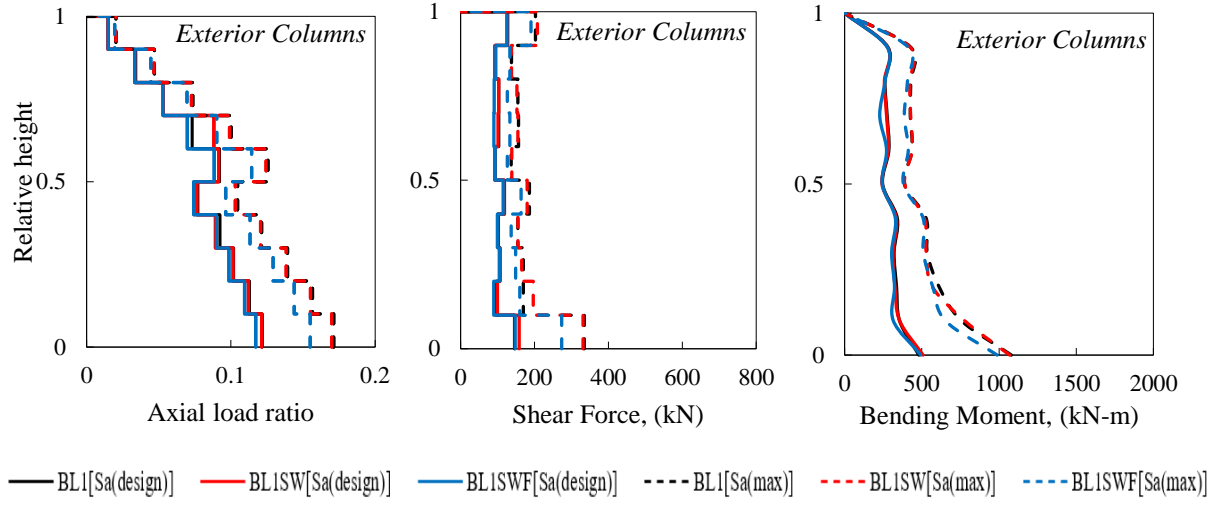
(a) Frames resisting 25% of seismic loads
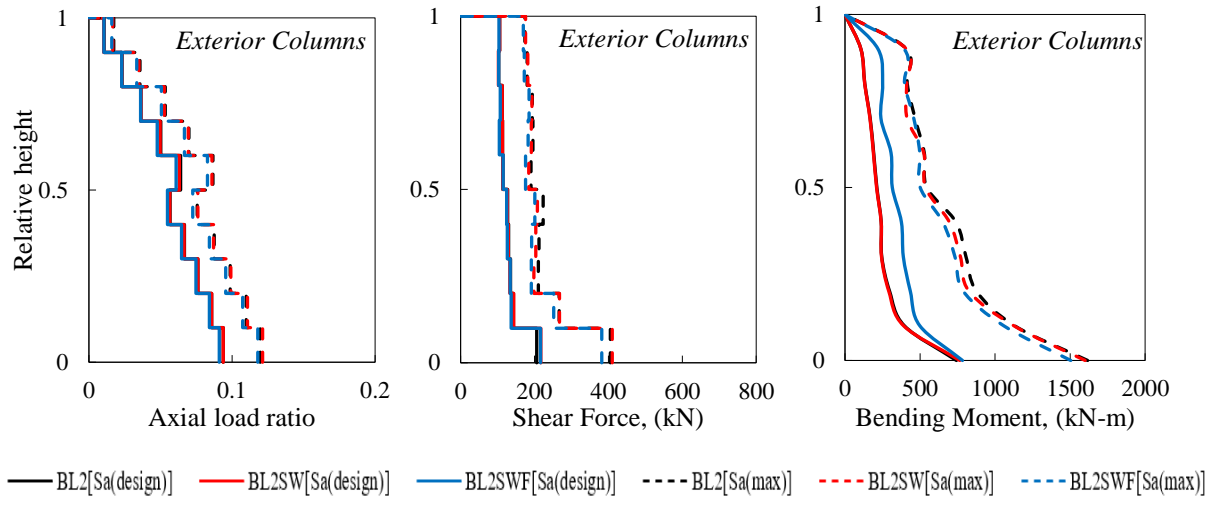
(a) Frames resisting 50% of seismic loads

Figure 5.9. Mean axial, shear, and bending moment envelopes for RC exterior columns

The mean lateral displacement of the steel and SE-SMA dual walls are shown in **Figure 5.10**. The displacement envelopes of BL1 are approximately linear starting from zero at the base and having maximum displacement occurring at the roof. For building BL2, the effect of the contribution of the RC frame on the system behaviour is more significant.

The maximum roof displacement of BL1, when subjected to low-intensity ground motions $S_{a(design)}$, is 0.125 m (0.4% drift). This is lower than the mean lateral displacement of

BL2 by 5%. A minor difference in the mean lateral displacement response exists between BL1 and BL1 SE-SMA buildings at low-intensity ground motions.

Figure 5.11 presents the inter-story drift distribution along the height. Regardless of the type of reinforcement, the considered dual systems exhibit a similar distribution of inter-story drifts considering low-intensity ground motions. The peak inter-story drift is reduced by 10% on average when the SE-SMA bars are used at the beam ends.

Figure 5.12 shows the mean residual displacements. The SMA-RC dual systems have the lowest residual displacements as compared to steel RC dual systems. At low seismic intensity, utilizing SE-SMA bars at the beam ends reduces the roof residual displacement by 37% and 15% for BL1SWF and BL2SWF, respectively. Increasing the intensity levels from the design level to the ultimate level reduces the residual displacements by 67% and 28% for BL1SWF and BL2SWF, respectively, as compared to BL1 and BL2.

(a) Walls resisting 75% of seismic loads   (b) Walls resisting 50% of seismic loads
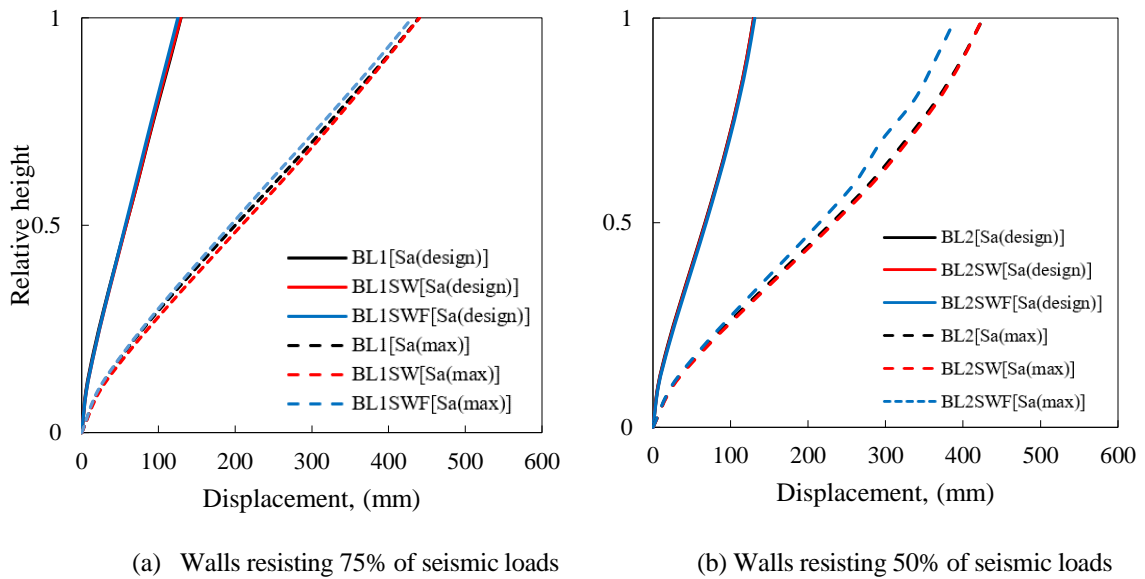
Figure 5.10. Mean envelope lateral displacement

(a) Walls resisting 75% of seismic loads   (b) Walls resisting 50% of seismic loads
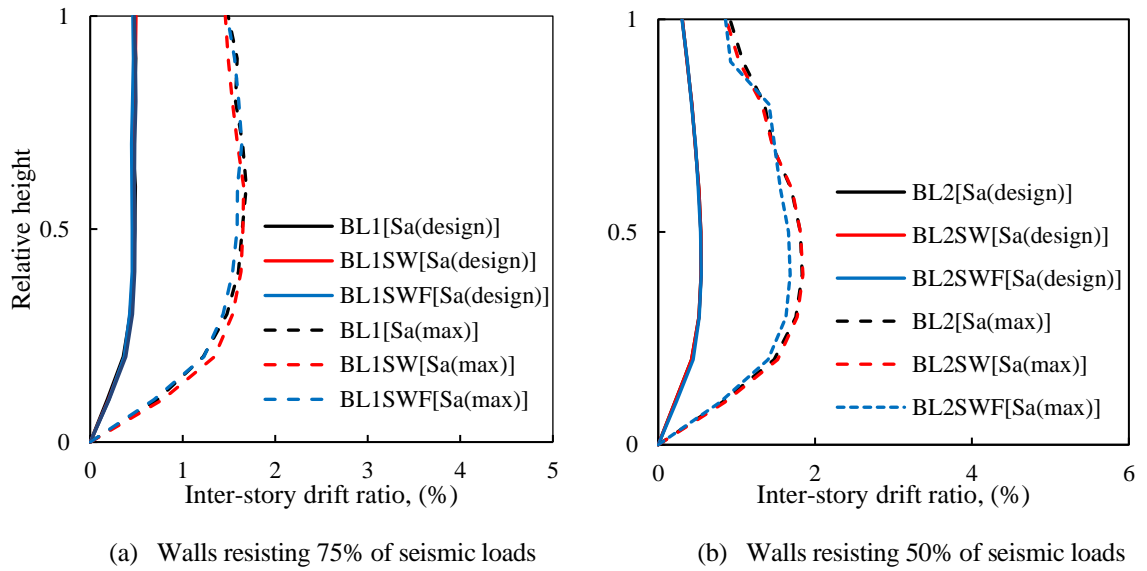
Figure 5.11. Mean envelope inter-story drift ratio

(a) Walls resisting 75% of seismic loads   (b) Walls resisting 50% of seismic loads
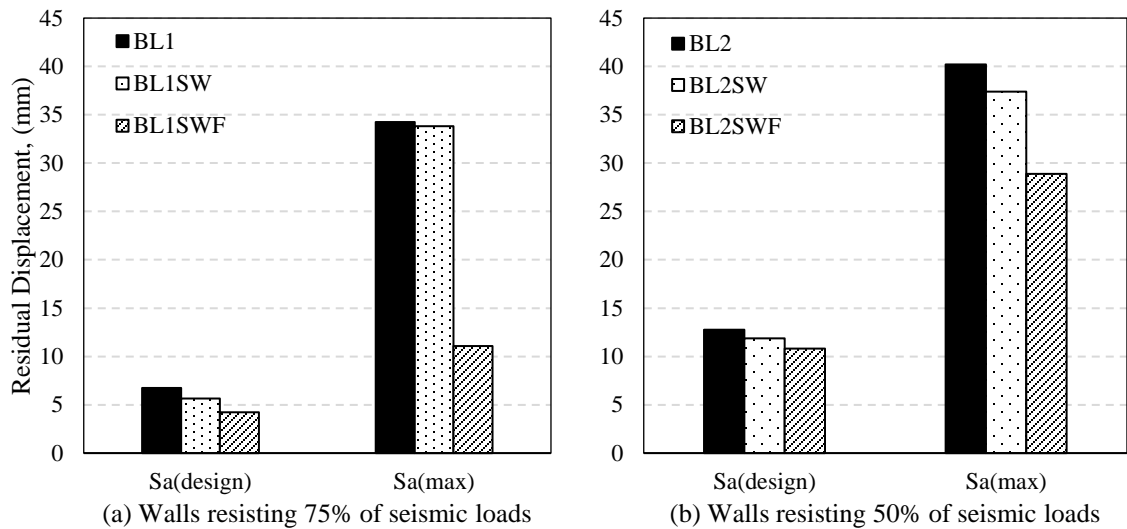
Figure 5.12. Mean residual displacement

5.7 SEISMIC FRAGILITY

Fragility functions describe the probability of damage for a given seismic intensity (IM). It can be expressed using Equation 5.4 (Baker, 2015): Incremental dynamic analysis (IDA) (Vamvatsikos and Cornell, 2004) is used to obtain the fragility. In this approach, the seismic intensity is incrementally increased until collapse occurs.

$$P(C \backslash IM = x) = \Phi \left[\frac{\ln\left(\frac{x}{\theta}\right)}{\beta} \right] \tag{5.4}$$

where P is the probability of exceeding a specific damage level C, Φ is the standard normal cumulative distribution, θ is the median of the fragility function, and β is the standard deviation of $ln\,(IM)$.

Figures 5.13 plots the fragility curves with respect to Sa for RC walls. FEMA P695 (2009) defines the collapse probability at 50% as the median collapse capacity $(\hat{S}_{CT})$, which is 0.61 and 0.27 for BL1SWF and BL2SWF, respectively. The fragility curves for the considered RC frames, as a function of spectral acceleration, are shown in **Figure 5.14**. A significant reduction in the frame fragility is found for BL1SWF and BL2SWF as compared to other considered frames. The effect of using SE-SMA bars is more pronounced for the BL1SWF. However, the considered walls reach the same probability of collapse at seismic intensity of about 0.85g. This is significantly higher than the spectral acceleration of the maximum considered earthquake.
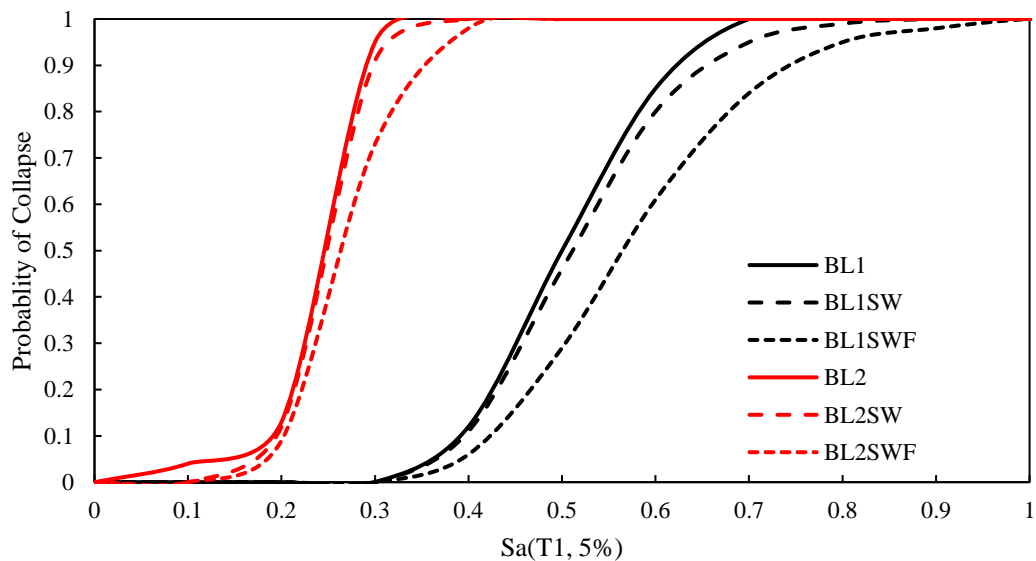
Figure 5.13. Collapse fragility curves with respect to spectral acceleration for RC walls
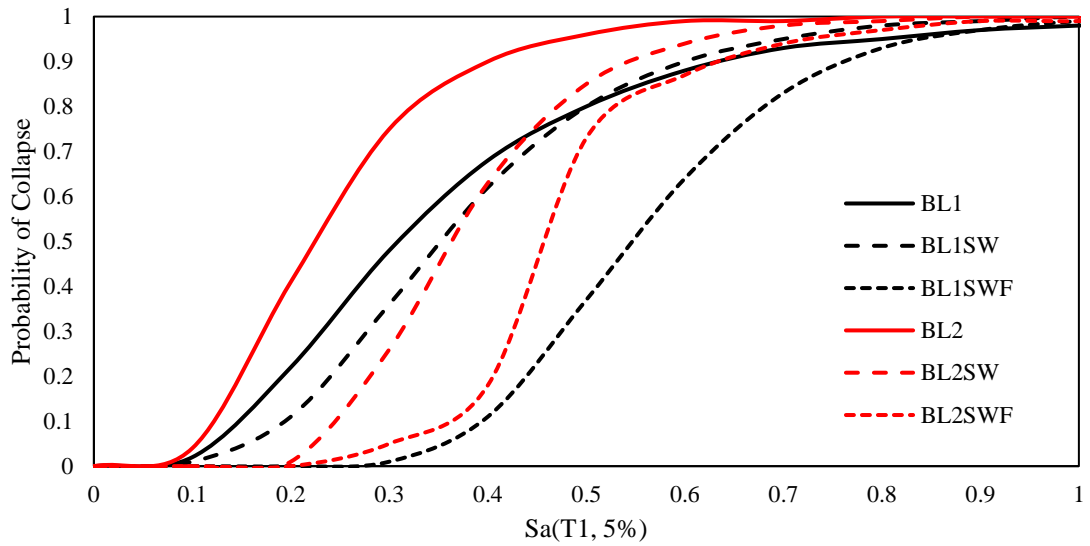
Figure 5.14. Collapse fragility curves with respect to spectral acceleration for RC frames

5.8 CONCLUSIONS

This chapter investigated the seismic performance of SE-SMA RC dual systems. Two 10-story buildings were designed to represent different stiffness ratios of RC walls to moment frames. The buildings are then redesigned using two layouts for SE-SMA bars. Based on the results of this study, the following conclusions were achieved.

1. A single plastic hinge is developed at the base of RC walls at $S_{a(max)}$ hazard level. The length of the formed plastic hinge is about 10% of the total wall height.
2. At seismic hazard $S_{a(design)}$, no notable difference is observed in the strain distributions between the steel and SE-SMA dual systems.
3. At seismic hazards of $S_{a(max)}$, the use of SE-SMA bars has reduced the shear forces of the external columns by 18% for BL1, where the walls resist 72% of the seismic forces.
4. There is no difference in the wall bending moments between SE-SMA and steel dual-systems at seismic hazard $S_{a(design)}$. For the seismic hazard $S_{a(max)}$, utilizing SE-SMA bars reduces the wall bending moments by about 10%.

5. A negligible difference is found in the mean inter-story drifts when SE-SMA bars are used.

6. Time history analysis showed a significant reduction, as expected, in the residual drifts when the SE-SMA bars are utilized.

7. Utilizing SE-SMA bars in the RC wall and RC frame resulted in a reasonable margin of safety against collapse. However, utilizing SE-SMA in the walls and frames in BL1 has significantly diminished the collapse probability, which makes this design a better option.

5.9 REFERENCES

Abdulridha, A. (2012). Performance of superelastic shape memory alloy reinforced concrete elements subjected to monotonic and cyclic loading. Ph.D. thesis: University of Ottawa, Ottawa.

Abraik, E., & Youssef, M. (2015). Cyclic performance of shape memory alloy reinforced concrete walls. Response of structures under extreme loading (pp. 326-333). Lansing, MI: The fifth international workshop on performance, protection, and strength of structures under extreme loading.

Abraik, E., & Youssef, M. (2016). Performance assessment of three-story shape memory alloy reinforced concrete walls. CSCE 5th International Structural Specialty Conference, 852. London, ON, Canada.

Aktan, A., & Bertero, V. (1984). Seismic response of R/C frame-wall structures. Journal of Structure Engineering, 110(8), 1803-1821.

Alam, M., Youssef, M. A., & Nehdi, M. (2008). Analytical prediction of the seismic behaviour of superelastic shape memory alloy reinforced concrete elements. Engineering Structures, 30(12), 3399-3411.

ASCE 41. (2013). Seismic evaluation and retrofit of existing buildings. Reston, VA: American Society of Civil Engineering.

Chang, G., & Mander, J. (1994). Seismic energy based fatigue damage analysis of bridge columns: Part I-evaluation of seismic capacity. Buffalo, New York: NCEER-94-0006. State University of New York.

Christopoulos, C., Tremblay, R., Kim, H., & Lacerte, M. (2008). Self-Centering Energy Dissipative Bracing System for the Seismic Resistance of Structures: Development and Validation. ASCE Journal of Structural Engineering, 134(1), 96-107.

Emori, K., & Schnibrich, W. (1978). Analysis of reinforced concrete frame-wall structures for strong motion earthquake. Structural research series no 434.

Ghorbanirenani, I., Tremblay, R., Léger, P., & Leclerc, M. (2012). Shake table testing of slender RC shear walls subjected to Eastern North America seismic ground motions. Journal of Structural Engineering, 138(12), 1515-1529.

Goodsir, W., Paulay, T., & Carr, A. (1982). The inelastic seismic response of reinforced concrete frame-shear-wall structures. Christchurch, New Zealand: University of Canterbury.

Hurlebaus, S., & Gaul, L. (2006). Smart structure dynamics. Mechanical system and signal, 20(2), 255-281.

Ibarra, L., Medina, R., & Krawinkler, H. (2005). Hysteretic models that incorporate strength and stiffness deterioration. Earthquake Engineering and Structural Dynamics, 34(12), 1489-1511.

Kim, J., Stanton, J., & MacRae, G. (2004). Effect of beam growth on reinforced concrete frames. ASCE Journal of Structural Engineering, 130(9), 1333-1342.

Kolozvari, K. (2013). Analytical Modeling of cyclic shear-flexural interaction in reinforced concrete structural walls. Ph.D. thesis: University of California, Los Angeles.

Lignos, D., & Krawinkler, H. (2012). Development and Utilization of Structural Component Databases for Performance-Based Earthquake Engineering. Journal of Structural Engineering, ASCE, 139(2), 1382-1394.

Luco, N., & Cornell, C. (1998). Seismic drift demands for two SMRF structures with brittle connections. Structural Engineering World Wide 1998, Elsevier Science Ltd, Paper T158-3.

Menegotto, M., & Pinto, P. (1973). Method of analysis of cyclically loaded RC plane frames including changes in geometry and non-elastic behavior of elements under normal force and bending. Preliminary Report ABSE, vol 13.

Michaud, M., & Lèger, P. (2014). Ground motions selection and scaling for nonlinear dynamic analysis of structures located in Eastern North America. Canadian Journal of Civil Engineering, 41(3), 232-244.

Pacific Earthquake Engineering Research (PEER). (2015). Retrieved from ground motions database available online: http://ngawest2.berkeley.edu/

Panagiotou, M. (2008). Seismic design, testing, and analysis of reinforced concrete wall buildings. San Diego: UC: San Diego.

Paulay, T., & Priestley, M. (1992). Seismic Design of Reinforced Concrete And Masonry Buildings.

PEER. (2016). Retrieved from Open System for Earthquake Engineering Simulation.: http://opensees.berkeley.edu.

Priestley, M., Calvi, G., & Kowalsky, M. (2007). Displacement-based seismic design of structures. Pavia, Italy: IUSS Press.

Priestly, M., & Park, R. (1987). Strength and ductility of concrete bridge columns under seismic loading. ACI Struct Journal, 84(1), 61-76.

Saiidi, S., O'Brien, M., & Sadrossadat-Zade, M. (2008). Cyclic Response of Concrete Bridge Column Using Superelastic Nitinol and Bendable Concrete. ACI Structural Journal, 106(1), 69-77.

SAP2000. 2015. A Structural Analysis Program software. V15. (n.d.).

Tazarv, M., & Saiidi, M. (2013). Analytical studies of the seismic performance of a full-scale SMA-reinforced bridge column. International Journal of Bridge Engineering, 1(1), 37-50.

TBI. (2010). Guidelines for performance-based seismic design of tall buildings, Report No. 2010/05. Pacific Earthquake Engineering Research Center, University of California, Berkeley, CA.

The National Building Code of Canada. (2015). Ottawa: Canadian Commission on Building and Fire Code, National Research Council.

The National Building Code of Canada. (1985). Ottawa: Canadian Commission on Building and Fire Code, National Research Council.

Tuna, Z. (2012). Seismic performance, modeling, and failure assessment of reinforced concrete shear wall buildings. Ph.D. thesis: University of California, Los Angeles.

Vamvatsikos, D., & Cornell, C. (2001). Incremental dynamic analysis. Earthquake Engineering and Structural Dynamics, 31(3), 491-514.

Youssef, M., & Elfeki, M. (2012). Seismic performance of concrete frames reinforced with superelastic shape memory alloys. Smart Structures and Systems, 9(4), 313-333.

Youssef, M., Alam, M., & Nehdi, M. (2008). Experimental investigation on the seismic behaviour of beam-column joints reinforced with superelastic shape memory alloys. Journal of Earthquake Engineering, 12(7), 1205-1222.

CHAPTER 6

SEISMIC PERFORMANCE OF REINFORCED CONCRETE CORE WALLS EQUIPPED WITH SHAPE MEMORY ALLOY BARS

6.1 INTRODUCTION

RC structural walls are widely used to resist lateral loads. During earthquake events, they experience significant damage (Aguilar et al., 1989; Tsai et al., 2000; Elwood et al., 2011; Westenenk et al., 2012). This observation has led to numerous experimental and analytical studies to enhance their seismic performance (Riva et al., 2003; Su and Wong, 2007; Ganesan et al., 2013). Their most common failure mode is characterized by out-of-plane instability (Paulay & Priestley, 1993). RC core walls have the advantage of resisting lateral loads in two directions as well as mitigating the out-of-plane instability (Chai & Elayer, 1999).

P´egon et al. (2000) tested U-shaped RC walls under different load patterns and observed that their failure was initiated by fracture of the longitudinal bars followed by crushing of the compression flange. Beyer (2007) tested two half-scale U-shaped RC walls under bi-directional cyclic loading. The first wall failed due to bar fracture, whereas the second wall failed due to web failure and diagonal shear cracks. Lowes et al. (2013) tested three identical U-walls under quasi-static cyclic loading. Different types of failures, including sliding at the wall base, bar fracture, and concrete crushing, were observed.

Various types of dampers were utilized to mitigate seismic residual displacements (Hashemi et al. 2016; Di Cesare et al. 2017). Another potential solution is to utilize superelastic shape memory alloy (SE-SMA) bars, which dissipate the seismic energy and significantly reduce seismic residual deformations (Abraik and Youssef, 2018). SE-SMA has two fundamental and characteristic properties: the shape memory effect (SME) and superelasticity (SE). The SME is the ability of atoms to reassemble, causing the material to regain its original shape when

heated (Alam et al. 2007). SE is a stress-induced transformation between the austenite and martensite phases, as in **Figure 6.1**, which causes the material to recover its shape even if it undergoes large inelastic deformations.
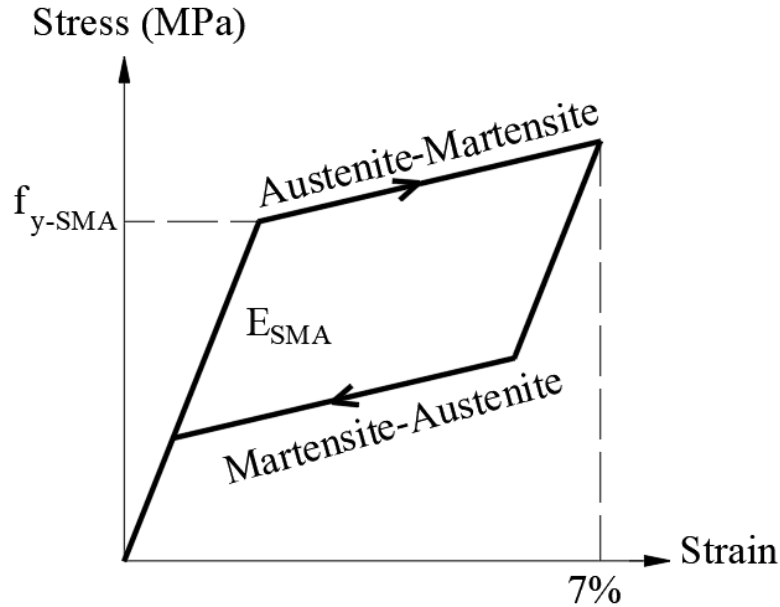
Figure 6.1. Loading and unloading of SE-SMA bar

Abdulridha (2012), Abraik and Youssef (2015), Abraik and Youssef (2016), and Abraik and Youssef (2018) examined the seismic performance of concrete walls reinforced with SE-SMA bars. A study conducted by Effendy et al. (2006) utilized SE-SMA material to enhance the seismic performance of existing RC walls. Results showed that the retrofitted RC walls were able to tolerate higher load and displacement capacities as compared to steel RC walls. The main objective of this chapter is to extend the previous research effort that focused on RC walls to RC core walls. The following sections provide details about the modeling assumptions, validation, and a numerical study.

6.2 NUMERRICAL MODEL

The wide column model (WCM), developed by Clough et al. (1964) for plane RC walls, was later extended by MacLeod and Hosny (1977) to be used for non-planar walls. The model consists of vertical frame elements located at the center of the webs and flanges. The vertical

elements are connected with horizontal rigid links, as shown in **Figure 6.2**. To account for the shear flexibility of the RC core wall, each vertical frame element is divided into two elements that are connected using zero-length in-plane and out-of-plane shear springs (Beyer et al., 2008a).

The finite element software Open System for Earthquake Engineering Simulation (OpenSees, 2018) is used in the analysis. Nonlinear displacement beam elements are used to model the vertical frame elements. The vertical spacing between the horizontal rigid links (h_{sp}) is taken equal to one-fifth of the shear span of the core wall (wall height) as recommended by Stafford-Smith and Girgis (1986). To account for shear flexibility in each wall element, zero-length spring elements are introduced at the nodes located at mid-height. Two horizontal springs (in-plan and out of plan) are added in the two horizontal translational degrees. The in-plane shear flexibility stiffness (K_s) for the shear springs is calculated using Eq 6.1, and the out-of-plane shear stiffness is taken as 25% of K_s as recommended by Beyer (2007). Rayleigh damping with a 2.5% damping ratio is assumed.

$$K_s = \frac{G_c A_{sh}}{h_{sp}} \tag{6.1}$$

where G_c is the concrete shear modulus, and A_{sh} is the shear area taken equal to 80% of the cross-section area.

The constitutive stress-strain relationships developed by Mander and Priestley (1988) and Menegotto and Pinto (1973) are used to model concrete and steel reinforcement, respectively. The SE-SMA reinforcement is represented using the self-centering uniaxial material proposed by Christopoulos et al. (2008). The SE-SMA is assumed to have an asymmetric bilinear stress-strain relationship with a modulus of elasticity (E_{SMA}) of 38,000 MPa, a linear stress limit (f_{y-SMA}) of 380 MPa, and a superelastic strain of 7%.

The global failure criteria proposed by PEER-TBI (2017) are adopted in this analysis, i.e., global failure is assumed for a mean inter-story drift of 3%, a maximum inter-story drift of 4.5%, a mean residual drift of 1%, or a maximum residual drift of 1.5%. Criteria defining local failure are as follows: a strain of 5% in the longitudinal steel bars (Panagiotou, 2008), a strain of 7% in the longitudinal SMA bars, and a concrete compression strain of 2% (Panagiotou, 2008).
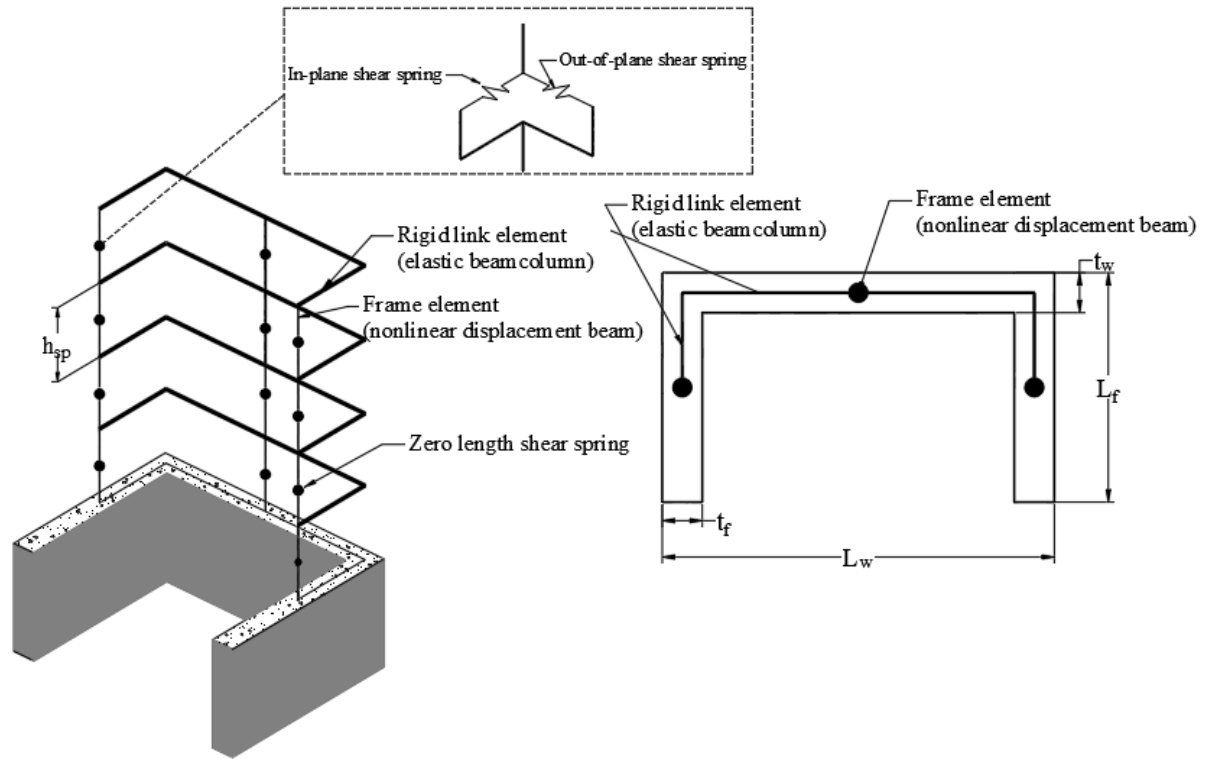
Figure 6.2. Wide column numerical model

6.2.1 Model validation

The numerical model is validated by comparing its results with the experimental data by Beyer (2007). The U-shape RC core wall, shown in **Figure 6.3(a)**, is selected as a validation case. The tested wall has a shear span ratio, i.e., moment/shear (M/V) of 2.95 and a wall thickness of 150 mm. The ratios of the web thickness (t_W) to the web length (l_W) and the flange thickness (t_f) to the flange length (L_f) are 0.12 and 0.14, respectively. Meanwhile, the uniformly distributed vertical and horizontal reinforcement ratios are 0.71% and 0.30%, respectively. The wall was tested under a constant axial load of 780 kN. Four different lateral load directions, shown in **Figure 6.3(b)**, are considered; parallel to the web (Load 1), parallel to flanges & web in tension (Load 2), parallel to flange & web in compression (Load 3), and diagonal (Load 4). **Figure 6.4** shows a comparison between the experimental and numerical results of the pushover analysis. The model accurately captures the ultimate displacement, failure, and load capacity with a maximum error of 7.8% for load 2 and 7.2% for load 3, respectively.
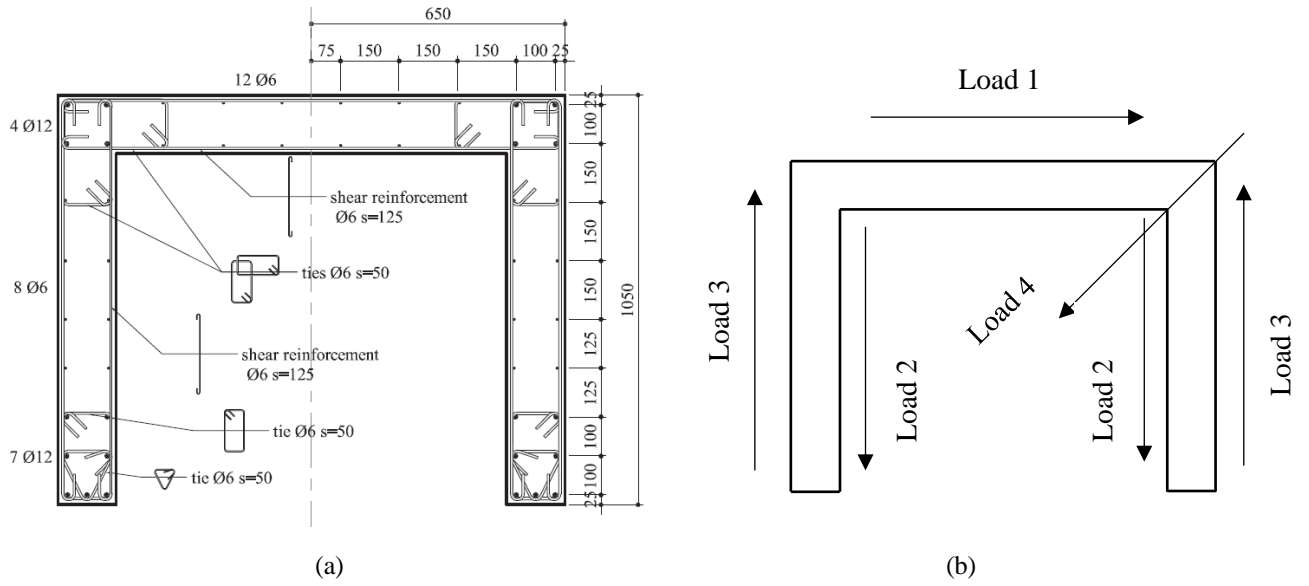
Figure 6.3. Core Wall by Beyer (2007) (a) core wall details; (b) load direction
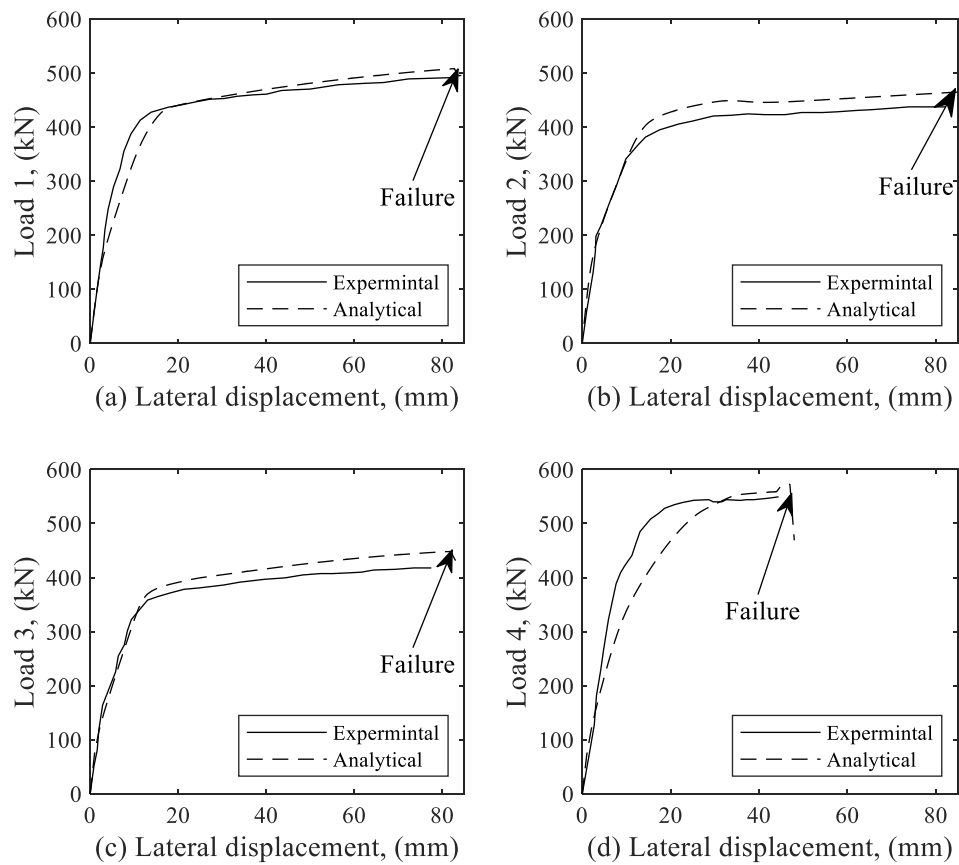
Figure 6.4. Numerical model versus experimental data: (a) load 1; (b) load 2; (c) load 3; (d) load 4

6.2.2 SE-SMA RC core wall

SE-SMA bars are assumed to replace the steel bars in the plastic hinge zone. Plastic hinge length can be calculated using Eq 6.2(a) or 6.2(b) as recommended by Beyer et al. (2008b) or using Eq 6.3 (CSA A23.3, 2014).

$$L_p = 0.08H + 0.022d_bf_y, MPa \qquad (6.2a)$$

$$L_p = 0.2L_w + 0.044H, MPa \qquad (6.2b)$$

$$L_p = 0.5L_w + 0.1H, MPa \qquad (6.3)$$

where H is the effective wall height, d_b is the diameter of the main reinforcement, f_y is its yield strength in (MPa), L_w is the wall length parallel to the loading direction.

To decide on using Eqs 6.2(a) and 6.2(b) or Eq 6.3, the U-shaped RC core wall (shown in **Figure 6.3**) was subjected to cyclic loading after replacing the steel bars in the plastic hinge zone with SE-SMA bars. Two lengths for the SMA bars were examined, which are based on the plastic hinge length given by Beyer et al. (2008a) and CSA A23.3 (2014). **Figure 6.5** shows the cyclic response of the core walls for three load directions per different SE-SMA lengths. The residual displacement was not affected by the length of the SE-SMA bars. However, the method of Beyer et al. (2008a) resulted in a lower lateral drift in the diagonal direction, which is a design advantage. Therefore, Eqs 6.2(a) and 6.2(b) are utilized to determine the SE-SMA length in the following sections of this chapter.
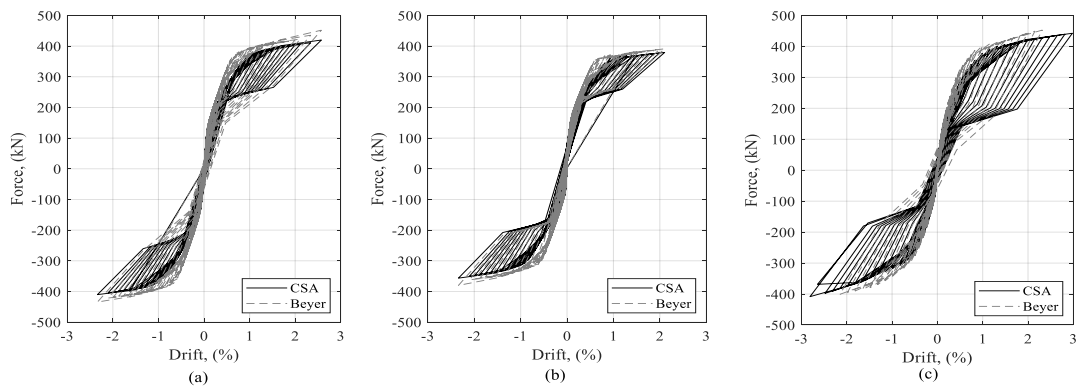
Figure 6.5. Cyclic response of SE-SMA core wall: (a) load parallel to web; (b) load parallel to flange; (c) load in the diagonal direction

6.3 CASE STUDY BUILDING

A nine-story RC commercial building, shown in **Figure 6.6(a)**, is assumed to be located in Vancouver, BC. The selected building is 28 m by 28 m with a typical story height of 3.40 m. The concrete core wall is designed as a ductile RC wall per CSA A23.3 (2014). The force modification factor (R_d) and overstrength factor (R_0) are taken equal to 3.5 and 1.6, respectively (NBCC, 2015). The concrete compressive strength and the steel yield strength are assumed to be 30 MPa and 400 MPa, respectively. The soil profile is class D. The total dead weights of a typical story, and the roof (including 25% snow load) are 5,884 kN and 7,140 kN, respectively. The center of mass (CM) and the center of rigidity (CR) are shown in **Figure 6(a)**. The axial gravity load supported by the core wall is assumed to be 6.6% of its axial capacity. The influence of accidental torsion is accounted for by assuming a torsional eccentricity of 10% in both directions (NBCC, 2015).

(a)   (b)
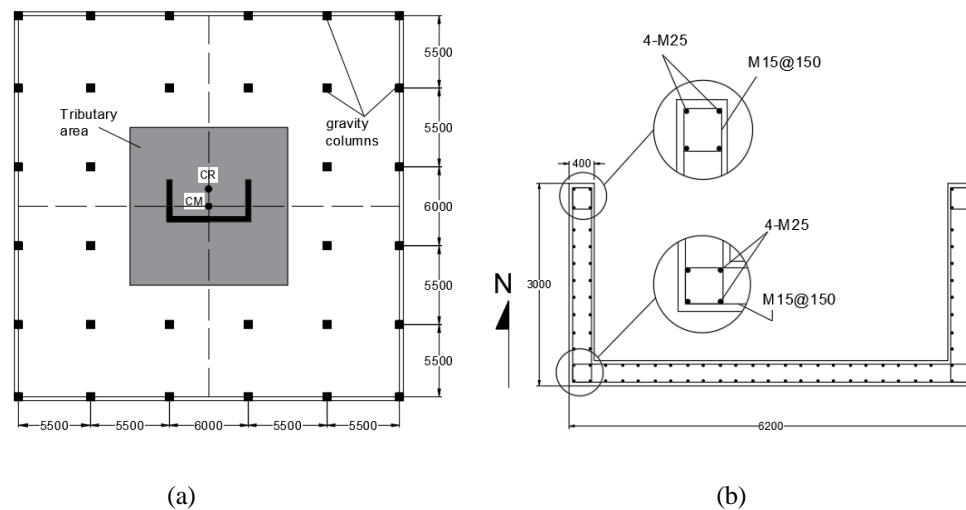
Figure 6.6. Selected building: (a) building plan view; (b) core wall details

The designed building is first analyzed to evaluate its structural period (T). the structural period in the east-west direction (T_{E-W}), north-south direction (T_{N-S}), and torsional (T_t) are found to be 3.27, 1.38, and 0.55 seconds, respectively. Thus, the building is not considered a tall structure as T <3.5 s. Thus, the equivalent lateral load can be used for design. The resulting core wall dimensions and reinforcement details are shown in Figure 6.6(b).

Table 6.1. Structural Period (in seconds)

Period	Torsional Eccentricity					
	5%		10%		20%	
	Steel	SE-SMA	Steel	SE-SMA	Steel	SE-SMA
T_{E-W}	2.66	2.79	3.27	3.40	4.07	4.11
T_{N-S}	1.39	1.45	1.38	1.42	1.34	1.35
T_t	0.47	0.49	0.55	0.56	0.73	0.73

6.4 NONLINEAR SEISMIC ANALYSIS

To evaluate the effect of torsional eccentricity on the seismic performance of core walls, the building is also analyzed at 5%, 10%, and 20% torsional eccentricities. **Table 6.1** summarizes the structural periods considering different torsional eccentricities. The first period was found to increase with increasing the mass eccentricity due to the coupling between torsional mode and the first mode.

The plastic hinge length is calculated, and the SMA bars are assumed to replace the steel bars over this length. Dynamic analysis is then conducted for the steel and SMA RC cores, considering the three mentioned torsional eccentricities.

Six ground motions, given in **Table 6.2**, were selected from the PEER ground motion database (2017). They were scaled to match the design spectra using the Mean Square Error (MSE). The scaled ground motions cover periods from $0.2T_2$ to $1.5T_1$.

where T_1 and T_2 are the structural periods at a mass eccentricity of 10% (design according to NBCC, 2015). **Figure 6.7** shows the spectral acceleration for the selected ground motions as well as the maximum considered earthquake (MCE) for Vancouver, BC.
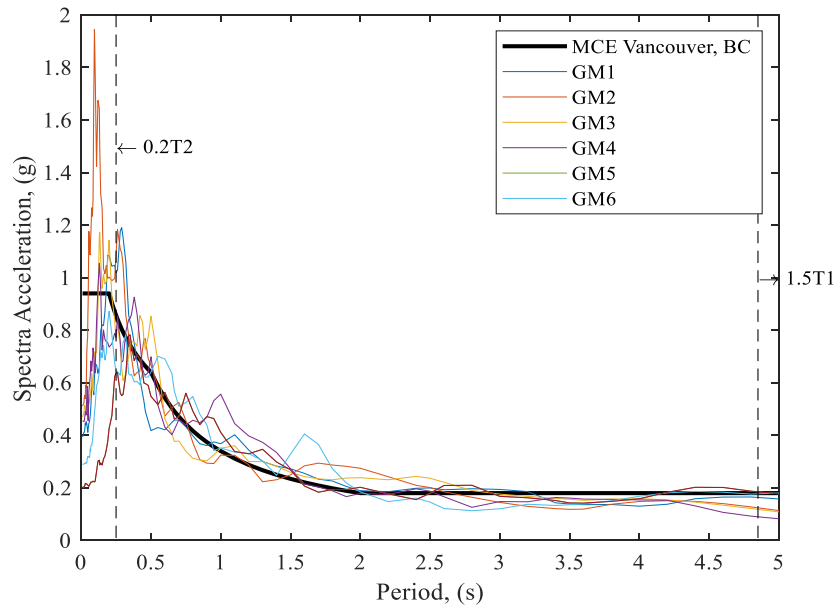
Figure 6.7. Design spectra and ground motions

Table 6.2. Properties of chosen ground motions

Ground Motion	Earthquake	Station	Magnitude	Scale Factor
GM1	Imperial Valley-06	Calipatria Fire	6.53	2.60
GM2	Imperial Valley-06	El Centro Array #1	6.53	2.00
GM3	Lander	Mission Creek	7.28	2.29
GM4	Kobe	Abeno	6.90	1.40
GM5	Chi-Chi	TCU038	7.62	1.00
GM6	Darfield	Hulverstone Drive Pumping	7.00	1.21

The analysis was first conducted by considering each of the seismic excitations to be acting on the core wall either in the E-W direction or the N-S direction. This was followed by bidirectional analysis, where the seismic excitations were assumed to be applied in both directions simultaneously. Floor accelerations, lateral displacements, inter-story drift ratios, and residual displacements were determined at the building center of rigidity, whereas the diaphragm rotation was determined with reference to the building corners.

6.4.1 Unidirectional seismic excitations

Each ground motion is applied independently in each direction (72 cases in total). **Figure 6.8** shows the mean floor acceleration along the building height relative to the peak ground acceleration (PGA) considering different torsional eccentricities. The difference in the floor accelerations between the steel and the SE-SMA RC core walls is negligible considering 5% and 10% eccentricities. For 20% torsional eccentricity, using SE-SMA bars decreases the floor accelerations by an average value of 8%. This reduction can be due to the lower SE-SMA stiffness.

Figures 6.9 and **6.10** show the mean maximum lateral displacements and inter-story drift ratios considering different torsional eccentricities. A negligible difference exists in the E-W direction between the steel and the SE-SMA core walls. The calculated lateral displacements in the E-W direction decrease with the increase in torsional eccentricity. The decline in lateral displacements at high torsional eccentricity may be resulting from the associated increase in the structural period, **Table 6.1**. In the N-S direction, the lateral displacement of the SE-SMA RC core wall is lower than the steel RC core wall by about 7% at 5% torsional eccentricity. The results of the inter-story drifts in both directions have the same trend as obtained from lateral displacements. The SE-SMA bars decrease the mean inter-story drifts in the N-S direction by about 20% on average for 5% and 10% torsional eccentricity. This is because the steel yielding strain is much lower than the SE-SMA strain limit.
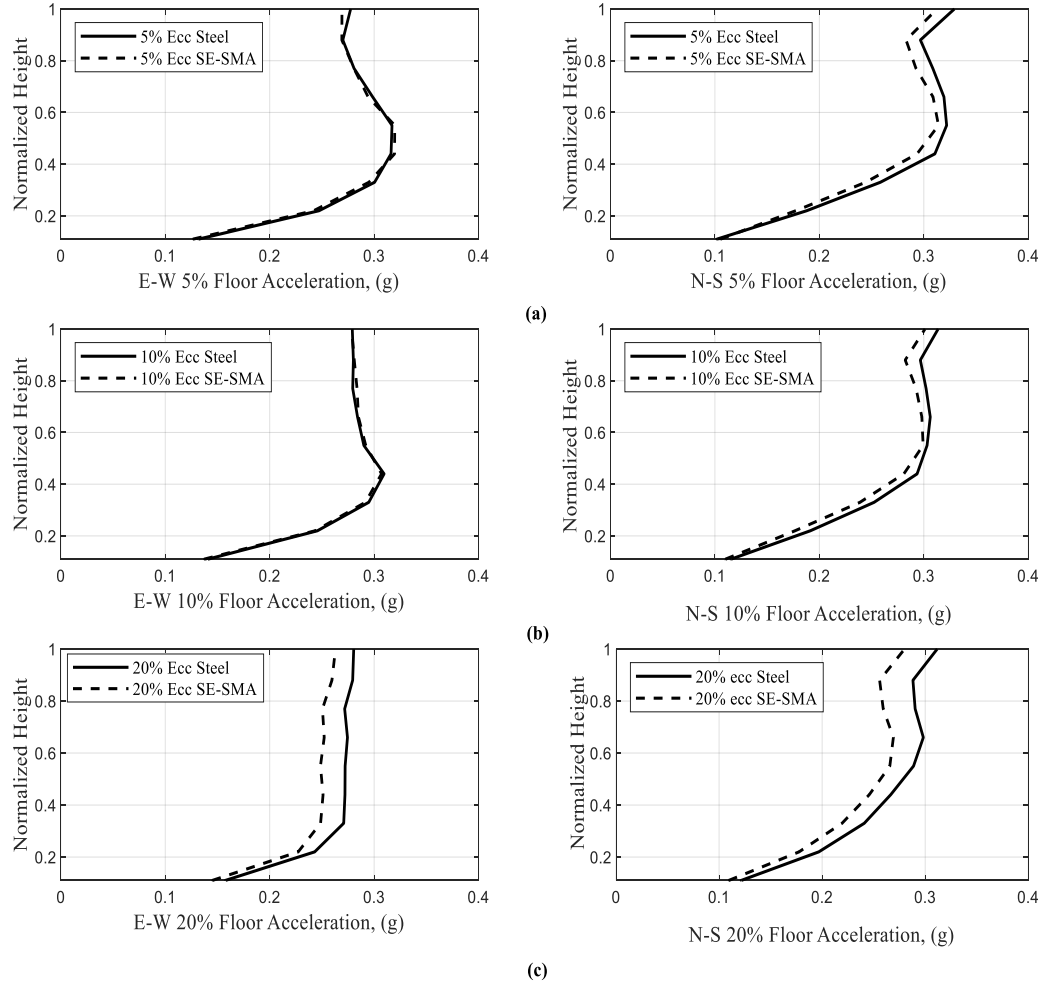
Figure 6.8. Mean floor accelerations: (a) 5% Ecc; (b) 10% Ecc; (c) 20% Ecc
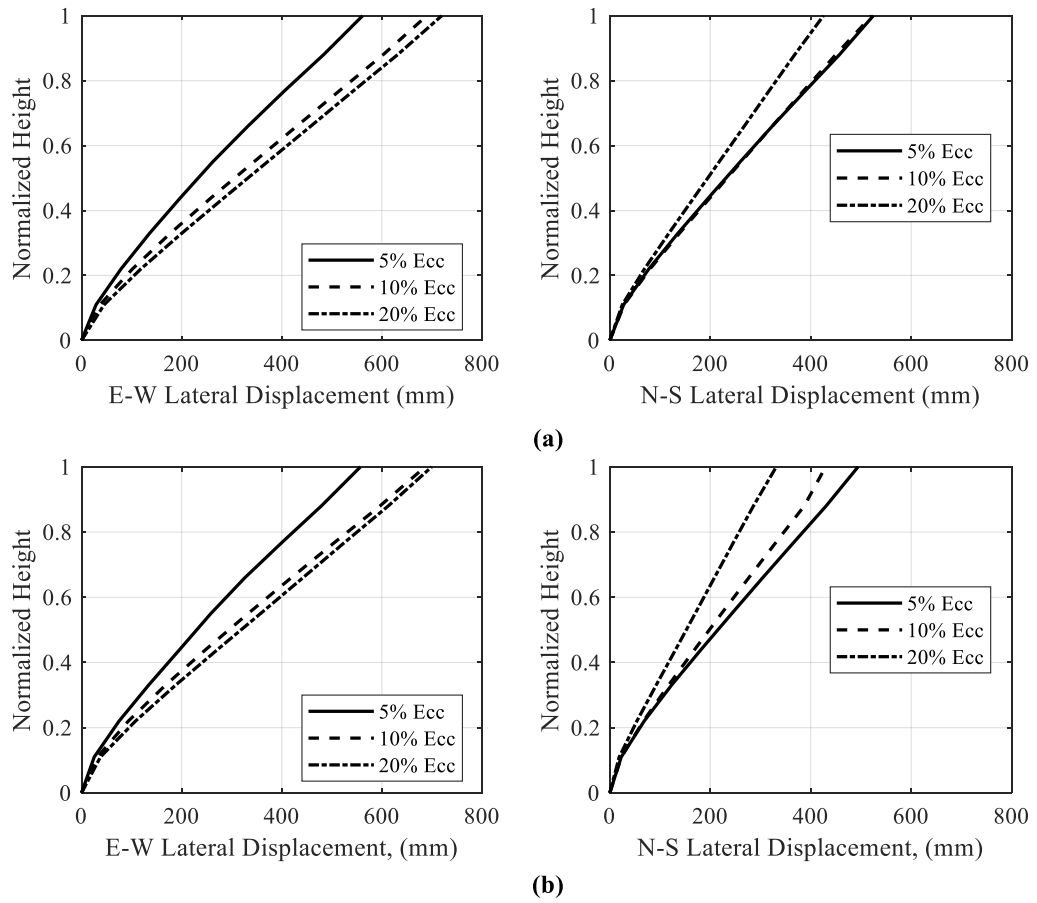
Figure 6.9. Mean maximum lateral displacements: (a) steel RC core wall; (b) SE-SMA RC core wall
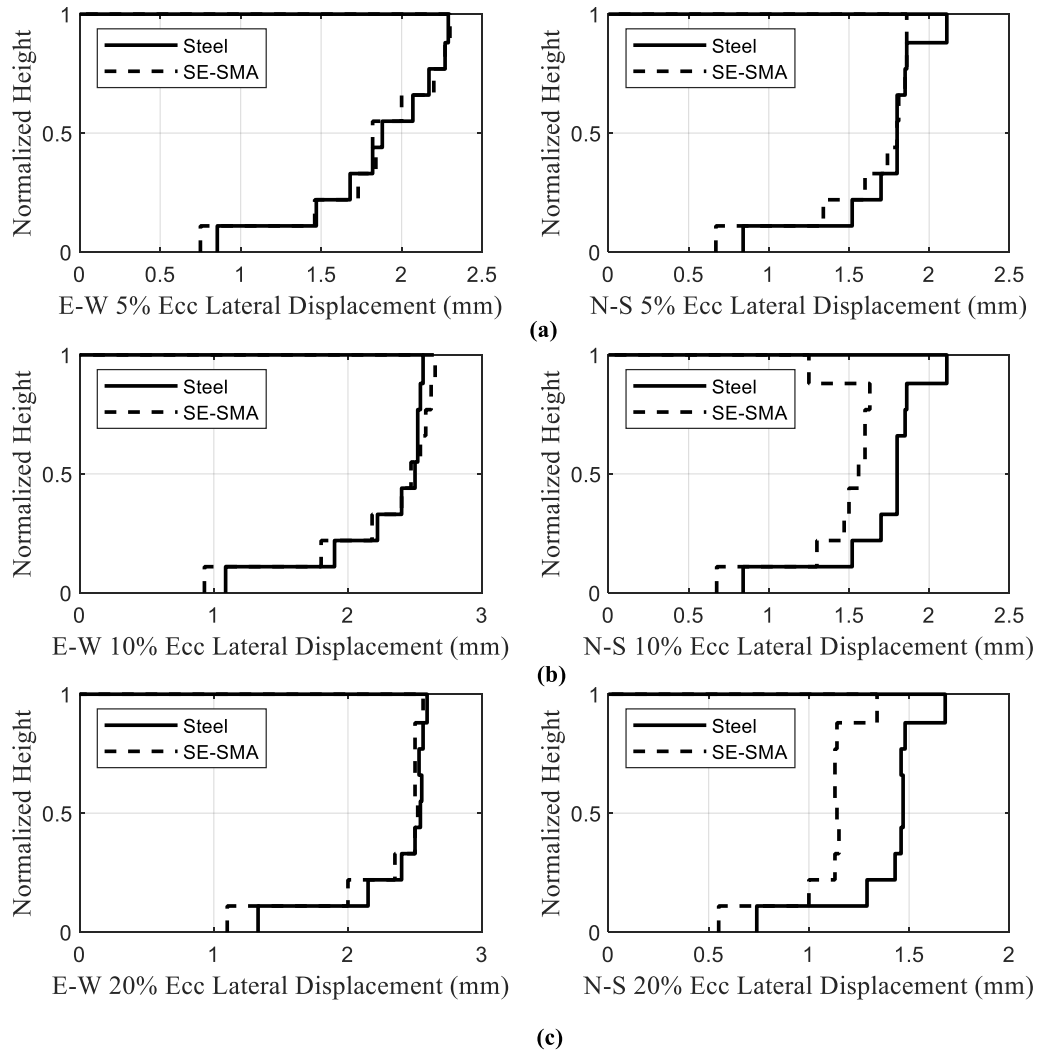
Figure 6.10. Mean inter-story drift ratios: (a) 5% Ecc; (b) 10% Ecc; (c) 20% Ecc

The influence of mass eccentricity on residual displacements is illustrated in **Figure 6.11**. The change in residual displacements in the N-S direction is small when the mass eccentricity increases beyond 10% for the steel and SE-SMA RC core walls. However, the SE-SMA bars reduce the residual roof displacements by 39%, 36%, and 35% for torsional eccentricity of 5%, 10%, and 20%, respectively. The obtained residual displacements of the SE-SMA RC core wall in the E-W direction are less than those of steel RC core wall by 50%, 32%, and 30% for a mass eccentricity of 5%, 10%, and 20%, respectively.
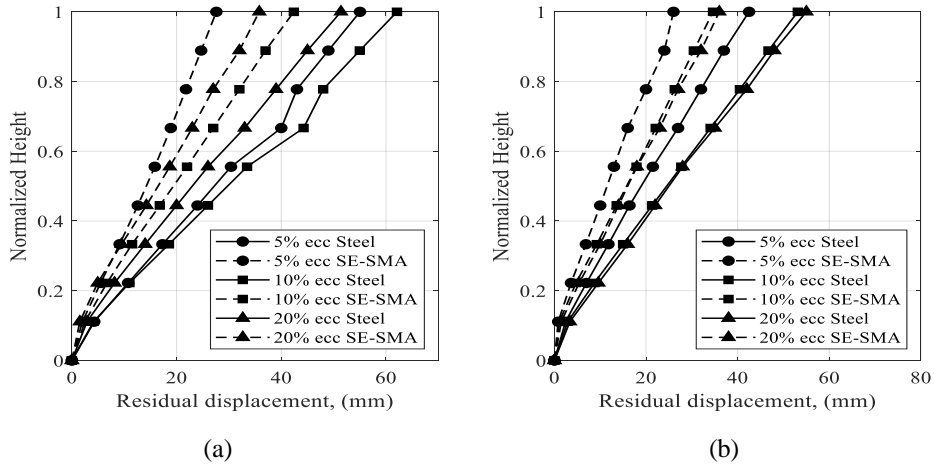
Figure 6.11. Mean residual displacements: (a) E-W direction; (b) N-S direction

Torsional ratio β is defined as the ratio of the largest maximum story displacement to the average of the maximum and minimum displacement measured at the building corners. The β values are calculated, considering both E-W and N-S directions and are shown in **Figure 6.12**. In the E-W direction, the β value of SE-SMA RC core wall at 5% mass eccentricity reflects a higher torsional irregularity as compared with the steel RC core wall but does not exceed the code limit of 1.7. The β values at other eccentricities in the E-W and N-S directions are almost the same for steel RC and SE-SMA RC core walls. This finding confirms that both core walls can be classified as torsionally insensitive for the considered mass eccentricities.
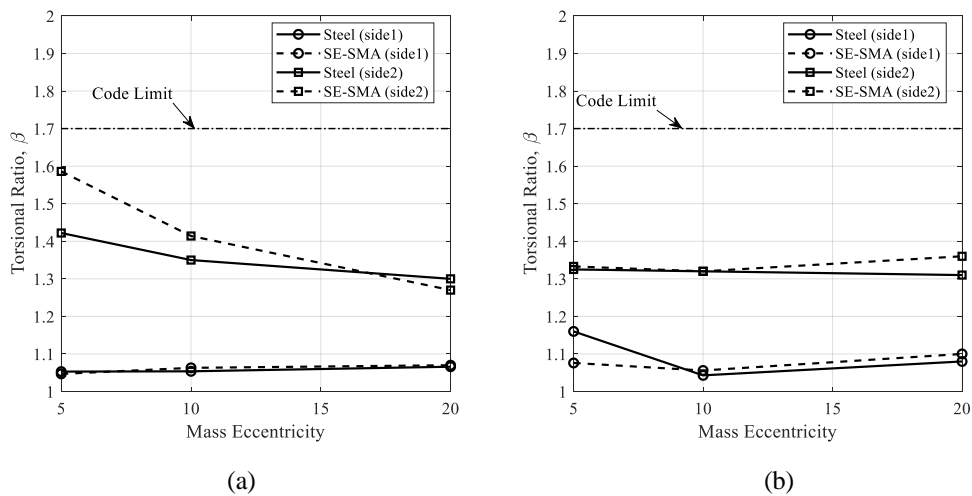
Figure 6.12. Mean diaphragm rotations: (a) E-W direction; (b) N-S directions

6.4.2 Bidirectional seismic excitations

Ground motions are applied alternatively in each direction (36 cases in total). The steel and SMA core wall responses are compared in terms of the mean peak acceleration at the top floor and the mean lateral displacement at the roof level, as shown in **Figures 6.13** and **6.14**. In both directions, the floor acceleration of the SE-SMA RC wall is lower than the steel RC core wall considering different mass eccentricities, i.e., similar to the unidirectional seismic excitations. As shown in **Table 6.1**, this reduction becomes negligible with the increase in the mass eccentricity due to the higher flexibility for both core walls.

The difference in lateral displacements between the two considered core walls in the E-W direction is minor under unidirectional and bidirectional seismic excitations. In the N-S direction, the SMA RC core wall exhibits a lower lateral displacement when subjected to unidirectional excitation as compared to the steel RC core wall for 10% and 20% torsional eccentricity. Under bidirectional excitation, both walls exhibit the same lateral displacement.
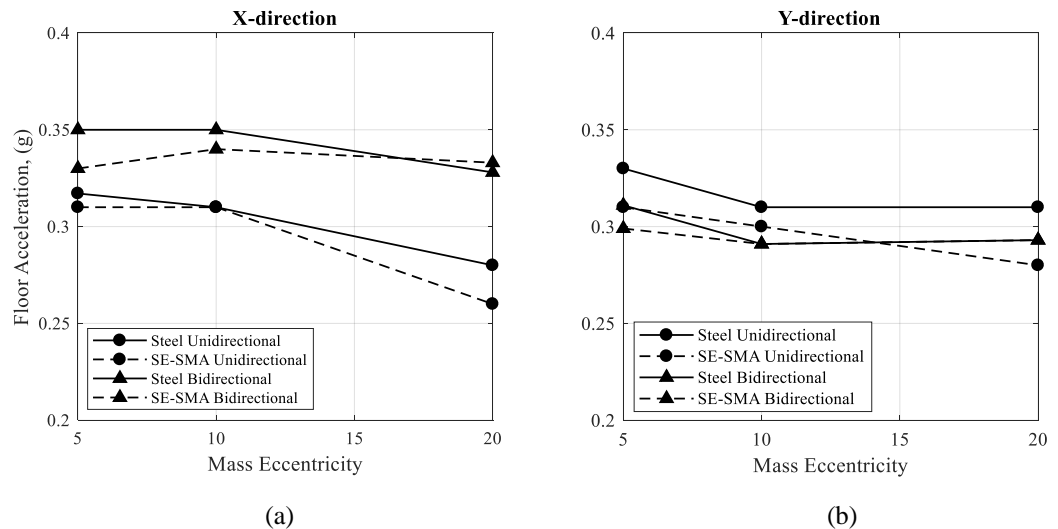
Figure 6.13. Mean roof accelerations under unidirectional and bidirectional excitations: (a) E-W direction; (b) N-S direction

Figure 6.15 shows the mean residual displacement in both directions. In the E-W direction, the use of SE-SMA bars reduces the residual displacements caused by unidirectional and bidirectional ground motions by about 45% on average, considering the torsional eccentricity range between 5% and 10%. At 20% eccentricity, a negligible difference exists in the residual displacement of SE-SMA core walls when subject to unidirectional and bidirectional seismic

excitations. The re-centering capability of SMA is reduced by increasing the mass eccentricity due to the increase in structural flexibility. In contrast to the E-W direction, the SE-SMA core wall exhibits 37%, 50%, and 57% lower residual displacement as compared to steel RC core walls for 5%, 10%, and 20% torsional eccentricities, respectively.
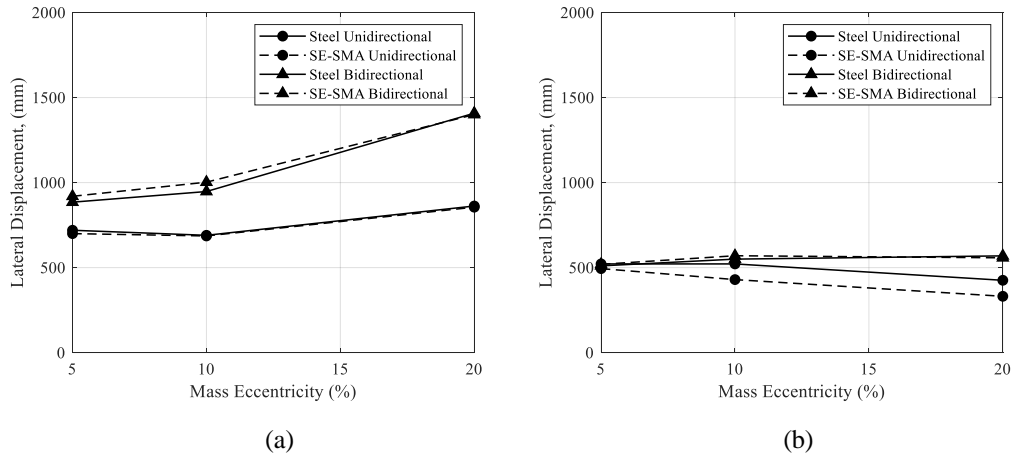
Figure 6.14. Mean lateral displacements under unidirectional and bidirectional; excitations: (a) E-W direction; (b) N-S direction

Figure 6.16 shows a comparison between the residual in-plane rotations for both core walls. At a lower level of eccentricities, both core walls reach a maximum roof residual rotation. The in-plane rotation of the SMA RC core wall is lower than the steel RC core wall by 53%, 36%, and 35% for 5%, 10%, and 20% torsional eccentricities, respectively. The rate of decreasing the in-plane residual rotations decreases substantially at a sufficiently large eccentricity level. Also, the difference in results between the bidirectional and unidirectional is negligible at higher torsional eccentricities.
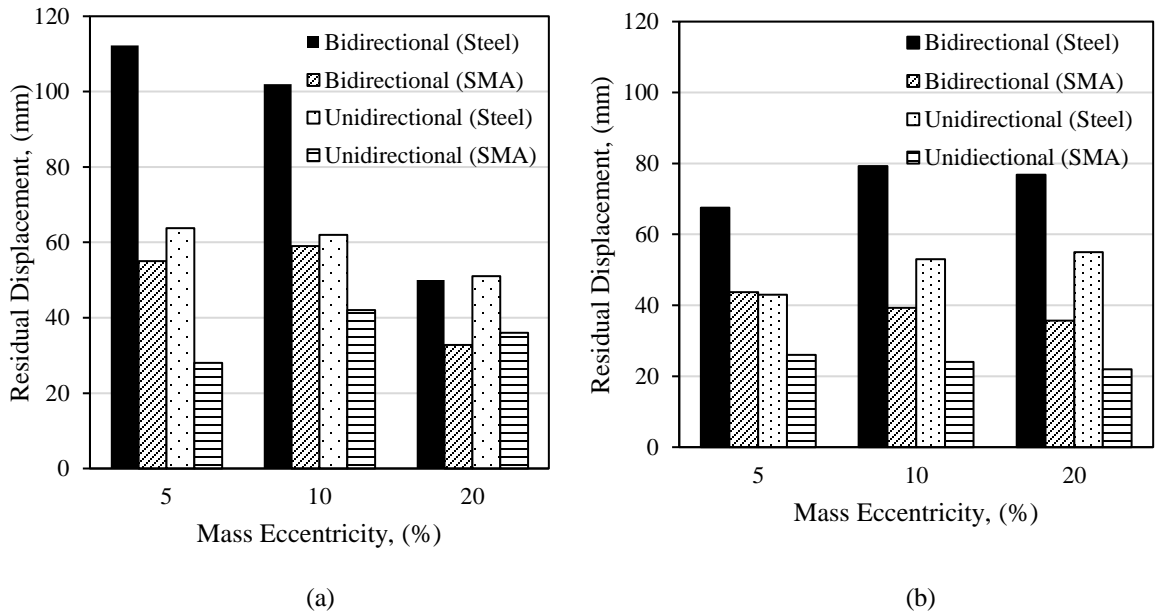
Figure 6.15. Mean residual displacements under unidirectional and bidirectional excitations: (a) E-W direction; (b) N-S direction
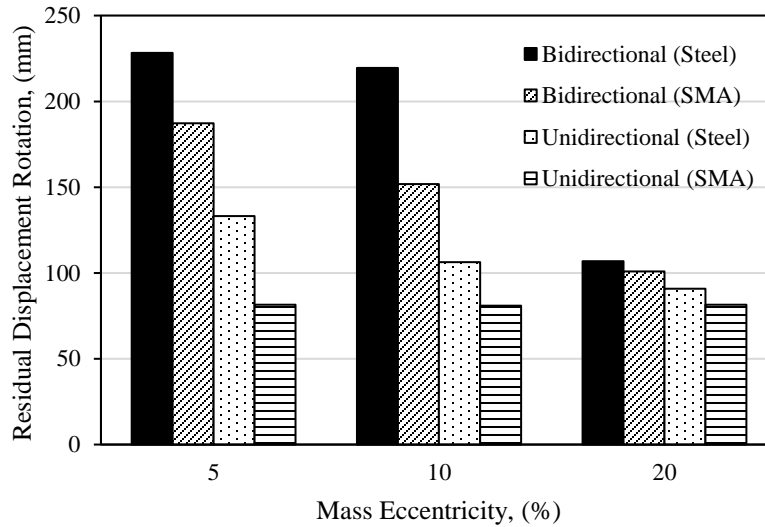
Figure 6.16. Mean residual displacements rotation under unidirectional and bidirectional excitations

Tables 6.3 and **6.4** summarize the mean inter-story drift ratios (MIDs) and the mean residual inter-story drift ratios (MRIDs) for both walls considering the different mass eccentricities. The difference between the considered walls in terms of the MIDs is minimal compared with

corresponding MIDs values. For instance, the SE-SMA RC core wall at 20% eccentricity is held within about 2.0% MIDs compared to 1.8% MIDs for the steel RC core wall. Regardless of the reinforcement type, the effect of bidirectional excitation on the MIDs results is large. The global damage criteria for serviceability and acceptable repair are defined at residual drift values of 0.3% (Henry et al., 2016) and 0.5% (McCormick et al., 2008). For the bidirectional excitation in the E-W direction, the MRIDs for steel RC core wall reaches a maximum value of 0.5% and 0.43% for a mass eccentricity of 5% and 10%, respectively. Using SE-SMA bars reduces the average MRIDs by 42% and 33% for 5% and 10% mass eccentricity, respectively.

Table 6.3. MIDs and MRIDs for E-W direction mass eccentricity

	Mass Eccentricity in E-W direction (%)											
	5				10				20			
	Steel		SE-SMA		Steel		SE-SMA		Steel		SE-SMA	
	MID (%)	MRID (%)	MID (%)	MRID (%)	MID (%)	MRID (%)	MID (%)	MRID (%)	MID (%)	MRID (%)	MID (%)	MRID (%)
Unidirectional	2.23	0.20	2.26	0.10	2.25	0.24	2.23	0.18	2.25	0.21	2.25	0.13
Bidirectional	2.56	0.50	2.56	0.29	2.50	0.50	2.40	0.30	2.63	0.21	2.50	0.12

Table 6.4. MIDs and MRIDs for N-S direction mass eccentricity

	Mass Eccentricity in N-S direction (%)											
	5				10				20			
	Steel		SE-SMA		Steel		SE-SMA		Steel		SE-SMA	
	MID (%)	MRID (%)	MID (%)	MRID (%)	MID (%)	MRID (%)	MID (%)	MRID (%)	MID (%)	MRID (%)	MID (%)	MRID (%)
Unidirectional	1.75	0.18	1.78	0.07	1.6	0.21	1.78	0.14	1.81	0.23	1.99	0.13
Bidirectional	1.49	0.10	1.42	0.06	1.43	0.30	1.46	0.21	1.56	0.11	1.58	0.02

6.4 CONCLUSIONS

The seismic performance of steel RC and SE-SMA RC core walls with different mass eccentricity are investigated in this study. Floor acceleration, residual displacement, diaphragm rotations, and residual diaphragm rotations are evaluated under bidirectional and unidirectional seismic ground motions. The following conclusions can be drawn from this study:

1- SE-SMA RC core wall has less damage for non-structural components associated with lower floor accelerations compared to the steel RC core walls considering various mass eccentricities. The effectiveness of SE-SMA bars on mitigating the floor accelerations occur beyond the 10% mass eccentricity.

2- Floor accelerations resulting from unidirectional excitation are lower than that those from bidirectional excitation. However, for both directions, the SE-SMA bars attenuated the floor accelerations.

3- The steel RC core wall and the SE-SMA RC wall exhibited the same lateral displacement envelopes given the increased period associated with increasing the mass eccentricity. In contrast, the SE-SMA bars are observed to reduce the lateral displacement when the structural period is reduced while reducing the mass eccentricity

4- Utilizing SE-SMA bars in the plastic hinge substantially reduces the residual displacements caused by unidirectional and bidirectional excitation by 36% on average, but the rate of this reduction reduces with increasing the mass eccentricity.

5- SE-SMA bars reduce the diaphragm rotations by 6% to 58%. The maximum diaphragm rotations for both walls occur at 5% mass eccentricity. Therefore, this mass eccentricity is adequate to account for the torsional amplification for static or dynamic analysis.

6.5 REFERENCES

A23.3-14. (2014). Design of Concrete Structures. Canadian Standards Association. Mississauga, ON, Canada.

Abdulridha, A. (2012). Performance of superelastic shape memory alloy reinforced concrete elements subjected to monotonic and cyclic loading. Ottawa: Ph.D. thesis: University of Ottawa.

Abraik, E., & Youssef, M. (2015). Cyclic performance of shape memory alloy reinforced concrete walls. Response of structures under extreme loading (pp. 326-333). Lansing, MI: The fifth international workshop on performance, protection, and strength of structures under extreme loading.

Abraik, E., & Youssef, M. (2016). Performance assessment of three-story shape memory alloy reinforced concrete walls. CSCE 5th International Structural Specialty Conference, 852. London, ON, Canada.

Abraik, E., & Youssef, M. (2018). Seismic Fragility assessment of superelastic shape memory alloy reinforced concrete shear walls. Journal of building engineering, 19, 142-153.

Aguilar, J., Juarez, H., Ortega, R., & Iglesias, J. (1989). The Mexico earthquake of September 19,1985-statistics of damage and of retrofitting techniques in reinforced concrete buildings affected by the 1985 earthquake. Earthquake Spectra, 5(1), 145-151.

Alam, M. S., Youssef, M. A., & Nehdi, M. (2007). Utilizing shape memory alloys to enhance the performance and safety of civil infrastructure: a review. Canadian Journal of Civil Engineering, 34(9), 1075-1086.

Beyer, K. (2007). Seismic design of torsionally eccentric buildings with U-shaped RC walls. Pavia, Italy: Ph.D thesis: European School for Advanced Studies in Reduction of Seismic Risk (Rose School).

Beyer, K., Dazio, A., & Priestley, M. J. (2008a). Inelastic wide-column models for U-shaped reinforced concrete walls. Journal of Eartthquake Engineering, 12(S1), 1-33.

Beyer, K., Dazio, A., & Priestley, M. J. (2008b). Quasi-static cyclic tests of two U-shaped reinforced concrete walls. 12(7), 1023-1053.

Chai, Y. H., & Elayer, D. T. (1999). Lateral stability of reinforced concrete columns under axial reversed cyclic tension and compression. Structural Journal, 96(5), 780-790.

Christopoulos, C., Tremblay, R., Kim, H., & Lacerte, M. (2008). Self-centering energy dissipative bracing system for the seismic resistance of structures: development and validation. ASCE Journal of Structural Engineering, 134(1), 96-107.

Clough, R. W., King, I. P., & Wilson, E. L. (1964). Structural analysis of multistory buildings. Journal of the Structural Division, 90(3), 19-34.

Di Cesare, A., Ponzo, F., Nigro, D., Pampanin, S., & Smith, T. (2017). Shaking table testing of post-tensioned timber frame building with passive energy dissipation systems. Bull Earthq Eng, 15(10), 4475-4498.

Effendy, E., Liao, W., Song, G., Mo, Y., & Loh, C. (2006). Seismic behavior of low rise shear walls with SMA bars. Earth & Space, 3, 377-388.

Elwood, K. J., Pampanin, S., & Kam, W. Y. (22). February 2011 Christchurch earthquake and implications for the design of concrete structures. In Proceedings of the International Symposium on Engineering Lessons Learned from the 2011 Great East Japan Earthquake (pp. 1157-1168).

Ganesan, N., Abraham, R., Beena, P., & Anil, R. (2013). Influence of horizontal reinforcement on ultra high performance concrete wall panels under two way in plane action. International Journal of Scientific & Engineering Research, 4(5), 149-152.

Hashemi, A., Masoudnia, R., & Quenneville, P. (2016). Seismic performance of hybrid self-centring steel-timber rocking core walls with slip friction connections. J Constr Steel Res, 126, 201-213.

Henry, R., Sritharan, S., & Ingham, J., (2016). Residual drift analyses of realistic self-centering concrete wall systems. Eng Struct, 10(2), 409-428.

Lowes, l., Lehman, D., Kuchma, D., Mock, A., & Behrouzi, A. (2013). Large scale tests of C-shaped reinforced concrete walls. summary report from nees project warehouse. Technical report, NEES project.

Macleod, I. A., & Hosny, H. M. (1977). Frame analysis of shear wall cores. Journal of the Structural Division, 103(10), 2037-2047.

McCormick, J., Aburano, H., Ikenaga, M., & Nakashima, M. (2008, October). Permissible residual deformation levels for building structures considering both safety and human elements. In Proceedings of the 14th world conference on earthquake engineering (pp. 12-17).

Mander, J. B., & Priestley, M. J. (1988). Theoretical stress-strain model for confined concrete. Journal of Structural Engineering. ASCE, 114(8), 1804-1826.

Menegotto, M. Pinto, E. (1973). Method of analysis of cyclically loaded RC plane frames including changes in geometry and non-elastic behavior of elements under normal force and bending. Preliminary Report IABSE, vol 13.

OpenSees. (2018). Open system for earthquake engineering simulation. Berkeley, CA.

P´egon, C., Plumier, A., Pinto, J., Molina, P., Gonzalez, P. C., & Hubert., O. (2000). U-shaped walls: Description of the experimental test set-up. Ispra, Italy: Technical report, TMR-ICONS-TOPIC 5, JRC.

Pacific Earthquake Engineering Research (PEER). (2018). Retrieved from ground motions database available online: http://ngawest2.berkeley.edu/

Panagiotou, M. (2008). Seismic design, testing, and analysis of reinforced concrete wall buildings. San Diego, CA: Ph.D thesis: UC: San Diego.

Paulay, T., & Priestley , M. (1993). Stability of ductile structural walls. ACI Structural Journal, 90(4).

Riva, P., Meda, A., & Giruriani, E. (2003). Cyclic behaviour of a full scale RC structural wall. Engineering Structures. 25(6), 835-845.

Stafford-Smith, B., & Girgis, A. (1986). Deficiencies in the wide column analogy for shear wall core analysis. Concrete International, 8(4), 58-61.

Su, R., & Wong, S. M. (2007). Seismic behaviour of slender reinforced concrete shear walls under high axial load ratio. Engineering Structures, 29(8), 1957-1965.

TBI. (2017). Guidelines for performance-based seismic design of tall buildings, Report No. 2017/06. Berkeley, CA: University of California.

The National Building Code of Canada (NBCC). (2015). Ottawa: Canadian Commission on Building and Fire Code, National Research Council.

Tsai, K. C., Chiang, P. H., & Bruneau, M. (2000). Overview of Building Damages in 921 Chi-Chi Earthquake. Earthquake. Engineering and Engineering Seismology, 2(1), 93-108.

Westenenk, B., de la, L. J., Besa, J., Jünemann, R., Moehle, J., Lüders, C., & Hwang, S. J. (2012). Response of reinforced concrete buildings in concepcion during the Maule earthquake. Earthquake Spectra, 28(S1), S257-S280.

CHAPTER 7

SEISMIC PERFORMANCE OF HYBRID CORROSION-FREE SELF-CENTERING CONCRETE SHEAR WALLS

7.1 INTRODUCTION

Reinforced Concrete (RC) shear walls are commonly used as the lateral load system of residential and commercial buildings. During a seismic event, they are expected to provide adequate strength, stiffness, and ductility. As the current practice is moving towards sustainable buildings, which can be easily repaired following major seismic events, the need for novel materials that can mitigate seismic damage is increasing.

Fiber Reinforced Polymer (FRP) has high resistance to corrosion and chemical attacks, high tensile strength, and high stiffness-to-weight ratio (Bank, 2006). These properties have motivated their use as an alternative reinforcement in concrete structures. The behaviour of RC elements reinforced with FRP bars has been examined considering beams by Kassem et al. (2011), two-way slabs by El-Salakawy et al. (2005), columns by Tobbi et al. (2012), and walls by Mohamed et al. (2014). The latter conducted a series of experimental tests on concrete walls reinforced with different configurations of longitudinal Glass FRP (GFRP) subjected to cyclic loads. The GFRP-reinforced walls exhibited a self-centering behaviour up to the allowable drift limits with an acceptable lower level of energy dissipation. Yamakawa and Fujisaki (1995) tested seven shear walls reinforced with CFRP grid. The specimens showed an early degradation in the load capacity at a 1% drift associated with lower energy dissipation.

Super-Elastic (SE) Shape Memory Alloy (SMA) has a flag-shaped hysteresis that allows the recovery of inelastic strains upon unloading (McCormick et al., 2007). This unique ability has made SE-SMA a potential design option for attaining sustainable seismic force-resisting systems. Meshaly et al. (2014), Araki et al. (2016), Qiu and Zhu (2017), and Sultana and Youssef (2018) explored the use of SMA in the vertical bracing of RC and

steel buildings. Eliminating the seismic residual deformations by using SE-SMA was also explored for beam-column joints (Youssef et al., 2008), beams (Saiidi et al., 2007), and columns (Tazarv and Saiidi, 2013). Abdulridha (2012) applied a cyclic load to a full-scale SE-SMA RC wall. The residual displacement of the SE-SMA wall was 85% less than a similar conventional RC shear wall. Abraik and Youssef (2015, 2016) investigated the effect of the location of SE-SMA bars on the seismic performance of RC walls. Abraik and Youssef (2018) assessed the collapse vulnerability of SE-SMA RC walls. The results showed that SE-SMA RC walls exhibited lower seismic damage, compared to steel RC walls. Although there has been an increase in the number of studies on the application of SE-SMA bars, their low stiffness and high cost limit their use to the localized critical sections.

Zafar and Andrawes (2014) developed an SE-SMA-FRP composite material that comprises a high elongation resin matrix and embedded small SE-SMA reinforcing wires. The flexural behaviour of concrete beams and frames reinforced with this material was experimentally examined by Zafar and Andrawes (2012, 2013), which showed that there is a high potential for SMA-FRP composites in earthquake resisting systems.

This chapter aims at evaluating the seismic performance of concrete shear walls reinforced with SE-SMA-FRP composites. An extensive parametric study is conducted to identify the effect of different geometric and material configurations. The seismic performance of steel, FRP, SMA, and SE-SMA-FRP RC walls are then compared. The following sections provide details about the SE-SMA-FRP composite bar, considered walls, modeling technique, parametric study, and analysis results.

7.2 SMA-FRP COMPOSITE BAR

Figure 7.1 shows the schematic diagram of the SE-SMA-FRP composite bar, which is comprises SMA wires, polymeric resin with high ultimate strain, and fiber reinforcement. The SMA wires have a diameter of $500 \, \mu m$, and are made of 51% Nickel (Ni) and 49% Titanium (Ti) (Zafa and Andrawes, 2015). The amount of SE-SMA ranges from 8.4% to 20.3% of the bar area.
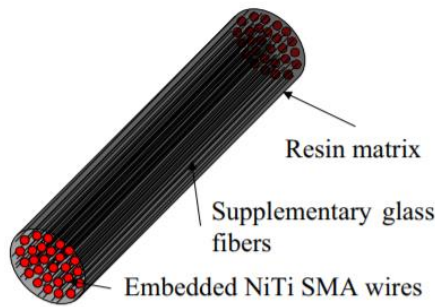
Figure 7.1. SE-SMA-FRP composite bar (Zafar and Andrawes, 2015)

7.3 WALL DESIGN

The reference RC shear wall (W1), shown in **Figure 7.2(a)**, is considered as the Seismic Force Resisting System (SFRS) of a 10-story building located in Vancouver, BC. The concrete compressive strength and steel yield strength are assumed 30 MPa and 400 MPa, respectively. The gravity load, acting during a seismic event, is taken equal to 1,248 kN per story. Assuming a ductile wall, the seismic load reduction factor ($R_d R_0$) is 5.6. The internal forces and moments are calculated using the equivalent static lateral force method as per the National Building Code of Canada (NBCC 2015). The design of the wall is conducted according to CSA A23.3 (2014). **Figure 7.2(b)** gives details about the cross-section and reinforcement details of the designed wall.

The SE-SMA bars and SE-SMA-FRP bars are utilized over the length of the expected plastic hinges. The designed wall is expected to develop two plastic hinges with a length of $0.2H_w$, one at its bottom and one at its mid-height. Mechanical bar couplers are assumed to connect the SE-SMA bars and SE-SMA-FRP bars to the FRP bars reinforcing the remaining of the wall height.

Six walls were considered in this research, as shown in **Figure 7.3**. The considered walls are reinforced with steel bars (W1), SE-SMA bars in the boundary elements over the two plastic hinge lengths and FRP bars elsewhere (W2), SE-SMA-FRP hybrid bars in the boundary elements over the two plastic hinge lengths and FRP bars elsewhere (W3), SE-SMA bars in the boundary elements and the web over the bottom plastic hinge length and

FRP bars elsewhere (W4), SE-SMA-FRP hybrid bars in the boundary elements and the web over the bottom plastic hinge length and FRP bars elsewhere (W5), and SE-SMA-FRP hybrid bars in the boundary elements over the bottom plastic hinge length and FRP bars elsewhere (W6).
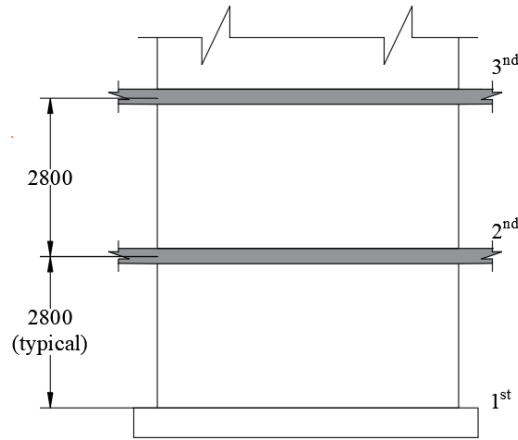
(a)
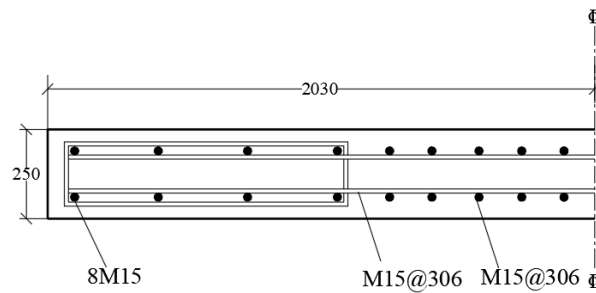
(b)

Figure 7.2. 10-story reference shear wall (dimension in mm): (a) wall elevation; (b) wall cross-section

(a) W1 (steel bars)   (b) W2 (SE-SMA+FRP)   (c) W3 (SE-SMA-FRP+FRP)

(d) W4 (SE-SMA+FRP)   (e) W5 (SE-SMA-FRP+FRP)   (f) W6 (SE-SMA-FRP+FRP)
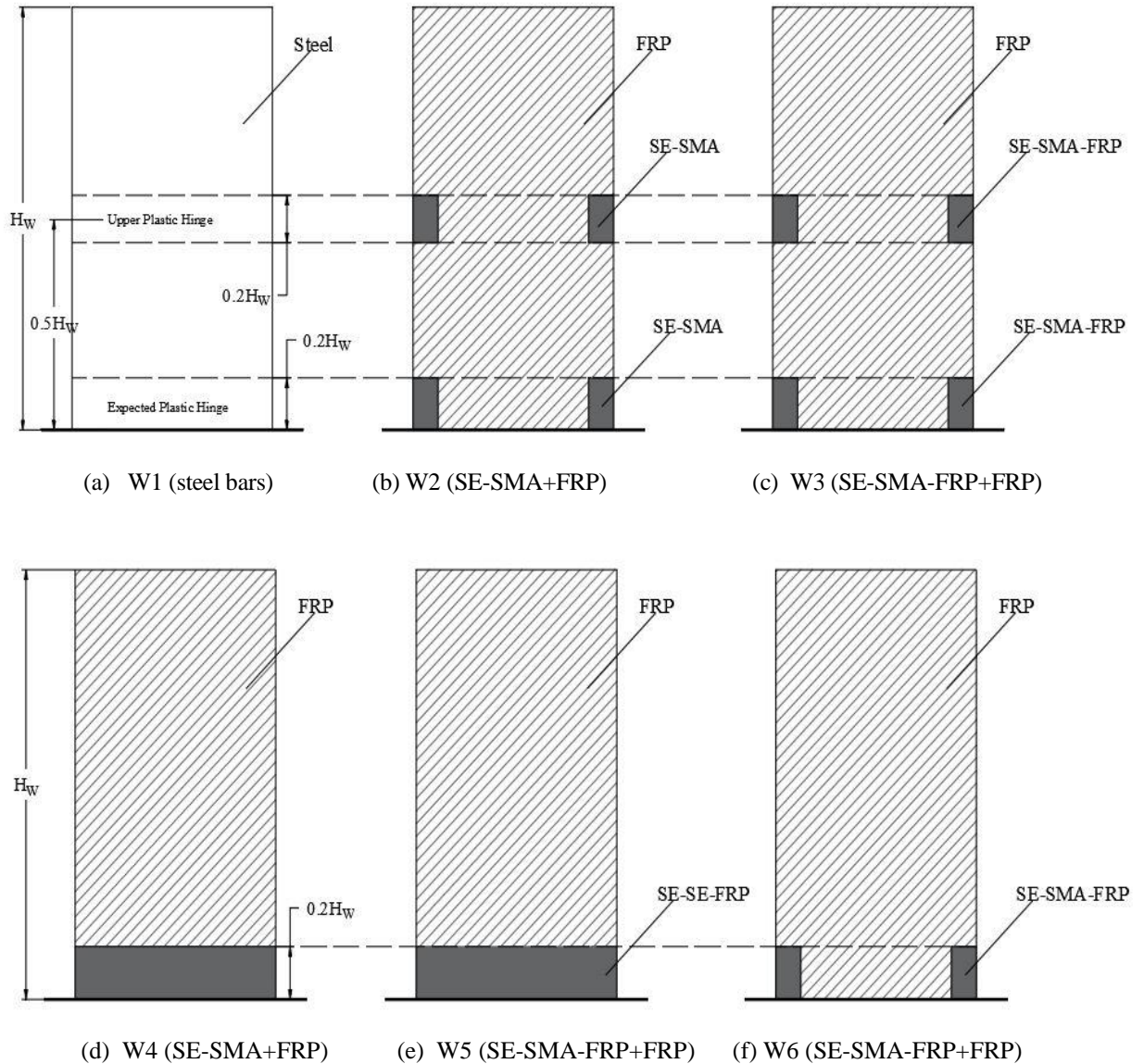
Figure 7.3. Elevation of the selected walls showing the type of longitudinal bars

7.4 NUMERICAL MODEL

The numerical model and nonlinear time history analyses are conducted using the "Open System for Earthquake Engineering Simulation" finite element software (OpenSees, 2018). The walls are modeled using distributed-plasticity fiber-section beam-column elements, as shown in **Figure 7.4**. These elements account for moment-axial force interaction at each analysis step. To account for shear deformations, a horizontal spring is assumed at mid-

height of each floor. The effective shear stiffness is calculated using Eq 7.2 (ASCE 41, 2006).

$$V_{eff} = 0.4E_C A_{cv} \tag{7.2}$$

$$A_{cv} = b_w L_w \tag{7.3}$$

where E_c is the concrete elastic modulus, b_w is the wall thickness, and L_w is the wall length.

(a)   (b)
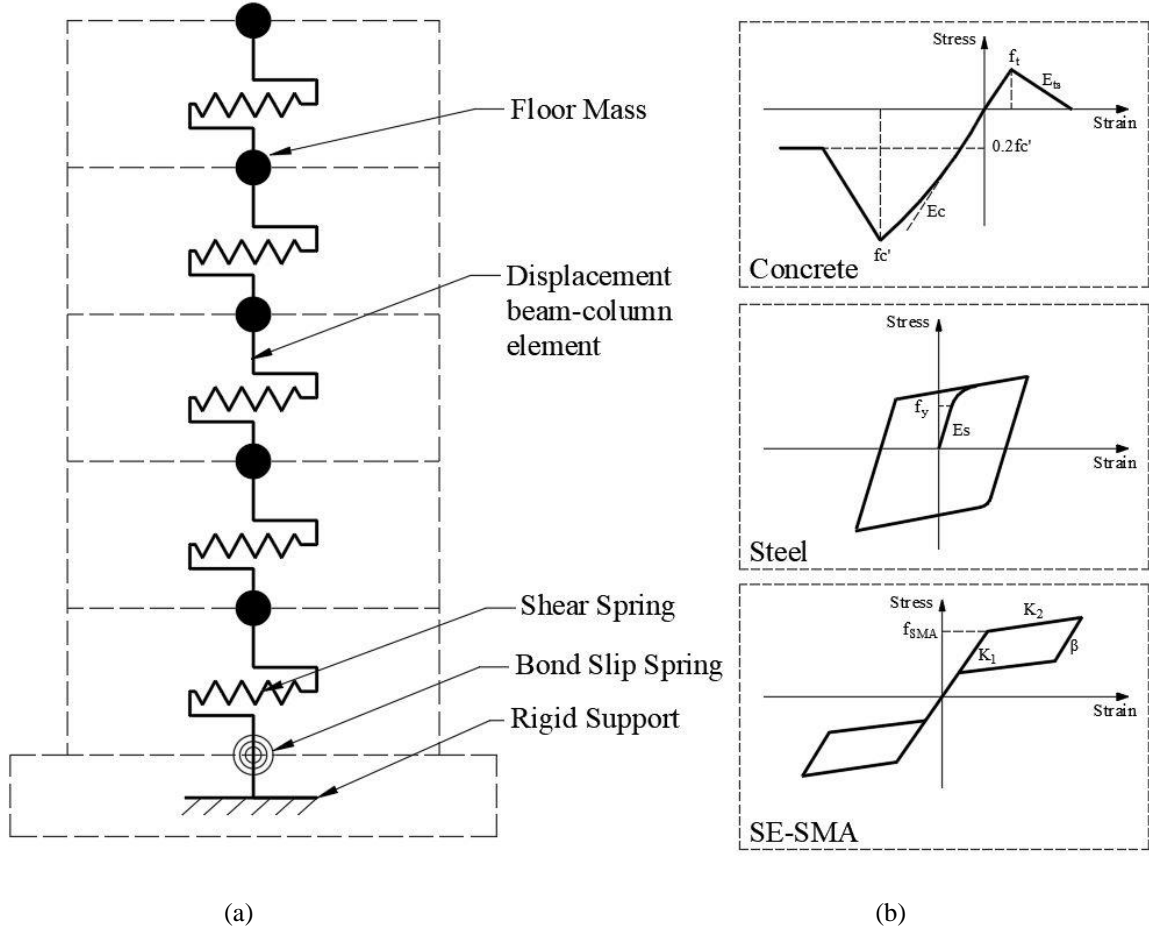
Figure 7.4. Numerical model of shear walls: (a) displacement beam-column model with fiber section; (b) material model

The Menegotto-Pinto (1973) uniaxial material relationship is used to model steel reinforcement. The steel yield strength (f_y) and its modulus of elasticity (E_s) are assumed to be 400 MPa and 200 GPa, respectively. Confined and unconfined concrete are modeled using the uniaxial material model of Mander et al. (1988). The concrete compressive strength (f_c') is assumed to be 30 MPa. The FRP and the resin are modeled using linear

elastic and elastic-perfectly plastic uniaxial materials as recommended by Mohamed et al. (2014) and Zafa and Andrawes (2014), respectively. The (NiTi) SE-SMA bars are modeled using the self-centering material constitutive model. The assumed mechanical properties are presented in **Table 7.1** and are based on the experimental results by Abdulridha (2012). Parallel material command, shown in **Figure 7.5(a)**, defines the material model for the hybrid SE-SMA-FRP bars. **Table 7.2** illustrates the input parameters of the numerical model. The effect of reinforcement bond-slip is considered in the numerical model at the base of the wall using a rotational spring as proposed by Tazarv and Saiidi (2014).

Table 7.1. SE-SMA bars

Material	Parameter	Value
NiTi SE-SMA (55.9% Nickel and 44.1% Titanium)	Austenite yield strength, f_{y-SMA} (MPa)	380
	Austenite modulus, K_1 (MPa)	36,459
	Post-yield stiffness, K_2 (MPa)	365
	Recoverable strain	7%
	Lower plateau stress factor, β	0.55
	Austenite modulus of elasticity (E) (GPa)	36.6
	Austenite to Martensite finish stress (MPa)	520
	Martensite to Austenite start stress (MPa)	209
	Martensite to Austenite finish stress (MPa)	170
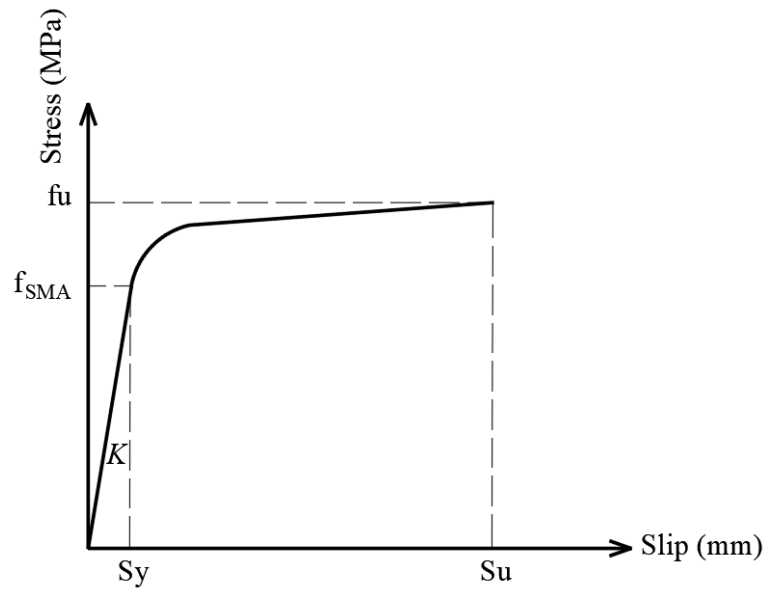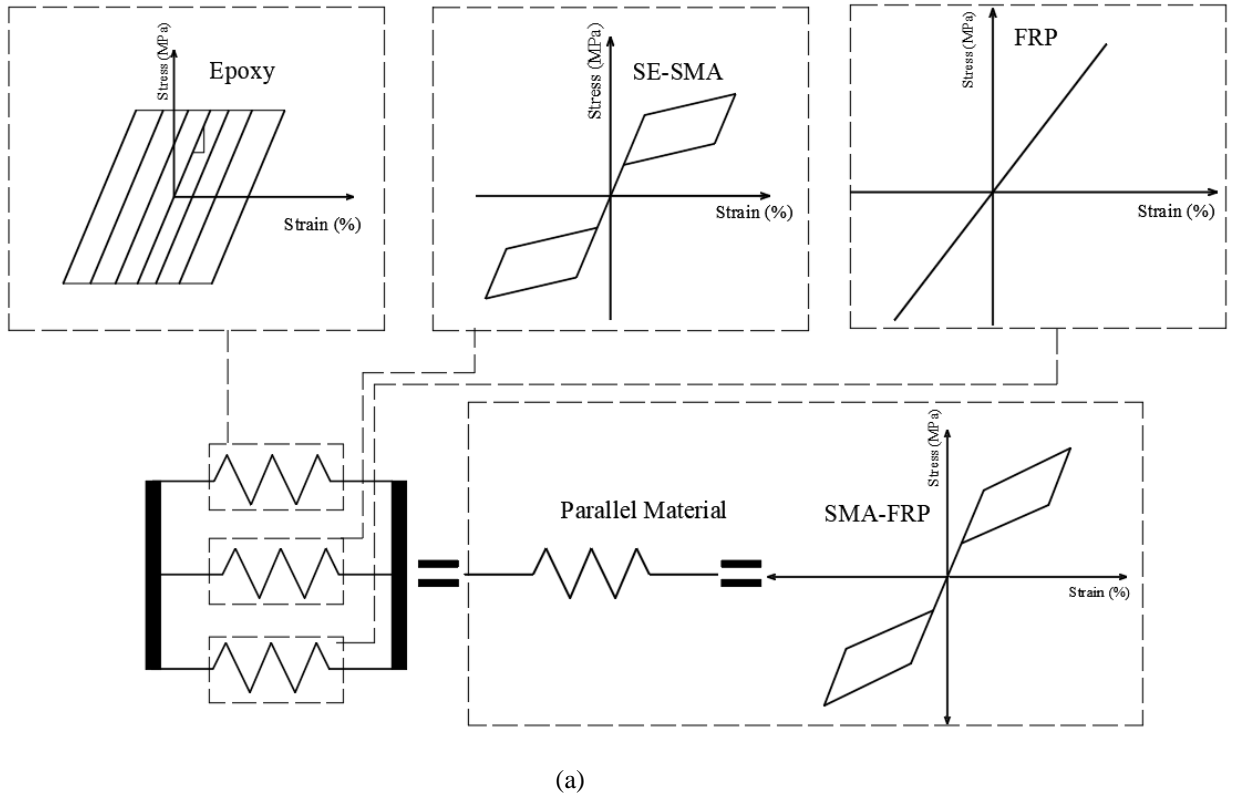
Figure 7.5. (a) SMA-FRP uniaxial model; (b) bond-slip model

Table 7.2. SE-SMA-FRP composite bar (Zafar and Andrawes, 2015)

Material	Parameter	Value
FPR	Modulus of elasticity (E)	86.7 GPa
	Rupture strain	3.0%
Resin	Modulus of elasticity (E)	1.57 GPa
	Yield stress	32.0 MPa
SE-SMA	Modulus of elasticity (E)	65.0 GPa
	Austenite to Martensite start stress	500 MPa
	Austenite to Martensite finish stress	510 MPa
	Martensite to Austenite start stress	135 MPa
	Martensite to Austenite finish stress	145 MPa

7.4.1 Failure Criteria

For local response, the serviceability strain defines the limit below which the expected damage is minor and does not require repair. Its values for concrete and steel can be taken equal to -0.004 and +0.015, respectively (Kowalsky, 2000). The damage control strain defines the limit for repairable damage. Its values for concrete and steel can be taken equal to -0.018 and +0.06, respectively (Kowalsky, 2000). There is no serviceability limit for GFRP and SE-SMA because of the linear behaviour of GFRP and the self-centering behaviour of SE-SMA. However, their damage control limits are +0.013 for GFRP (Sharbatdar and Saatcioglu, 2009) and +0.070 for SE-SMA (Hurlebaus and Gaul, 2006). The global damage criteria for serviceability and acceptable repair are defined at residual drift values of 0.3% (Henry et al., 2016) and 0.5% (McCormick et al., 2008).

7.4.2 Model Validation

Abdulridha (2012) performed full-scale tests on a steel RC wall and (NiTi) SE-SMA RC wall. Both specimens were identical in dimensions and materials except for the amount of boundary reinforcement, as listed in **Table 7.3**. The numerical model predictions are closely matching the experimental results, as shown in **Figure 7.6**.

Table 7.3. Shear walls tested by Abdulridha (2012)

Wall	H (mm)	L_w (mm)	b_w (mm)	f_c'(MPa)	f_y(MPa)	ρ_{vb}	$\rho_{vw} = \rho_{hw}$
Steel	2200	1000	150	30	425	1.33	0.88
SE-SMA					380	1.68	

where H is the wall height; Lw is the wall length; b_w is the wall thickness; f_c' is a concrete compression strength; f_y is steel yielding; ρ_{vb} is the vertical steel ratio at boundaries; ρ_{vw} is vertical steel ratio at web; ρ_{hw} is a horizontal steel ratio in the web.

(a)

(b)

(c)
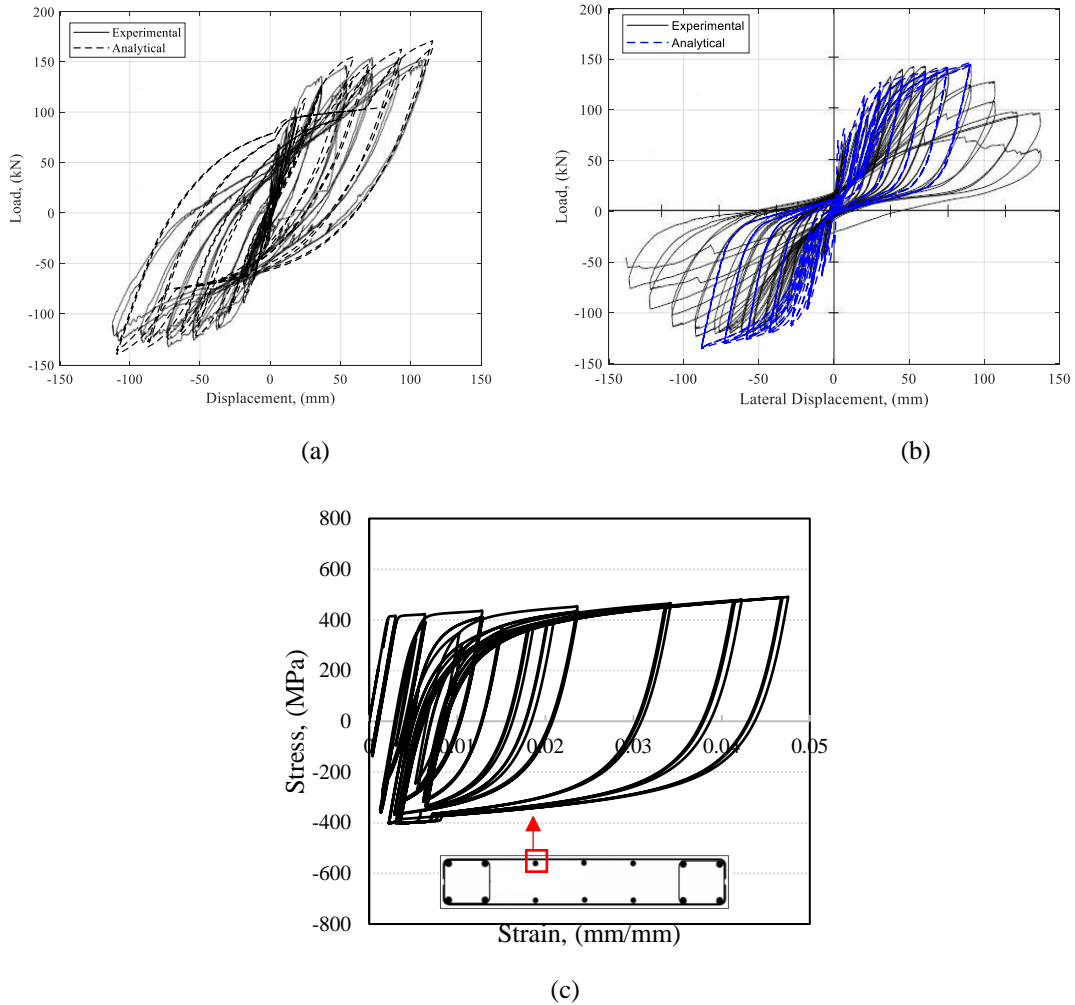
Figure 7.6. Validation using Experimental Results by Abdulridha (2012): (a) steel RC wall; (b) SE-SMA RC wall; (c) strain-stress for steel bar

Billah and Alam (2012) experimentally tested an RC column reinforced with SE-SMA bars at the plastic hinge and FRP bars at the remaining column height. The column dimensions

are 450 mm by 450 mm with a height of 3200 mm. It is reinforced with 8M20. The properties of the used materials are listed in **Table 7.4**. **Figure 7.7** shows the numerically predicted results against the experimental results.

Based on the experimental validations, the numerical model accurately captures the overall response of the experimental test, including ultimate capacity, initial stiffness, ultimate displacement, and residual displacement.

Table 7.4. SMA and FRP RC Column tested by Billah and Alam (2012)

Material	Property	
Concrete	f_c'(MPa)	38.3
	Corresponding strain	0.0029
	Elastic modulus (GPa)	23.1
	Tensile strength (MPa)	3.33
SE-SMA	Modulus of elasticity (GPa)	54.2
	Austenite-to-martensite starting stress (MPa)	414
	Austenite-to-martensite finishing stress (MPa)	530
	Superelastic plateau strain length (MPa)	6.2
FRP	Modulus of Elasticity (GPa)	52.2
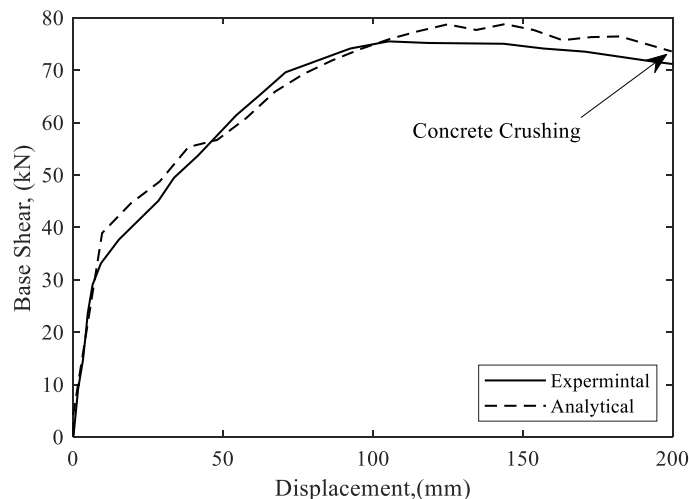
Figure 7.7. Validation using Experimental Results by Billah and Alam (2012)

7.5 LATERAL FORCE-DISPLACEMENT RESPONSE

A nonlinear static analysis (pushover analysis) is carried out to determine the influence of the design parameters on wall capacity curves. **Table 7.5** lists the parametric study cases. The studied variables are axial load ratio, boundary length, boundary reinforcement ratio, and web reinforcement ratio.

Table 7.5. Range of parameters selected in the parametric study

Case	Axial load ratio (%)	Boundary length (mm)	Case	Boundary reinforcement ratio (%)	Web reinforcement ratio (%)
1	0	500	6	1.28	0.25
2	10	500	7	1.28	0.40
3	15	500	8	1.28	1.00
4	10	600	9	1.50	0.25
5	10	700	10	2.00	0.25

7.5.1 Effect of axial load ratio (Case 1, 2, and 3)

Axial load ratios ($\frac{P}{A_g f'_c}$) in practical RC walls have a range of 0 to 0.15 for low-to-moderate height buildings (Priestley et al. 2007). **Figure 7.8** shows the effect of the applied axial load on the load-displacement curves for the studied walls. As shown in the figure, increasing the axial load ratio, up to 15%, increases the load capacity of the considered walls. All considered walls exhibit a ductile behaviour at zero axial load ratio. An increase in the axial load ratio has also reduced the initial stiffness of the RC walls slightly.
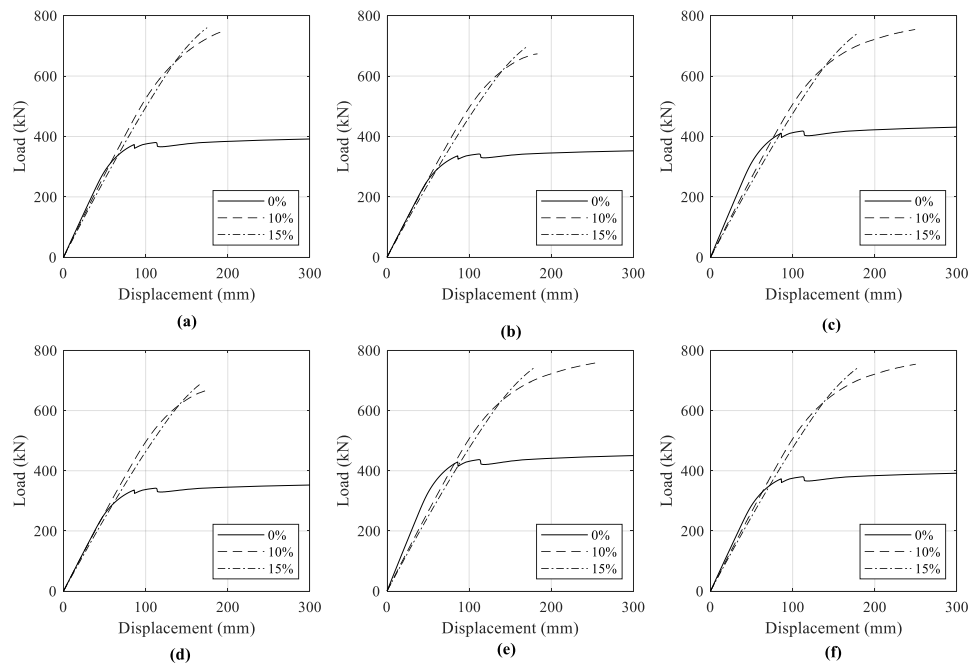
Figure 7.8. Effect of axial load ratio: (a) W1; (b) W2; (c) W3; (d) W4; (e) W5; (f) W6

7.5.2 Effect of boundary element length (Case 2, 4, and 5)

The effect of increasing the wall boundary length on the load-displacement behaviour for all considered walls when subjected to 10% axial load is shown in **Figure 7.9**. Increasing the boundary length of the reference wall W1 from 500 mm to 700 mm increases the load capacity and the lateral displacement slightly. The load capacity and lateral displacement of W2 and W4 walls, shown in **Figures 7.9(b)** and **7.9(d)**, increased by 3% and 20%, respectively, while the maximum displacement for both walls increased. Significant improvement in load capacity of W3, W5, and W6 walls is observed by increasing the boundary length, as shown in **Figures 7.9(c)**, **7.9(e)**, and **7.9(f)**. The failure displacement results reveal a significant difference between the steel wall (W1) and SMA-FRP walls (W3, W5, and W6) as the failure displacement of W3, W5, and W6 increased by about 68% on average relative to W1, when wall boundaries increased from 500 mm to 700 mm.
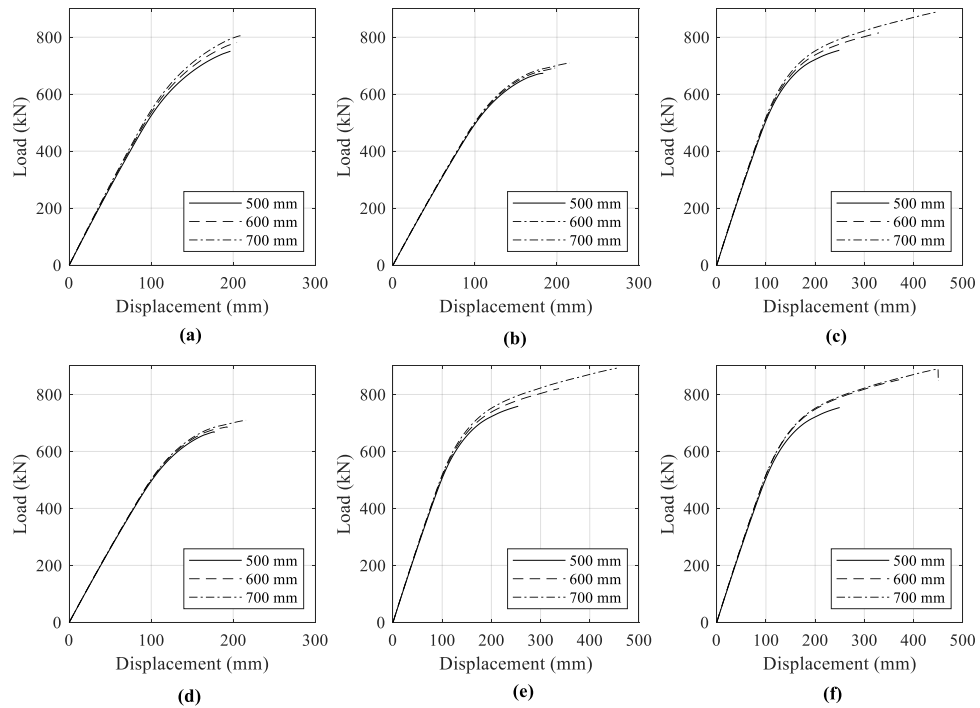
Figure 7.9. Effect of boundary element length: (a) W1; (b) W2; (c) W3; (d) W4; (e) W5; (f) W6

7.5.3 Effect of boundary element reinforcement ratio (Case 6, 9, and 10)

Figures 7.10 shows the effect of the longitudinal reinforcement ratios on the load-displacement performance. All walls are subjected to a constant axial load ratio of 10%. Increasing the boundary reinforcement ratio of the reference wall W1 from 1.28% to 2.0% increases the load capacity by approximately 11%, and the lateral displacement is slightly improved for this reinforcement ratio. Increasing the longitudinal reinforcement in the boundary region of walls W2, W3, W4, W5, and W6 does not affect the displacement capacity due to the elastic behaviour of SE-SMA bars at the boundaries of the walls, whereas increasing the reinforcement ratio improves load and displacement capacity by about 6% on average for all walls.
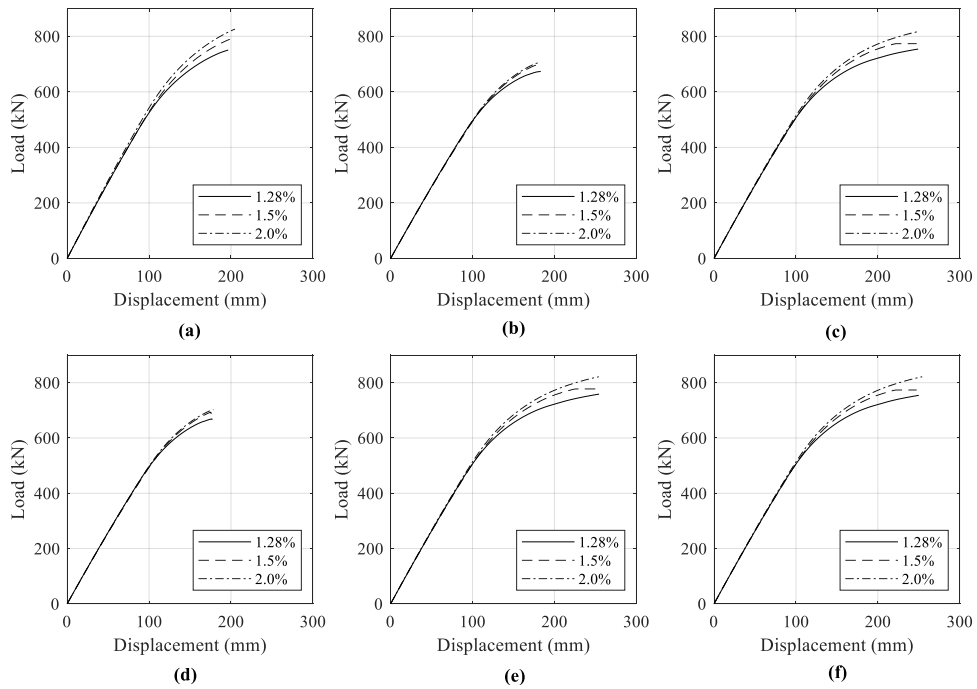
Figure 7.10. Effect of boundary reinforcement ratio: (a) W1; (b) W2; (c) W3; (d) W4; (e) W5; (f) W6

7.5.4 Effect of web reinforcement ratio (Case 6, 7, and 8)

Figure 7.11 shows the effect of web reinforcement on the load-displacement curves for the studied shear walls. Increasing the web reinforcement from 0.25% to 0.4% for wall W1 increases the load capacity by 8%. The effect of increasing the web reinforcement ratio on load and displacement capacity, however, is negligible beyond 0.4%. In contrast, W2, W3, W4, W5, and W6 walls showed an increase in load-capacity by about 4% on average, accompanied by a decrease in the displacement capacity by approximately 5%.
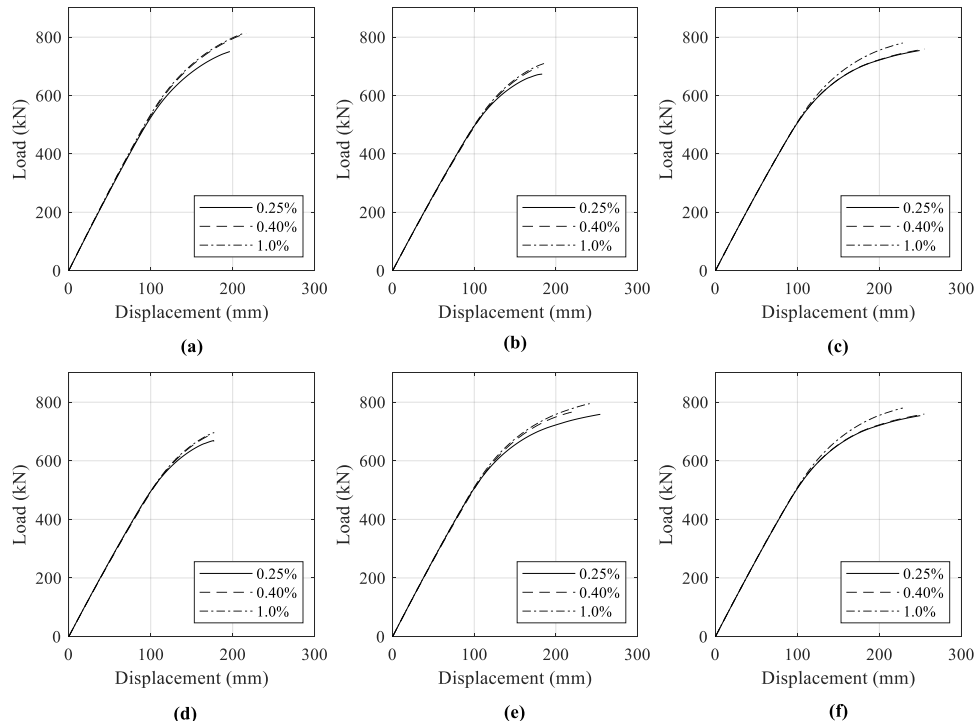
Figure 7.11. Effect of web reinforcement ratio: (a) W1; (b) W2; (c) W3; (d) W4; (e) W5; (f) W6

7.6 DYNAMIC ANALYSIS

Eigenvalue analysis is performed for each modeled wall. The minimum (T_{1S}) and maximum (T_1) fundamental periods were 1.69 and 1.71, respectively. Seven ground motions were selected to represent the ground motion hazard spectra of Vancouver, BC, for 2% and 10% probabilities of exceedance in 50 years. Although the NBCC 2015 requires design considering 2% in 50, this chapter also examines the effect of seismic ground motions with a moderate probability of exceedance. The ground motions are selected to represent a range between 0.2 T_{1S} and 1.5 T_1. The ground motions are selected and scaled to match the hazard spectra using the Mean Square Error (MSE), as shown in **Figure 7.12**.

Seven ground motions were selected to represent the ground motion hazard spectra of Vancouver, BC, for 2% and 10% probabilities of exceedance in 50 years. Although the NBCC 2015 requires design considering 2% in 50, this chapter also examines the effect of seismic ground motions with a moderate probability of exceedance. The ground motions

are selected to represent a range between 0.2 T_{1S} and 1.5 T_1. The ground motions are selected and scaled to match the hazard spectra using the Mean Square Error (MSE), as shown in **Figure 7.12**.

(a)   (b)
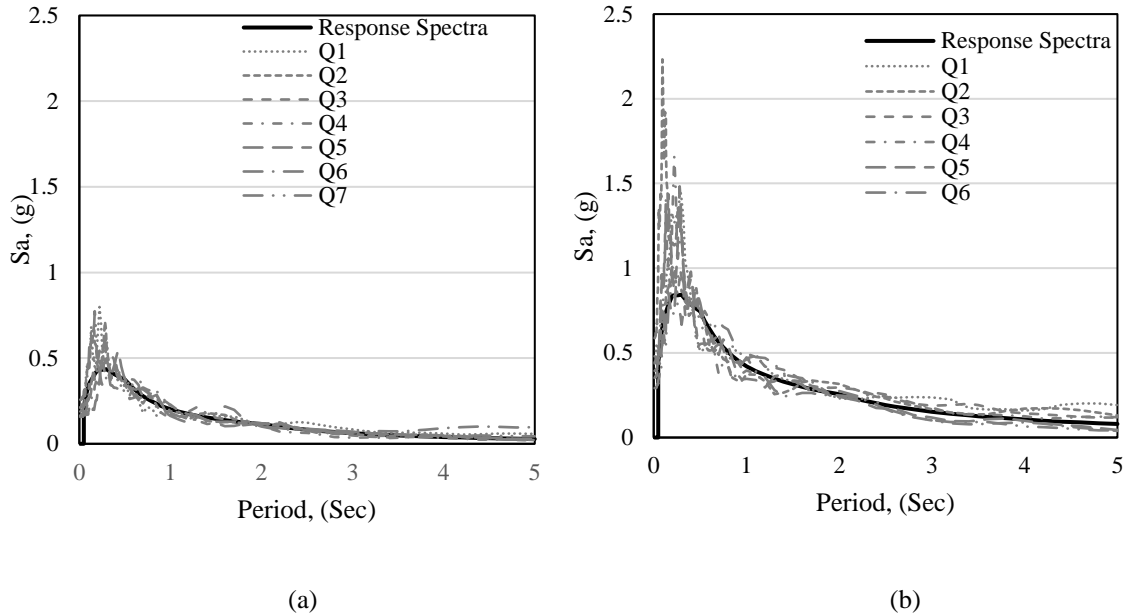
Figure 7.12. Acceleration spectra for individual motions with target spectra: (a) 10% in 50; (b) 2% in 50

Nonlinear time history analysis is carried out to evaluate the response of the walls when subjected to 10/50- and 2/50-year seismic events. Investigated response parameters are lateral displacement, inter-story drift, residual drift, floor acceleration, shear forces, bending moments, and internal concrete/reinforcement strains. The mean and 84th percentile of the lateral displacement response for the 10/50 and 2/50-years are shown in Figures 7.13 and 7.14, respectively. Table 7.6 summarizes the Maximum Inter-story Drift (MID) and Maximum Residual Inter-Drift (MRID) values of all considered walls at different seismic intensity levels.

7.6.1 Lateral displacement

Figure 7.13 shows that the difference in the lateral displacement between W2, W4, and W6 from the reference wall W1 is negligible for the frequent 10/50-years earthquake.

Walls W3 and W5 have an average reduction of 11% in the lateral displacement, relative to W1.

For the 2/50-year seismic event, the mean and the 84th percentile lateral displacements of W2 to W6 walls are higher than W1 by an average of 18% and 31%, respectively. The performance of W3 and W5 in the 2/50-year seismic event seems very good as their mean and 84th percentile lateral displacements remain small 10% and 12% higher than W1 for W3 and 20% and 24% higher than W1 for W5.

At 10/50 hazard level, the mean and 84th percentile inter-story displacement response of all walls is similar with average values of 0.66% and 0.95%, respectively. Under the 2/50 frequency level, the mean and 84th percentile inter-story displacements of W3 and W5 develop a large inter-story drift ratio as compared to W1, W2 and W4, while the mean and the 84th percentile inter-story drift ratios of the W2 and W4 walls are 30% and 38% on average higher than W1.

7.6.2 Residual displacement

Residual displacements are observed for the 10/50 and 2/50 frequent events and reported in **Figures 7.15** and **7.16**, respectively. For the high-intensity level, the residual displacement response of W5 is clearly favourable as compared to other walls as the mean and 84th percentile residual displacements are reduced by about 80% and 74% as compared to W1.

The mean and the 84th percentile residual drift for all considered walls are less than 0.3% under the 10/50 level ground motions. These residual drifts are considered to be within acceptable limits and require a minor repair. For the 2/50-year seismic events, the mean residual drift demands in (W2 and W4) and (W3, W5, and W6) walls are reduced by about 30% and 57% relative to W1, which is higher than the residual displacement acceptable range. Considering the 84th percentile seismic risk, the residual drift was minimum for W4, reaching a value that corresponds to the acceptable repair level.
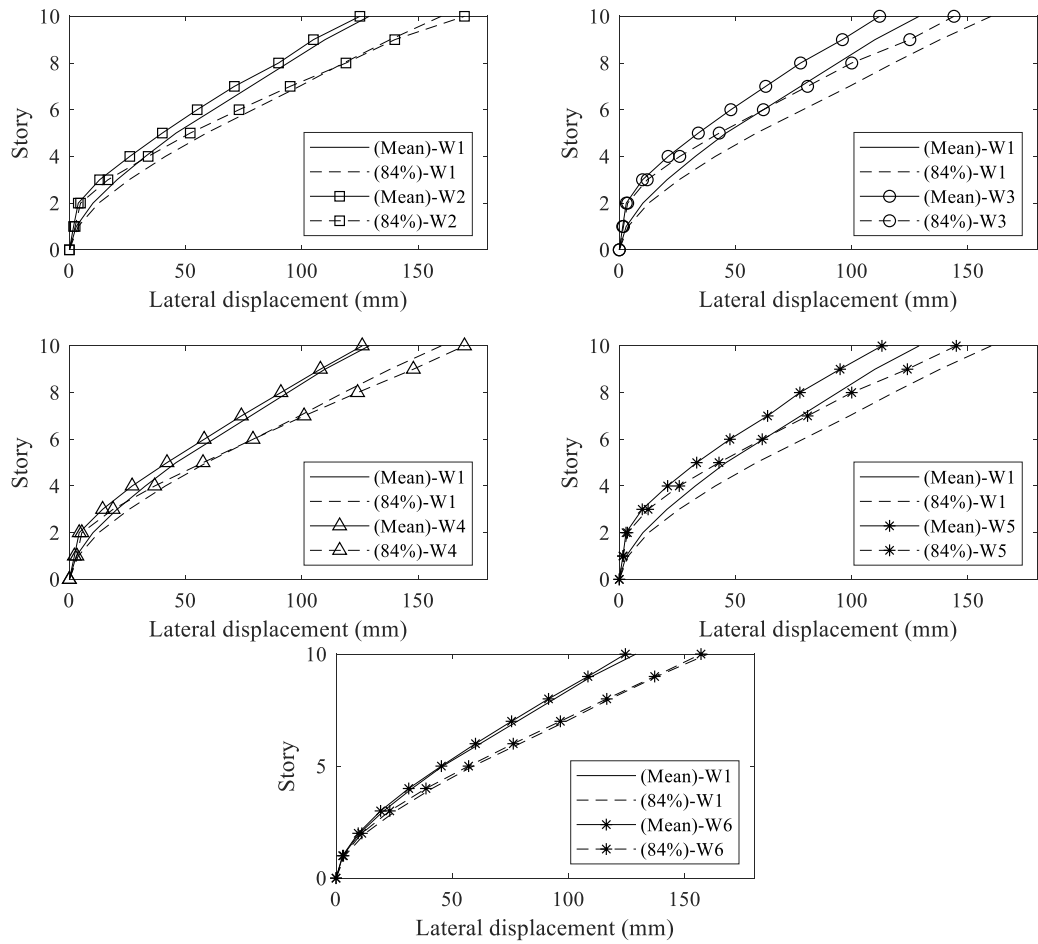
Figure 7.13. Lateral displacement at 10/50
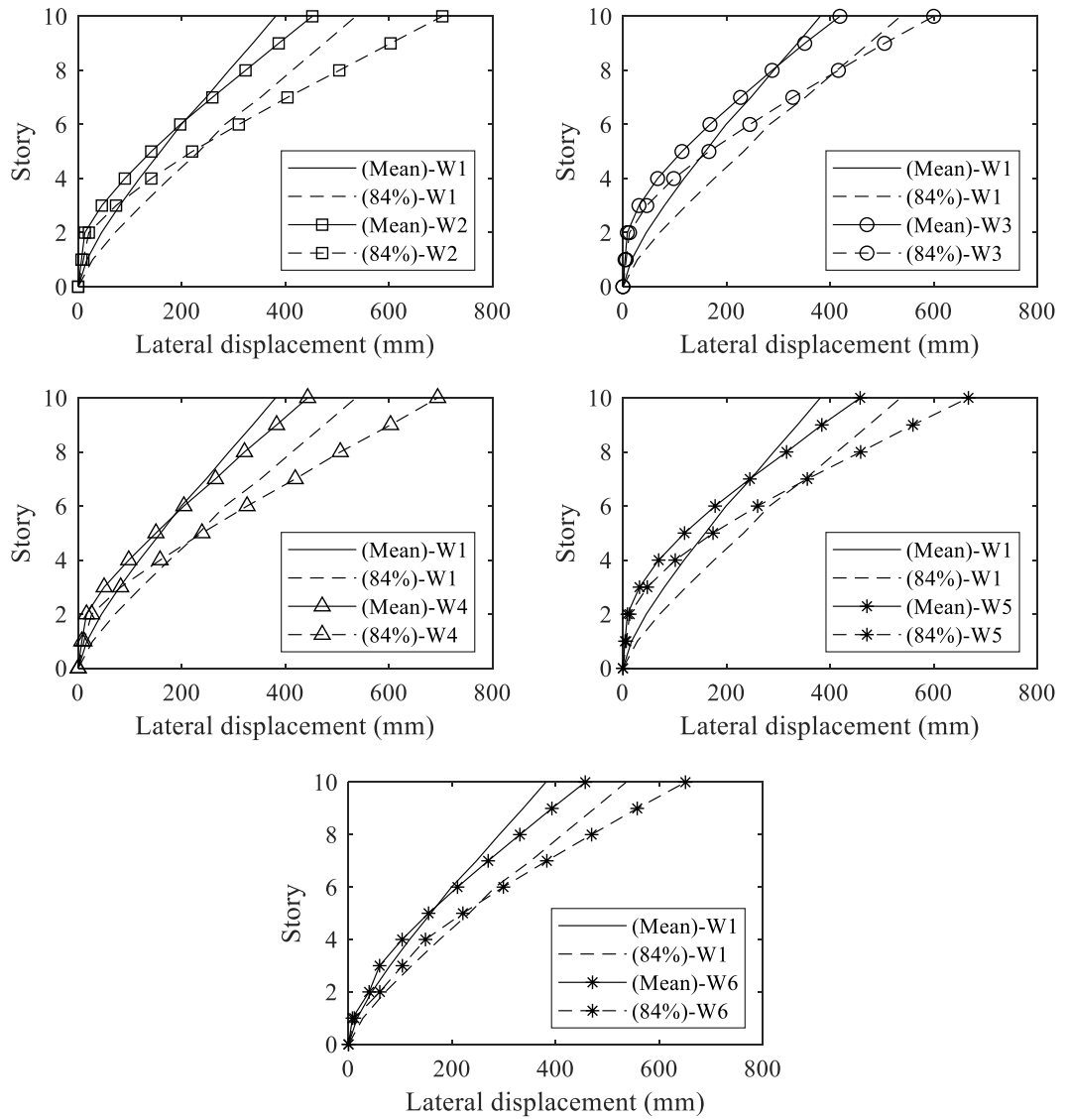
Figure 7.14. Lateral displacement at 2/50
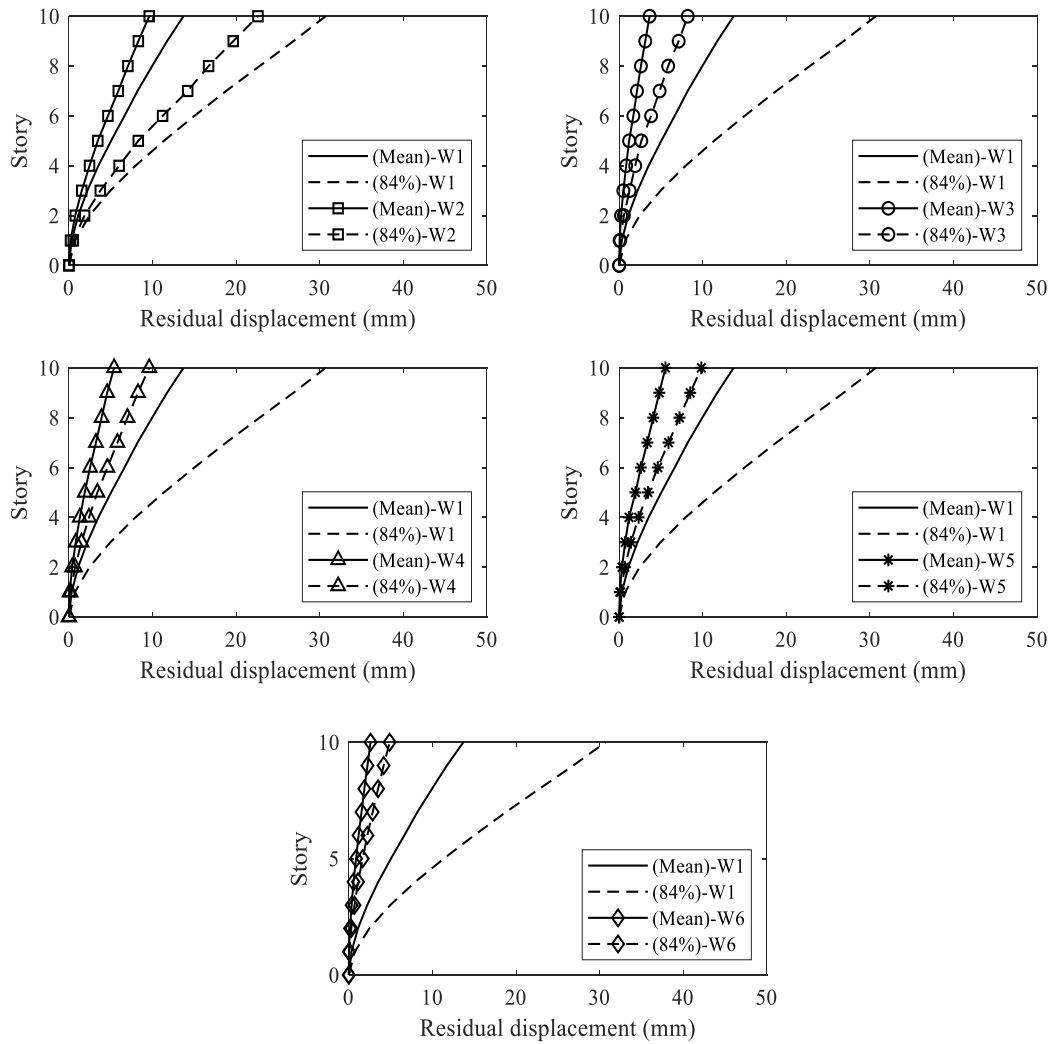
Figure 7.15. Residual displacement at 10/50

155
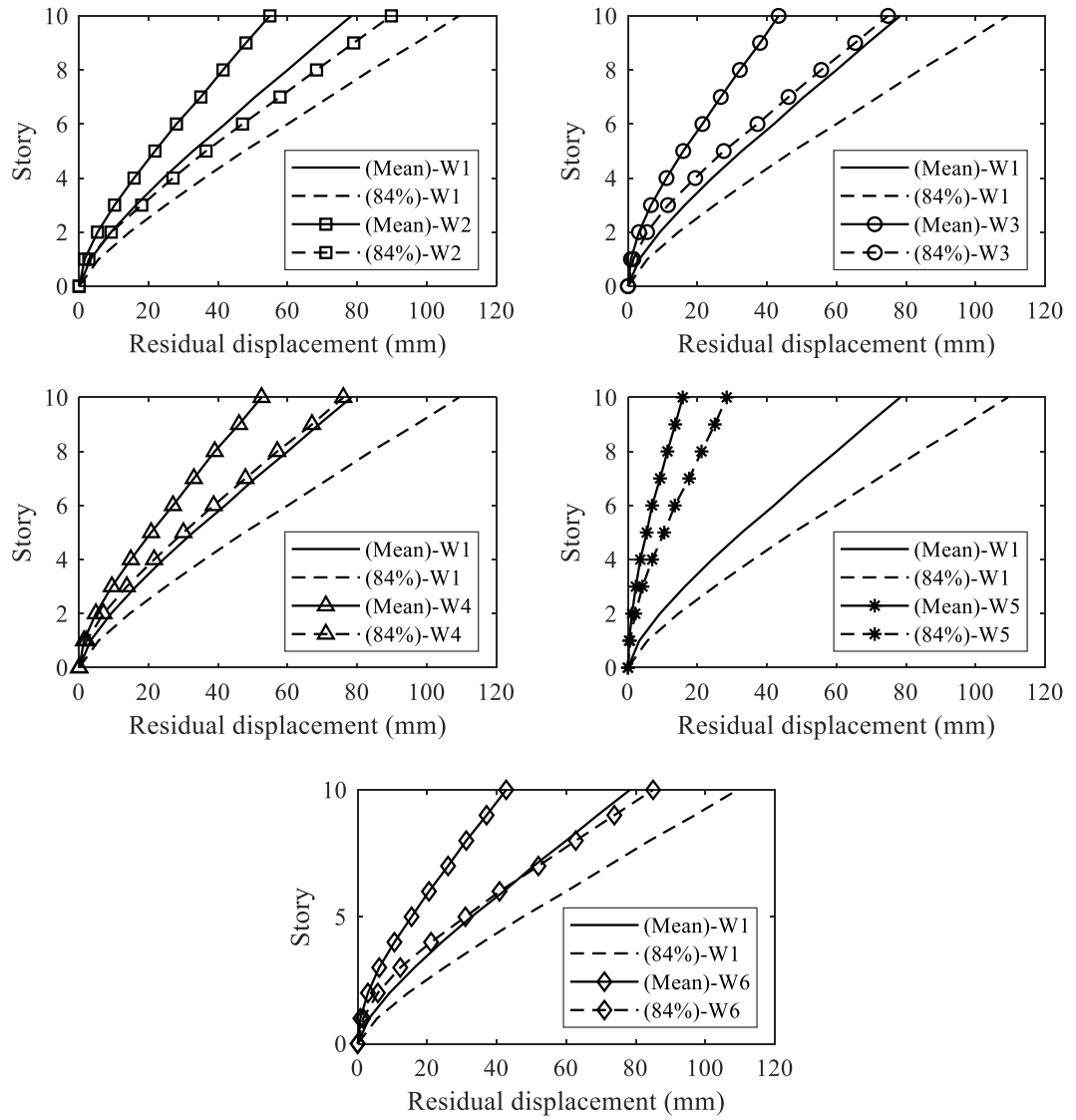
Figure 7.16. Residual displacement at 2/50

Table 7.6. MID and MRID for the considered walls

Wall	Seismic Risk	ID (%)		RID (%)	
		MEAN	84%	MEAN	84%
W1	10/50	0.67	0.80	0.07	0.14
	2/50	1.70	2.48	0.33	0.43
W2	10/50	0.70	1.04	0.04	0.11
	2/50	2.29	3.59	0.24	0.38
W3	10/50	0.63	0.87	0.02	0.04
	2/50	2.40	3.40	0.20	0.34
W4	10/50	0.64	0.84	0.03	0.05
	2/50	2.55	3.27	0.23	0.29
W5	10/50	0.64	0.85	0.03	0.05
	2/50	2.45	3.36	0.08	0.13
W6	10/50	0.57	0.71	0.013	0.03
	2/50	2.29	3.33	0.20	0.40

7.6.3 Floor acceleration

Floor acceleration can be used to represent the damage level to the non-structural components. The allowable floor acceleration (a_f) is given by Eq 7.6 (ASCE, 2016).

$$a_f = 0.4S_{DS}(1 + 2z/h_{total}) \tag{7.6}$$

where S_{DS} is the design spectral response acceleration parameter at short periods; z is the height of the component measured from the base, and h is the roof height of the structure measured from the base.

The peak floor acceleration is amplified at the 2/50-years hazard level by a factor of 1.9 on average, as shown in **Figure 7.17**. The damage to non-structural components for all considered walls is acceptable as floor accelerations are less than the allowable at both hazard levels.

(a)   (b)
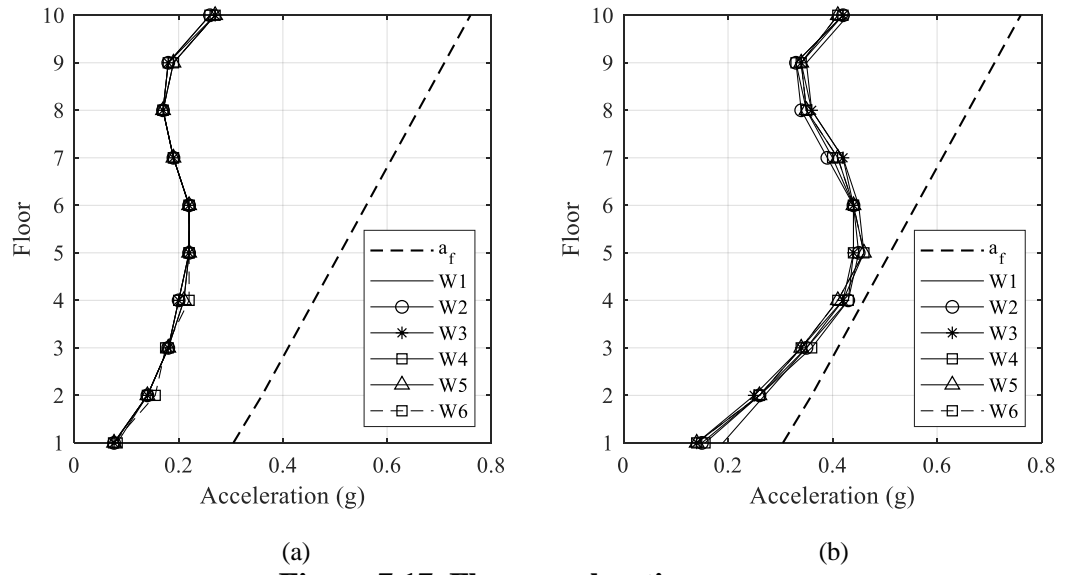
Figure 7.17. Floor acceleration

7.6.4 Internal forces and moments

Figures 7.18 shows the shear forces and bending moment envelopes at each story for the 10/50-year intensity motions. The mean story shear for W1 is about 10% higher than the computed mean shear forces for the other walls. The reduction of story shear forces results in a decrease in bending moments reaching 17%. **Figure 7.19** shows the internal forces and bending moments for the 2/50-year seismic event. Shear forces and bending moments for walls W2 and W4 are lower than W1 by about 11% and 24%, respectively. While, the difference in the story shear forces of W3, W5, and W6 is negligible, the bending moment values are amplified by a factor of 1.35 on average.

(a)

(b)
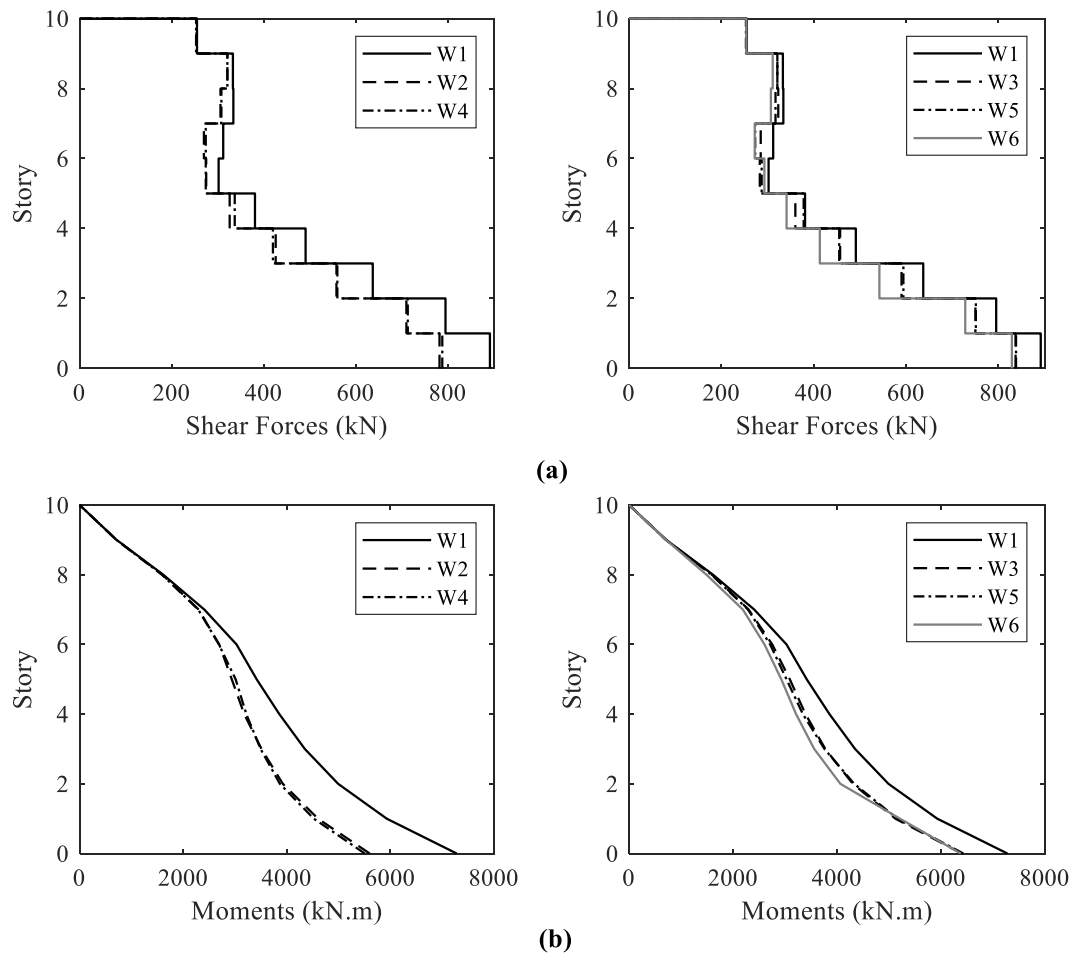
Figure 7.18. Shear forces and bending moments at 10/50

(a)

(b)
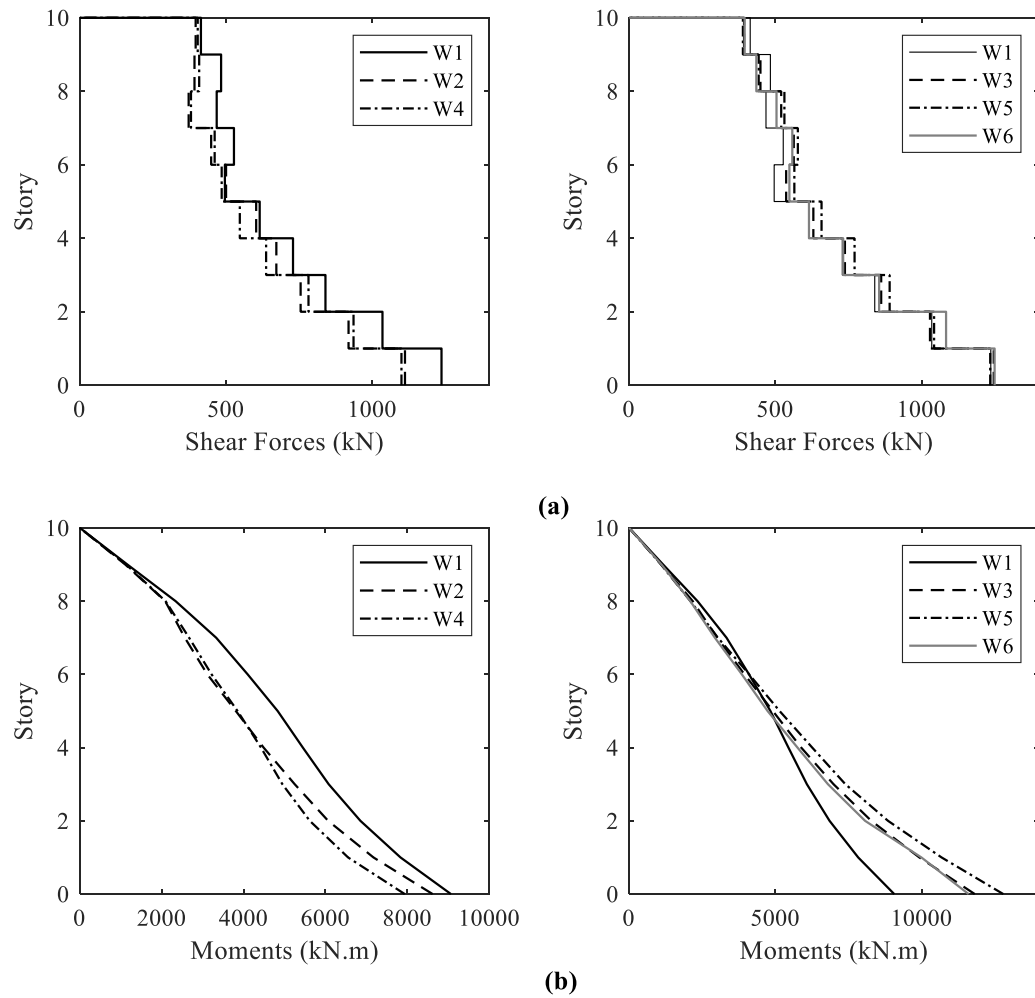
Figure 7.19. Shear forces and bending moments at 2/50

7.6.5 Damage Level

The damage level of RC walls can be related to the strains in the concrete and reinforcement. **Figures 7.20** and **7.21** show the peak steel and concrete maximum strains during each ground motion (EQ). For 10/50-year seismic events, the outermost steel reinforcement bars reach a peak strain value of 0.005, which is higher than the serviceability limit. The SMA-FRP reinforcement strains in W3, W5, and W6 walls are below the serviceability state level. The concrete strains are also below the serviceability limit for all walls. For the 2/50-year events, the maximum tensile strain for W1 reaches a value of 0.055, which is higher than the damage level.

The strain history of the reinforcement considering the second ground motion at 2/50-year shaking level is plotted in **Figure 7.22**. Although all considered walls are below the damage level, three peak strain values are observed with strains reaching 0.02 and 0.03 for walls W2 and W4, respectively. The strain histories of W3 and W5 exhibit a constant pulse distribution with a maximum strain of about 0.007. Bars in W6 reaches a maximum strain of 0.01.
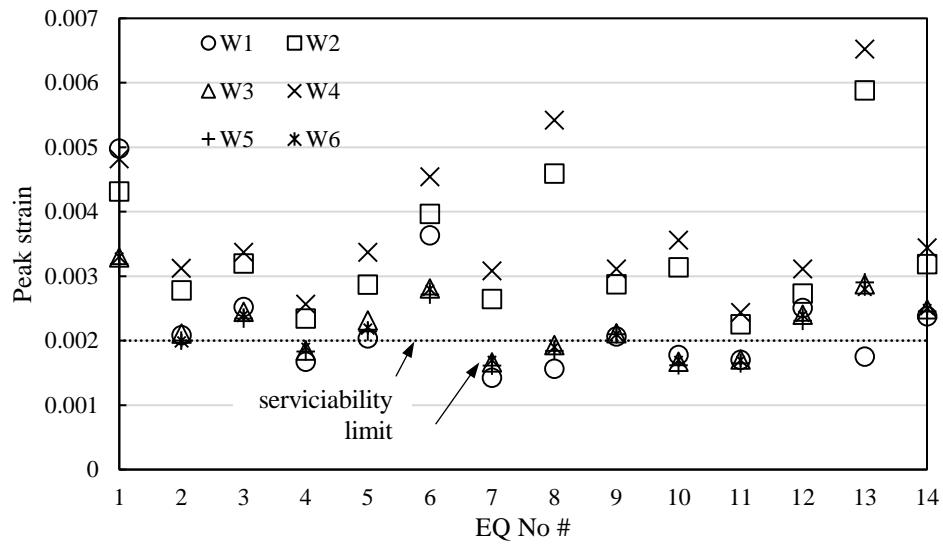
(a)
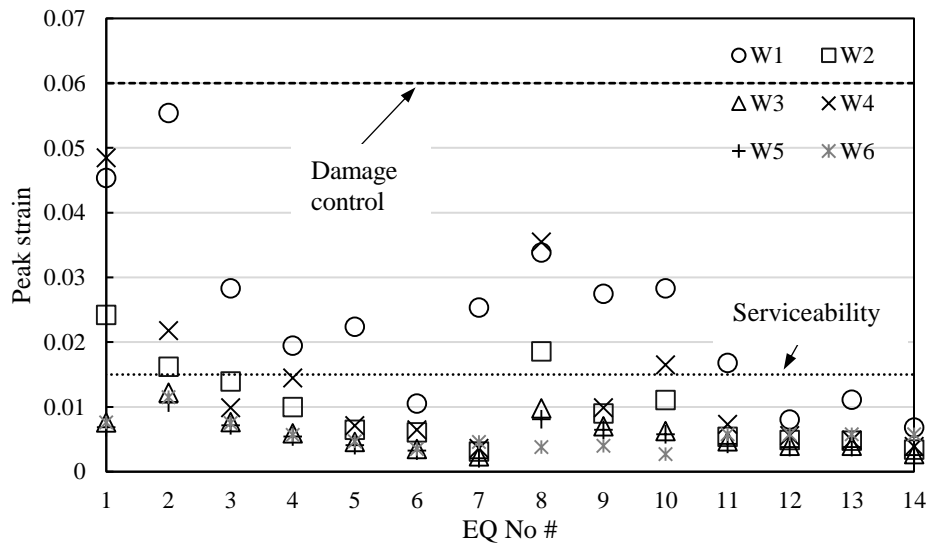
(b)

Figure 7.20. Strains outermost reinforcement bars in boundary elements: (a) 10/50; (b) 2/50

(a)

(b)
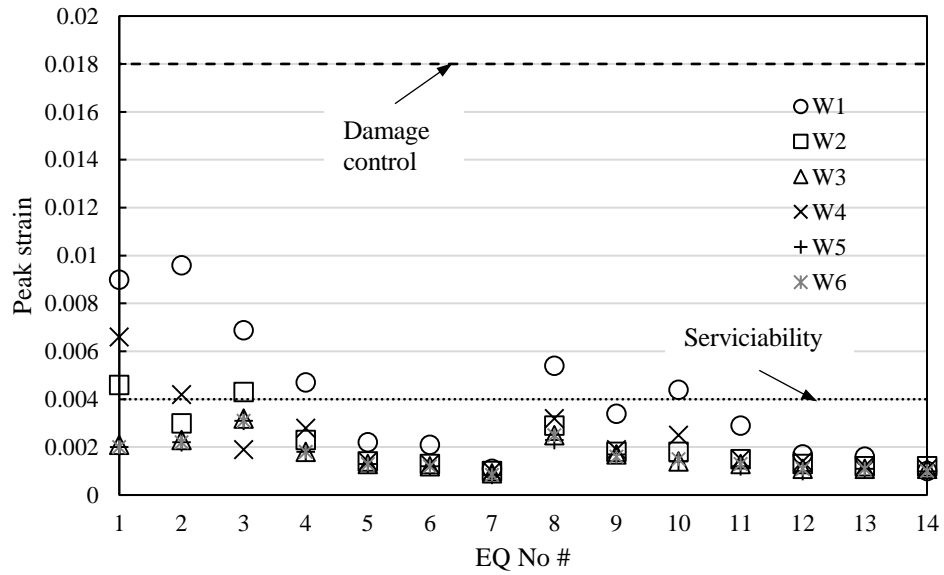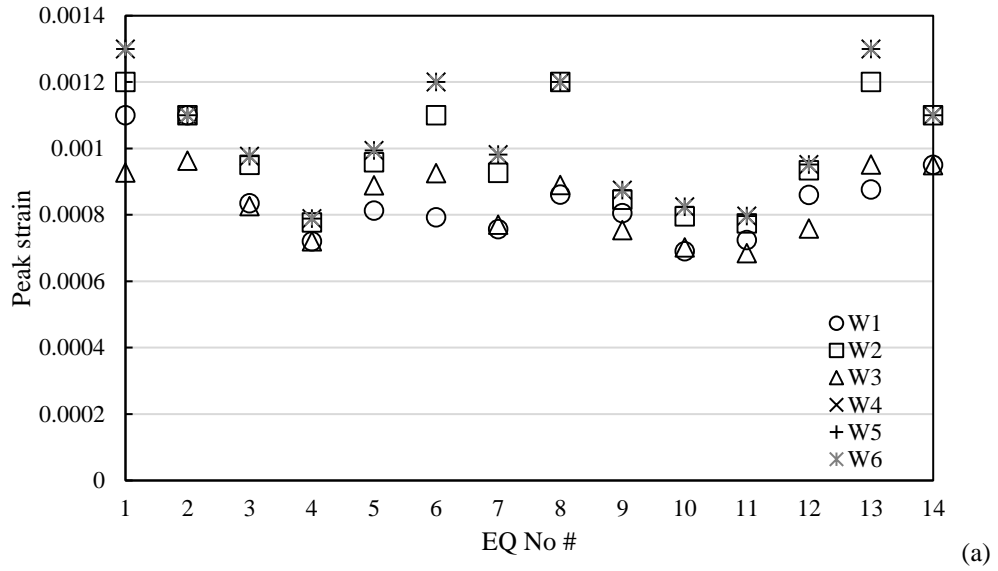
Figure 7.21. Strains outermost confined concrete in boundary elements: (a) 10/50; (b) 2/50
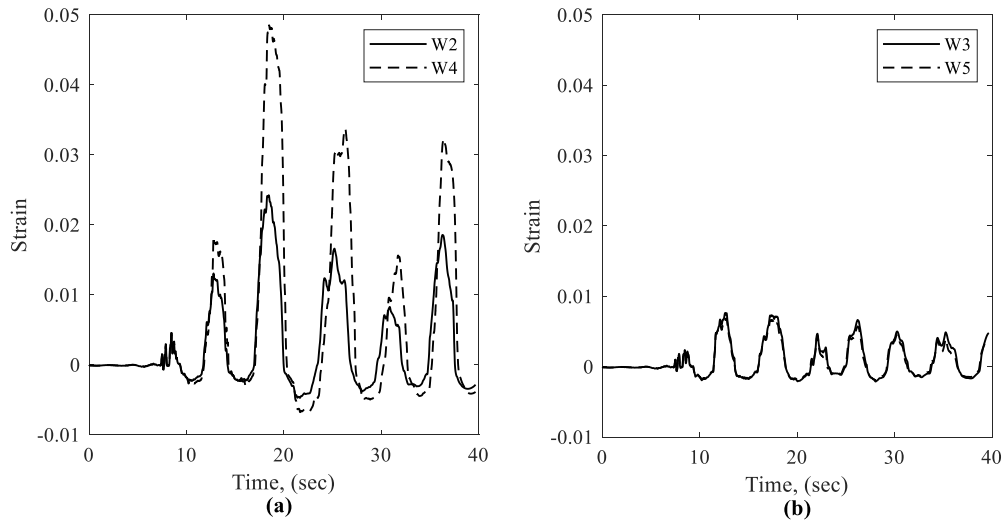
Figure 7.22. Strains history of reinforcement bar caused by second motion: (a); SE-SMA; (b) SMA-FRP

Figure 7.23 shows the average reinforcement and concrete strains of the lower corner boundary region. As shown in the figure, wall W1 is subjected to lower strains at 10/50-year events. For the 2/50 events, the average tensile reinforcement strain is reduced from 0.0226 (wall W1) to 0.0053 (for wall W3, W5, and W6). The concrete strains in walls W3, W5, and W6 are reduced by 60% as compared to wall W1.
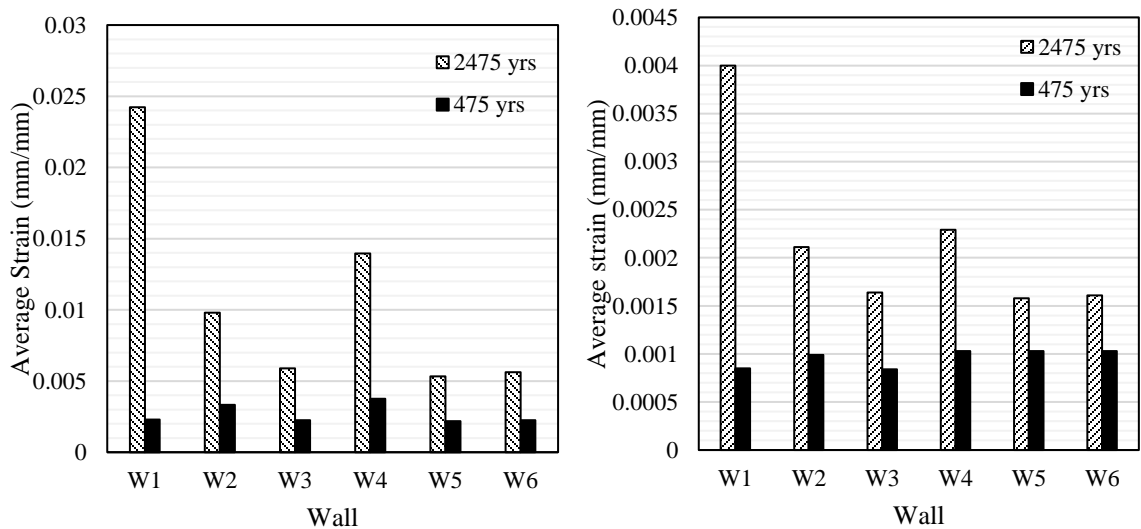
Figure 7.23. Average strain: (a) reinforcement; (b) concrete

Figure 7.24 shows the envelope steel strain distribution along the height of all walls. At the 10/50 shaking level, the average tensile strain for W1 is 0.0023. The average tensile strains for W2 and W4 have peak values of 0.0033 and 0.0037, respectively. An almost negligible difference exists in the mean computed strains of W3, W5, and W6 walls at the two hazard levels.
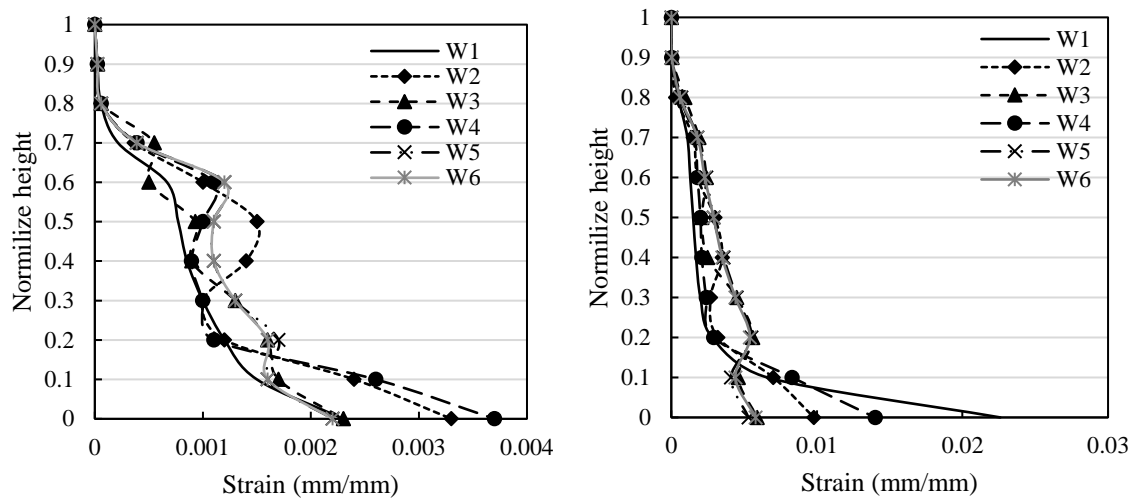
(a)   (b)
Figure 7.24. Average strain along the height: (a) 10/50; (b) 2/50

7.7 CONCLUSIONS

This research study investigates the behaviour of the 10-story RC building with a lateral force resisting system of concrete shear walls reinforced with different composite materials. All walls are subjected to seven sets of ground motions that represent moderate and high intensity shaking levels for a site located in Vancouver, BC. All the walls are sized and reinforced similar to the reference wall W1. Based on the current study, it can be concluded that:

1- Using hybrid SE-SMA-FRP and FRP bars reinforcement (W3, W5, and W6) significantly improves seismic displacement capacity. However, the load capacity does not change considerably. The seismic performance can be further enhanced by modifying the boundary zone reinforcement and length. The effect of the web reinforcement parameter is negligible.

2- Using hybrid SE-SMA-FRP provides high seismic resiliency.

164

3- The developed mean shear forces and bending moments in the studied walls are less than the calculated values of the conventional steel reinforced wall (W1) in the case of the moderate intensity level. For high-intensity shaking levels, the mean bending moment computed at the base of W3, W5, and W6 walls, i.e. utilize SE-SMA-FRP and FRP hybrid reinforcement is 30% higher than the conventional steel shear wall (W1). This effect should be considered in the design guidelines for the SE-SMA-FRP reinforced walls.

4- The strain results from both reinforcements and concrete imply a significant margin of safety against damage for SMA-FRP walls. In other words, the hybrid SE-SMA-FRP reinforcements increase the load and displacement capacity as compared with steel and SE-SMA RC walls.

7.8 REFERENCES

Abdulridha, A. (2012). Performance of superelastic shape memory alloy reinforced concrete elements subjected to monotonic and cyclic loading. Ottawa: Ph.D. Thesis: University of Ottawa.

Abraik, E., & Youssef, M. (2015). Cyclic performance of shape memory alloy reinforced concrete walls. Response of structures under extreme loading (pp. 326-333). Lansing, MI: The fifth international workshop on performance, protection, and strength of structures under extreme loading.

Abraik, E., & Youssef, M. (2016). Performance assessment of three-story shape memory alloy reinforced concrete walls. CSCE 5th International Structural Specialty Conference, 852. London, ON, Canada.

Abraik, E., & Youssef, M. (2018). Seismic fragility assessment of superelastic shape memory alloy reinforced concrete shear walls. Journal of building engineering, 19, 142-153.

Araki, Y., Shrestha, K., Maekawa, N., Koetaka, Y., Omori, T., & Kainuma, R. (2016). Shaking table tests of steel frame with superelastic Cu-Al-Mn SMA tension braces. Earthq Eng Struct D, 45(2), 297–314.

ASCE. (2016). Minimum design loads for buildings and other structures. ASCE/SEI 7-10: Reston, VA.

ASCE/SEI 41-06 Supplement #1, American Society of Civil Engineers. 2006. (n.d.). Reston, VA: Seismic rehabilitation of existing buildings.

Bank, L. C., (2006). Composites for Construction: Structural Design with FRP Materials. Hoboken, New Jersey: John Wiley & Sons, Inc.

Billah, A. M., & Alam, M.. S, (2012). Seismic performance of concrete columns reinforced with hybrid shape memory alloy (SMA) and fiber reinforced polymer (FRP) bars. Construction and Building Materials, 28(1), 730-742.

CSA. A23.3-14. (2014). Design of Concrete Structures. Canadian Standards Association. Mississauga, ON, Canada.El-Salakawy, E., Benmokrane, B., El-Ragaby, A., & Nadeau, D. (2005). Field investigation on the first bridge deck slab reinforced with glass FRP bars constructed in Canada. J. Composites for Construction, 9(6), 470-479.

FEMA 273. (1996). NEHRP guidelines for the seismic rehabilitation of buildings. FederalEmergency Management Agency.

Henry, R., Sritharan, S., & Ingham, J., (2016). Residual drift analyses of realistic self-centering concrete wall systems. Eng Struct, 10(2), 409-428.

Hurlebaus, S., & Gaul, L. (2006). Smart structure dynamics. Mechanical system and signal. 20(2), 255-281.

Kassem, C., Farghaly, A. S., & Benmokrane, B. (2011). Evaluation of flexural behavior and serviceability performance of concrete beams reinforced with FRP Bars. J. Composites for Construction, 15(5), 682-695.

Kowalsky, M. J. (2000). Deformation limit states for circular reinforced concrete bridge columns. J Struct Eng, 126(8), 869-878.

Mander, J. B., Priestley, M. J & Park, R. (1988). Theoretical stress-strain model for confined concrete. Journal of Structural Engineering. ASCE, 114(4), 1804-1826.

McCormick, J., Tyber, J., DesRoches, R., Gall, K., & Maier, H. (2007). Structural engineering with NiTi. II: mechanical behavior and scaling. J Eng Mech, 133(9), 1019-1029.

McCormick, J., Aburano, H., Ikenaga, M., & Nakashima, M. (2008, October). Permissible residual deformation levels for building structures considering both safety and human elements. In Proceedings of the 14th world conference on earthquake engineering (pp. 12-17).

Menegotto, M., & Pinto, P. (1973). Method of analysis of cyclically loaded RC plane frames including changes in geometry and non-elastic behavior of elements under normal force and bending. Preliminary Report ABSE, vol 13.

Meshaly, M. E., Youssef, M. A., & Abou Elfath, H. M. (2014). Use of SMA bars to enhance the seismic performance of SMA braced RC frames. Earthquakes and Structures, 6(3), 267-280.

Mohamed, N., Farghaly, A., Benmokrane, B., & Neale, K. (2014). Experimental investigation of concrete shear walls reinforced with glass fiber-reinforced bars under lateral cyclic loading. Journal of Composites for Construction, 18(3), ISSN 1090-0268/A4014001(11).

OpenSees. (2018). Open System for Earthquake Engineering Simulation. Berkeley, CA.

Panagiotou, M., & Restrepo, J. I. (2009). Dual-plastic hinge design concept for reducing higher-mode effects on high-rise cantilever wall buildings. Earthquake Engineering and Structural Dynamics, 38(12), 1359-1380.

Priestley, M. J. N., Calvi, G. M., Kowalsky, M. J. (2007) Displacement-based seismic design of structures. IUSS Press, Pavia.

Qiu, C., & Zhu, S. (2017). Shake table test and numerical study of self-centering steel frame with SMA braces. Earthquake Engineering & Structural Dynamics, 46(1), 117-137.

Saiidi, M. S., Sadrossadat-Zadeh, M., Ayoub, C., & Itani, A. (2007). Pilot study of behavior of concrete beams reinforced with shape memory alloys. J Mater Civil Eng, 19(6), 454-461.

Sultana, P., & Youssef, M. A. (2018). Seismic Performance of Modular Steel-Braced Frames Utilizing Superelastic Shape Memory Alloy Bolts in the Vertical Module Connections. Journal of Earthquake Engineering, 1-25.

Sharbatdar , M. K., & Saatcioglu, M. (2009). Seismic Design of FRP Reinforced Concrete Structures. Asian Journal of Applied Sciences, 2(3), 211-222.

Tazarv, M., & Saiidi, M. S. (2013). Analytical studies of the seismic performance of a full-scale SMA-reinforced bridge column. International Journal of Bridge Engineering, 1(1), 37-50.

Zhao, J., & Sritharan, S. (2007). Modeling of strain penetration effects in fiber-based analysis of reinforced concrete structures. ACI Structural Journal, 104(2), pp. 133-141.

The National Building Code of Canada. (2015). Ottawa: Canadian Commission on Building and Fire Code, National Research Council.

Tobbi, H., Farghaly, A. S., & Benmokrane, B. (2012). Concrete columns reinforced longitudinally and transversally with glass fiber-reinforced polymer bars. ACI Struct. J, 109(4), 551-558.

Yamakawa, T., & Fujisaki, T. (1995, August). A study on elasto-plastic behavior of structural walls reinforced by CFRP grids. In Non-Metallic (FRP) Reinforcement for Concrete Structures: Proceedings of the Second International RILEM Symposium (Vol. 29, p. 306). CRC Press.

Youssef, M. A., Alam, M. S., & Nehdi, M. (2008). Experimental investigation on the seismic behaviour of beam-column joints reinforced with superelastic shape memory alloys. Journal of Earthquake Engineering, 12(7), 1205-1222.

Zafar, A., & Andrawes, B. (2012). Incremental dynamic analysis of concrete moment resisting frames reinforced with shape memory composite bars. Journal of Smart Materials & Structures, 21(2), 025013.

Zafar, A., & Andrawes, B. (2013). Experimental flexural behavior of SMA-FRP reinforced concrete beam. Frontiers of Structural and Civil Engineering, 7(4), 341-355.

Zafar, A., & Andrawes, B. (2014). Fabrication and cyclic behavior of highly ductile superelastic shape memory composites. Journal of Materials in Civil Engineering, 26 (4), 622-632.

Zafar, A., & Andrawes, B. (2015). Seismic behavior of SMA–FRP reinforced concrete frames under sequential seismic hazard. Engineering Structures, 98, 163-173.

CHAPTER 8

CONCLUSIONS AND RECOMMENDATIONS

8.1 SUMMARY

Superelastic shape memory alloy (SE-SMA) bars can recover their inelastic deformations upon unloading. Their utilization in concrete structure can significantly reduce seismic residual deformations, which are the main factor to judge about the repairability of a seismically damaged structure. However, the high cost of SE-SMA is the main barrier for their wide use in the construction industry. On the negative side, the lower energy dissipation and lower modulus of elasticity of SE-SMA may reduce the global lateral stiffness resulting in excessive inter-story drifts during seismic excitation. This thesis investigates the possibility of using SMA economically in different types of RC walls to improve the seismic performance. The following subsections briefly summarize the five major chapters and highlight the achieved contributions.

8.1.1 Seismic fragility assessment of super-elastic shape memory alloy reinforced concrete shear walls

This chapter investigated the effect of utilizing SE-SMA bars in RC shear walls designed according to the current Canadian code. The seismic performance of ten and twenty-story steel and SE-SMA RC walls is compared using a multi-hazard dynamic analysis. The strain profile along the steel RC wall height identified two plastic hinges at the wall base and at its mid-height. The length of each plastic hinge is about 20% of the wall's height. Steel bars within the boundary elements at the plastic hinge locations are replaced with SE-SMA bars. The study led to the following conclusions:

❖ The use of novel SE-SMA bars at both wall hinges improved the seismic performance compared to steel RC walls because they resulted in reducing the shear forces and bending moments at wall mid-height. The residual displacement of the SE-SMA walls was 42%, on average lower than that of steel RC walls.

- ❖ Although the steel RC walls perform well under low probability seismic events, using SE-SMA bars in the plastic hinge regions significantly reduced the permanent lateral deformations compared to those of steel RC walls. However, the efficiency in recovering the inter-story drifts is reduced for low-intensity seismic events and higher walls.

- ❖ The dispersion of fragility results associated with residual drifts is considerably larger than the dispersion of fragility results associated with inter-story drifts. Hence, the results of this study suggest that the fragility results relying on inter-story drifts cannot be used to assess damage state in steel versus SE-SMA RC walls.

- ❖ Steel RC walls exhibit higher fragility than SE-SMA RC walls in terms of inter-story drifts and residual drifts. This renders SE-SMA RC walls as less vulnerable to seismic damage. However, a negligible difference exists between steel and SE-SMA walls in term of inter-story drifts.

8.1.2 Ductility and overstrength of shape memory alloy reinforced concrete shear walls

In this chapter, the response modification factor (R) and the Overstrength factor (Ω) for SE-SMA RC walls were evaluated through a numerical study. The SE-SMA bars were only used in the plastic hinge zone. Two potential arrangements were considered: SE-SMA bars only at the wall boundary elements (SMABW) and SE-SMA bars replacing all web and boundary element steel bars (SMAPH). 972 wall cases were analyzed to identify the effect of wall design parameters on the seismic performance and to estimate the seismic design parameters. FEMA P695 (2009) methodology was then performed to assess the proposed seismic design parameters. The proposed values have led to an adequate margin of safety against collapse. Conclusions from this study are summarized below.

- ❖ Analyzing trends of displacement ductility and the overstrength data, shown in Figure 4.14, indicated that the location of SE-SMA bars and wall aspect ratio are the main factors affecting these design factors. Thus, for code-based seismic design, the measuring data of ductility and overstrength are compiled in four groups according to the SE-SMA bar located within the RC wall and the wall aspect ratio.

❖ For walls with $\frac{H_w}{L_w} < 2.0$, the mean proposed response modification factor R is 2.5 and 3.5 for SMAPH and SMABW walls, respectively. For walls with $\frac{H_w}{L_w} > 2.0$, the proposed R value is 3.0 and 4.0 for SMABW and SMABW walls, respectively. The recommended overstrength factor is 2.25 for both SMAPH and SMABW walls.

❖ Increasing wall thickness and web reinforcement has a negligible effect on ductility and overstrength. In contrast, the displacement ductility is slightly increased with increasing the axial load ratio, and this is related to the change of the wall failure mode. Concrete crushing was found to limit the wall ductility, especially for the case of SMAPH walls.

❖ Increasing the reinforcement ratio of the SE-SMA bars at the boundary elements from 0.5% to 1.0% results in a reduction in wall ductility by 17% on average. Increasing the reinforcement ratio of the SE-SMA bars above 1.0% does not affect the SMAPH wall ductility, whereas it reduced the SMABW wall ductility by 29%. This finding suggests that a reinforcement ratio larger than 1.5% for SMAPH walls and 1.0% for SMABW walls should be avoided.

❖ Utilizing SE-SMA bars in the RC walls designed using the proposed values has resulted in a significant displacement recovery and an adequate margin of safety against collapse. However, SMABW walls experienced a lower lateral displacement, which makes them a better design option.

8.1.3 Seismic response of shape memory alloy reinforcement dual system

This chapter investigated the seismic performance of SE-SMA RC dual systems. Two groups of 10-story buildings were designed to represent different stiffness ratios between the RC walls to the ductile moment frames. The considered buildings are assumed to be in the high seismic zone of Canada. Based on the results of this study, the investigation led to the following conclusions:

❖ A single plastic hinge is developed at the base of RC walls at $S_{a(max)}$ hazard level. The length of the formed plastic hinge is 10% of the total wall height.

❖ At seismic hazard $S_{a(design)}$, no notable difference is observed in the strain distributions of the RC beams and RC columns at the locations of SE-SMA.

❖ At seismic hazards of $S_{a(max)}$, the use of SE-SMA bars has reduced the shear forces of the external columns by 18% for BL1SW and BL1SWF. A small reduction in the shear forces is found for BL2SW and BL2SWF.

❖ There is no difference in the wall bending moments between SE-SMA and steel dual-systems at seismic hazard $S_{a(design)}$. For the seismic hazard $S_{a(max)}$, utilizing SE-SMA bars in the dual systems reduces the wall bending moments at the base by about 10% as compared to BL1 and BL2.

❖ A negligible difference is found in the mean inter-story drifts when SE-SMA bars are used.

❖ Time history analysis showed a significant reduction, as expected, in the residual drifts when the SE-SMA bars are utilized.

❖ Utilizing SE-SMA bars in the RC wall and RC frame resulted in a reasonable margin of safety against collapse. However, utilizing SE-SMA in BL1SWF significantly diminishes the collapse probability, which makes them a better design option.

8.1.4 Seismic performance of reinforced concrete core walls equipped with shape memory alloy bars

The seismic performance of steel RC and SE-SMA RC core walls with different mass eccentricity has been investigated in this study. Floor acceleration, residual displacement, diaphragm rotations, residual diaphragm rotations have been evaluated under biaxial and uniaxial seismic ground motions. The observations from this study led to the following conclusions:

❖ The SE-SMA RC core wall showed less damage to non-structural components associated with lower floor accelerations as compared to the steel RC core wall in N-S direction with various mass eccentricity, whereas the effect of SE-SMA bars on mitigation of floor accelerations in E-W direction is effective for mass eccentricities higher than 10%.

❖ The steel RC core wall and the SE-SMA walls exhibited the same lateral displacement envelopes in the E-W direction. Contrary to E-W direction, the SE-SMA bars reduced the

N-S direction lateral displacements by 22%, 15.5%, and 5.8% for 5%, 10%, and 20% mass eccentricity, respectively.

❖ The SE-SMA bars are observed to increase the mean inter-story drift in N-S direction by a factor of 1.3 relative to the steel reinforcement at 5% mass eccentricity, but the rate of increase drops off with increasing the mass eccentricity.

❖ Utilizing the SE-SMA bars in the plastic hinge can substantially reduce the residual displacements but the rate of reducing residual displacements beyond the 5% eccentricity has no clear trend.

❖ The maximum diaphragm rotations for both walls occur at 5% mass eccentricity, which means that 5% mass eccentricity is sufficient to account for the torsional amplification for static or dynamic analysis. However, beyond 5% eccentricity, the SE-SMA bars significantly reduced the torsional irregularity for the RC core wall.

❖ The SE-SMA RC core wall is favourable as compared with the steel RC core wall, as the mean residual rotational displacements for both directions are substantially lower than those of the steel RC core wall.

❖ Floor accelerations and residual displacements results from unidirectional excitations are lower than those results from bidirectional excitations. However, for both cases, the SE-SMA bars attenuated the floor accelerations as compared to steel RC core wall.

❖ Results of bidirectional excitations indicated that the relative benefit of SE-SMA bars on mitigation of permanent displacement rotations somewhat smaller for a lower and high level of eccentricity. However, the influence of the SE-SMA bars on reducing the residual rotations ranged from 6% to 58% as compared to the steel reinforcements.

8.1.5 Seismic performance of hybrid concrete shear walls reinforced with shape memory alloy and fibre

This research study investigated the behaviour of the 10-story RC building with a lateral force resisting system of concrete shear walls reinforced with different composite materials. All walls are subjected to seven sets of ground motions that represent moderate and high intensity shaking levels for a site located in Vancouver, BC. All the walls are sized and reinforced similar to the reference wall W1. Based on the current study, it can be concluded that:

- ❖ Using hybrid SE-SMA-FRP and FRP bars reinforcement (W3, W5, and W6) significantly improves seismic displacement capacity. However, the load capacity does not change considerably. The seismic performance can be further enhanced by modifying the boundary zone reinforcement and length. The effect of the web reinforcement paraeter is negligible.
- ❖ Using hybrid SE-SMA-FRP provides high seismic resiliency.
- ❖ The developed mean shear forces and bending moments in the studied walls are less than the calculated values of the conventional steel reinforced wall (W1) in the case of moderate intensity level. For high-intensity shaking levels, the mean bending moment computed at the base of W3, W5, and W6 walls, i.e. SE-SMA-FRP and FRP hybrid EC walls, is 30% higher than the conventional steel shear wall (W1). This effect should be considered in the design guidelines for the SE-SMA-FRP reinforced walls.
- ❖ The strain results from both reinforcement and concrete imply a significant margin of safety against damage for SE-SMA-FRP walls. In other words, the hybrid SE-SMA-FRP reinforcements increase the load and displacement capacity as compared with steel and SE-SMA RC walls.

8.2 MAJOR RESEARCH CONTRIBUTIONS

The following is an outline of significant research contributions:

- ❖ The developed Fragility curves for SE-SMA RC walls can be implemented in PACT software to allow estimating seismic losses.
- ❖ New overstrength and ductility are proposed to design SE-SMA RC walls. The proposed values provide a tool for the designer to design a sustainable structural system, which can recover the residual deformation after the earthquake events.
- ❖ The Ph.D. thesis is the first to explore using SE-SMA bars to improve the seismic performance of dual systems and core walls.
- ❖ The Ph.D. thesis investigated the use of new innovative materials, including SE-SMA and GFRP. The results showed significant improvement in both capacity and residual deformation with lower inter-story drift.

8.3 LIMITATIONS

❖ The used numerical model accurately predicts the wall response for the steel RC wall and the SE-SMA RC wall. However, future studies to improve the accuracy of the numerical model are needed. This includes accounting for bond-slip between the SMA bars and the mechanical couplers. The improvements need to be confirmed for shear walls with other heights and other ground motions.

❖ Additional experimental studies are needed to confirm the results of this research. Also, future studies should account for the vertical ground excitation.

❖ The materials properties used in the numerical model were based on previous experimental research. Uncertainty in material and numerical modeling should be considered in future studies.

❖ The selected ground motions in each chapter are satisfying the minimum code requirement. However, more ground motions are needed to enhance the accuracy of the numerical results.

❖ Mean square error is the methodology used to select the ground motions. Several other approaches should be considered for future studies.

8.4 RECOMMENDATIONS FOR FUTURE STUDIES

Excessive seismic residual deformations of structures may make the repair uneconomical or even impossible. This Ph.D. thesis investigated the use of SE-SMA material in RC walls to reduce the seismic residual deformations. The following recommendations are made for further investigations:

1- The proposed values for seismic design parameters can be extended to account for different SE-SMA structural systems such as coupled walls and dual system or wall with upper plastic hinges.

2- The behaviour of the SE-SMA RC dual system with different stiffness should be studied in three-dimensions in order to consider the torsion effect.

3- Numerical studies should be conducted to study the effect of torsion on SE-SMA RC core walls with a higher mode effect.

4- An experimental investigation is required to further understand the seismic behaviour of SE-SMA RC walls.

5- An experimental investigation is required to compare the seismic performance of walls reinforced with conventional steel bars, SE-SMA bars, and SMA-GFRP bars.

6- A numerical study on the influence of coupling the gravity system with the lateral system needs to be conducted.

CURRICULUM VITAE (NOV 12)

Emad A. Abraik

Ph.D. Candidate, EIT

Dept. of Civil and Environmental Engineering

Western University

PROFESSIONAL PREPARATION:

**-M.Sc. in Structural Engineering and Structural Dynamics
2010**

Utah State University, USA

Thesis: "Compassion the Seismic Performance of Buckling Restrained Braced Frame with Conventional Steel Frame"

**-B.S. in Structural Engineering
2003**

Omar Al-Mukhtar University, Libya

Graduated with Honors

PROFESSIONAL SUMMARY:

- Analysis and Design of Steel and Concrete Structures
- Base-Isolation Systems and structural control.
- Design of RC and Steel Bridges using AASHTO LRFD Bridge Design Specifications
- Performance-Based Earthquake Engineering
- Nonlinear Dynamic Analysis
- Risk-Assessment Methodology
- Design of Prestress Structures

AWARDS AND HONORS:

- Libyan Graduate Scholarship: 2008 ~ 2010
- Libyan Graduate Scholarship: 2014 ~ 2019
- 1_{st} in Bachelor of Engineering (B.Sc.) Examination (of 50 Students), Omar Almukhtar University, July 2003.

TEACHING EXPERIENCE:

Teaching Assistant at Western University

- Structural Dynamics, Fall 2014
- Concrete Design I, Fall 2016, Fall 2017, Fall 2018.
- Concrete Design II, Winter 2015, Winter 2016, Winter 2017

Lecture at Omar Almukhtar University

- Concrete Design I and II
- Bridge Design
- Design of Steel Structures I and II

TECHNICAL SKILLS:

- Engineering Tools: OpenSees, SAP 2000, STAAD PRO, ETABS, Revit, MATLAB, AutoCAD, Tekla Structures.
- Packages: MS Word, Excel, PowerPoint, Latex
- Code Provisions: AISC Manual for Steel Construction, AISC-ASD, AISC-LRFD, AISC-341, ASCE 7-16, ACI 318-14, IBC 2010, A23.3-14, NBCC 2015, ASHTO LRFD.
- Seismic analysis, retrofitting and capacity design of concrete and steel structures.

PROFESSIONAL AFFILIATIONS:

- Member, American Society of Civil Engineers (ASCE)
- Member, Canadian Society of Civil Engineers (CSCE)

JOURNAL PUBLICATIONS:

- **E. Abraik**, M. A. Youssef, "Seismic Fragility Assessment of Superelastic Shape Memory Alloy Reinforced Concrete Shear Walls," Journal of Building Engineering Research, 2017.
- **E. Abraik**, M.A.Youssef, " Ductility and overstrength of shape-memory-alloy reinforced concrete shear walls," Journal of Bulletin of Earthquake Engineering. Second review.

CONFERENCE PROCEEDINGS:

- **Emad Abraik**, M.A. Youssef, "Mitigation of seismic damage of conventional steel reinforced concrete shear walls," 12th Canadian Conference on Earthquake Engineering (12CCEE), Quebec, Canada, 2019, pp.

- **Emad Abraik**, M.A. Youssef, "Seismic performance of shape memory alloy reinforced concrete dual systems," 16th European Conference on Earthquake Engineering (16ECEE), Thessaloniki, Greece, Europ, 2018, pp. 326-333.
- **Emad Abraik**, M. A. Youssef, "Performance Assessment of Three-story Shape Memory Alloy Reinforced Concrete Walls". 5th International Structural Specialty Conference, London, ON, 2016.
- **Emad Abraik**, M. A. Youssef, "Cyclic Performance of Shape Memory Alloy Reinforced Concrete Walls." PROTECT2015 Conference on Response of Structures under Extreme Loading. MI, USA, 2015
- K.L. Ryan, P.J. Sayani, N.D. Dao, **E. Abraik**, Y.M. Baez, "Comparative life-cycle analysis of conventional and base-isolated theme buildings" 9th US National & 10th Canadian Conference on Earthquake Engineering, At Toronto, Canada, 2010